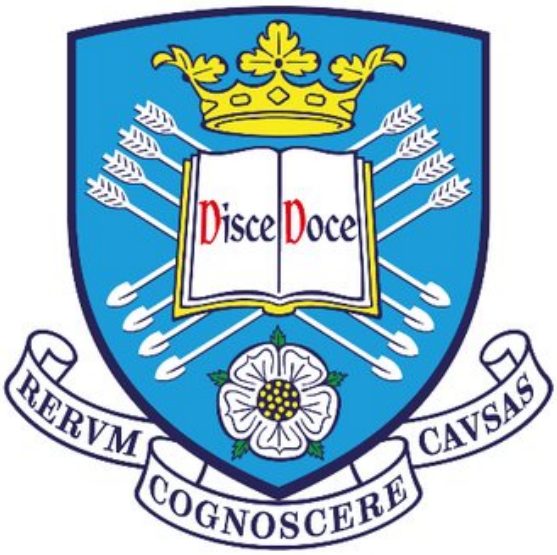

Investigation of Performance Improvement of Doubly Salient Synchronous Reluctance Machine with Current Harmonic Injection

Kai Zhang

A thesis submitted for the degree of Doctor of Philosophy

Department of Electronic and Electrical Engineering

The University of Sheffield, UK

4/19/2020

ABSTRACT

This thesis investigates some novel current harmonic injection methods to improve the electromagnetic performance of doubly salient synchronous reluctance machines (DS-SRMs). These machines will have different winding configurations, slot/pole number combinations and phase numbers. The theoretical analyses (both static and dynamic) are carried out based on Fourier Series analysis, and validated by 2-dimensional finite element method and also experiments using several prototype machines.

Based on the analytical torque model in *abc*-axis frame, a powerful insight into the mechanism of torque generation of the DS-SRMs with pure sinewave current supply can be achieved. The electromagnetic torque (both magnitude and phase angle) produced by each order of inductance harmonic can be predicted, which allows us to obtain the dominant torque ripple components for such machines. Therefore, the appropriate current harmonic (3^{rd}, 5^{th} and 7^{th}) can be injected to generate torque ripple components in order to compensate that produced by the fundamental current, and hence to achieve an overall reduced torque ripple. On the other hand, the average torque of the DS-SRMs can also be improved by properly selecting the current harmonics in terms of harmonic order, amplitude and phase angle. However, it is found that the current harmonics, although can improve torque performance, will often cause extra losses (both copper and iron losses) and undesirable distortion in the phase voltages, which could lead to negative impact on the machine efficiency and dynamic performance. Therefore, in order to fully evaluate the potential of the proposed harmonic current injection method, comprehensive studies about losses, efficiency and dynamic performances such as torque-speed curves of 3-phase and multi-phase DS-SRMs have been carried out. In order to simplify the investigation of dynamic performance analyses such as the torque speed curves and efficiency maps, novel analytical torque model in *dq0*-axis frame has also been proposed. The findings in this thesis can provide some useful guidelines for torque performance improvement of DS-SRMs using harmonic current injections.

ACKNOWLEDGEMENTS

First and foremost, I would like to express my sincerest thanks to my supervisor Dr. Guang-Jin Li for his continuous encouragement and support during the whole PhD study. Without his professional guidance, illuminating instruction, impressive kindness and patience, I could not have completed my PhD and this thesis. His enthusiastic and vigorous academic attitude inspire me not only in PhD study but also in my future career. I would also like to thank Professor Zi-Qiang, Zhu and Professor Geraint Jewell for their instructive advices to this thesis and publications from this work.

My sincere appreciation also goes to all my colleagues of the EMD group of the University of Sheffield. Thank you, Mr. Rui Zhou, Dr. Bo Ren, Dr. Xi-Yun Ma, Dr. Yan-Xin Li, Dr. Li-Ren Huang, Dr. Pei-Lin Xu and Mr. Xi-Meng Wu etc. for their valuable academic discussions and experimental assistances. I appreciate their encouragement and patience.

I owe much to my dear parents Mr. Yong-He Zhang and Mrs. Xie-Hai Yan, who have given the top educational resource and the opportunity to go abroad. Without their endless support and great love on me, it is impossible that I can complete my PhD study and this thesis.

Last, but not the least, I would like to express my gratitude to my beloved wife, Mrs. Ming-Hui Li for her love and encouragement.

CONTENTS

LIST OF ABBREVIATION

DS-SRM	Doubly salient synchronous reluctance machine
SRM	Switched reluctance machine
SynRM	Synchronous reluctance machine
SL	Single layer
DL	Double layer
FP	Fully pitched
MC	Mutually coupled
CSRM	Conventional switched reluctance machine
VFRM	Variable flux reluctance machines
MMF	Magneto-motive force
d-axis	Direct axis
q-axis	Quadrature axis
FEA	Finite element analysis
PF	Power factor
DC	Direct current
AC	Alternating current
ele. deg.	Electrical degree
mech. deg.	Mechanical degree
PM	Permanent magnet
VSI	Voltage source inverter
TSF	Torque sharing function
DITC	Direct instantaneous torque control
DTC	Direct torque control

PTC	Predictive torque control
RMS	Root-mean-square
CRMS	Constant RMS current condition
CPC	Constant peak current condition
2D	Two-dimensional
3D	Three-dimensional
SVPWM	Space-vector pulse-width-modulation

NOMENCLATURES

N_s	Stator slot number	
N_r	Rotor pole number	
p	Pole pair number	
T_e	Electromagnetic torque	Nm
i	Instantaneous phase current	A
θ	Rotor position	mech. deg.
θ_e	Rotor position	ele. deg.
ψ_a, ψ_b, ψ_c	Flux linkages of phases A, B and C	Wb
i_a, i_b, i_c	Instantaneous phase current of phases A, B and C	A
L_a, L_b, L_c	Self-inductances of phases A, B and C	mH
M_{ab}, M_{bc}, M_{ca}	Mutual-inductances of between phases	mH
v	Current harmonic order	
I_{rms}	Phase RMS current	A
I_1, I_v	Magnitude of fundamental and v^{th} order current harmonics	A
β_1, β_v	Phase angle of fundamental and v^{th} order current harmonics	ele. deg.
n	Inductance harmonic order	
L_0, L_n	Magnitude of fundamental and n^{th} order self-inductance harmonics	mH

M_0, M_n	Magnitude of fundamental and n^{th} order mutual-inductance harmonics	mH
α_n	Phase angle of n^{th} order self-inductance harmonic	ele. deg.
α'_n	Phase angle of n^{th} order mutual -inductance harmonic	ele. deg.
T_f, T_h	Torques due to fundamental or harmonic currents	Nm
T_{f0}, T_{h0}	Average torques due to fundamental or harmonic currents	Nm
T_{frip}, T_{hrip}	Torque ripple due to fundamental or harmonic currents	Nm
T_{fsel}, T_{hsel}	Torques due to self-inductances	Nm
T_{fmut}, T_{hmut}	Torques due to mutual-inductances	Nm
T_{max}	Maximum instantaneous torque	Nm
T_{min}	Minimum instantaneous torque	Nm
m	Phase number	
W_s	Average stator slot width	mm
W_t	Stator tooth width	mm
h_s	Slot height	mm
γ	Stator slot opening	mech. deg.
S_i	Stator inner radius	mm
R	Phase resistance	Ω
ρ	Resistivity of material	Ωm
S	Cross-sectional area of the copper wire	m^2

N	Number of turns per phase	
P_{cop}	Copper loss	W
B_m	Magnitude of flux density	T
B_r	Radial flux density	T
B_t	Tangential flux density	T
k_h	Hysteresis loss coefficients	W/kg/hz/T^2
k_e	Eddy current loss coefficients	W/kg/hz^2/T^2
P_{Fe}	Iron loss	W
P_{mech}	Mechanical loss	W
ω	Electrical rotor speed	rad/s
ω_m	Mechanical rotor speed	rad/s
P_{out}	Output power	W
η	Machine efficiency	
L_d, L_q, L_0	*d*-, *q*- and 0-axis inductances	mH
ψ_d, ψ_q, ψ_0	*d*-, *q*- and 0-axis flux linkages	Wb
v_d, v_q, v_0	*d*-, *q*- and 0-axis voltages	V
i_d, i_q, i_0	*d*-, *q*- and 0-axis currents	A
V_{max}	Maximum voltage	V
V_{dc}	DC link voltage	V
I_{max}	Maximum current	A

T_a, T_b, T_c	Self-torques of phases A, B, C	Nm
T_{ab}	Mutual-torque between phases A and B	Nm
$v_\alpha, v_\beta, v_\gamma$	α-, β- and γ-axis voltages	V

Chapter 1 GENERAL INTRODUCTION

1.1 INTRODUCTION

Due to the advantages of high torque density, high efficiency, high power factor and reliability, the permanent magnet (PM) machines are extensively used in industrial applications, such as electric vehicles, aerospace actuation and renewable energy. However, the main disadvantages such as high price due to rare-earth PMs reduces the attraction of PM machine in cost-sensitive applications such as domestic appliances and handhold power tools, etc. Additionally, potential irreversible demagnetization due to high currents or temperatures and the fragile properties of PM are also challenges facing the design of PM machines.

As a result, the motivation to develop PM free machine without sacrificing too much torque capability are increasingly strong. The switched reluctance machines (SRMs) are one of the most popular research directions. As shown in Fig. 1.1 (a), with no PM and windings on the rotors, it can essentially reduce the machine costs, and their simple and robust structure, high manufacturability, good fault tolerance and high speed and high temperature operation capabilities brought them strong competitiveness for automotive and aerospace applications [1]. However, the doubly salient structure leads to inherent drawbacks, such as high torque ripple, vibrations and acoustic noise, which significantly limit their market penetration into sectors that are sensitive to these issues. Moreover, due to the unbalanced phase current excitation, an unconventional converter (asymmetrical H-bridge inverter as shown in Fig. 1.2) is required for SRMs, which is another factor that limits the wide use of such machines.

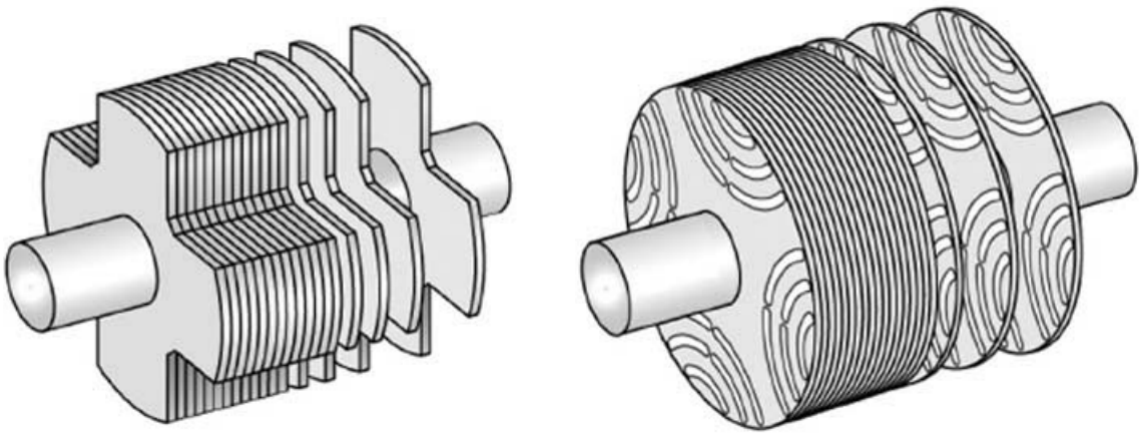

(a) SRM (b) SynRMs

Fig. 1.1 Rotor structures for SRMs and synchronous reluctance machines (SynRMs) [2].

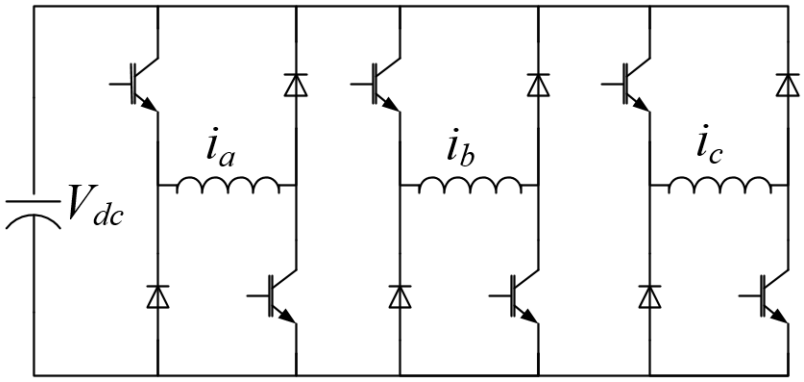

Fig. 1.2 3-phase asymmetrical half-bridge converter for SRMs [3].

Similar to SRMs, the synchronous reluctance machines (SynRMs) also have no magnets or field windings on the rotor as shown in Fig. 1.1 (b). However, the SynRMs are supplied with sinewave current, so that the conventional off-the-shelf voltage source inverter (VSI) for synchronous machines or induction machines can also be employed for SynRMs. In order to increase the saliency ratio and performance, the SynRMs have flux barriers inside the rotors [2]. However, it potentially leads to lower rotor robustness and lower manufacturability compared to SRMs. In order to combine the benefits of adopting a standard VSI and also achieving robust salient pole rotor, the SRMs were supplied with sinewave current in [4], which essentially becomes a doubly salient synchronous reluctance machines (DS-SRMs). Compared with conventional SynRMs (distributed winding), the short-pitched concentrated winding can reduce the copper loss, improve the efficiency and torque density of the DS-SRMs [5]-[7]. However, the main weakness of the DS-SRMs is the relatively high torque ripple, which to some extent reduces the attractiveness of this configuration.

To cope with this issue, numerous researches focus on the design aspects, such as, stator/rotor shewing and shaping [8]-[10] to make the airgap flux density more sinusoidal. Other researches from control aspects have also been carried out, for example, the torque sharing function [11]-[13], the direct instantaneous torque control (DITC) [14] and phase current optimization [15],[16], etc. Therefore, in this chapter, the state-of-the-art SRMs, SynRMs and the relevant methods for torque performance improvement are reviewed, providing a powerful insight into the potential of reluctance machines. TABLE 1.1 lists the comparison features of three types of machines that are widely investigated in academia and also industry.

TABLE 1.1 THE COMPARATIVE FEATURES OF THREE TYPES OF MACHINES [17], [18]

	Advantages	Disadvantages
PM machines	• High torque density • High efficiency • Low weight and volumetric dimension • Low acoustics noise	• High cost • Low rotor robustness • Prone to irreversible demagnetization • High potential short-circuit current
SRM	• Simple structure • No permanent magnets • Low manufacture cost • High temperature and speed	• Doubly salient structure • Asyemmtric converter • High torque ripple • High vibration and acoustics noise
SynRM	• No permanent magnets • High efficency • Off-the-shelf converter	• Lower rotor robustness (with respect to SRM) • Lower manufacturability (with respect to SRM)

1.2 DEVELOPMENT OF SWITCHED AND SYNCHRONOUS RELUCTANCE MACHINES

1.2.1 SWITCHED RELUCTANCE MACHINES

SRMs are stepper motors which only produce reluctance torque and were first presented by Robert Davidson in 1839 [19]-[21]. The torque of the SRMs is produced due to the tendency of the rotor moving towards a position where the permeability of the exciting winding is the maximum. The conventional SRMs (CSRMs) have salient poles on both the stator and the rotor. The simplest SRMs is with 2 stator slots and 2 rotor poles, written as 2s/2p, which is a single phase machine, as shown in Fig. 1.3 (a). The two coils on the stator are excited at the same time. At the specific rotor position as shown in Fig. 1.3 (a), the rotor tends to be rotated anticlockwise to the aligned position as shown in Fig. 1.3 (b), in order to minimize the airgap length. Therefore, this type of machine can only produce torque in a limited arc of rotation, which is relevant to the stator pole arc. Moreover, the unaligned position, as shown in Fig. 1.3 (c), is where the winding inductance is the minimum.

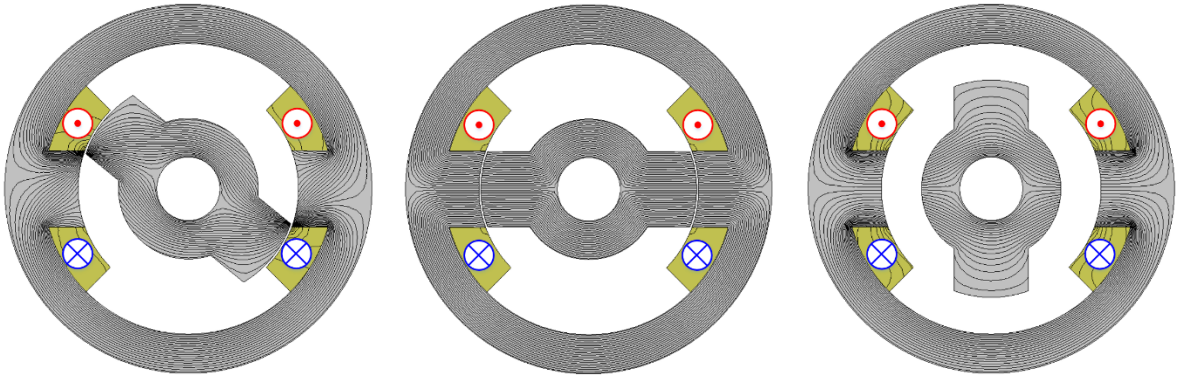

(a) Start of overlap (b) Aligned position (c) Unaligned position

Fig. 1.3 Flux distribution at different rotor positions for a 2s/2p single phase SRM.

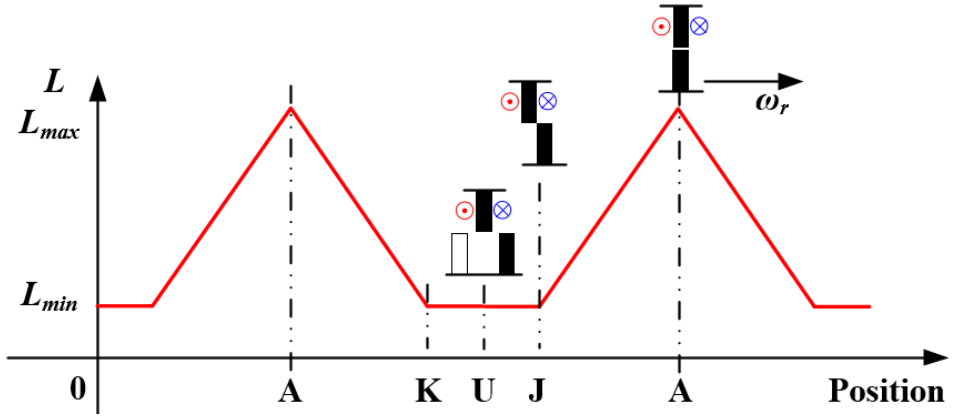

(a) Ideal inductance waveform

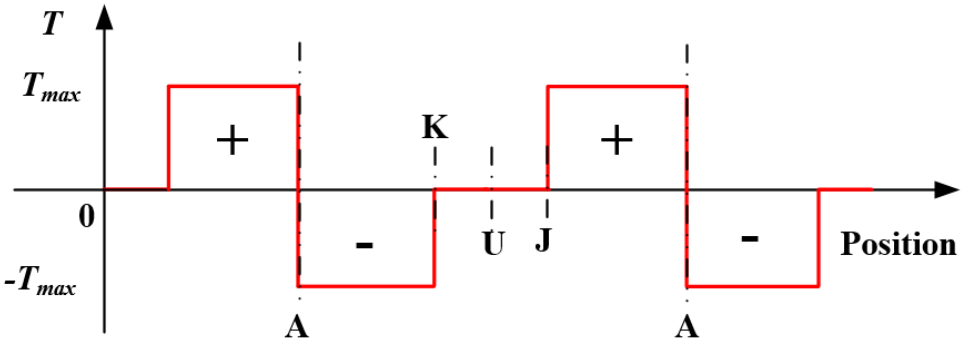

(b) Ideal torque waveforms waveform

Fig. 1.4 Ideal inductance and torque waveforms *vs* rotor position with constant coil current. A: aligned position; U: unaligned position; J: start of overlap; K: end of overlap.

For such simple machine, when the coil is excited with a constant current I_{max}, the idealised inductance waveform respects to rotor position can be shown in Fig. 1.4 (a). If anticlockwise is defined as the positive rotation direction, the positive torque only occurs when the inductance is rising in positive direction, which is from position J to A. After the rotor passes through the aligned position, the torque direction will be reversed and the breaking torque will be generated

to bring the rotor back to the aligned position. As a result, the positive and negative torques will cancel one another out, and the resultant average torque during one electrical period is always zero. Therefore, in order to remove the negative torque, the current in the coils has to be switched off when the rotor passes the aligned position, i.e. A to K.

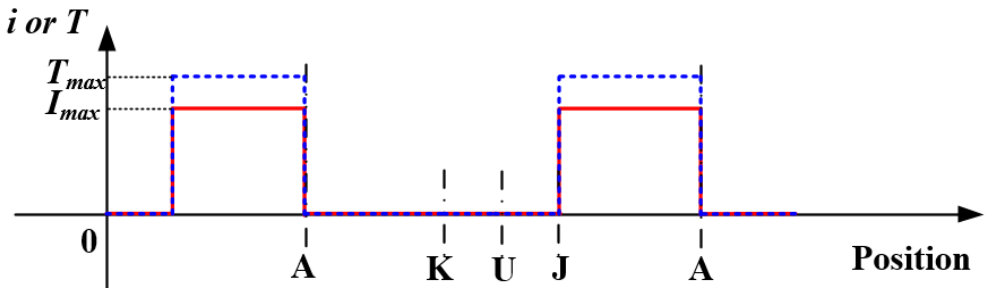

Fig. 1.5 Torque and ideal unipolar current waveform for SRMs.

Therefore, the ideal unipolar currents are a series of pulse and excited when the inductance is rising. The ideal torques have the same waveforms as the pulse current as shown in Fig. 1.5. The torque equation at linear condition of a single phase machine is given by (1.1).

$$T = \frac{1}{2} i^2 \frac{dL}{d\theta} \tag{1.1}$$

It is worth noting that the duration of the torque production due to a single coil excited is called one stroke. In order to obtain continuous torque, several more phase coils are required to fill the gaps in the torque waveform shown in Fig. 1.5. The common converter used to produce the unipolar pule current is asymmetrical half-bridge converter. Here, Fig. 1.2 shows the converter topology for a typical 3-phase SRMs. It is worth noting that in practice, the current in the coil cannot be excited in the perfect step fashion, due to the fact that the inductance at start of the stroke (position J) is not zero. Despite all that, the inductance along UJ is still very small, which leads to a significant current rise in a very short period, i.e. high *di/dt*. Consequently, the power electronics were always the main challenge of controlling SRMs and limited their application until 1965 [22]. With the development of power semiconductors and also microcontrollers with high speed processing capability, the SRMs started to attract increasing interest for variable speed applications [23].

Based on the concept of the simplest SRMs, over the years, researchers have proposed several configurations to improve the performance of SRMs. These innovations can be initially classified into two parts, i.e. stator and rotor topologies, as shown in Fig. 1.6. And this section will briefly review the existing topologies of SRMs and their achievements and limitations up to date.

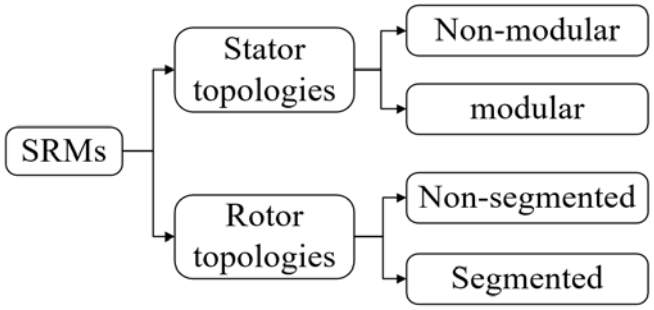

Fig. 1.6 Classification of SRMs.

1.2.1.1 STATOR TOPOLOGIES

A). NON-MODULAR STATORS

Conventional SRMs (CSRM) with non-modular salient poles on the stator and short pitched concentrated winding are the most common structures [19]. Using a common 3-phase 6s/4p CSRM for example, as shown in Fig. 1.7 (a), the magnetic polarities of phase A are NS. It can be found that such winding configuration maximizes the self-linked magnetic flux, while the mutual-flux between adjacent phases can be neglected. Each phase will be excited in sequence to contribute to the continuous torque. However, in order to increase the electromagnetic utilization of the machine, a new SRM topology with fully pitched windings (FP) has been developed, as shown in Fig. 1.7 (b) [24],[25]. At a cost of longer end-winding, the torque capability can be significantly improved. Moreover, there are two or more phases conducting at any instant for the FPSRM, therefore, for the same output power, each phase will carry out half of the current compared to the CSRM, which may bring benefits for the power converter. However, due to longer end-winding and also higher phase resistance, the advantage of FPSRM could be compromised, depending upon load condition and excitation sequence. In order to combine the advantages of CSRM (short end-winding) and FPSRM (high torque capability), the mutually coupled SRMs (MCSRMs) have been proposed in [17],[26],[27]. As shown in Fig. 1.7 (c), different from CSRM, the magnetic polarities of the phase A for MCSRMs are NN. This is the same for other phases such as phases B and C. With such winding configuration, the magnetic paths of exciting coil are changed and the magnetic flux in stator yoke are forced into different flux paths. As a result, the MCSRMs is less sensitive to magnetic saturation than the CSRM and the FPSRM. This means that the MCSRMs can achieve better overload capability [28].

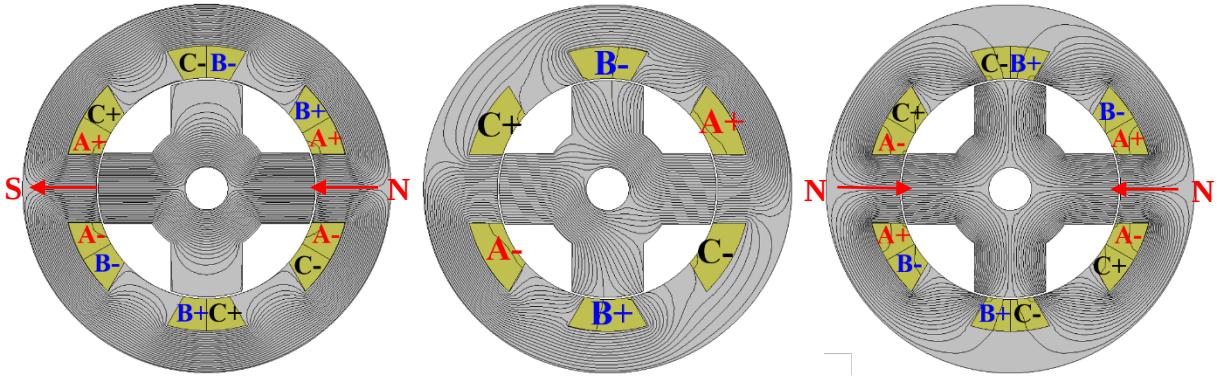

(a) CSRM (b) FPSRM (c) MCSRM

Fig. 1.7 Winding configurations and flux line distributions of typical 3-phase 6s/4p SRMs. In these figures, only the phase A is supplied with a DC current.

Due to flux distribution, the optimum excitation sequence for different winding topologies are different. In [29],[30], the influence of conduction angles for three stator winding and their single layer counterparts have been investigated. It has been found that the unipolar 120° elec. conduction shows the best performance for the CSRMs, while the bipolar 360° elec. conduction presents the best performance for the FPSRMs and the bipolar 360° elec. conduction is more suitable for the MCSRMs.

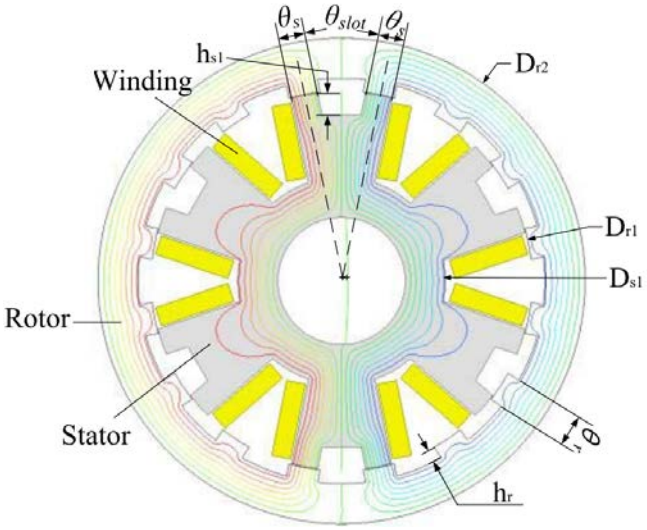

Fig. 1.8 SRMs with multiple teeth per stator pole External rotor [31],[32].

On the other hand, some novel SRMs with multiple teeth per stator pole was designed and analysed in [31],[32], as shown in Fig. 1.8. The topologies combined the advantage of multi-teeth and higher rotor pole number. Due to higher output torque, efficiency and lower torque ripple compared with CSRM, the multiple teeth stator with external rotor structure is potentially a promising candidate of light weight EV application.

B). MODULAR STATORS

Modular stators, due to the advantages such as simpler manufacture process, higher reliability, better fault-tolerant capability and less material consumption compared to non-modular stators, are attracting growing interests for SRMs. The two typical types of SRMs with modular stator or segmented stator, i.e. E-core and C-core, are presented in [33] and [34], respectively. In [33], a 2-phase modular SRM with E-core as shown in Fig. 1.9 (a) has been proposed and compared with a 4s/2p CSRM. It has been found that the E-core stator can significantly reduce the stator material consumption by up to 22%, which reduces the total machine cost. Moreover, the torque density and efficiency of such machine are improved. In order to further improve the performance of the E-core SRM, a 9s/12p topology has been proposed by increasing the number of E-cores from 2 to 3 as shown in Fig. 1.9 (b). Due to the adjacent spaces that have been fully utilized, the torque density (Nm/kg) can be increased by 14%.

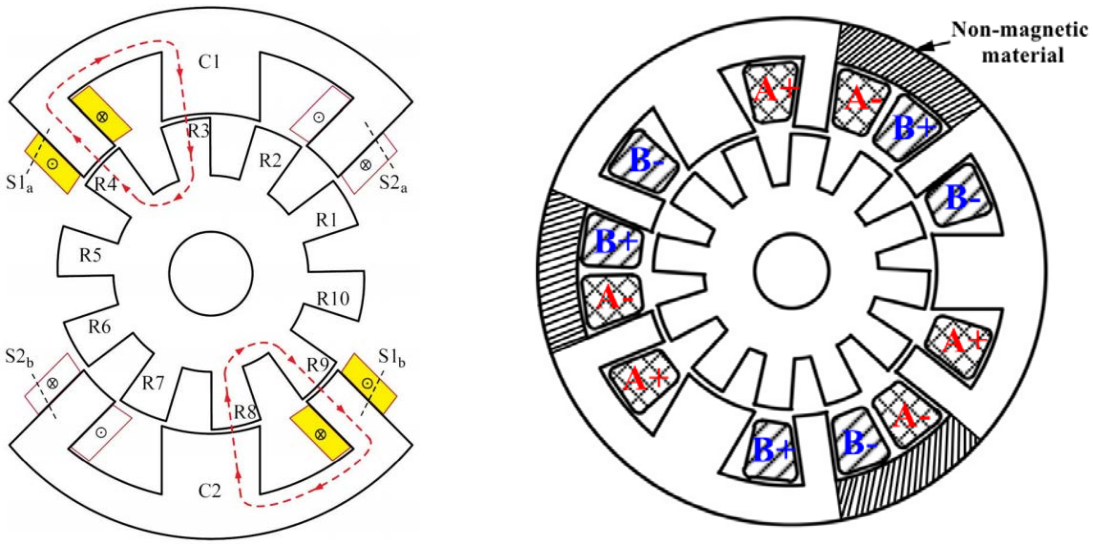

(a) 2 E-core stator (b) 3 E-core stator

Fig. 1.9 2-phase SRMs with E-core modular stators [33],[35].

In [35], researchers adopted the E-core stator SRMs with a stator-slot/rotor-pole number combination of 12s/14p and investigated the influence of flux gap widths on the machine performance. It has concluded that the modular SRMs are promising candidates for lower vibration and acoustic noise applications, due to their lower radial force.

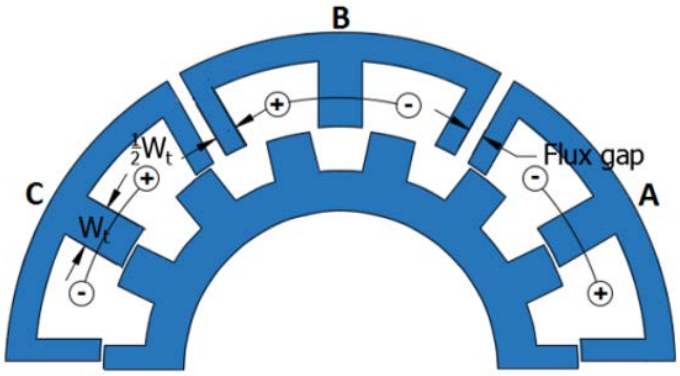

Fig. 1.10 Cross-section of 12s/14p SRM with E-core stator [35].

In [36], a novel 3-phase E-core modular SRM with different rotor topologies is analysed, modelled and experimentally tested. The two modular SRMs, in Fig. 1.11, show almost the same electromagnetic performance. However, the one with segmented rotor enables 40.3% cost saving in rotor iron core. Moreover, it achieves much faster acceleration (low inertia) compared with conventional non-segmented rotor counterpart. It has been proved that these two modular SRMs, no matter with segmented rotor or not, offer higher torque density and lower torque ripple compared with CSRMs.

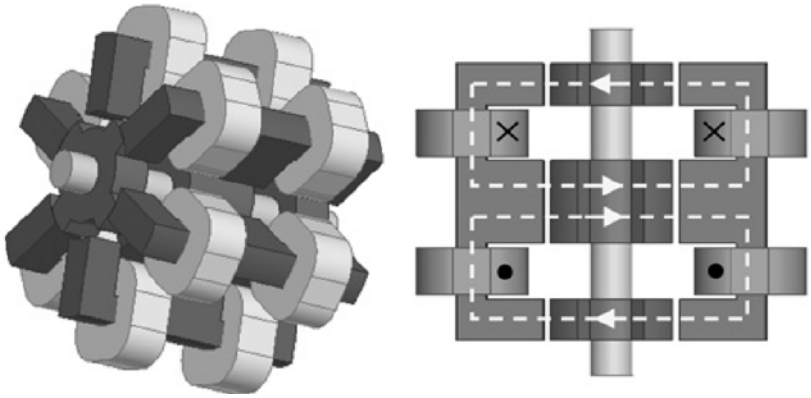

(a) E-core stator with segmented rotor

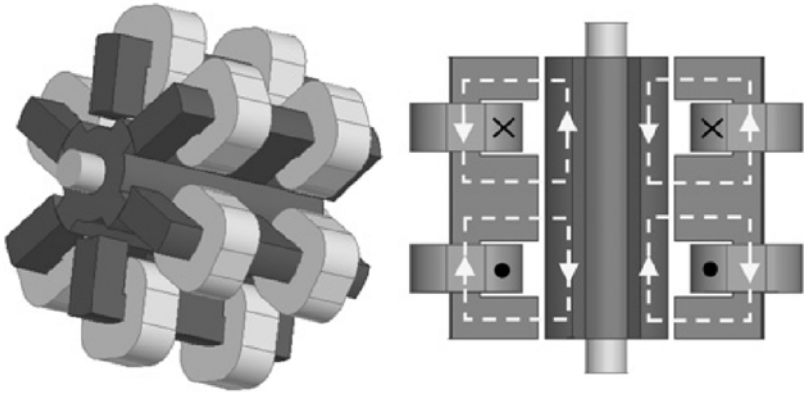

(b) E-core stator with conventional non-segmented rotor

Fig. 1.11 Modular SRMs with toroidal winding and segmented and non-segmented rotors [36].

Apart from the E-core stator, the C-core is another common modular stator structure for SRMs. In [34], the author proposed a 3-phase 6s/5p modular with C-core stator as shown in Fig. 1.12 (a). Since each phase has an independent group of C-core segments, which leads to physical, thermal and also electromagnetic isolations between windings of different phases, the motor achieves excellent fault-tolerant capability. However, higher vibration and acoustic noise due to unbalanced radial forces is one of the main disadvantages of such topology. Therefore, in [37],[38], two different topologies for the C-core SRMs were proposed to improve the performance and also to achieve lower acoustic noise. In [39],[40], a toroidal winding SRM with C-core stator is proposed, which is much similar to the winding shown in Fig. 1.12 (b) and with single coil wound in the back iron of the stator. Such structure also provides physical, thermal and also electromagnetic isolations between phase windings, consequently offering a better fault tolerant capability. Moreover, shorter magnetic flux paths of this modular SRM reduces the stator and rotor core iron losses compared to the CSRMs. Similarly, in [41], a novel radial-field 4-phase C-core modular SRM is proposed, as shown in Fig. 1.13. This topologies has shorter magnetic flux path, which offers higher efficiency compared with the CSRM. In addition, its flexible structure is also a good fit for EV application, where the rotor can be easily removed without affecting the stator.

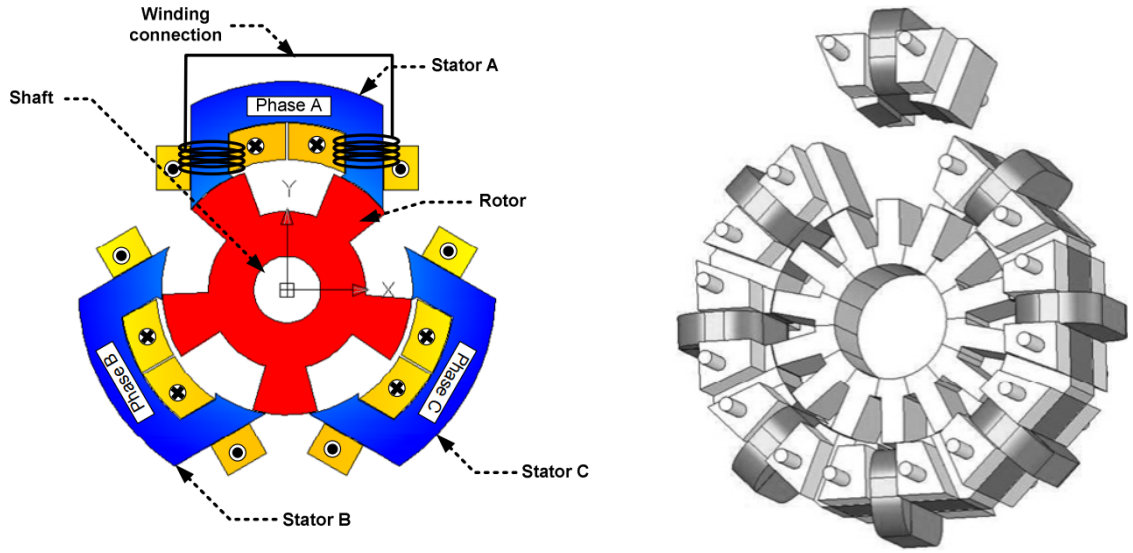

(a) 6s/5p (a) 16s/14p

Fig. 1.12 Modular SRMs with C-core segmented stator [34],[39],[40].

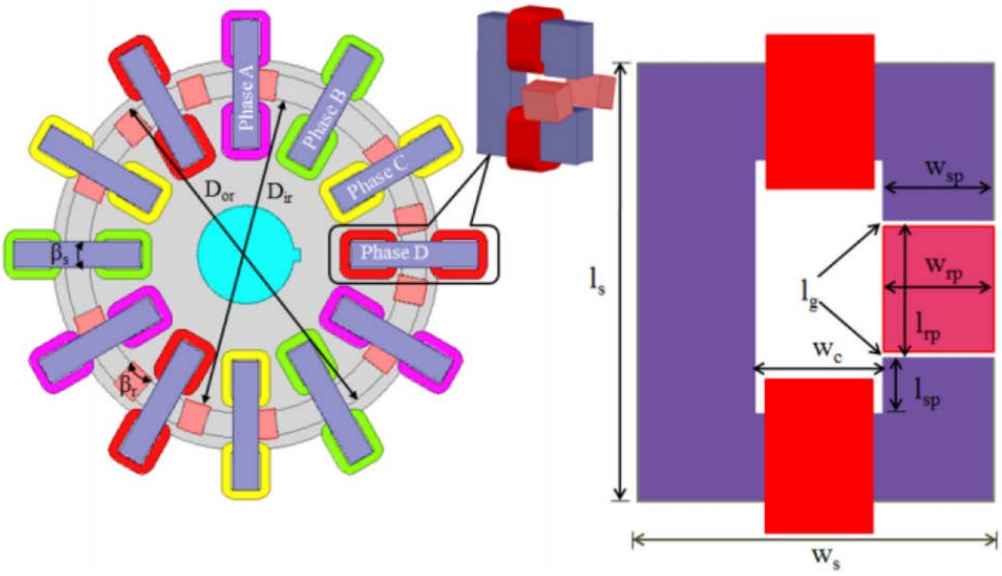

Fig. 1.13 4-phase 12s/15p radial field SRMs with C-core segmented stator [41].

1.2.1.2 Rotor Topologies

A). Non-Segmented Rotors

Since the CSRMs already have very simple and robust rotor structure, there are only limited parameters to play with the conventional salient pole rotor. The parameters that can be changed are the number of rotor poles, rotor pole arc and length of tooth body, etc. In [42], for the conventional doubly salient structure, the authors have concluded that the slot/pole number combinations can be 6n/2n, 6n/4n and 6n/8n for 3-phase machines; 8n/6n and 8n/10n for 4-phase machines, where n is integer number from 1 to 4. The groups with 6n/2n slot/pole number combination can potentially reduce the acoustic noise and improve the starting torque of the machine. In [43], authors introduced some SRMs with slot/pole number combination n/(2n+2), i.e. 6/14 SRM, for reducing the acoustic noise. In [44],[45], a novel rotor pole design formula were proposed, i.e. $N_r = 2N_s - 2$, where N_s is the stator slot number and should be larger than 4 and N_r is the rotor pole number. It is proven that such redundant rotor pole design can exploit torque capability and suppress the torque ripple compared with the CSRM.

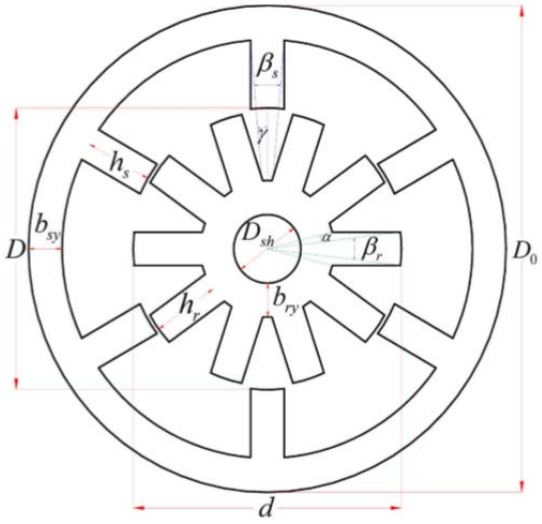

Fig. 1.14 Geometrical dimensions of the 6s/10p SRM [44].

B). SEGMENTED ROTORS

On the other hand, many researchers have also been focusing on the SRMs with segmented rotors for potential machine performance improvement. The first synchronous reluctance machine with segmented rotor is developed by Lawrenson in 1960s [22],[46]. In 2002, Mecrow proposed a novel segmented rotor structure for SRMs, as shown in Fig. 1.15 (a) [47]. The new machine has doubled the active airgap area compared to a CSRM, hence, achieves better magnetic circuit utilization. It has proven that the machine produces over 40% more torque than its conventional counterpart. However, its copper consumption is increased due to its longer end-winding (fully-pitched – FP winding has been adopted). To address the long end-winding issue, in [48],[49], a novel segmented rotor SRM with concentrated winding has been proposed, as shown in Fig. 1.15 (b). It not only retains all the advantages of the fully-pitched segmented rotor SRM, but also has much shorter end-winding and hence produces lower copper losses at the same phase current. In [50], a redundant segmented rotor design has been proposed, which has been compared with existing segmented rotor machine. Higher number of rotor segments than stator poles offers significant advantages at low speed and low current, while with increasing speed and phase current, the torque performance is compromised, due to higher iron loss and also magnetic saturation. The influence of slot/pole number combinations and phase number on the performance of the segmented rotor SRMs has been investigated in [51]. It is found that machines with high multiplicity (such as 12s/8p, 18s/12p, 24s/16p, etc.) compared to 6s/4p can achieve higher torque capability and wider speed operation at a cost of lower efficiency at low load condition and higher inverter power rating.

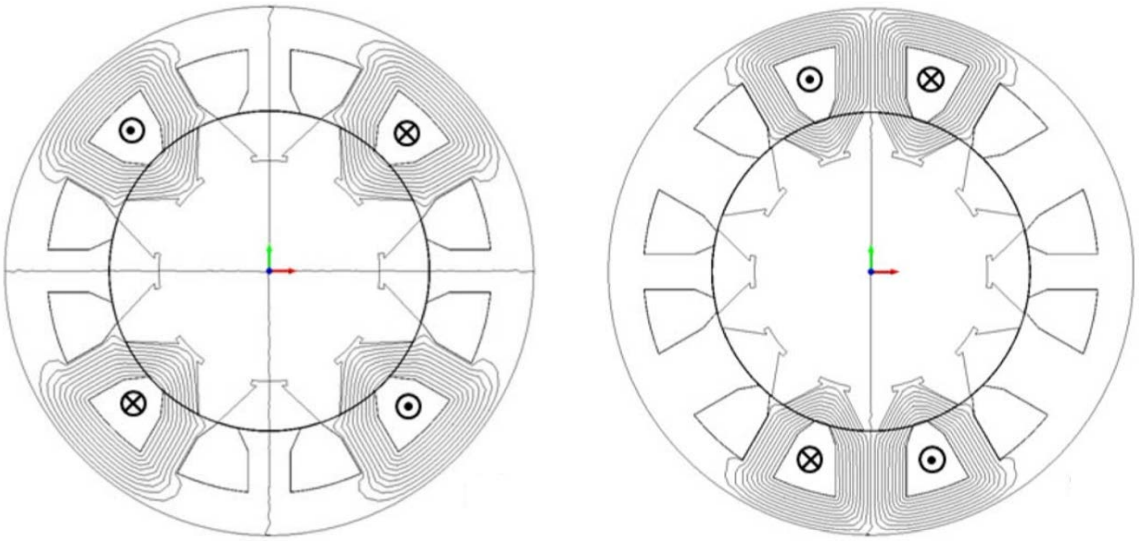

(a) 12s/8p FP (a) 12s/10p SL

Fig. 1.15 Two typical winding configuration of segmental rotor SRMs [47]. FP stands for fully-pitched and SL stands for single layer.

1.2.2 SYNCHRONOUS RELUCTANCE MACHINE

Synchronous reluctance machines (SynRMs) are competitive candidates for the high performance and low price applications. Due to the fact that sinewave current is supplied, SynRM can use exactly the same drives as that of induction machines and PM machines, leading to reduced power converter cost. SynRMs are considered as a singly salient machine in which only the stator is constructed with mechanically and magnetically salient poles [52]. However, the rotor is not mechanically salient (only magnetically salient to generate reluctance torque). Their stators often employ the distributed overlapping winding, which is the same as that of induction machine as shown in Fig. 1.16 (a). Such structure can produce more sinusoidal rotating magneto motive force (MMF) in the airgap, so as to retain the main benefits of SRMs such as magnet free and simple machine structure while at the same time it can overcome the main disadvantages such as high acoustic noise and torque ripple.

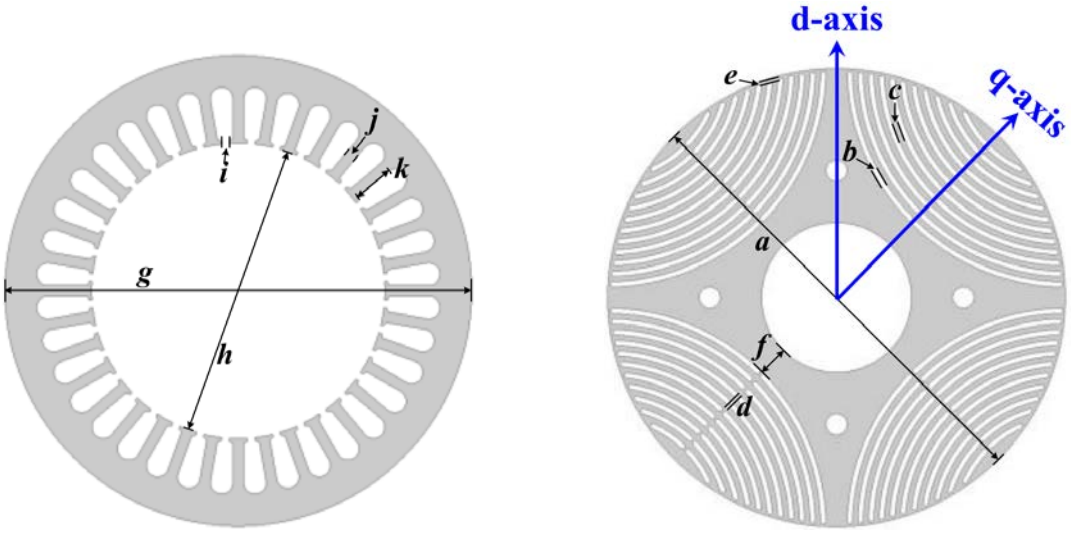

(a) Stator (b) Rotor

Fig. 1.16 Stator and rotor for a typical SynRM [53].

The electromagnetic torque of SynRMs is purely due to the reluctance variation against rotor position, which can be calculated by (1.2). The *dq*-axis currents relating to the space vector components of stator winding MMF along the direct- (*d*-) and quadrature- (*q*-) axes are shown in Fig. 1.17.

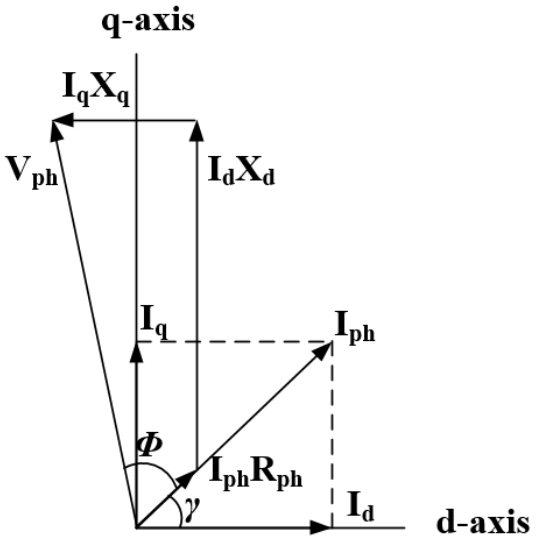

Fig. 1.17 Phasor diagram of a typical SynRM.

$$T = mpI_dI_q\left(L_d - L_q\right) = \frac{mp}{2}I_{ph}\sin 2\gamma\,(L_d - L_q) \tag{1.2}$$

where *m* is the phase number, *p* represents the pole pair number, γ is current phase angle, I_d, I_q are *d*- and *q*-axis current, respectively, I_{ph} is phase peak current and the L_d and L_q are the *d*- and *q*-axis inductances, respectively. It is worth noting that X_d and X_q are the impedance of *dq*-

axis and can be calculated by $2\pi f L_d$ and $2\pi f L_q$, respectively, where f is the synchronous frequency of the phase current. According to (1.2), the torque production is proportional to the difference between dq-axis inductances and the maximum torque occurs when γ is equal to 45°. This is under the assumption that the magnetic material is linear and no saturation occurs. It is worth noting that the saliency ratio ($\xi = \frac{L_d}{L_q}$) is one of the most important factors for SynRM, which not only determines the torque capability of the machine, but also the power factor (PF) and the constant torque speed region, etc.[54]. Generally speaking, higher ξ often means better machine performance. SynRMs are always considered as machines with poor power factor, which is closely corresponding to the inverter power rating. The PF for fundamental current supply with the phase resistance being neglected can be calculated by [54]:

$$\mathrm{PF} = \cos\phi = (\xi - 1)\sqrt{\frac{\sin 2\gamma}{2(\tan\gamma + \xi^2 \cot\gamma)}} \tag{1.3}$$

$$\mathrm{PF}_{max} = \cos\phi = \frac{\xi - 1}{\xi + 1} \text{ with } \tan\gamma = \sqrt{\xi} \tag{1.4}$$

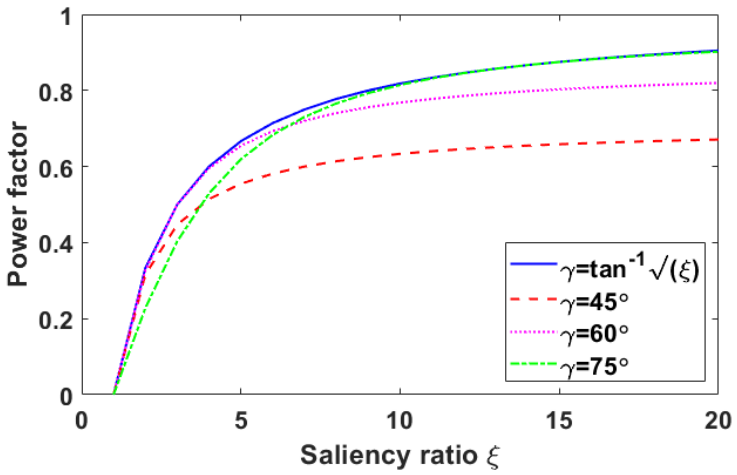

Fig. 1.18 Power factor vs saliency ratio.

Fig. 1.18 shows the power factor versus saliency ratio for different current phase angles. It can be seen that for the SynRM with a saliency ratio of 9, the maximum power factor can be 0.8. However, when $\gamma = 45°$ (maximum torque production), the PF is still less than 0.7 even the saliency ratio is increased to 20. Therefore, the improvement of saliency ratio remains one of the most important challenges facing the SynRMs.

1.2.2.1 ROTOR TOPOLOGIES

The first theoretical and technological analysis of SynRM can be traced back to 1923 by Kostko [55]. He proposed a cylindrical rotor with several flux barriers along the *d*-axis, as shown in Fig. 1.19 (a). This study established the direction for the designs of rotors for SynRM, including the flux barriers, segmentations and reluctance slots. Kostko also pointed out that the salient pole shown in Fig. 1.19 (c) generates poor saliency ratio. This is due to the fact that although the *q*-axis inductance is extremely reduced, the pole arc is reduced as well, leading to the undesired reduction in *d*-axis inductance. The researchers in [55] proved that the saliency ratio of salient pole structure was less than 3.8.

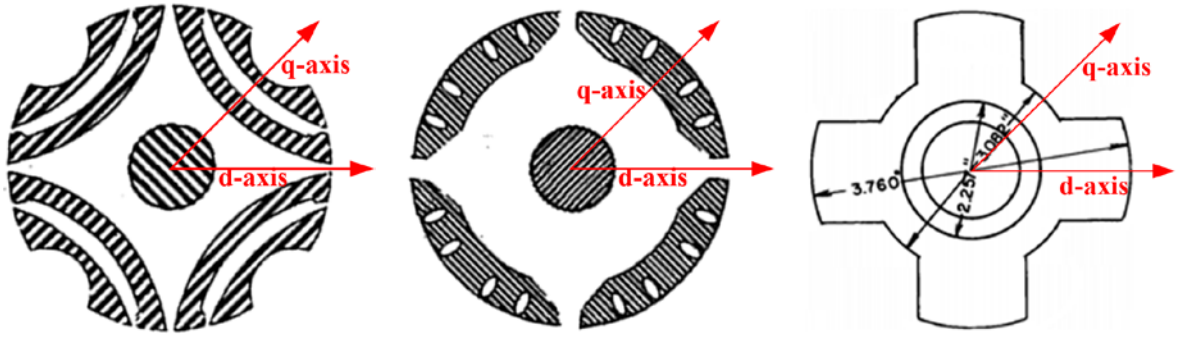

(a) Segmented iron pieces and flux barriers (b) Segemented rotor (c) Salient pole rotor

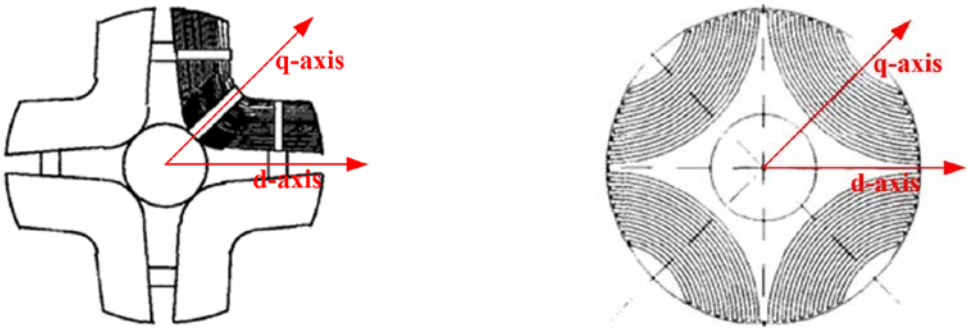

(d) Axially laminated rotor (e) Transversally laminated rotor

Fig. 1.19 Typical rotor structures of SynRMs [22],[52],[55],[56].

In 1960s, the segmented rotor was highly developed and the highest value of saliency ratio can be 10.7 (no-load) and 5.3(on-load) shown in Fig. 1.19 (b) [22],[57]. Apart from the segmented rotor, the axisially laminated rotor as shown in Fig. 1.19 (d) is another solution which can achieve higher torque density and power factor [51]. However, such structure is extreme challenging for manufacturing, which limits its practical applicability. Moreover, axially laminated rotor is not suitable for high speed operation due to larger iron losses and potentially lower mechanical stiffness. In practice, the transversally laminated rotor, as shown

in Fig. 1.19 (e), is much more manufacturing friendly [2] due to the fact that all laminations have the same shape with several flux barriers in each lamination. The narrow iron bridges between flux barriers provide some mechanical support against the centrifugal force, which is still a problem for high speed operation. Overall, the transversally laminated rotor has attracted increasing interest for modern industry, and further review will be carried out in following section.

1.2.2.2 FLUX BARRIERS

In the existing literature, lots of researches have been carried out to optimise the flux barriers of SynRMs, and the optimization can be classified into two categories, namely, barrier shapes and numbers. For the shapes of flux barriers, the round and angled shapes as shown in Fig. 1.20 are the most popular options [58]. The optimal parameters of angled flux barrier is more than that of the round ones. It has been found that the round shape flux barrier offers slightly higher average torque than the angled flux barriers [59]. Moreover, due to the regular shape of angled flux barrier, permanent magnets can be inserted into the rotor, leading to a PM assisted SynRM, which can achieve higher torque capability and wider constant torque speed range.

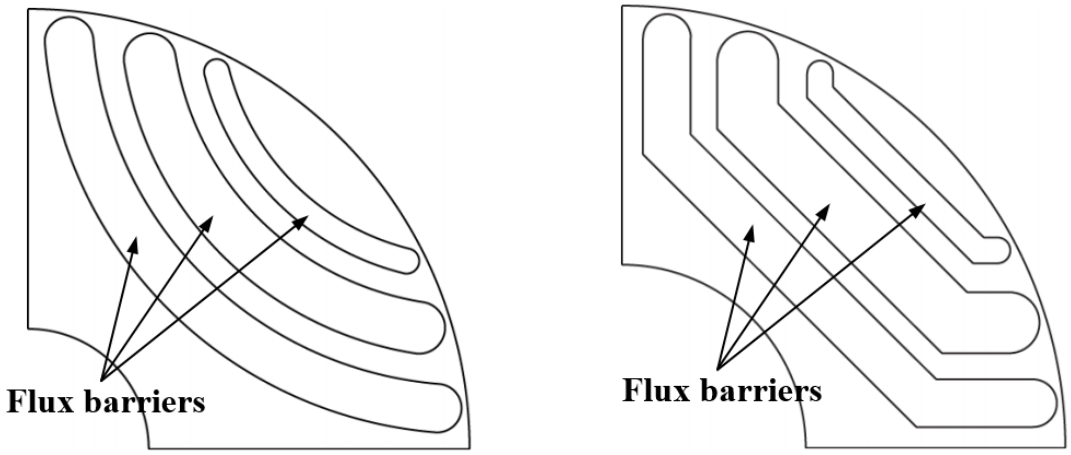

(a) Round flux barriers (b) Angled flux barriers

Fig. 1.20 Flux barriers with different shapes [58].

The number of flux barrier is another factor that can influence the performance of SynRMs. Fig. 1.21 shows the rotors with different numbers of flux barriers from 1 to 6. In the literature, it has been found that higher number of flux barrier shows good potential in average torque [54]. In order to achieve the minimum torque ripple, the machine should be designed so that the number of slot, the number of rotor poles and also the number of flux barriers should match the rule expressed by (1.5) [60].

$$n_r = n_s \pm 4 \tag{1.5}$$

where n_s represents the number of stator slots per pole pair and n_r is the number of equivalent rotor slots per poles pair. Once n_s is fixed, n_r can be controlled by changing the number of flux barriers to achieve the minimum torque ripple. Authors in [61],[62] have drawn a similar conclusion. For example, for a 24s/4p SynRM, 3 flux barriers can achieve the lowest torque ripple. Moreover, authors in [60] pointed out that the stator core iron losses are increased with increasing number of flux barriers, while opposite trend has been observed for the rotor iron losses. Hence, the number of flux barriers for mimium iron losses needs to be analysed on a case by case basis and no general rule can be established.

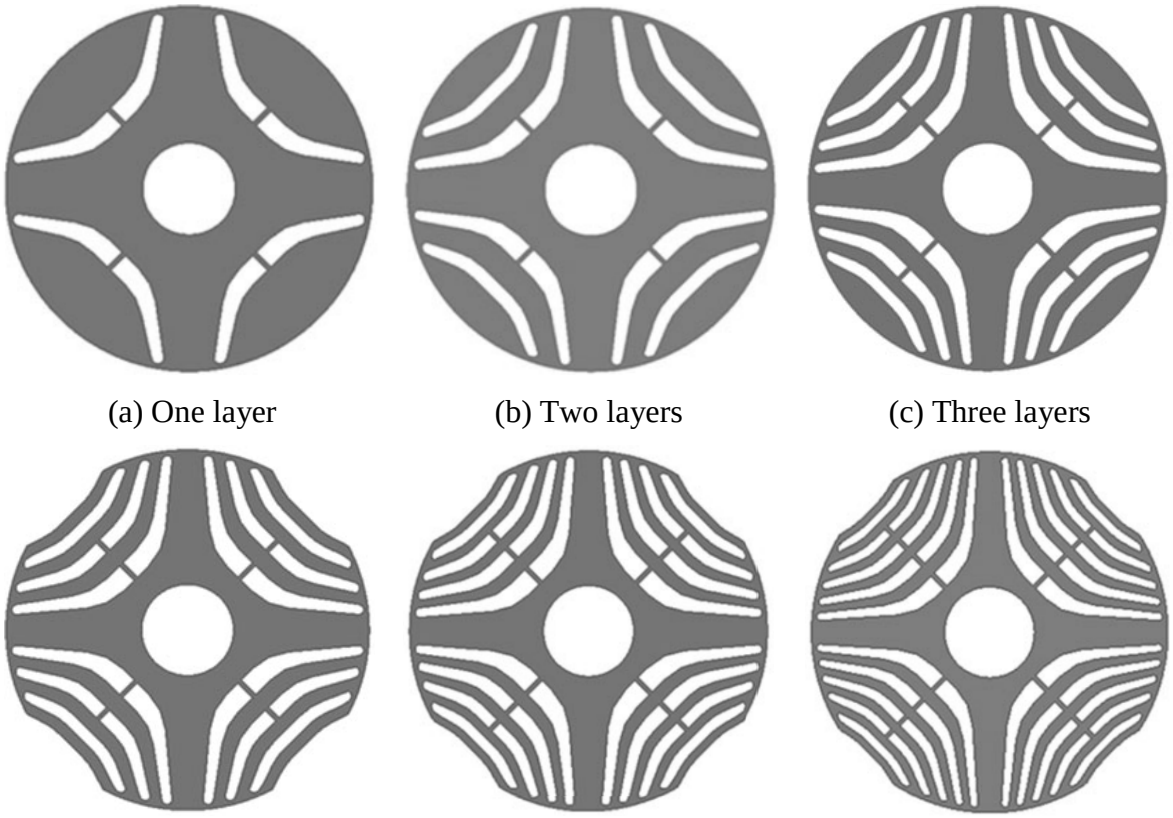

(a) One layer (b) Two layers (c) Three layers

(d) Four layers (e) Five layers (e) Six layers

Fig. 1.21 Rotor topologies with different numbers of flux barriers [63].

1.2.2.3 WINDING CONFIGURATIONS

Conventional SynRMs often adopt the integer slot distributed winding for less harmonic in the airgap flux. Therefore, the stator slot number can be simply calculated by:

$$N_s = kpm \tag{1.6}$$

where *p* is the rotor pole number, *m* represents the phase number and *k* is the slot number per pole per phase. For fixed phase number, e.g. 3-phase, there are two ways to change the slot/pole

combinations, i.e. p and k. Keeping k as a constant value 1, the influence of p (from 4 to 8) on the torque production has been investigated in [62]. The conclusion can be drawn that the torque capability is reduced with increasing pole number, while the torque ripple is hardly affected if the same slot/pole number ratio (N_s/p) is maintained.

On the other hand, fixing the rotor pole number as 4, a comparative study with increasing k has also been carried out in [61], i.e. 12-slots, 24-slots and 48-slots. It has been found that higher value of k (higher number of stator slots) offers higher average torque. Moreover, due to more sinusoidal MMF in the airgap, the torque ripple can be reduced by increasing the stator slots. The same conclusions on average torque and torque ripple have also been proven by the authors in [62].

Moreover, a SynRM with novel multilayer ac winding is proposed, analysed and experimentally tested in [64]. There are three layer per stator slot for a 3-phase machine, and each phase winding lied in all the stator slot with properly designed numbers of turns. Such winding provides shorter end-winding (with respect to FP winding) and more sinusoidal airgap MMF. The proposed winding maintains the same level of torque capability but achieves 25.4% loss reduction compared with an induction machine with the same size. The power factor of the SynRM with multilayer winding can be as high as 0.72 and offers 3.9% efficiency increase compared with the induction machine counterpart. Moreover, the temperature rise of the new winding configuration is lower than that of the induction machine with distributed winding and exhibits better thermal steady-state performances.

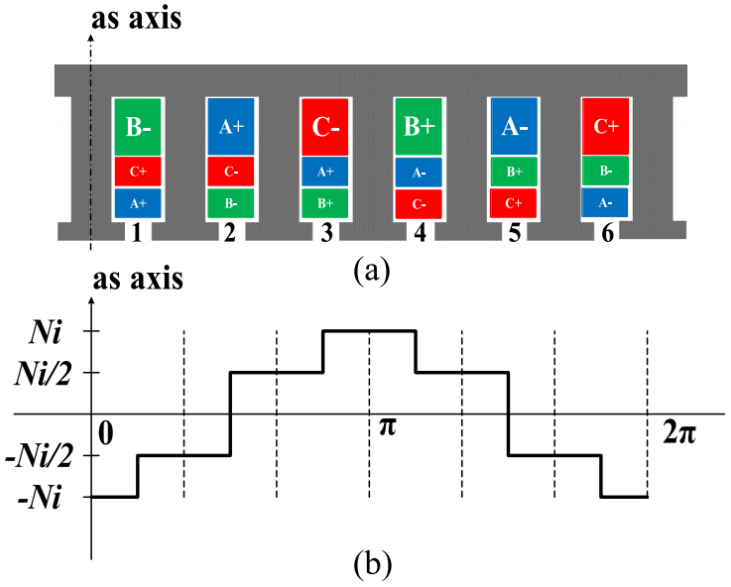

Fig. 1.22 (a) Novel six-slot multilayer winding for SynRMs and (b) corresponding airgap MMF [64].

Apart from the FP distributed winding and multilayer winding, SynRMs with fractional slot concentrated winding have also been developed in the last two decades, due to the inherent advantages, e.g. shorter end-winding, higher packing factor and relatively small machine size [5],[65],[66]. It was found that fractional slot can not only improve the torque capability and efficiency, but also can increase the thermal conductivity due to higher slot fill factor, hence improving the thermal performance. However, these improvements come with a price such as higher torque ripple, higher iron losses and lower power factor. In order to further increase the robustness and to simplify the rotor manufacturing process, authors in [10],[67] adopted the salient rotor pole with fractional slot winding, essentially the same machine structure as SRMs but with sinewave current supply. However, although exhibits a series of advantages, such doubly salient structure and concentrated winding often generate relatively higher torque ripple.

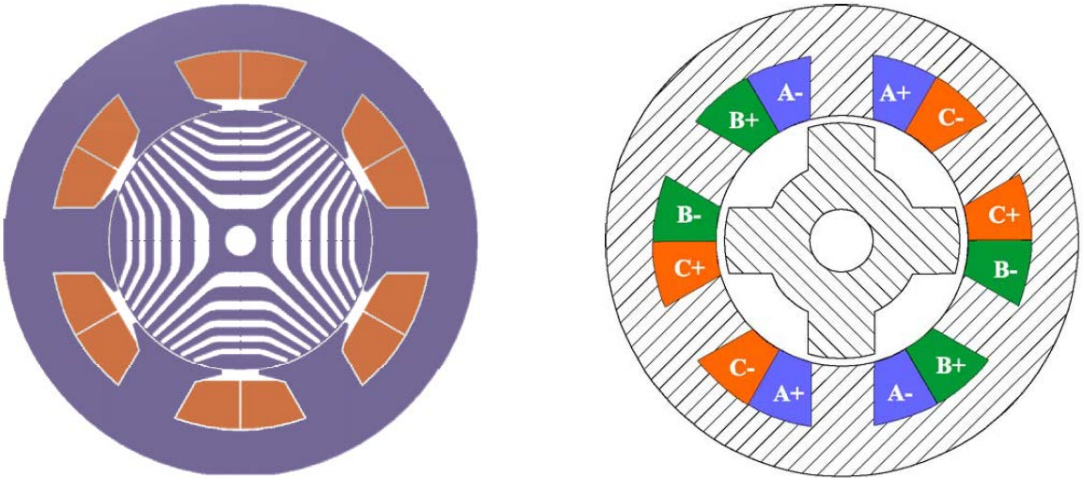

(a) Transversally lanminated rotor (b) Salient pole rotor

Fig. 1.23 6s/4p SynRMs with fractional slot concentrated winding [64], [10].

1.3 TORQUE RIPPLE REDUCTION

Generally, torque ripple minimization can be achieved by both machine design and machine control. Fig. 1.24 shows the classification of the possible methodologies for torque ripple reduction, which will be detailed in the following sections.

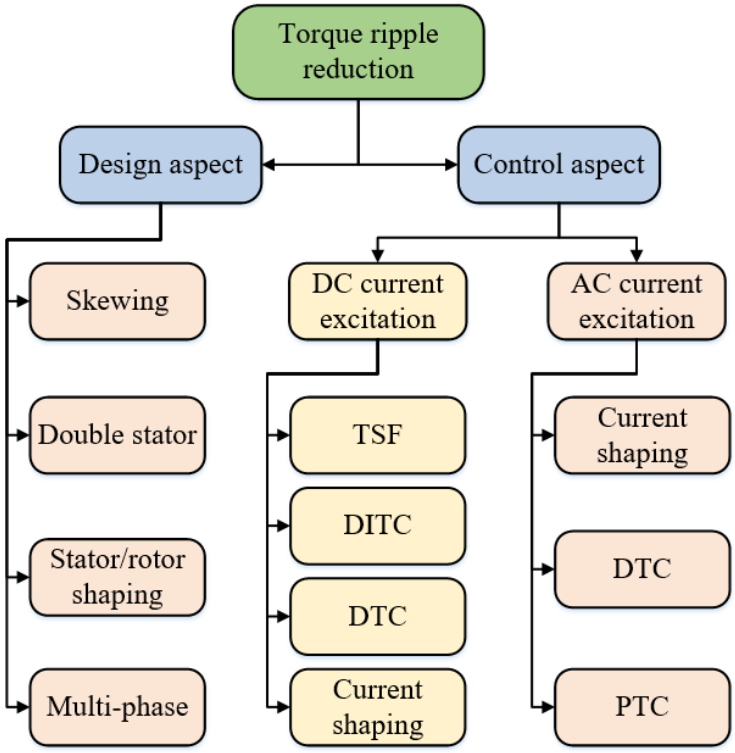

Fig. 1.24 Existing methodologies for reducing the torque ripple of SRMs. TSF: torque sharing function; DITC: direct instantaneous torque control; DTC: direct torque control; PTC: predictive torque control.

1.3.1 Design Aspects

Based on the reviews of both SRMs and SynRMs in previous sections, numerous machine topologies can potentially achieve lower torque ripple and lower noise. For example, SRMs with higher rotor pole number or segmented rotor, and SynRMs with increased number of stator slots or with rotors with properly designed flux barriers (including barrier number and shape). This section will further elaborate the electromagnetic performance improvement from the machine design point of view.

1.3.1.1 Skewing Structure

The skewing has been widely used in permanent magnet machines to reduce their torque ripple and is becoming more and more popular in SRMs to reduce the torque ripple and also to reduce the vibrations and acoustic noise. In the [68], the effectiveness of skewing on both the cogging torque and on-load torque ripple of a permanent magnet machine has been proven. However, the effectiveness of skewing under high magnetic saturation is limited and even diminished. To solve this problem, authors in [69] proposed an improved skewing method with

optimized skewing angle and current advance angle. Although proposed method produces higher torque ripple at lower load condition than that of conventional skewing, the stringent torque ripple requirement for a full range of load conditions can be fully met.

In order to reduce the vibrations and acoustic noise as well as the torque ripple, the skewing method was implemented for SRMs as well [9],[70],[71], in which the SRMs with different skewing angle for both the stator and the rotor have been investigated and compared. It has been proven that the skewing method can significantly mitigate the radial force with slightly reduced average torque and torque ripple.

(a) Stator (b) Rotor

Fig. 1.25 SRM with skewed rotor structure [71].

In order to suppress the torque ripple of the SRMs, an improved rotor skew has been proposed and tested in [72]. Authors divide the stator into three identical stacks corresponding to three identical rotor stacks. There will be a properly designed skew angle between adjacent rotor stacks. In addition, the current through the winding in each stack are controlled independently. Using the case in Fig. 1.26 for example, the coils,v_{11} and v_{12} in stack 1, u_{21} and u_{22} in stack 2, and w_{31} and w_{32} in stack 3 are excited at the same time, and the rotor is forced to rotate in clockwise direction. The results show that with a skew angle of 20°, this technique can significantly reduce both the torque ripple and the radial force.

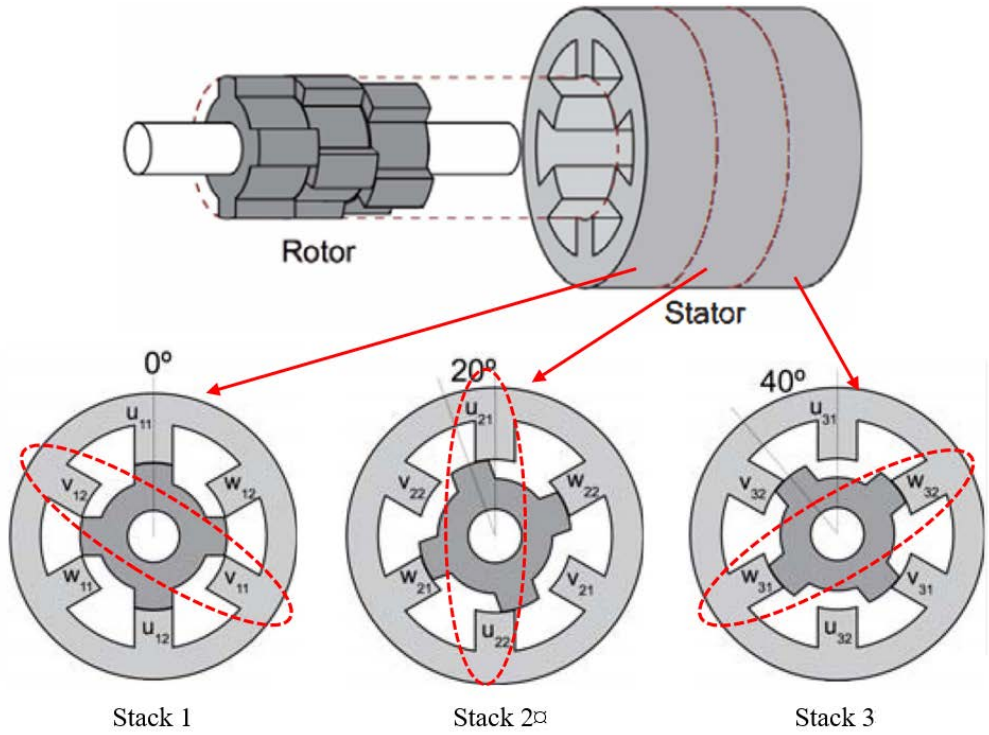

Fig. 1.26 Improved rotor skew concept to reduce the torque ripple [72].

1.3.1.2 DOUBLE STATOR STRUCTURE

In [73], a novel SRMs with double-stator configuration (DSSRM) was proposed and analysed. As shown in Fig. 1.25, the DSSRM has a structure of outer and inner stators with segmented rotor assembled between them, and the magnetic force is produced by both stators. The DSSRM enables a flexible design due to specific structure, which shows potential for the structural optimization in order to obtain a smooth torque profile [74]. Moreover, Compared with conventional SRMs, the DSSRM reduces the radial force and offers higher percentage of motional forces (tangential force) [75],[76]. Hence, it is a promising candidate for higher power density and lower acoustic noise application.

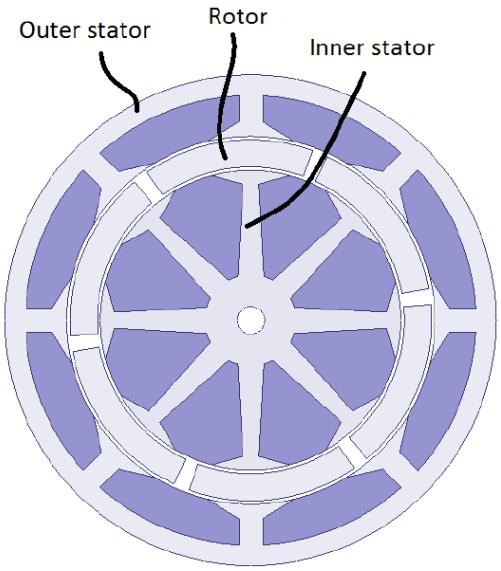

Fig. 1.27 Double stator SRMs structure [75].

1.3.1.3 STATOR AND ROTOR POLE SHAPING

Stator and/or rotor pole shaping as shown in Fig. 1.28 is another effective way to reduce the torque ripple. The method such as optimizing the stator and rotor pole arcs has been proposed for an 8s/6p SRM [Fig. 1.28 (a)]. This method can increase average torque and at the same time reduce the torque ripple. Another SRM geometry that can achieve reduced torque ripple and potential higher average torque is proposed in [10], as shown in Fig. 1.28 (b). With punching hole in one side of each rotor pole, the derivatives of self- and mutual-inductances with respect to rotor position are forced to be more sinusoidal, leading to a significant reduction in the torque ripple without sacrificing the average torque. In [74], four novel rotor shaping methodologies for variable flux reluctance machines (VFRMs) have been proposed to reduce the torque ripple. Such machine has the same doubly salient structure as the SRMs, therefore has been included in this review. It has found that the inverse cosine shaping method [Fig. 1.28 (c)] presents the best performance in torque ripple reduction (suppressing 94% torque ripple) although the average torque is also reduced by 10%. And the inverse cosine 3rd harmonic and multi-step shapping reduce 90-92% torque ripple with only 3% reduction in the average torque. However, the main disadvantage of the proposed methods is that they can only be applicable for limited slot/pole number combinations.

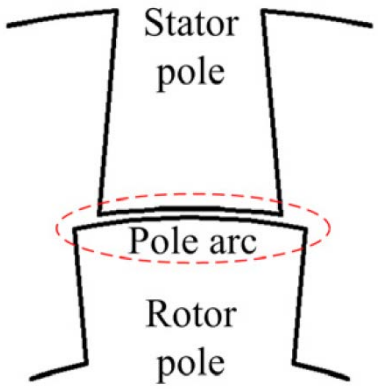

(a) Stator and rotor pole arc shaping

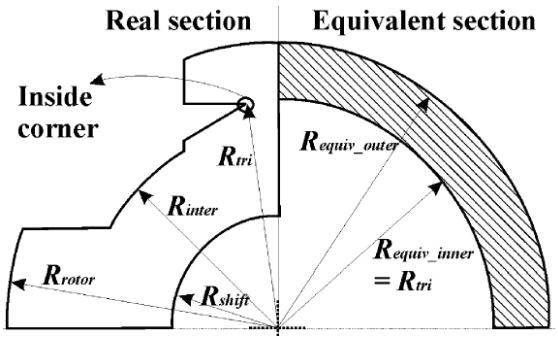

(b) Rotor pole with punching hole

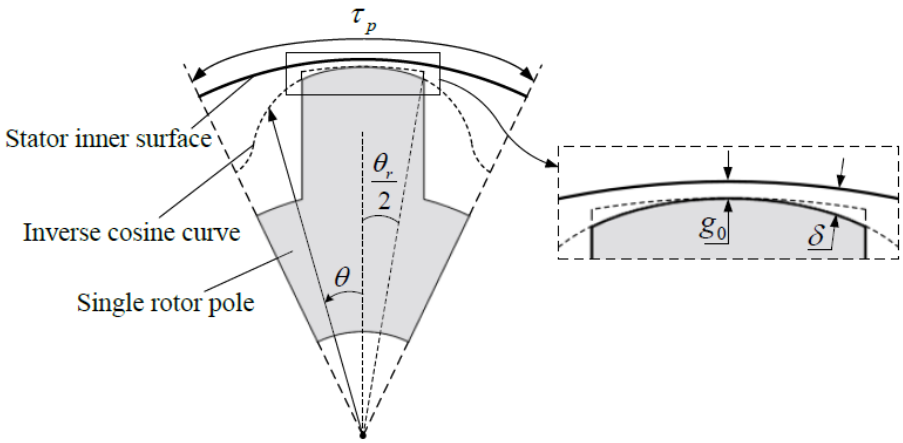

(c) Rotor pole shaping

Fig. 1.28 Stator and rotor pole shaping for torque ripple reduction [8],[10],[77].

1.3.1.4 MULTI-PHASE STRUCTURE

Increasing phase number can be an effective and simple way to reduce the torque ripple. Multi-phase machines are attracting increasing interest for a wide range of applications from electric vehicles through more electric aircraft to renewable energy. Lots of researches have been carried out for multi-phase PM machines, and more and more research papers about multi-phase SR type machines have been published in recent years. This section will select a few typical examples to reveal the opportunity and also challenges facing multi-phase machines. In [78], comparative study between a 5-phase and a 3-phase PM generators has been carried out. Due to the smooth torque profile, the ripple of the output power can be significantly reduced by adopting the 5-phase machine. Moreover, the 5-phase machine offers an excellent fault-tolerant feature and it can achieve 71-73% rated power when two non-adjacent phases have failed, such as open-circuited. In [79], the same conclusion can be drawn for the 5-phase 15s/4p interior PM machine.

Generally, for a SRM, with increasing phase number, the number of stroke per mechanical period can be increased and commutation region between phases is reduced, consequently lower torque ripple can be obtained. In [80],[81], a 4-phase 8s/6p SRMs is proposed for aerospace application, which is considered as a good compromise between complexity and fault-tolerant. However, if one phase is faulted, due to inherent independent phases, there will be a significant torque dip at faulted phase position, which is highly undesirable for many applications. To solve this problem, in [82],[83], 12s/10p 6-phase SRMs with different winding configurations are introduced. With properly designed current schemes, the SRMs with winding configurations in Fig. 1.29 (a) can achieve highest average torque, while that in [Fig. 1.29 (b)] can achieve relatively lower torque ripple compared with the3-phase CSRM. It is worth noting that the winding configuration in Fig. 1.29 (a) (with NN) increases the number of flux paths and reduces flux density in the stator back iron. As a results, it presents lower iron loss and higher torque performance at high phase current condition. However, although the multi-phase machine can increase the torque capability, reduce torque ripple and increase the fault-tolerant capability, this might come with a price in increasing the cost of power electronic devices.

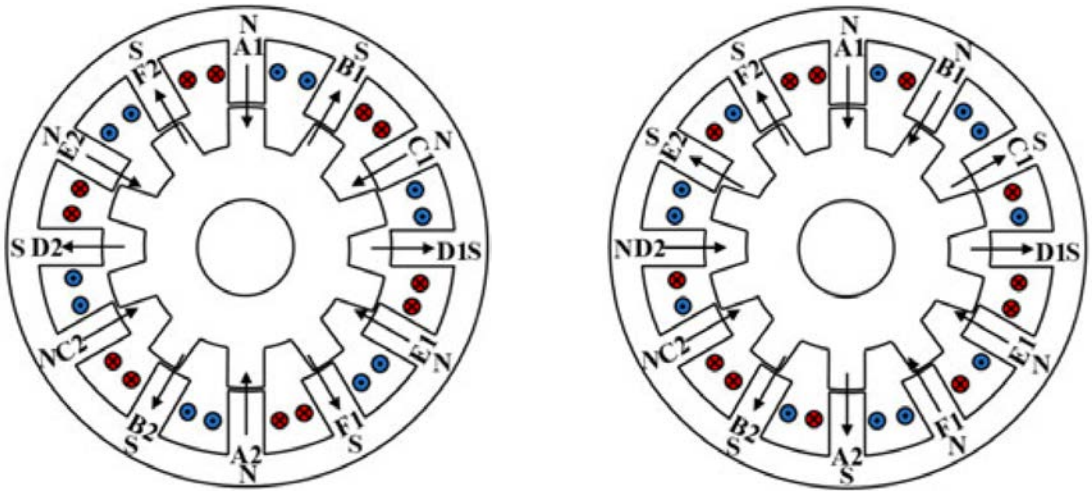

(a) NSNSNSNSNSNS (b) NNSSNNSSNNSS

Fig. 1.29 Winding configuration of 6-phase 12s/10p SRMs [78].

1.3.2 Control Aspects

Compared to the machine design technologies for reducing the torque ripple, implementing control methods can be much easier and more economical. Therefore, this section will try to review some existing torque ripple reduction methods from the machine control aspects.

1.3.2.1 DC CURRENT EXCITATION

Due to the specific operation principle of the SRMs, their torque ripple can ascribe to the coupling between the phase current, rotor position, conduction angle and the machine geometry. Moreover, the torque declines mainly during the phase commutation region. Hence, many control stratagems have been proposed to address this issue, such as, torque sharing function (TSF), direct instantaneous torque control (DITC), direct torque and flux control (DTFC) and etc.

A). TORQUE SHARING FUNCTION

Torque sharing function (TSF) is one of the most effective techniques to reduce the torque ripple of the SRMs [12]. As mentioned previously, the phase commutation region is a dominant region that produces the torque ripple, the idea of TSF is therefore to properly divide and share the reference torque with one or more phases during commutation or overlapping region. The torque control block diagram with TSF is shown in Fig. 1.30. It is worth noting that the torque-to-current block is represented using a look-up table which contains the torque, rotor position and phase current, in order to increase the accuracy of the controller. Some of the widely used TSFs are based on linear, sinusoidal, cubic and exponential expressions of instantaneous torque in terms of electric rotor positions [12]. TSF curves should be properly designed based on the specification of SRMs.

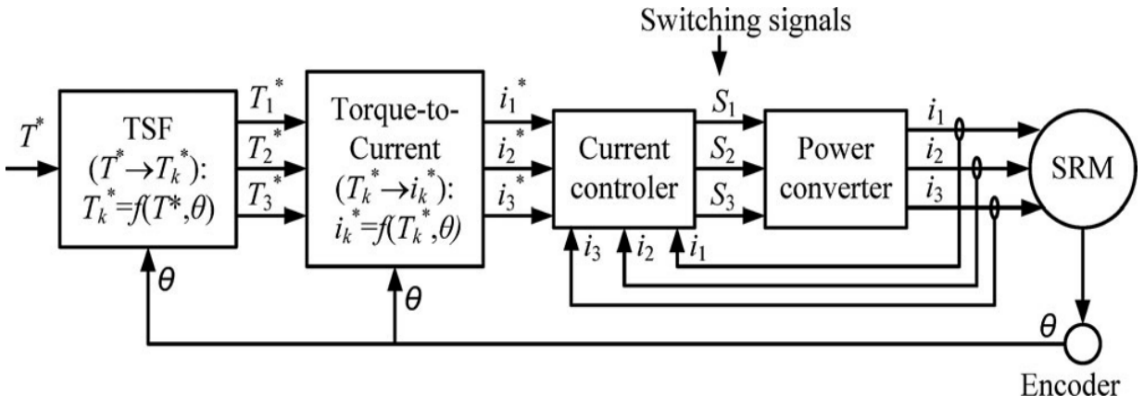

Fig. 1.30 Block diagram of TSF control scheme [84].

Based on the machine specification, there are three parameters should be designed for both linear or non-linear TSF, and they are the switched on/off angles $\theta_{on/off}$ of phase current and overlapping region between two phases θ_{ov}, as shown in Fig. 1.31. Based on the torque profiles, the TSF can be defined by (1.7)-(1.9).

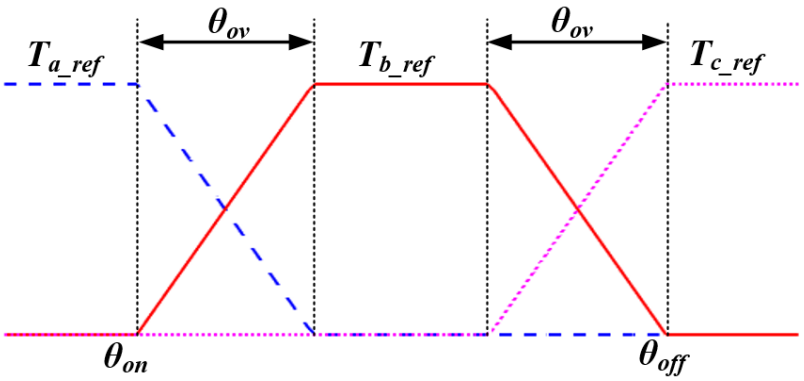

(a) Linear expression

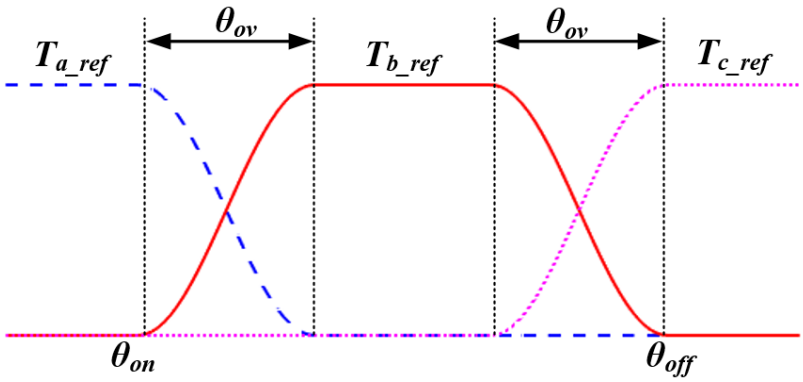

(b) Sinusoidal expression

Fig. 1.31 Profiles of linear and sinusoidal TSF.

$$T^* = \begin{cases} 0 & 0 \le \theta \le \theta_{on} \\ T^* \cdot f_{rise}(\theta) & \theta_{on} \le \theta \le \theta_{on} + \theta_{ov} \\ T^* & \theta_{on} + \theta_{ov} \le \theta \le \theta_{off} - \theta_{ov} \\ T^* \cdot f_{fall}(\theta) & \theta_{off} - \theta_{ov} \le \theta \le \theta_{off} \\ 0 & \theta_{off} \le \theta \le \theta_{al} \end{cases} \tag{1.7}$$

with

$$f_{rise}(\theta) = \begin{cases} \dfrac{\theta - \theta_{on}}{\theta_{ov}} & Linear \\ \left[\sin\left(\dfrac{\pi}{2}(\theta - \theta_{on})/\theta_{ov}\right)\right]^2 & Sinusoidal \end{cases} \tag{1.8}$$

$$f_{fall}(\theta) = 1 - f_{rise}(\theta + \theta_{ov} - \theta_{off} + \theta_{on}) \tag{1.9}$$

Both conventional linear and sinusoidal TSFs can reduce the torque ripple at relatively low speed. However, the performance of TSFs will be compromised at high speed due to the delay of current rising and falling. In order to address this issue, the TSFs with extended negative torque region was introduced in [85]. Extended TSFs provide enough time to increase or decrease the current. As a result, this control strategy enables better torque performance even at a relatively high speed. Moreover, the power losses and inverter power rating can be reduced.

In [11], a novel online compensation TSF is proposed to minimize the torque ripple of SRMs. The positive and negative compensations are provided for the outgoing and incoming phases, respectively, during the commutation region.

B). DIRECT INSTANTANEOUS TORQUE CONTROL

In [14], a novel direct instantaneous torque control (DITC) for the SRMs was developed and analysed. The new control scheme effectively limits the torque ripple into a boundary, where exact knowledge of rotor position is not required. Fig. 1.31 shows the block diagram of the DITC. As can be seen, the torque reference is directly used and no current closed loop is required. The instantaneous torque estimation block is a look-up table from SRM terminal. However, the main drawback of such method is the need for priori-knowledge of machine parameters [86].

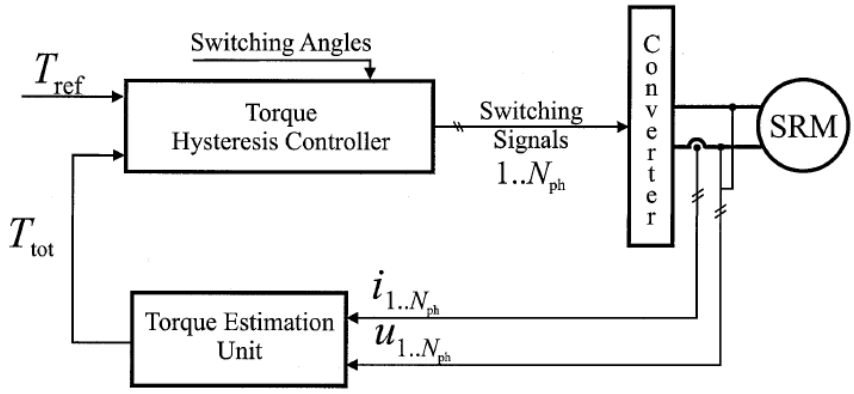

Fig. 1.32 Block diagram of DITC [14].

There are three possible switching states for one single phase of the SRMs, i.e. 1 ($+V_{dc}$), 0 (freewheeling) and -1 ($-V_{dc}$). The torque ripple of single active period can be easily controlled in a boundary by the hysteresis controller as shown in Fig. 1.33 (a). In order to smooth the torque dips during the commutation region, two hysteresis controller are defined for two active phases, respectively. For incoming phase, state 1 ($+V_{dc}$) is used to increase the torque, while state 0 (freewheeling) is preferred to decrease the torque, so that the torque can be remained in the inner boundary (Δh) as long as possible to reduce the switching frequencies. The outgoing phase remains state 0 (freewheeling) until the torque is out of control (outer boundary) of the incoming phase, i.e. $|T^* - T_{est}| > \Delta H$. By doing so, the resultant torque ripple can be controlled within the designed boundary.

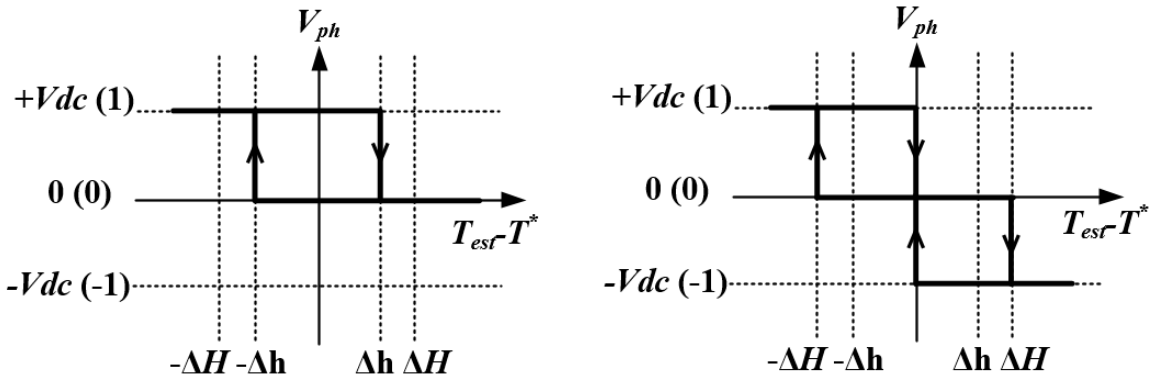

(a) Incoming phase (or single active period) (b) Outgoing phase

Fig. 1.33 Switching states for two active phase during commutation region.

Moreover, in [87], an improved direct instantaneous torque and force control has been proposed. The new method offers a great potential in reduction of torque ripple and acoustic noise. However, higher device losses and limited operation speed range remain impeding factors for its wide adoption in industry.

C). DIRECT TORQUE CONTROL

The same direct torque control (DTC) strategy that often used in conventional ac machines can also be implemented for SRMs [88]. The current of each phase of the SRMs is adjusted in sequence by the proposed DTC in order to produce a rotating magnetic flux, which is very much similar to that in the ac machines. However, a new winding configuration is required for the control scheme, which is uneconomical and inconvenient. In order to implement the DTC for the SRMs without changing winding or current excitation, a novel DTC algorithm has been proposed in [89]. The torque and torque ripple can be directly controlled by the hysteresis controller. Moreover, the priori-knowledge of nonlinear magnetization is not necessary during this operation.

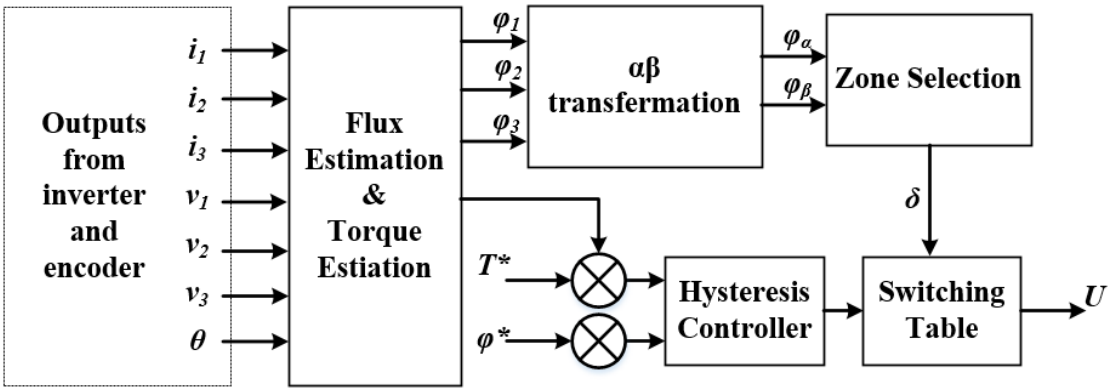

Fig. 1.34 Block diagram of DTC for SRMs [89].

Six voltage vectors with the same magnitude have been selected for SRMs, as shown in Fig. 1.35 (a), they are separated by $\pi/3$. The space are divided into six zones and the voltage state vectors are lying in the zone centers. If the phase resistance is neglected, the stator flux is given by (1.10).

$$\psi(k) = \psi(k-1) + V(k)\Delta T \tag{1.10}$$

The behavior of stator flux with different voltage vectors is shown in Fig. 1.35 (b). If the components after projecting $V(k)$ to $\psi(k-1)$ are positive [same direction as $\psi(k-1)$], then $V(k)$ can be selected to increase the flux, and vice versa. In addition, the torque increases when $V(k)$ provides positive current phase angle with respect to the rotor position, i.e. $\Delta\theta > 0$, and vice versa. Therefore, the switching table can be obtained and an example is listed in TABLE 1.2.

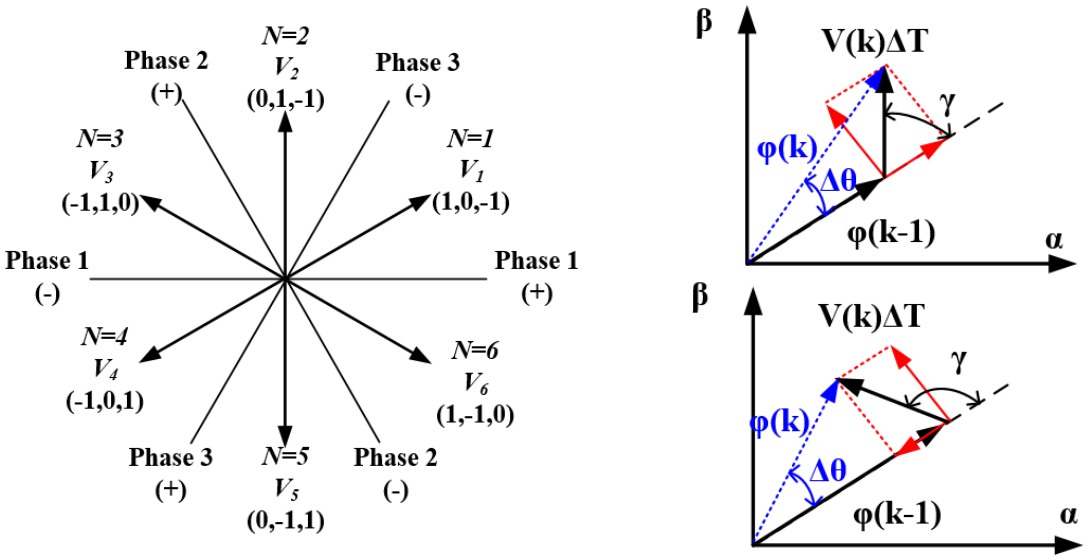

(a) Voltage vector s (b) Flux control

Fig. 1.35 Definition of SRM voltage vectors and flux control for DTC.

TABLE 1.2 SWITCHING TABLE

ψ ↑ T ↑	ψ ↑ T ↓	ψ ↓ T ↑	ψ ↓ T ↓
V_{k+1}	V_{k+2}	V_{k-1}	V_{k-2}

Although the torque ripple of the SRMs can be significant reduce by the DTC scheme, undesired negative torque due to flux hysteresis control and inappropriate voltage vector selection is unavoidable, which can lead to low torque/ampere ratio. In [90], an improved DTC with nine space sectors has been developed, the extra three sectors provide corresponding voltage vectors to avoid the negative torque. In [91], the number of space sectors is increased

to twelve, and the voltage vectors selection can be more reasonable and flexible. The negative torque is significantly suppressed, consequently, the torque/ampere ratio is improved by 18.43%, compared with a conventional DTC. Moreover, torque ripple can be reduced by 56.5%. In [92], a DTC for 6-phase SRMs with novel inverter has been introduced. The torque ripple can be reduced from 32.1% to 6% whilst the cost of electronic power devices is reduced by half.

D). CURRENT SHAPING

For SRMs, the conventional trapezoidal current is not sufficient to reduce the torque ripple. Therefore, the stator current optimization is regarded as the most straightforward option to reduce the torque ripple in the literature. In [93], an off-line current profile based on the specification of the SRM has been designed, which achieves a considerable reduction in torque ripple. However, with increasing speed, the benefits is compromised, since the phase current can no longer track the reference current due to limited DC voltage. To cope with this issue, a real time compensation method is introduced in [94]. The extra outgoing phase has been proven to be able to compensate the lower torque due to track error at high speed region. In [95], a novel technique of current reference optimization is presented. A multiple reference frame controller was designed to precisely realize the current waveforms. Moreover, authors in [96] have quantified the average torque and torque ripple due to various current harmonics in SRMs. It is found that the 1^{st} and 2^{nd} order current harmonics mainly contribute to the average torque, whilst the 4^{th} and 5^{th} order current harmonics are potential candidates for torque ripple reduction.

1.3.2.2 AC CURRENT EXCITATION

It is well-established that, compared to the conventional DC current excitation with 120 degree conduction, the sinewave current excitation can significantly reduce the vibrations and acoustic noise of SRMs [97]-[99]. Moreover, the conventional off-the-shelf inverter, together with numerous existing sophisticated control schemes for ac machines can also be adopted. Therefore, to reveal the full potential of SRMs, this section will introduce some existing control methodologies to reduce the torque ripple for SRMs with AC current excitation.

A). CURRENT SHAPING

Torque ripple of AC excitation machine is commonly caused by back-EMF harmonics, cogging torque, non-uniform permeability and the dead time of inverter, etc. And the current optimization can be one of the most straightforward methods to mitigate their effects for both

PM and reluctance machines. In [100], the current optimization method is introduced to compensate the cogging torque for flux switching PM machine. Although, the torque ripple due to cogging torque can be compensated perfectly, with increasing phase current, the torque ripple due to reluctance torque cannot be handled. To solve this issue, in[101]-[103], a torque ripple compensation based on instantaneous torque prediction was proposed and experimentally validated for synchronous machines. The electromagnetic torque model for synchronous machine has been built, which can accurately predict the on-load torque of synchronous machines. Hence, based on the analytical torque model, the compensated *q*-axis current can be calculated and fed forward (open-loop) or backward (close-loop) to the system. Two different synchronous machines (with and without PM) were tested for the proposed methods and the torque ripple of both machines was reduced by around 50%. In addition, in order to implement the model, the priori-knowledge of the machine, such as, cogging torque and PM flux as a function of rotor position, is required. Moreover, it is worth noting that since the variation of inductance is negligible, the feed forward method is not applicable for the SynRMs, while feed backward scheme is effective to reduce the torque ripple of the latter. Moreover, in [104], the novel stator current design method was developed to reduce torque ripple with minimizing copper losses, as shown in Fig. 1.36. Experimental results showed that torque ripple can be effectively suppressed under both transient and steady states.

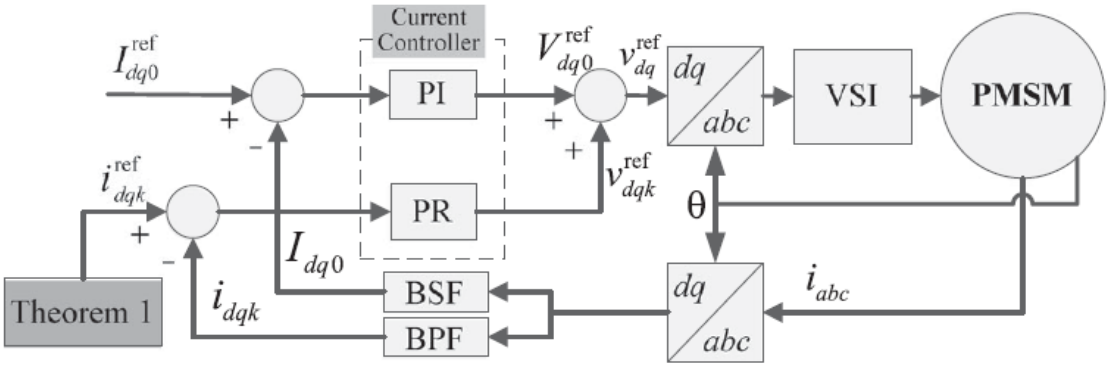

Fig. 1.36 Block diagram with current harmonic injection for torque ripple minimization. BSF: band-stop filter; BPF: band-pass filter [104].

In [105], the torque ripple suppression method of open-winding PM (OW-PM) machine is introduced. The *q*-axis harmonic current is injected to counteract the torque ripple due to zero-sequence current. Moreover, a novel switching sequence is introduced, where zero vector (111) is abandoned, consequently, the switching frequency can be reduced by 33.3%.

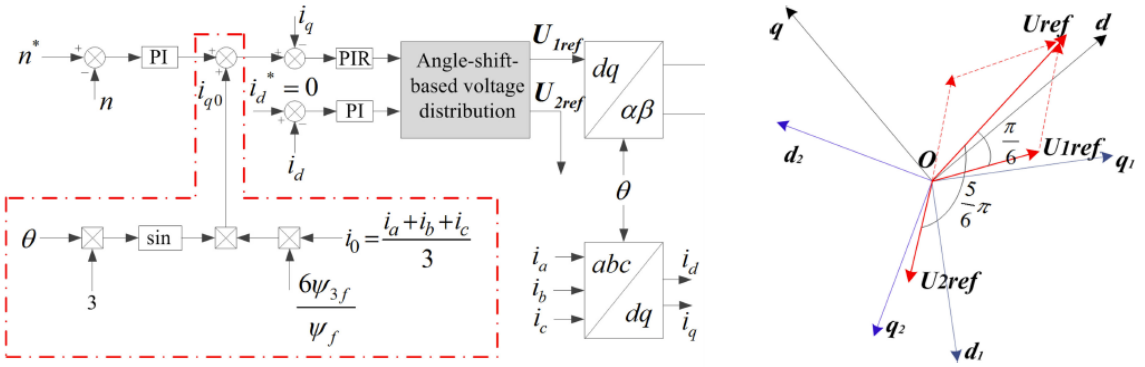

(a) Current harmonic injection (b) Angle-shift-based systems

Fig. 1.37 Block diagram of current harmonic injection for OW-PM machine [105].

Previous current optimization method is based on the feedback of machine operating point, and it does not need to know the current characteristic, which is estimated automatically by the system. In order to investigate the torque production mechanism in-depth, in [106], the influence of the 3rd order current harmonic, including the magnitude and phase angle, was investigated for a five phase PM machine and the control diagram is shown in Fig. 1.38. It is found that the average torque can be increased by 17.3% when the fundamental and the 3rd order current harmonics have the same phase. However, the effectiveness of torque ripple reduction in this case is restricted. The same conclusion had been drawn in [107], although the average torque is increased, the efficiency of the machine is reduced due to extra copper and iron losses brought by the current harmonics. Similar technique was been implemented for SynRMs with both salient pole rotor and flux barriers rotor in [108],[109]. It is found that it was possible to improve the torque performance of the SynRMs with the 3rd order current harmonic injection. However, the effect of the magnitude and phase angle of the current harmonics were not comprehensively investigated for such machines.

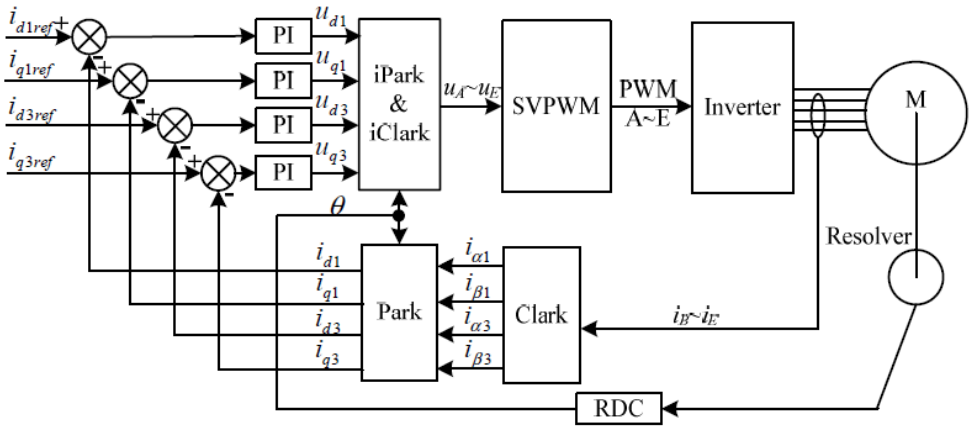

Fig. 1.38 Block diagram of 5-phase machine with current harmonic injection [106].

Moreover, the phase current of the SynRMs can also be optimised online by the adaptive linear neural network method proposed in [110],[111]. Thanks to the online learning capability of the neural networks, the torque ripple can be significantly reduced. However, for more accurate torque control, longer learning time is often required.

B). DIRECT TORQUE CONTROL

Direct torque control (DTC) is attracting increasing interest for ac machines, due to significant advantages such as no current regulator, parameter independent and no coordinate transformations etc. However, the hysteresis control with various sampling frequency causes undesired torque and stator flux ripple. To solve this problem, a novel DTC with constant switching frequency was proposed in [112]. The idea is to process the voltage vector duty ratio within a constant period T_s before the estimated torque T_e reaches the hysteresis band Δh, as shown in Fig. 1.39. Hence, the torque ripple can be effectively reduced. However, the machine parameters, such as machine inductance and PM flux, are required to calculate the duty ratio. Therefore, in [113], a parameter-free DTC was introduced. Although the torque ripple can be reduced, there will be a discrepancy between the torque reference and feedback under high load or high speed conditions. To improve this issue, DTC with duty ratio regulator is proposed in [114], where a simple method is adopted to design a range of key parameters. The control diagram is shown in Fig. 1.40. The proposed DTC not only inherits the feature of parameter independent and excellent transient response of conventional DTC, but also solves the problems of steady-state error and achieves lower torque ripple. A similar technique was proposed for a SynRM in [115], where a triangular carrier is adopted and compared with output PI torque regulator in Fig. 1.41, in order to obtain the constant switching frequency. And it properly adjusts the voltage vectors during the entire switching cycle, and hence achieves lower torque ripple.

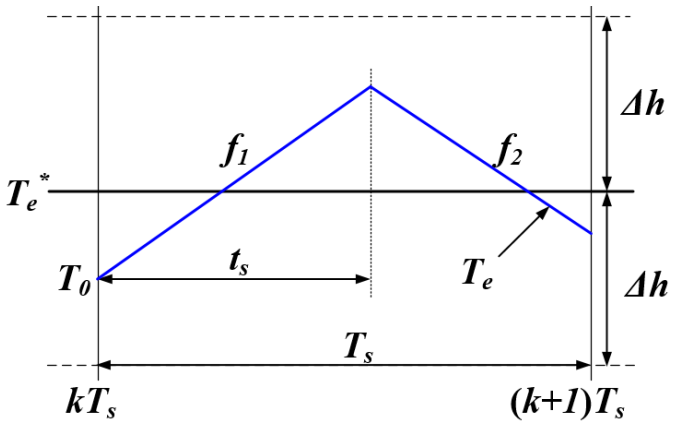

Fig. 1.39 The typical steady-state torque waveform of DTC with constant switching frequency.

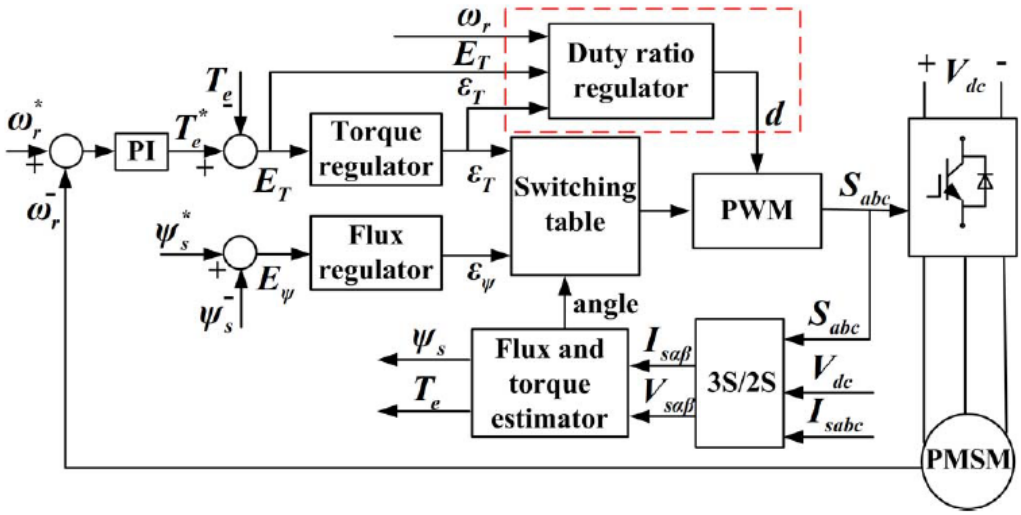

Fig. 1.40 Control diagram of DTC with duty ratio regulator for PMSM [114].

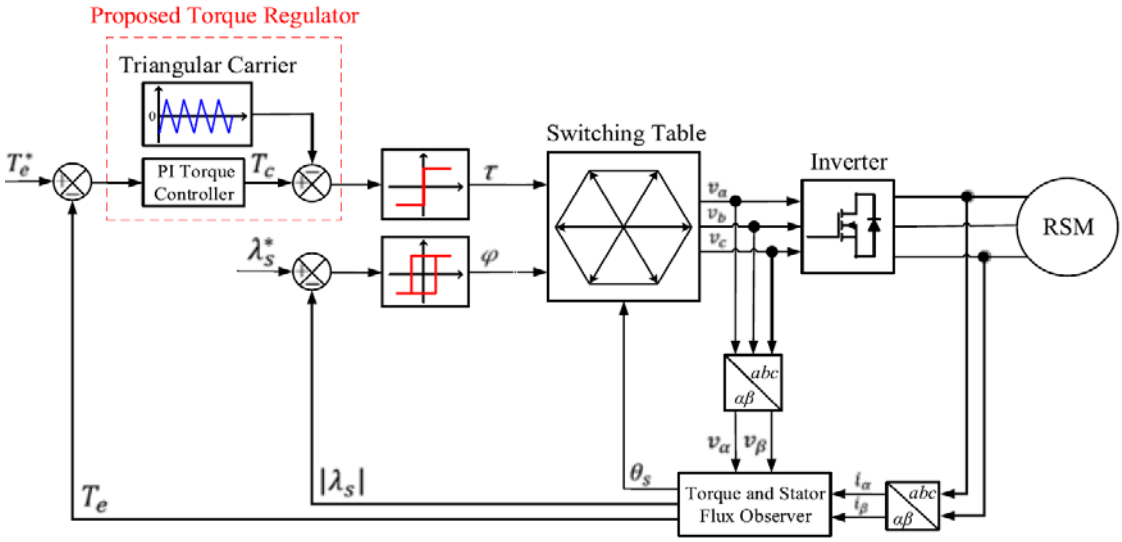

Fig. 1.41 Control diagram of DTC with triangular carrier for SynRM [115].

C). PREDICTIVE TORQUE CONTROL

Apart from current harmonic shaping and DTC schemes, the predictive torque control (PTC) can be another potential candidate to suppress the torque ripple of synchronous machine. In [116],[117], a novel PTC strategy has been proposed and experimentally tested. The changes in stator flux $\Delta\psi_s$ together with stator current i_s are utilized to predict the voltage control angle which forces the torque error ΔT_e to zero, accordingly achieving minimum torque ripple. The output of predictive control block in Fig. 1.42 is fed to a conventional space-vector pulse-width-modulation (SVPWM) to obtain an accurate torque control.

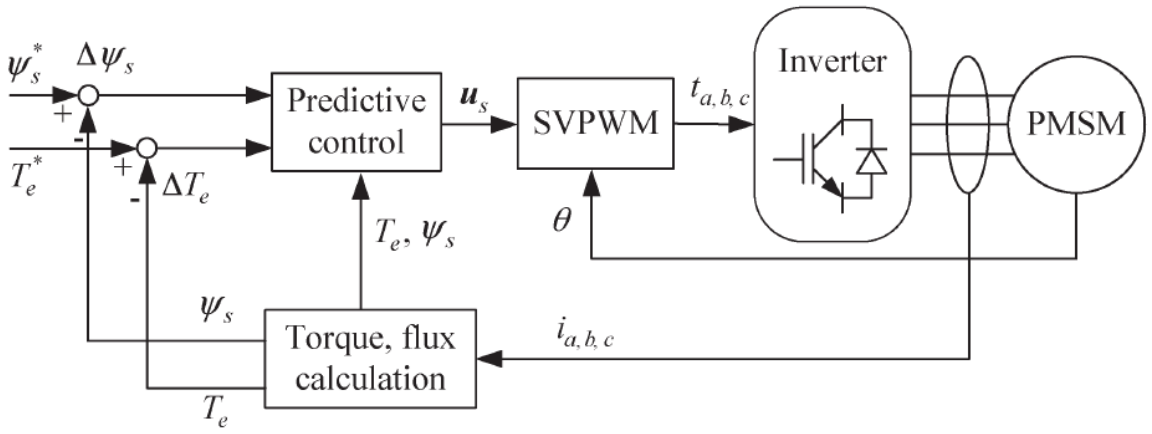

Fig. 1.42 Control diagram of PTC for PM machine [116].

Moreover, a finite control set model predictive control is another possible method to achieve minimized torque ripple. The idea is to build the predictive load model and corresponding cost function can be defined for the controlled parameters. Finally, the voltage vector which minimizes the cost function is selected to achieve desired objectives. Therefore, in [118],[119], a finite-control-set-based predictive torque control has been proposed for a PM machine in order to reduce the torque ripple. A cost function including torque tracking and duty ratio optimization is designed to optimize the voltage vectors which is realized by the SVPWM. Both simulation and experimental results show that it can realize a lower and constant sampling frequency and torque ripple minimization. Moreover, without considering PM components, the similar PTC can also be implemented for SynRMs [120],[121]. Although it is a novel attempt on such machines, PTC presents good potential to achieve lower torque ripple with lower copper losses.

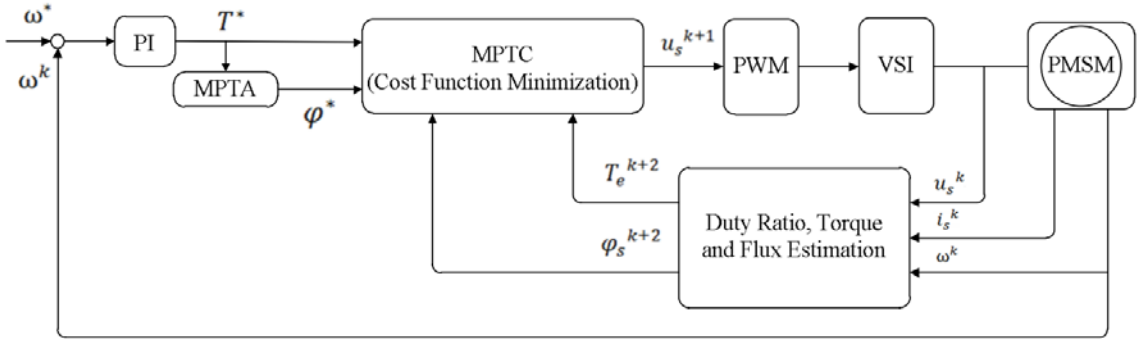

Fig. 1.43 Control diagram of finite-control-set-based PTC for PM machine [119].

1.4 RESEARCH SCOPE AND CONTRIBUTION OF THESIS

1.4.1 RESEARCH SCOPE

The electromagnetic performances of novel doubly salient synchronous reluctance machines (DS-SRMs) have been investigated in [67]. Although they can produce relatively high average torque, lower vibration compared with CSRM, due to fractional slot, concentred winding and doubly salient structure, the inherent torque ripple of such machine is much higher. Therefore, the main topic of this thesis is to propose a novel, economical and convenient current harmonic injection method to minimize the torque ripple and/or improve average torque for the DS-SRMs. Moreover, the proposed method will be implemented on the DS-SRMs with different winding configurations, slot/pole number combinations and phase numbers, in order to make sure this method can be applicable to a wide range of DS-SRMs. This thesis consists of 7 chapters and a brief description of each chapter is given as follows:

- Chapter 1 provides a general introduction of SRMs and SynRMs, followed by the working principle and development of topologies. Moreover, the existing methodologies to minimize the torque ripple, vibrations and acoustic noise are also reviewed in this chapter.
- Chapter 2 proposes a current harmonic injection method for torque ripple reduction in 3-phase 12s/8p single layer DS-SRMs. An analytical torque model with fundamental and harmonic current injection has been developed, which can quantify the torque contribution of each order of inductance harmonic. Based on this analytical model, the current harmonic order, magnitude and phase angle can be properly selected to improve the torque performance.
- Chapter 3 implements the current harmonic injection method for three typical DS-SRMs with different winding configurations, i.e. double/single layer, fully pitched. The comparative studies of torque generation mechanism for different machines have been carried out. And the limitations of the proposed method for some topologies have been investigated.
- Chapter 4 comprehensively investigates the contribution of each harmonic inductance to the torque (average torque and torque ripple) of multi-phase DS-SRMs. And novel method by combining current harmonic injection with multi-phase machines is proposed in order to further improve the torque performance of the DS-SRMs.

- Chapter 5 investigates the effectiveness of current harmonic injection method for different DS-SRMs in terms of copper losses, iron losses, efficiency and dynamic performances, i.e. torque- and efficiency maps. To this end, a new analytical model in *dq0*-axis frame is developed, which can estimate the voltage distortion due to the interaction between inductance harmonic and stator current, therefore accurately predict machine dynamic performance even with current harmonic injections.
- Chapter 6 experimentally tests the effectiveness of current harmonic injection method for torque performance improvement. Both static and dynamic tests have been carried out for both 3-phase and 6-phase DS-SRMs. In order to inject the zero-sequence current in an economical way, the three-phase four-leg inverter is adopted and corresponding pulse-width-modulation (PWM) has been introduced.
- Chapter 7 gives a general conclusion of the thesis and proposes some future research directions.

1.4.2 RESEARCH CONTRIBUTION

The main novelty and contributions of this thesis are listed as follows:

- An analytical model for DS-SRMs has been established, accordingly the torque generation mechanism can be investigated in-depth. The torque due to each harmonic inductance can be quantified based on the analytical torque model.
- Based on the analytical torque model, a current harmonic injection method is proposed to reduce the torque ripple and/or to increase the average torque of the DS-SRMs, which is very easy to implement.
- The analytical torque model can be extended for any phase number and slot/pole combination. The mechanism about why certain phase numbers can have inherently lower torque ripple while others cannot, can be investigated. This will be helpful to find optimal measures in order to reduce torque ripple of the DS-SRMs either from machine design or machine control perspectives.
- The *dq0*-axis electromagnetic model is also developed, which can not only reproduce the current harmonic injection in *abc*-axis frame, but also can estimate the voltage distortion due to flux harmonics (introduced by current and inductance harmonics). It reduces the model complexity and provides a simple and effective method to analyse the dynamic performance of the DS-SRMs.

- An economical and convenient method to control the zero-sequence current of the DS-SRM has also been proposed, which has been used for both modelling and also experimental validation.

During this PhD study, 6 papers have been published including 3 IEEE journal papers and 3 conference papers (1 conference paper has won the best paper award) and 1 journal paper is currently under review. The publication list is given below:

1. G. J. Li, **K. Zhang**, Z. Q. Zhu, and G. W. Jewell, "Comparative studies of torque performance improvement for different doubly salient synchronous reluctance machines by current harmonic injection," *IEEE Trans. Energy Convers.*, vol. 34, no. 2, pp. 1094-1104, Jun. 2019.
2. **K. Zhang**, G. J. Li, Z. Q. Zhu, and G. W. Jewell, "Investigation on contribution of inductance harmonics to torque production in multiphase doubly salient synchronous reluctance machines," *IEEE Trans. Mag.*, vol. 55, no. 4, pp. 1-10, Apr. 2019.
3. **K. Zhang**, G. J. Li, Z. Q. Zhu, and G. W. Jewell, "Analytical modelling of dynamic performance with harmonic current injection for doubly salient SynRMs," *IEEE Trans. Int. Appl.*, Mar. 2020. (Accepted)
4. **K. Zhang**, G. J. Li, Z. Q. Zhu, and G. W. Jewell, "Torque performance improvement of doubly salient synchronous reluctance machines by current harmonic injection," *in Proc. IEEE Int. Ele. Mach. & Dri Conf (IEMDC)*, pp. 1222-1227, 12-15 May 2019.
5. **K. Zhang**, G. J. Li, R. Zhou, Z. Q. Zhu, and G. W. Jewell, "Losses in different doubly salient synchronous reluctance machines with current harmonic injection," *Int. Conf. Ele. Mach. Sys. (ICEMS)*, pp. 1-6, 11-14 Aug. 2019.
6. **K. Zhang**, G. J. Li, R. Zhou, Z. Q. Zhu, and G. W. Jewell, "Dynamic performance investigation of doubly salient synchronous reluctance machines with current harmonic injection," *Int. Conf. Ele. Mach. Sys. (ICEMS)*, pp. 1-6, 11-14 Aug. 2019. (**Best paper award**)
7. **K. Zhang**, G. J. Li, Z. Q. Zhu, and G. W. Jewell, "Impact of current harmonic injection on performance of multi-phase synchronous reluctance machines", *IEEE Trans. Energy Convers.*, 2020. (Under review)

Chapter 2 TORQUE PRODUCTION MECHANISM WITH CURRENT HARMONIC INJECTION

In this chapter, a current harmonic injection method is proposed for torque ripple reduction and/or average torque enhancement in 3-phase, 12-slot/8-pole single layer mutually coupled switched reluctance machines (MCSRMs), which are essentially doubly salient synchronous reluctance machines (DS-SRMs) with sinewave current supply. Initially, the torque generation mechanism with pure sinewave current supply of DS-SRMs is analysed based on some analytical torque models with both the self- and mutual-inductances being considered. These analytical models can accurately predict which inductance harmonic(s) contribute to average torque and which contribute to torque ripple and to which extent their contribution will be. Using similar analytical torque models, the current harmonics (3^{rd}, 5^{th}, 7^{th}, etc.) can be injected to reduce the torque ripple and/or to increase the average torque. In addition, the harmonic order, the amplitude and also phase angle compared to the fundamental component can be calculated for achieving the minimum torque ripple or the maximum average torque.

This chapter comes from the author's own paper [122].

2.1 INTRODUCTION

Switched reluctance machines (SRMs) have attracted increasing interest for high-performance applications due to their robustness, simplicity and low manufacturing cost [123],[124]. Without any permanent magnets or field windings on the rotor, SRMs are excellent for harsh environment and safety-critical applications [17],[125]. However, despite the SRMs have the above and other attractive features, the asymmetric converter is often needed due to the specific current supply mode, which is one of the most important impeding factors for a wider industrial application of the conventional SRMs (CSRMs). In addition, the doubly salient structure is often regarded as one of the main factors that contribute to their high torque ripple, high vibration and acoustic noise compared to other permanent magnet machines or induction machines.

In most of the available literature about SRMs, many researchers have devoted to investigate innovative methods to reduce the vibration and acoustic noise. Apart from the well-established fact that the radial force excitation is the primary source of vibrations and acoustic noise [126], the torque ripple of SRM has also been identified as another source determined by the tangential magnetic force [127]. In order to reduce the vibrations and acoustic noise, many studies have been carried out from the design or control aspects of the SRMs, In [128],[129], authors mounted two or more SRMs in parallel sharing the same rotor shaft in order to reduce torque ripple and acoustic noise. In [9],[10], rotor and/or stator shaping and skewing have been investigated to minimize the torque ripple. Apart from the aforementioned design techniques, control strategies such as adopting different current excitations can also significantly reduce torque ripple and vibrations. For the square wave current supply, authors in [130],[131] have proposed a torque share function to smooth the torque production during phase commutation. In [14],[132], the direct instantaneous torque control (DITC) is proposed to reduce the torque ripple. Sinusoidal excitation effects on radial force have also been investigated for SRMs [97],[133]. Moreover, other current waveform shaping methods have been considered to reduce torque ripple and vibrations and acoustic noise [104],[134].

In addition to the above methods, authors in [4] proposed a mutually coupled SRMs (MCSRM) that can also achieve lower vibrations and acoustic noise compared to the CSRMs, especially when the sinewave current supply is adopted. In this case, the classic off-the-shelf three-phase inverter for synchronous machines or induction machines can also be employed for the MCSRM, which in effect becomes a doubly salient synchronous reluctance machine

(DS-SRM). As a result, the cost for power converter and the whole drive system can be reduced. It has proven that the DS-SRMs with sinewave current supply can produce much higher average torque compared with the CSRMs although the irregular self- and mutual-inductances of DS-SRMs may cause relatively higher torque ripple [67].

It is worth noting that most existing SRMs are equipped with double layer (DL) concentrated armature windings. However, in order to further improve their torque capability, some single layer (SL) DS-SRM have been proposed in [67]. It has found that at low current density, the average torque of the proposed single layer DS-SRM can be twice as high as that of the double layer DS-SRM. However, both the SL and double layer DL produce higher torque ripple than the CSRM, leading to potentially higher vibration and acoustic noise.

In this chapter, a new method of current harmonic injection is proposed to reduce the torque ripple while keeping or even increasing its average torque. The idea is to adjust the order, the phase angle and the amplitude of the injected current harmonics so as to generate a torque ripple component opposite to that produced by the fundamental current, as shown in Fig. 2.1, leading to an overall reduction of the resultant torque ripple.

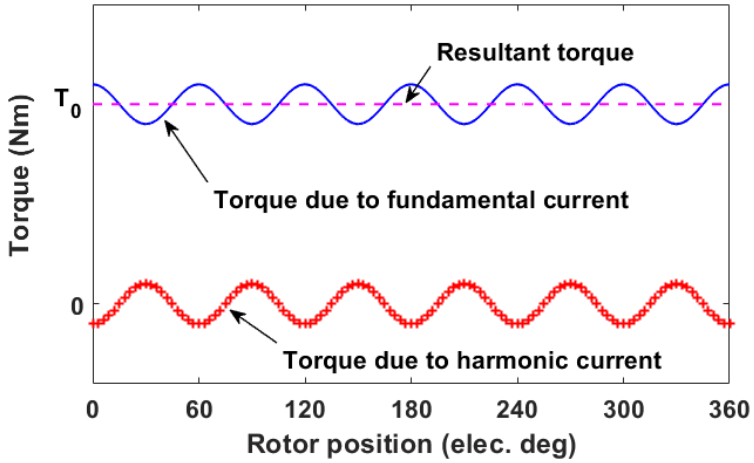

Fig. 2.1 Methodology of current harmonic injection.

A flow chart that summarizes the main steps of the proposed current injection method is shown in Fig. 2.2. In the first step, the derivation of instantaneous torque equation based on the inductances obtained by 2D-FEA is carried out. In the second step, based on the derived torque equation, the relationship between torque profile and the injected current harmonic is investigated. This allows an appropriate selection of the current harmonic (order, magnitude and phase angle) in order to achieve higher average torque and/or lower torque ripple.

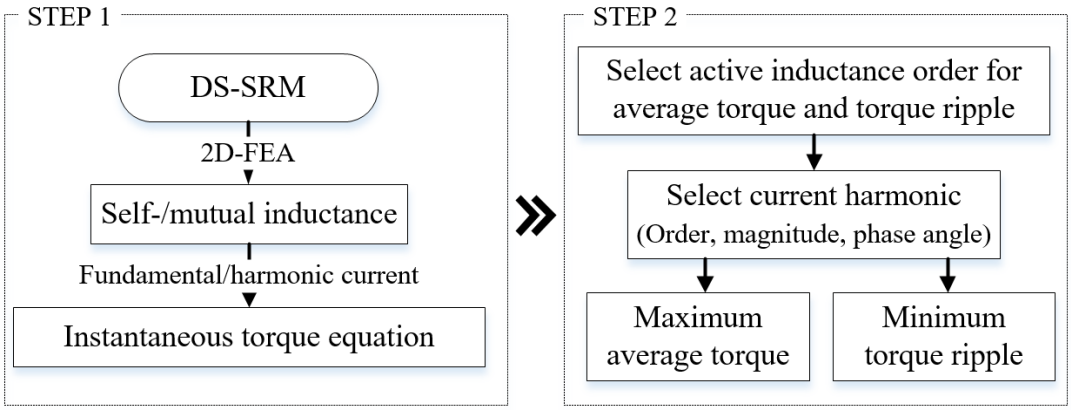

Fig. 2.2 Flow chart of proposed torque performance improvement method.

2.2 Analytical Torque Model with Fundamental Current

Fig. 2.3 shows the cross section and winding configuration of the investigated 12s/8p SL DS-SRM. The coil magnetic polarities of one phase are NN, which is different from that (NS) of the CSRM. Its main specifications are listed in TABLE 2.1 [67]. Each coil is wound around one stator tooth, leading to a concentrated winding structure just like its double layer counterpart.

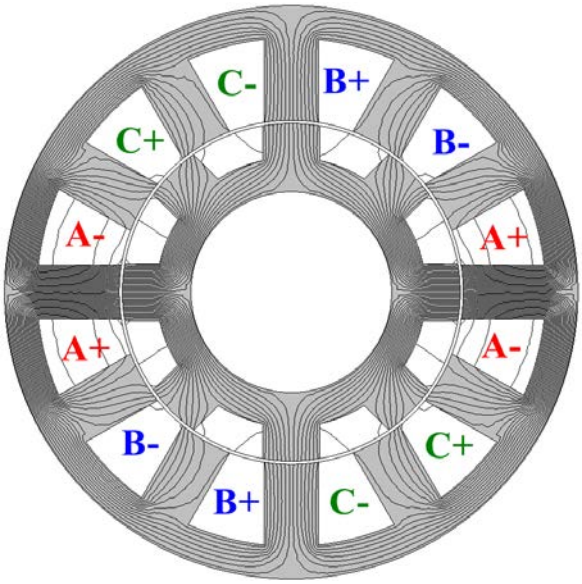

Fig. 2.3. Cross section and wingding configurations of a 12s/8p SL DS-SRM.

TABLE 2.1 MACHINE KEY DIMENSIONS AND DESIGN FEATURES

Stator slot number	12	Active length (mm)	60
Rotor pole number	8	Number of turns per phase	132
Stator outer radius (mm)	45	Coil packing factor	0.37
Air gap length (mm)	0.5	Rated RMS current (A)	10
Rotor outer radius (mm)	26.5	Current density (A_{rms}/mm^2)	5.68
Rotor inner radius (mm)	15.7		

According to [10], [96], if magnetic saturation is neglected, the instantaneous torque equation of SRMs as a function of both the rotor position and the phase current is given by

$$T_e(i,\theta) = \left\{\frac{1}{2}i_a^2\frac{dL_a}{d\theta} + \frac{1}{2}i_b^2\frac{dL_b}{d\theta} + \frac{1}{2}i_c^2\frac{dL_c}{d\theta} + i_a i_b\frac{dM_{ab}}{d\theta} + i_a i_c\frac{dM_{ac}}{d\theta} + i_b i_c\frac{dM_{bc}}{d\theta}\right\} \quad (2.1)$$

where i_a, i_b, i_c, L_a, L_b, L_c, M_{ab}, M_{bc} and M_{ac} are three phase currents, self- and mutual-inductances, respectively, whilst θ is the rotor mechanical position. The three phase fundamental currents can be written by

$$\begin{cases} i_a = I_1\sin(\theta_e + \beta_1) \\ i_b = I_1\sin\left(\theta_e - \dfrac{2\pi}{3} + \beta_1\right) \\ i_c = I_1\sin\left(\theta_e + \dfrac{2\pi}{3} + \beta_1\right) \end{cases} \quad (2.2)$$

where I_1 represents the amplitude of phase current, θ_e is the rotor electrical position and β_1 is the advance angle.

To simplify the calculations, the self- and mutual-inductances L and M can be expressed by Fourier series as

$$\begin{cases} L = L_0 + \sum_{n=1}^{\infty} L_n\cos(n\theta_e + \alpha_n) \\ M = M_0 + \sum_{n=1}^{\infty} M_n\cos(n\theta_e + \alpha'_n) \end{cases} \quad (2.3)$$

where L_0 and M_0 are the dc components of the self- and mutual-inductances while L_n, α_n, M_n and α'_n are the magnitude and phase of the n^{th} self- and mutual-inductance harmonics, respectively. The self- and mutual-inductances as well as their spectra are calculated by using 2D-FEA, as shown in Fig. 2.4, and their harmonic components are listed in TABLE 2.2 and

TABLE 2.3, which can be used for calculating both the average torque and torque ripple coefficient in the following sections.

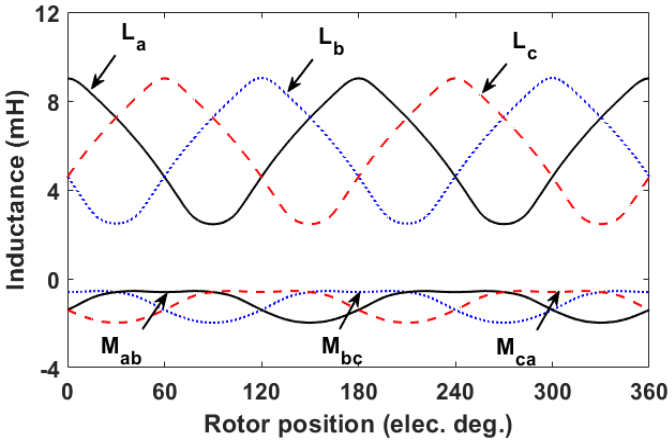

(a) Self- and mutual-inductances waveforms

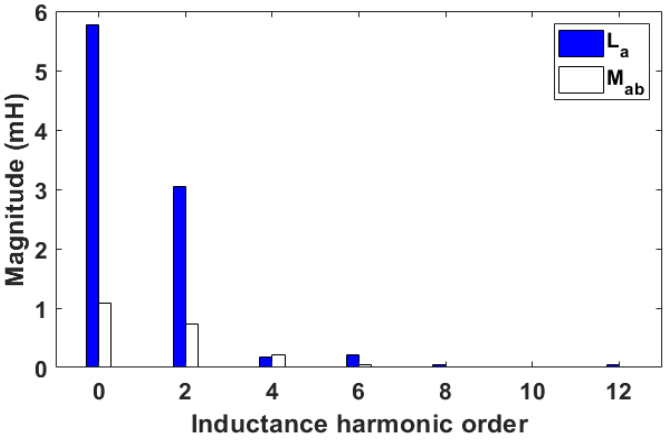

(b) Inductances Spectra.

Fig. 2.4 Phase inductances and their spectra. The armature windings are supplied with a 1A dc current.

TABLE 2.2 MACHINE SELF INDUCTANCES

Self-inductance magnitude (mH)		Self-inductance phase (rad)	
L_0	5.891	α_0	0
L_2	3.107	α_2	0.051
L_4	0.192	α_4	-3.038
L_6	0.210	α_6	0.153

TABLE 2.3 MACHINE MUTUAL INDUCTANCES

Mutual-inductance magnitude (mH)		Mutual-inductance phase (rad)	
M_0	1.101	α'_0	3.142
M_2	0.734	α'_2	-2.045
M_4	0.201	α'_4	-0.921
M_6	0.040	α'_6	3.101

By substituting (2.2) and (2.3) to (2.1), the instantaneous torque equation becomes

$$T_f = T_{f0} + T_{frip} = T_{fsel} + T_{fmut}$$

$$= \frac{3p}{2}\sum_{n=1}^{\infty}\left\{-\frac{n}{2}L_n I_1^2 \sin(n\theta_e + \alpha_n) \pm \frac{n}{4}L_n I_1^2 \sin\big((2 \pm n)\theta_e + 2\beta_1 \pm \alpha_n\big) + \frac{n}{2}M_n I_1^2 \sin(n\theta_e + \alpha'_n) \pm \frac{n}{2}M_n I_1^2 \sin\left((2 \pm n)\theta_e + 2\beta_1 \pm \alpha'_n - \frac{2\pi}{3}\right)\right\} \tag{2.4}$$

where T_f indicate torque due to the fundamental current; '0' and '*rip*' represent the average component and ripple component, respectively; '*sel*' and '*mut*' represent the components due to the self- and mutual-inductances, respectively. p is the rotor pole pair number. It can be proven that the frequency of torque ripple for a 12s/8p SRM is due to triplen harmonic. Therefore, T_f can be simplified and rewritten by (2.5), where k is a non-negative integer.

$$\begin{aligned} T_f = \frac{3p}{2}\sum_{k=0}^{\infty}\Bigg\{ & -\frac{3k}{2}L_{3k}I_1^2 \sin(3k\theta_e + \alpha_{3k}) \\ & + \frac{3k-2}{4}I_1^2 L_{3k-2}\sin(3k\theta_e + 2\beta_1 + \alpha_{3k-2}) \\ & + \frac{3k+2}{4}I_1^2 L_{3k+2}\sin(3k\theta_e - 2\beta_1 + \alpha_{3k+2}) \quad \Big\} T_{fsel} \\ & + \frac{3k}{2}I_1^2 M_{3k}\sin(3k\theta_e + \alpha'_{3k}) \\ & + \frac{3k-2}{2}I_1^2 M_{3k-2}\sin\left(3k\theta_e + 2\beta_1 + \alpha'_{3k-2} - \frac{2\pi}{3}\right) \\ & + \frac{3k+2}{2}I_1^2 M_{3k+2}\sin\left(3k\theta_e - 2\beta_1 + \alpha'_{3k+2} + \frac{2\pi}{3}\right)\Bigg\} \quad T_{fmut} \end{aligned} \tag{2.5}$$

Moreover, when the number k is equal to '0', (2.5) could give the average torque and can be expressed as (2.6). It is worth noting that the dc component has no effect on the torque production and the average torque only depends on the 2nd order harmonic when sinewave

current is supplied. It also can be proven by (2.1), that the average torque is proportional to the derivatives of self- and mutual-inductances rather than their absolute values.

$$T_{f0} = \frac{3}{4} I_1^2 L_2 \sin(-2\beta_1 + \alpha_2) + \frac{3}{2} I_1^2 M_2 \sin(-2\beta_1 + \alpha'_2 + \frac{2\pi}{3}) \quad (2.6)$$

According to (2.5)-(2.6), the torque (average or peak-to-peak value) produced by each inductance harmonic can be calculated, as shown in Fig. 2.5. It can be seen that the average torque is only produced by the 2nd inductance harmonic, as expected. Moreover, it is worth noting that the 4th, 6th, 8th and 12th inductance harmonics play a dominant role in the torque ripple production. The 4th, 6th and 8th inductances harmonics [k in (2.5) is 2 because the inductance harmonic orders are positive integers] produce a 6th order torque ripple while the 12th inductance harmonic generates a 12th order torque ripple, which is more obvious in Fig. 2.6.

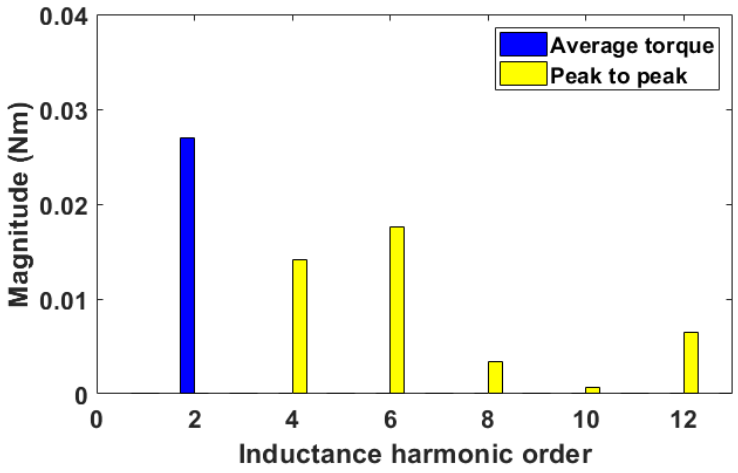

Fig. 2.5 Average torque and peak-to-peak torque produced by each order of inductance harmonic.

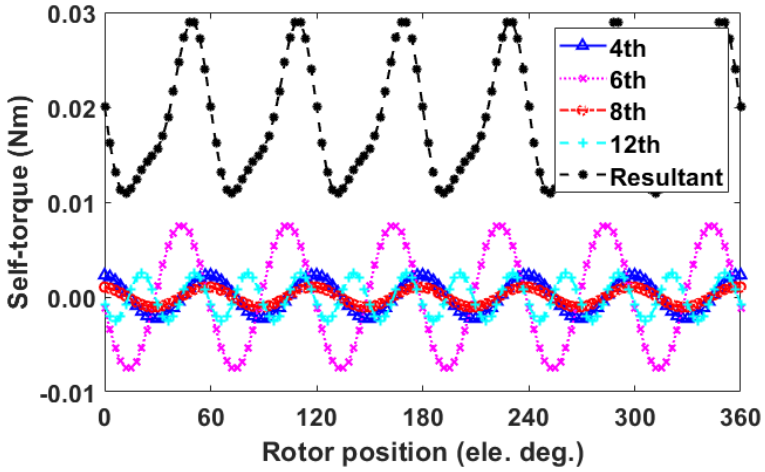

(a) Self-torques

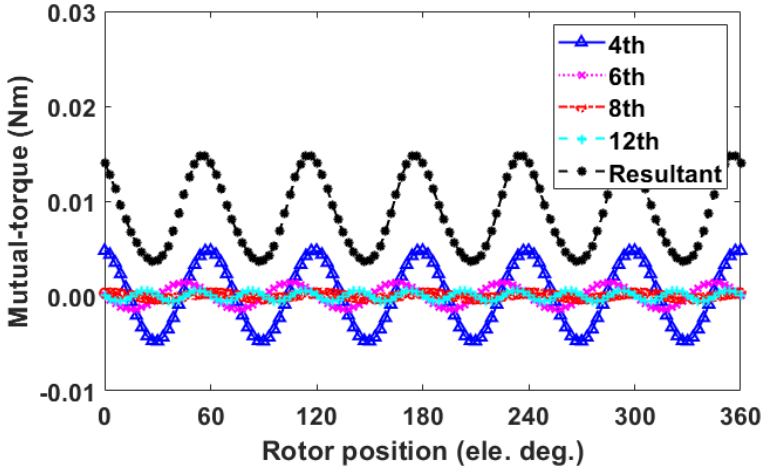

(b) Mutual-torques

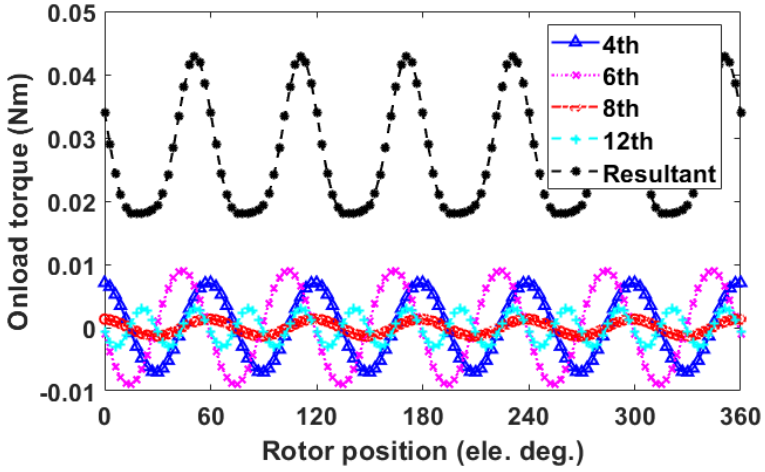

(c) Resultant on-load torques

Fig. 2.6 Instantaneous torque contribution of dominant inductance harmonics.

As shown in Fig. 2.7, the torque prediction has good agreements with the FE results, and as expected, the inductance harmonics such as the 2^{nd}, 4^{th}, 6^{th}, 8^{th} and 12^{th} dominate the torque (average or peak-to-peak) production and the effect of other inductance harmonics can be neglected.

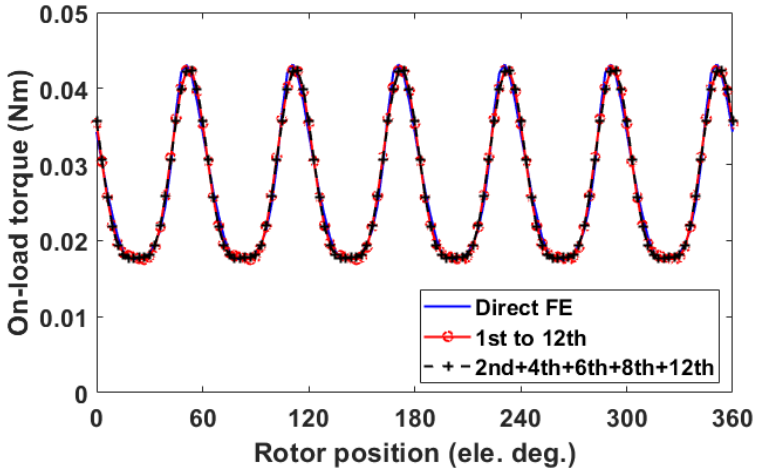

(a) On-load torque waveforms

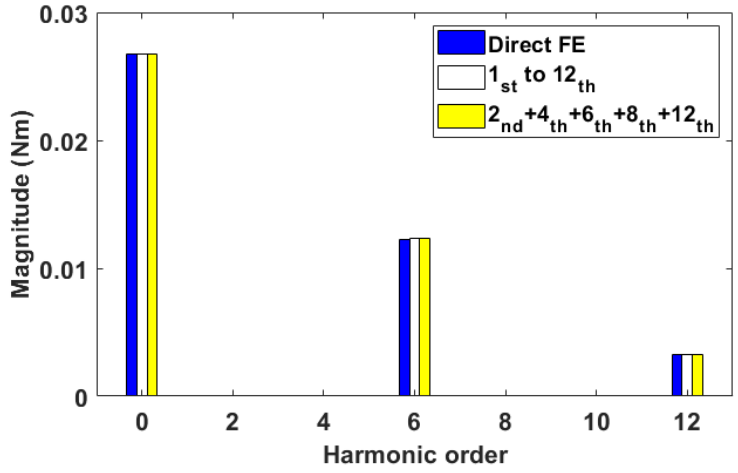

(b) Torque spectra

Fig. 2.7 Comparison of 2D-FE and analytically predicted torques. The three phases are supplied with 1 Arms AC current.

2.3 Analytical Torque Model with Harmonic Current

In order to reduce the torque ripple in the DS-SRM, the current harmonic injection method is investigated in this chapter. It is worth noting that in order to simplify the derivation of analytical model, the coupling effect between current harmonics will not be considered. Therefore, only one type of current harmonic will be injected for each case. Once the injected current harmonic order is determined, the current equation can be rewritten as:

$$\begin{cases} i_a = I_1 \sin(\theta_e + \beta_1) + I_v \sin(v\theta_e + \beta_v) \\ i_b = I_1 \sin\left(\theta_e - \frac{2\pi}{3} + \beta_1\right) + I_v \sin(v(\theta_e - \frac{2\pi}{3}) + \beta_v) \\ i_c = I_1 \sin\left(\theta_e + \frac{2\pi}{3} + \beta_1\right) + I_v \sin(v(\theta_e + \frac{2\pi}{3}) + \beta_v) \end{cases} \quad (2.7)$$

where v, I_v and β_v represent the order, the magnitude and the phase angle of the v^{th} current harmonic, respectively. Fig. 2.8 shows the phase a current waveform with different current harmonics injected.

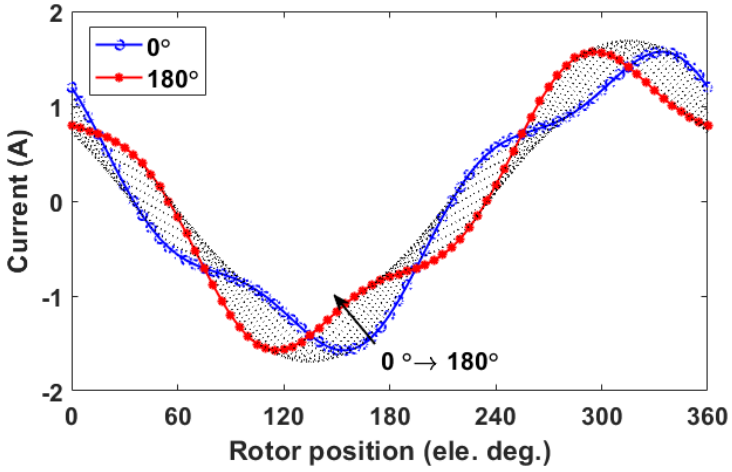

(a) I_1+I_{3rd}

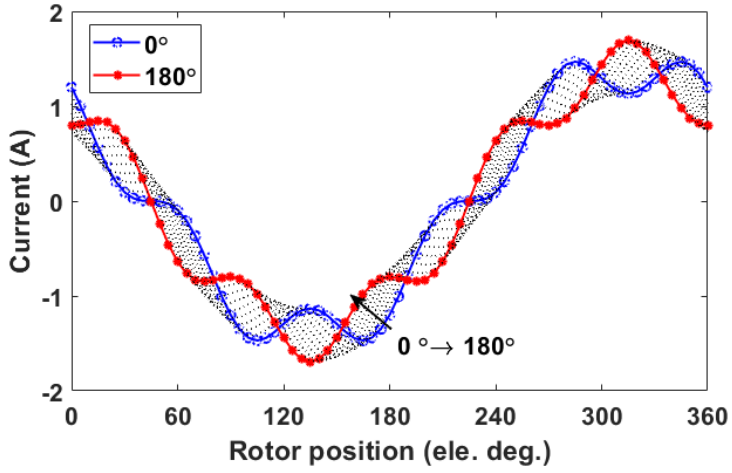

(b) I_1+I_{5th}

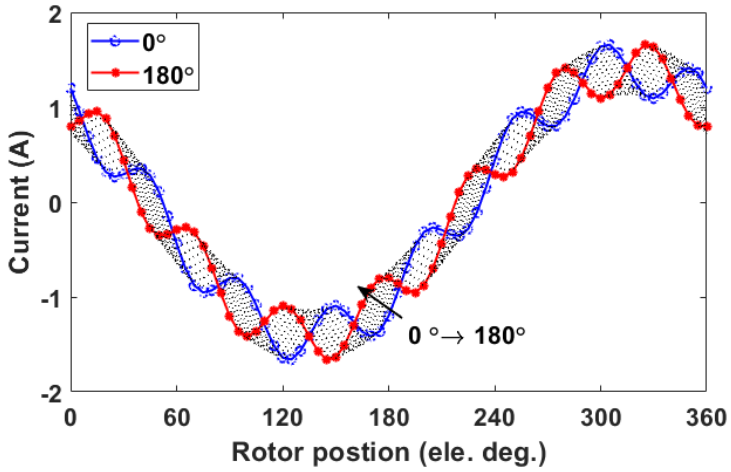

(c) I_1+I_{7th}

Fig. 2.8 Phase a current waveform with single current harmonic injection.

In a similar way, by substituting (2.3) and (2.7) into (2.1), the torque equation can be separated into three terms which are determined by ${I_1}^2$, $I_1 I_v$ and ${I_v}^2$. The fundamental current term ${I_1}^2$ is the same as in (2.5). The pure harmonic term ${I_v}^2$ is much smaller than ${I_1}^2$, hence its effect can be neglected as will be investigated later in this section. Therefore, more significant effect of harmonic injection is focused on the $I_1 I_v$ torque term. The torque equation can be simplified as follows:

$$T_h = T_{h0} + T_{hrip} = T_{hsel} + T_{hmut} \tag{2.8}$$

where T_{hsel} and T_{hmut} are self- and mutual-torques due to current harmonic and can be written as follows:

$$\begin{aligned} T_{hsel} = \frac{3p}{2}\sum_{n=1}^{\infty}\frac{nL_n}{2} I_1 I_v \{ & \sin(A\theta_e + \beta_1 + \beta_v + \alpha_n) \\ & - \sin(B\theta_e + \beta_1 + \beta_v - \alpha_n) \\ & - \sin(C\theta_e + \beta_1 - \beta_v + \alpha_n) \\ & + \sin(D\theta_e + \beta_1 - \beta_v - \alpha_n) \end{aligned} \tag{2.9}$$

And

$$
\begin{aligned}
T_{hmut} = \frac{3p}{2}\sum_{n=1}^{\infty}\frac{nM_n}{2}I_1 I_v \\
\Big\{\sin\Big(A\theta_e + \beta_1 + \beta_v + \alpha'_n - \frac{2\pi}{3}v\Big) \\
-\sin\Big(B\theta_e + \beta_1 + \beta_v - \alpha'_n - \frac{2\pi}{3}v\Big) \\
-\sin\Big(C\theta_e + \beta_1 - \beta_v + \alpha'_n + \frac{2\pi}{3}v\Big) \\
+\sin\Big(D\theta_e + \beta_1 - \beta_v - \alpha'_n + \frac{2\pi}{3}v\Big) \\
+\sin\Big(A\theta_e + \beta_1 + \beta_v + \alpha'_n - \frac{2\pi}{3}\Big) \\
-\sin\Big(B\theta_e + \beta_1 + \beta_v - \alpha'_n - \frac{2\pi}{3}\Big) \\
-\sin\Big(C\theta_e + \beta_1 - \beta_v + \alpha'_n - \frac{2\pi}{3}\Big) \\
+\sin\Big(D\theta_e + \beta_1 - \beta_v - \alpha'_n - \frac{2\pi}{3}\Big)\Big\}
\end{aligned}
\tag{2.10}
$$

and

$$
\begin{cases} A = 1 + v + n \\ B = 1 + v - n \\ C = 1 - v + n \\ D = 1 - v - n \end{cases} \text{ with } A, B, C, D = 0, \pm 3, \pm 6, \pm 9 \ldots \tag{2.11}
$$

It can be proven that the frequency of T_h correlates with the current and inductance harmonic orders as shown in (2.11). Generally, T_h will only contain the triplen harmonics, so does T_f. This means that the combination of *v* and *n* needs to generate multiples of three for *A* to *D*. By way of example, when *v* is equal to 3, the term *A* can contribute to torque only if *n* is equal to 2, 5, 8, etc. If this condition satisfies, the average torque T_{h0} can then be obtained, as described by (2.12), where the rotor position θ_e is equal to '0'. It is worth noting that the active inductances $v \pm 1$, e.g. 2nd [*C* in (2.11) is 0] and the 4th [*B* in (2.11)is 0] inductance harmonics when 3rd current harmonic injection, will produce average torque.

$$
\begin{aligned}
T_{h0} = -\frac{3pn}{4}I_1 I_v[L_{v\mp1}\sin(\beta_1 \mp \beta_v \pm \alpha_n) + M_{v\mp1}\sin\Big(\beta_1 \mp \beta_v \pm \alpha'_n \pm \frac{2\pi}{3}v\Big) \\
+M_{v\mp1}\sin\Big(\beta_1 \mp \beta_v \pm \alpha'_n - \frac{2\pi}{3}\Big)\Big]
\end{aligned}
\tag{2.12}
$$

When the 3rd current harmonic is injected, according to (2.5) and (2.8)-(2.11), the torque (average or peak-to-peak) produced by each inductance harmonic can be calculated, as shown in Fig. 2.9. It is apparent that only the 2nd inductance harmonic can influence the average torque

and the torque produced by the 4th inductance harmonic can be neglected due to its small inductance magnitude (see Fig. 2.4). Meanwhile, the injected 3rd current harmonic has little effect on the peak to peak torque for other inductance harmonics except for the 2nd order one that has the highest magnitude, which can be seen in Fig. 2.10. According to (2.11), the 2nd order inductance harmonic [n=2] together with the 3rd order current harmonic [v=3] produce a 6th order torque ripple harmonic [A in (2.11) is 6], which has the same frequency as the dominant torque ripple produced by the fundamental current (see Fig. 5.21). Therefore, it is possible to make these two torque harmonics opposite to each other in order to reduce the resultant torque ripple. This must be done by properly selecting the injected current harmonics in terms of harmonic order, amplitude and also phase angle.

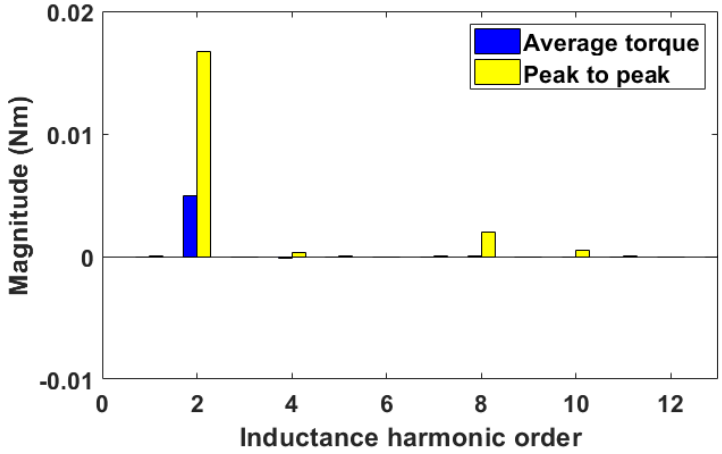

Fig. 2.9 Average torque and peak-to-peak torque produced by interaction between each inductance harmonic and current harmonic ($I_v = 30\%I_1$, $\beta_1 = 45°$ and $\beta_v = 53.6°$ see Section 2.4).

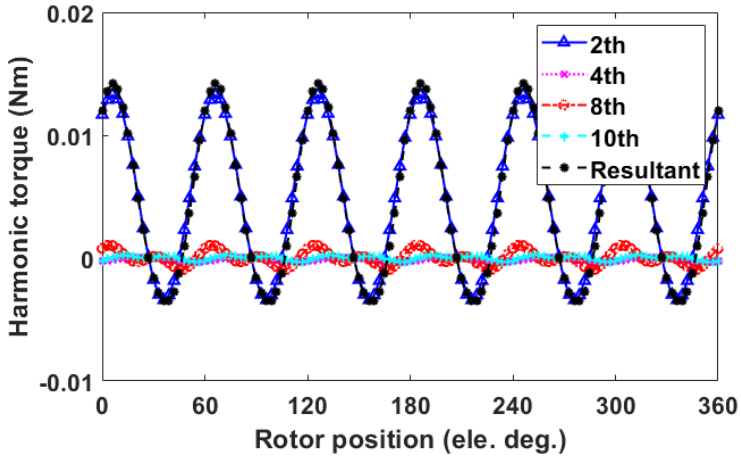

Fig. 2.10 Harmonic torque produced by active inductance harmonics when the 3rd order current harmonic is injected. ($I_v = 30\%I_1$, $\beta_1 = 45°$ and $\beta_v = 53.6°$ see Section 2.4).

TABLE 2.4 shows the active inductance harmonic orders influencing the average or the peak-to-peak torque which can be calculated by previous equations. It is also worth noting that the 2nd order inductance effect is much more significant compared with others.

TABLE 2.4 ACTIVE INDUCTANCE ORDER SELECTION FOR TORQUE PRODUCTION

Current Components	Average torque	6th torque ripple	12th torque ripple
Fundamental	2nd	4th, 6th, 8th	10th,12th, 14th
3rd harmonic	2nd and 4th	2nd, 4th, 8th, 10th	-
5th harmonic	4th and 6th	2nd, 10th, 12th	-
7th harmonic	6th and 8th	2nd, 12th, 14th	-

Note: "-" means the 12th torque ripple due to harmonic current injection is negligible.

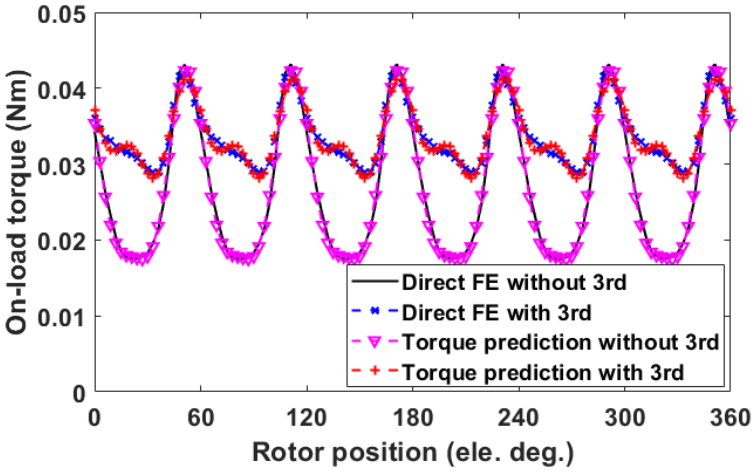

(a) I_1 =1 Arms

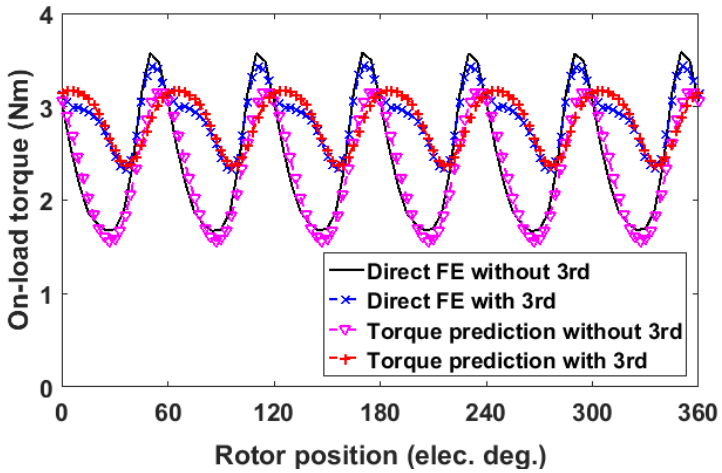

(b) I_1 =10 Arms

Fig. 2.11 Comparison of 2D-FEA and analytically predicted torque waveforms. ($I_{3rd} = 30\%I_1$, $\beta_1 = 45°$ and $\beta_v = 53.6°$ see Section 2.4).

By way of example, the torque waveforms with or without the 3rd current harmonic injections are predicted by (2.5) and (2.8)-(2.11) without considering the pure harmonic torque term $I_v{}^2$, as shown in Fig. 2.11. A good agreement between the FE and analytical torque models has been observed at low phase current, e.g. I_1 = 1Arms. The results for I_1 = 10Arms have also been calculated. It is found that the machine becomes saturated and there is a marginal discrepancy between the results obtained by direct FE and that obtained by the analytical torque model. However, the effect of current harmonic injection on torque ripple reduction is not compromised. In addition, as aforementioned, it can still be concluded that the effect of the pure harmonic torque term can be neglected for the torque analysis without sacrificing its accuracy.

Fig. 2.12 and Fig. 2.13 show comparisons of average torque and torque ripple coefficient versus phase rms current obtained by 2D-FEA and by the analytical torque equations. Here the torque ripple coefficient is calculated by:

$$T_{rip} = \frac{T_{max} - T_{min}}{T_0} \times 100\% \tag{2.13}$$

where T_{max} and T_{min} are the maximum and minimum torques for an electrical period, respectively. It should be noted that the inductances used in the torque equations are functions of phase rms current, which contains both the fundamental and the harmonic contents.

It has been found that the torque ripple coefficients of the DS-SRM are reduced significantly for all selected current harmonics, in which the 3rd order harmonic shows the best performance. It not only reduces the torque ripple by 56.3% but also increases the average torque by about 13%. It is also found that although the 5th order current harmonic has more significant reduction in torque ripple, the average torque is also slightly reduced. This is the same for the 7th current harmonic injection although its effect on torque ripple reduction is less significant. For different current harmonics, their phase angles (β_v) to achieve the minimum torque ripple are different. The selection of the best phase angle of each current harmonic will be detailed in the Chapter 2.4. It is worth noting that with increasing phase current, machine becomes highly saturated and there is an increasing discrepancy between the 2D-FE and analytical predictions. This would be the limitation of the developed analytical torque models. However, although the accuracy of the torque equation is reduced at high phase current, the effect of current harmonic injection on torque ripple reduction is not seriously compromised.

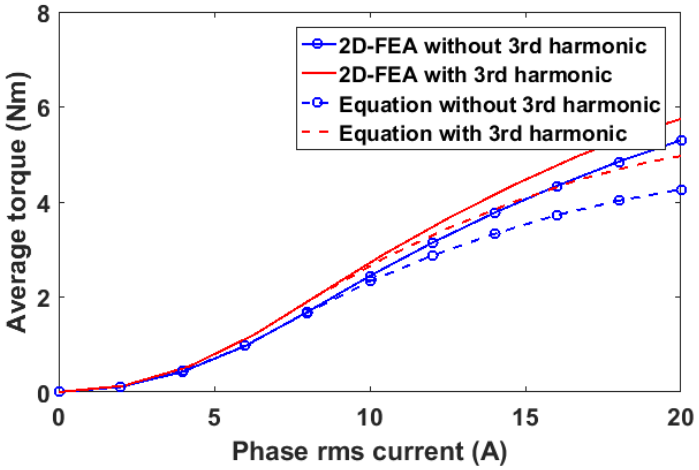

(a) I_{3rd}=30%I_1, $\beta_1 = 45°$ and $\beta_v = 53.6°$

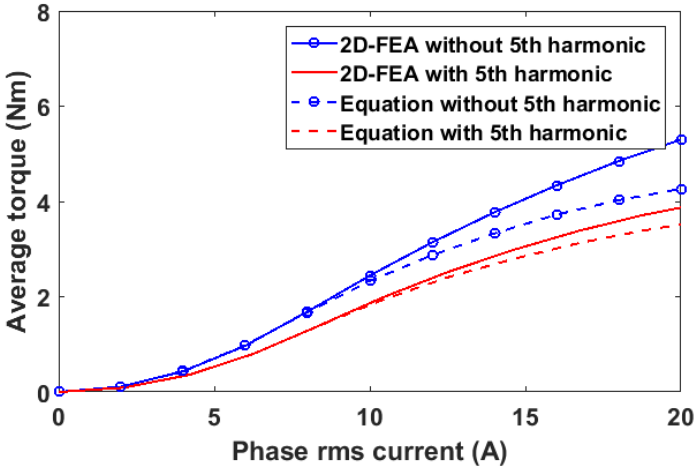

(b) I_{5th}=30%I_1, $\beta_1 = 45°$ and $\beta_v = 143.6°$

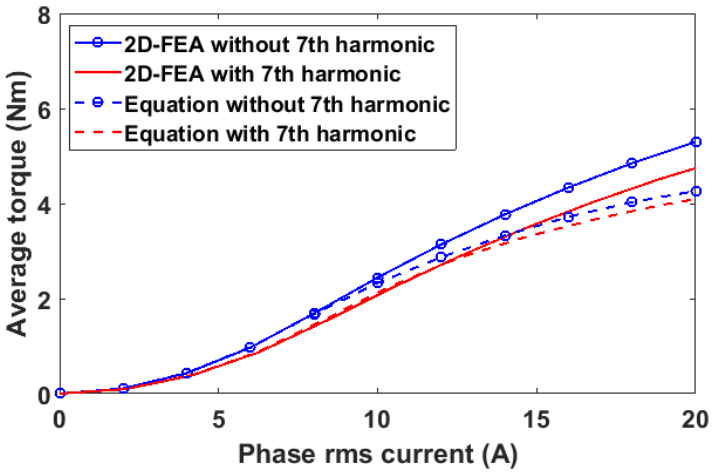

(c) I_{7th}=30%I_1, $\beta_1 = 45°$ and $\beta_v = 233.4°$

Fig. 2.12 Comparison of 2D-FEA and analytically predicted average torque with injected current harmonics. (Current harmonic selection see Section 2.4)

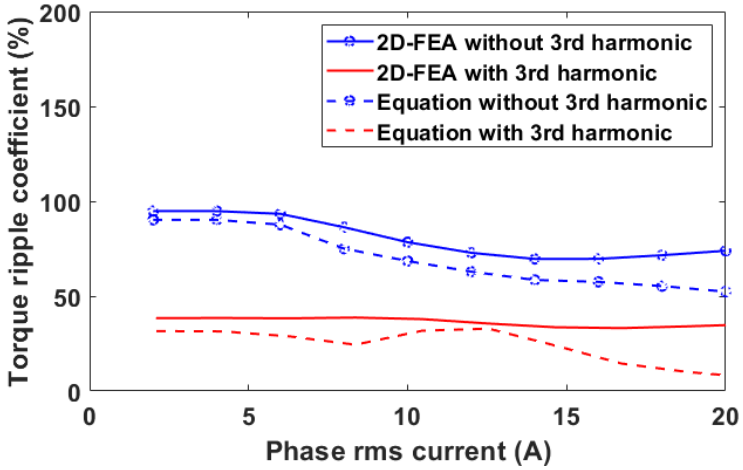

(a) I_{3rd}=30%I_1, $\beta_1 = 45°$ and $\beta_v = 53.6°$

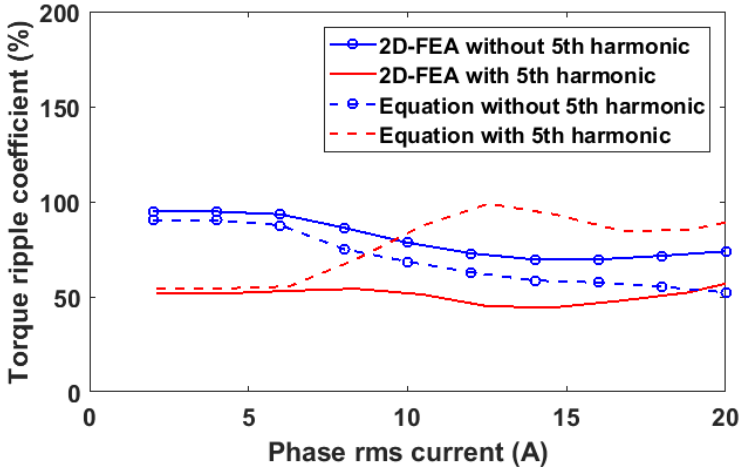

(b) I_{5th}=30%I_1, $\beta_1 = 45°$ and $\beta_v = 143.6°$,

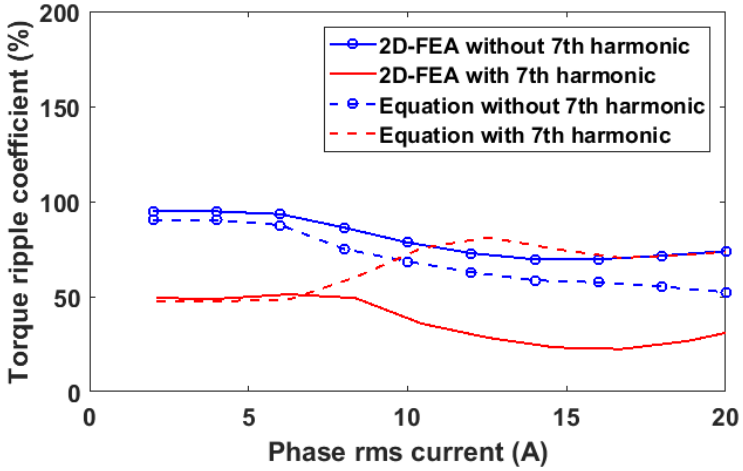

(c) I_{7th}=30%I_1, $\beta_1 = 45°$ and $\beta_v = 233.4°$

Fig. 2.13 Comparison of 2D-FEA and analytically predicted torque ripple coefficient with injected current harmonics. (Current harmonic selection see Section 2.4)

2.4 CURRENT HARMONIC SELECTION FOR DS-SRM

In previous section, analytical torque model has been carried out for both fundamental current and current harmonic injections. In this section, further analyses based on torque equation have been carried out in order to predict the current harmonic magnitude and phase angle where maximum average torque and minimum torque ripple can be achieved. It is well established that for the sinewave current supply, the maximum torque is obtained when the phase advance angle is $\beta_1 = 45°$ [67]. This is largely true when the magnetic saturation can be neglected. Hence, in the following calculations, the current phase advance angle for the fundamental current is $\beta_1 = 45°$ and is always kept unchanged.

2.4.1 ODD ORDER CURRENT HARMONIC INJECTION

Injected current harmonics can be classified into two categories: odd order current harmonic e.g. 3rd, 5th and 7th etc. and even order current harmonic e.g. 2nd, 4th and 6th etc.. Initial results shows that the odd order current harmonics, have the great potential to improve the torque performance. This section will focus on selecting the odd order current harmonic to increase average torque or reduce the torque ripple of DS-SRM.

2.4.1.1 CURRENT HARMONIC SELECTION FOR MAXIMIZING THE AVERAGE TORQUE

Based on the harmonic torque equations (2.8)-(2.10), the average torque is produced by $(v \pm 1)^{th}$ order inductance harmonic. Hence, the average torque equation can be simplified as

$$\begin{aligned} T_{h0}(\beta_v) &= \sum_{i=1}^{3} T_{Bi}\sin(\varphi_{B1} + \beta_v) + \sum_{i=1}^{3} T_{Ci}\sin(\varphi_{Ci} - \beta_v) \\ &= T_{H0}\sin(\beta_v + \varphi_{H0}) \end{aligned} \tag{2.14}$$

with

$$\begin{cases} \tan\varphi_{H0} = \dfrac{y}{x} \\ T_{H0} = \sqrt{x^2 + y^2} \end{cases} \tag{2.15}$$

$$\begin{cases} x = \sum_{i=1}^{3} T_{Bi}\cos(\varphi_{Bi}) + T_{Ci}\cos(\varphi_{Ci}) \\ y = \sum_{i=1}^{3} T_{Bi}\sin(\varphi_{Bi}) - T_{Ci}\sin(\varphi_{Ci}) \end{cases} \tag{2.16}$$

where T_{H0} and φ_{H0} are the resultant torque magnitude and phase angle, respectively. T_{Bi}, T_{Ci}, φ_{Bi} and φ_{Ci} (i=1, 2 and 3) are all constants when β_v is equal to 0, representing the magnitude and phase angle for three torque terms of *B* or *C* in (2.9) and (2.11). They can be easily calculated and will be used throughout this chapter. Therefore, it is apparent that if the harmonic magnitude is kept unchanged, the torque equation will be a function of the phase angle β_v of the current harmonics. In this case, there must be an angle that can produce the maximum average torque. These angles can be calculated by (2.17) and are 88.7°, 301.9° and 68.7° for the 3rd, 5th and 7th order harmonics, respectively. At the phase angle 88.7°, the 3rd harmonic injection could increase the average torque by 18%, while the torque ripple also could be reduced by 37.1%. Fig. 2.14 shows the average torque versus current harmonic phase angle at low phase current condition (1Arms). It can be seen that the current harmonic phase angle where the maximum average torque occurs can be accurately predicted by the proposed method.

$$\beta_{v\_Tmax} = \frac{\pi}{2} - \varphi_{H0} \tag{2.17}$$

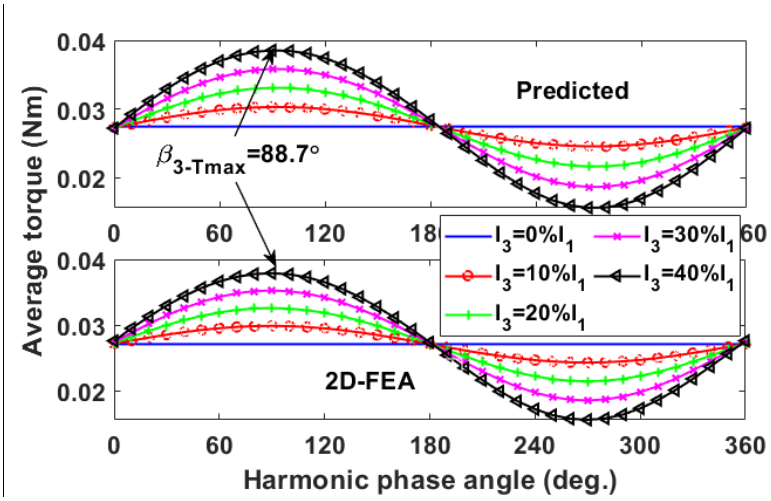

(a) I_1+I_{3rd}

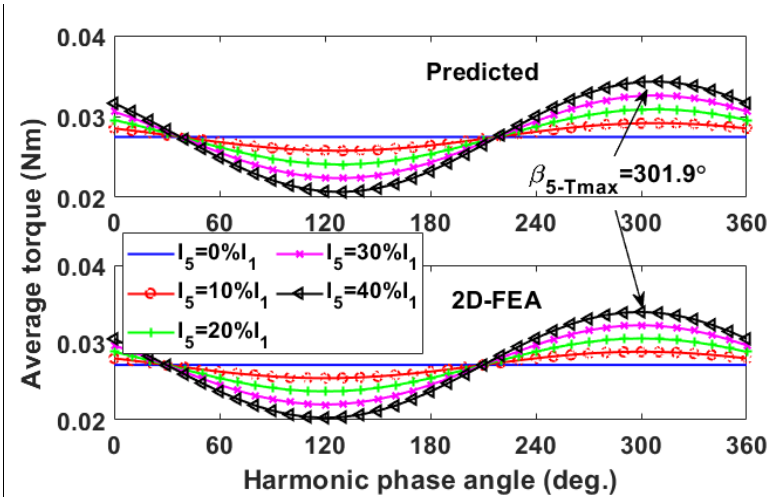

(b) I_1+I_{5th}

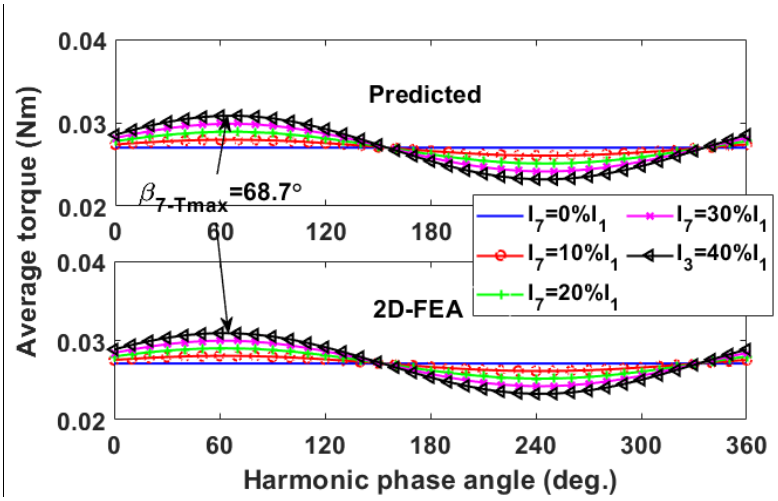

(c) I_1+I_{7th}

Fig. 2.14 Comparison of torque *vs* current harmonic phase angle. 1Arms current is supplied (Maximum average torque has been marked).

When 20Arms phase current is supplied, the machine is highly saturated. The comparison between analytical and 2D-FE predictions are shown in Fig. 2.15. It can be seen that there is about 15% prediction error in the magnitude of the average torque. This is mainly due to the fact that the inductance at high phase current condition cannot be calculated accurately without considering the coupling effect between each phases, which can be improved by using Frozen Permeability method [135],[136]. Nevertheless, the phase angle, where the maximum torque occurs, is not far away from that of the 2D-FE simulations.

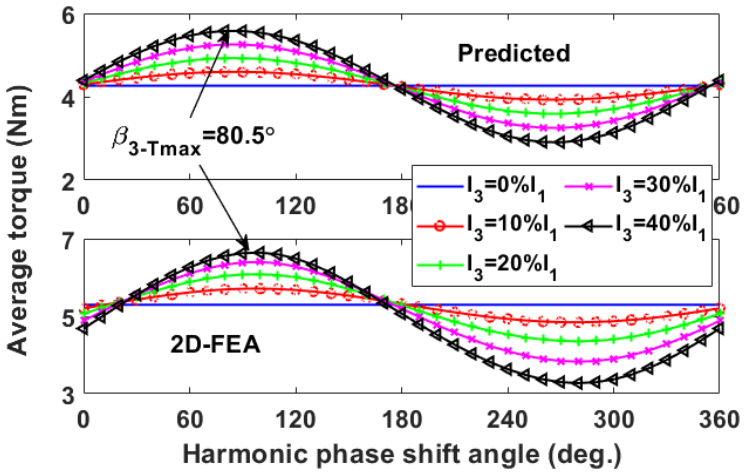

(a) I_1+I_{3rd}

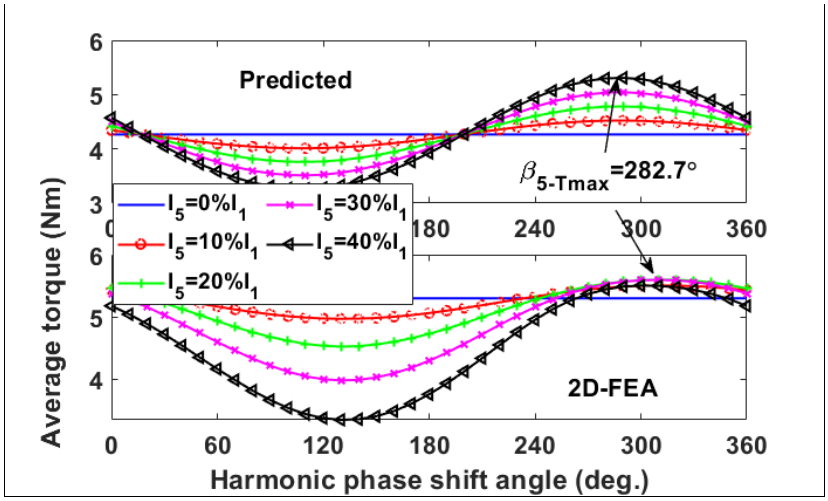

(b) I_1+I_{5th}

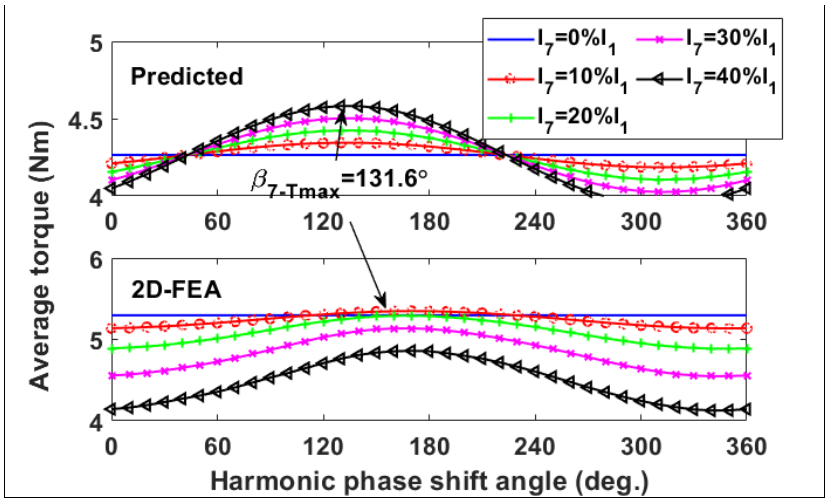

(c) I_1+I_{7th}

Fig. 2.15 Comparison of torque *vs* current harmonic phase angle. 20Arms current is supplied (Maximum average torque has been marked).

2.4.1.2 Current Harmonic Selection for Minimizing Torque Ripple

From the analytical study in the section 2.2, the dominant torque ripple harmonic order of the 12s/8p SL DS-SRMs is 6th. It has also been found that the dominant 6th order torque ripple is produced by the 4th, 6th and 8th order inductance harmonics (see Fig. 2.5). Therefore, in order to compensate the torque ripple, this chapter pays particular attention to the 6th order torque ripple harmonic component. The objective is to introduce an extra torque harmonic produced by the current harmonic, which needs to be opposite to the one produced by the fundamental current, and hence reducing the resultant torque ripple.

Based on the trigonometric function transformation, the torque ripple without current harmonic injection and produced by the 4th, 6th and 8th order inductance harmonics can be obtained from (2.5) and concisely expressed as

$$T_{frip} = T_{Frip}\sin\left(6\theta_e + \varphi_{Frip}\right) \tag{2.18}$$

According to TABLE 2.4, the 6th order torque harmonic is produced by different inductance harmonics for different current harmonics. However, as mentioned in section 2.3, the 2nd order inductance is the most significant component due to its highest magnitude. Therefore, only 2nd order inductance are considered to minimize the 6th order torque harmonic. According to (2.8)-(2.11), the 6th order torque harmonic can be rewritten as

$$\begin{aligned} T_{hrip}(\beta_v) &= \sum_{i=1}^{3} T_{Xi}\sin(6\theta_e + \varphi_{Xi} + \beta_v) \\ &= T_{Hrip}(0)\sin\left(6\theta_e + \varphi_{Hrip}(0) + \beta_v\right) \end{aligned} \tag{2.19}$$

with

$$\begin{cases} \tan\varphi_{Hrip}(\beta_v) = \dfrac{y(\beta_v)}{x(\beta_v)} \\ T_{Hrip}(\beta_v) = \sqrt{x(\beta_v)^2 + y(\beta_v)^2} \end{cases} \tag{2.20}$$

$$\begin{cases} x(\beta_v) = \displaystyle\sum_{i=1}^{3} T_{Xi}\cos(\varphi_{Xi} + \beta_v) \\ y(\beta_v) = \displaystyle\sum_{i=1}^{3} T_{Xi}\sin(\varphi_{Xi} + \beta_v) \end{cases} \tag{2.21}$$

where T_{Xi} and φ_{Xi} (X=A, B, C or D; i=1, 2 and 3) are all constant, representing the magnitude and phase angle for three torque terms of X, when β_v is 0. T_{Hrip} and φ_{Hrip} are the resultant torque and phase angle produced by the injected current harmonics. It is apparent that the resultant torque ripple can be controlled by β_v. As a result, in order to minimize the resultant torque ripple, (2.18) and (2.19) need to achieve the same magnitude but have a π phase shift angle. This leads to

$$\begin{cases} T_{Frip} = T_{Hrip}(I_v, \beta_v = 0) \\ \varphi_{Hrip}(0) + \beta_v - \varphi_{\mathrm{Frip}} = (2d+1)\pi \end{cases} \tag{2.22}$$

where d is an integer. When the 3rd order current harmonic is injected, φ_{Frip} and $\varphi_{Hrip}(0)$ can be calculated as $143.5°$ and $-90.1°$, respectively. Therefore, the phase angle to achieve the

minimum torque ripple can be obtained as $\beta_v = 53.6°$. It is the same for the 5th and 7th order current injections, β_v of which are 143.6° and 233.4°, respectively, as shown in Fig. 2.16.

Fig. 2.17 shows the torque ripple versus current harmonic phase angle for 20Arms phase current. It can be seen that there is a marginal discrepancy between the results obtained by 2D-FE and analytical prediction. Again, this is mainly due to the magnetic saturation. However, the effect of current harmonic injection on torque ripple reduction is not compromised.

Fig. 2.18 shows the comparison of analytically predicted and FE on-load torques when different current harmonics are injected, which can achieve the minimum torque ripple as calculated by (2.22). It is found that the harmonic torque ripple is opposite to the one produced by the fundamental current, as expected, leading to reduced resultant torque ripple.

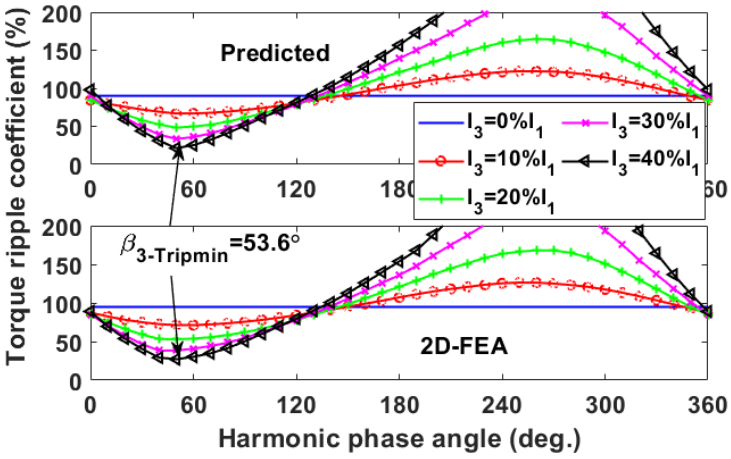

(a) I_1+I_{3rd}

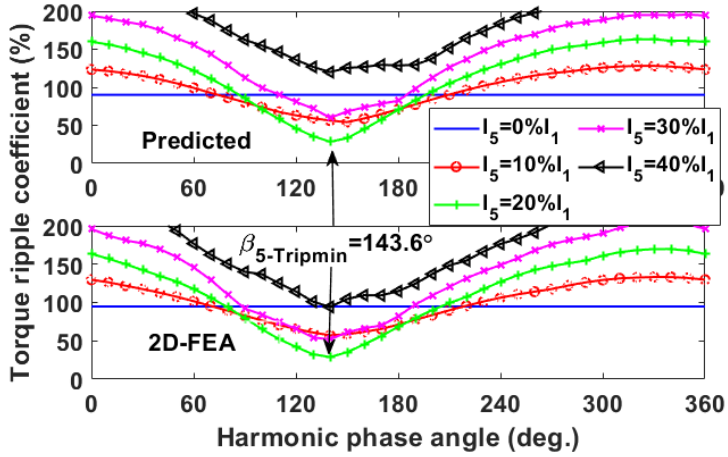

(b) I_1+I_{5th}

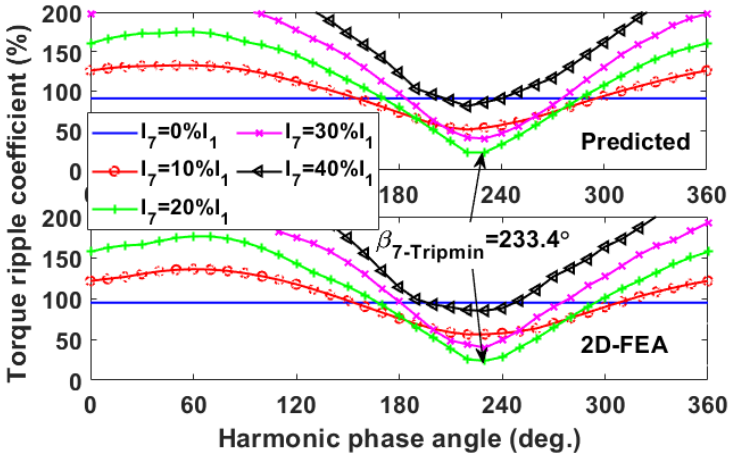

(c) I_1+I_{7th}

Fig. 2.16 Comparison of torque ripple *vs* current harmonic phase angle. 1Arms current is supplied (Minimum torque ripple has been marked).

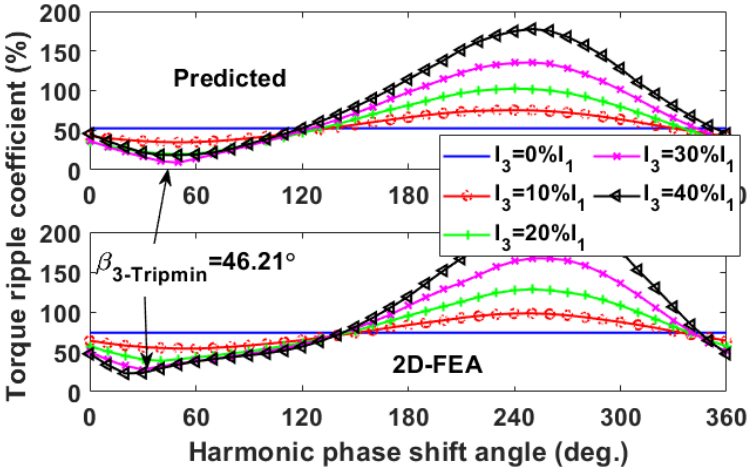

(a) I_1+I_{3rd}

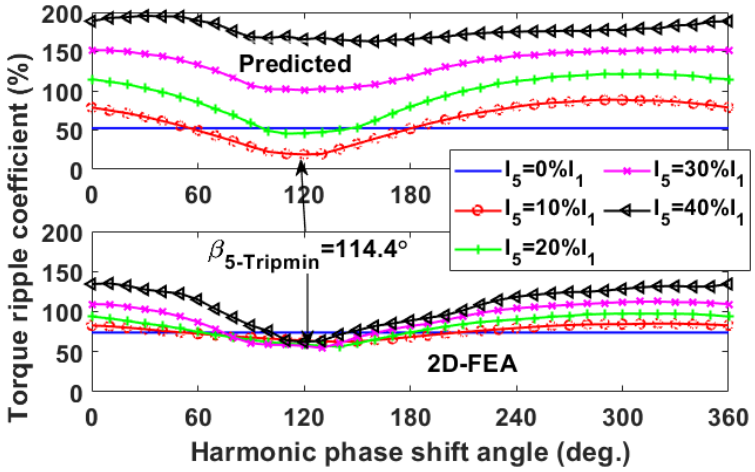

(b) I_1+I_{5th}

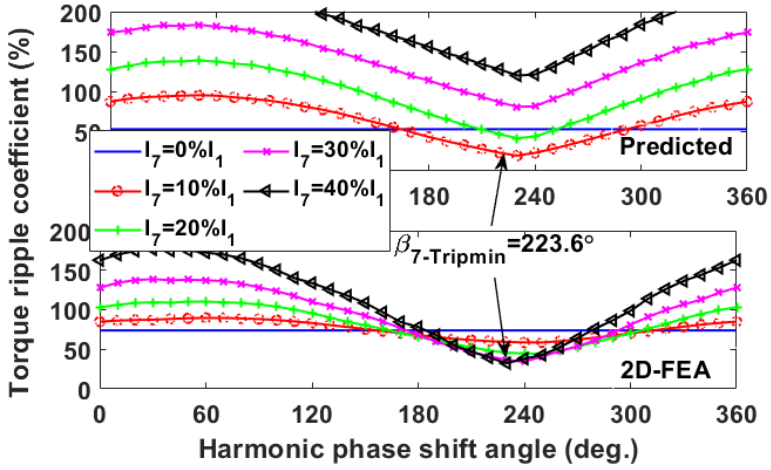

(c) I_1+I_{7th}

Fig. 2.17 Comparison of torque ripple *vs* current harmonic phase angle. 20Arms current is supplied (Minimum torque ripple has been marked).

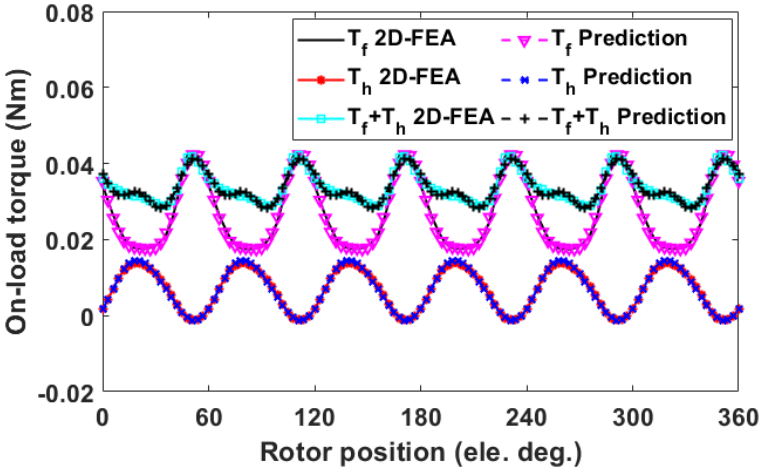

(a) I_1+I_{3rd}

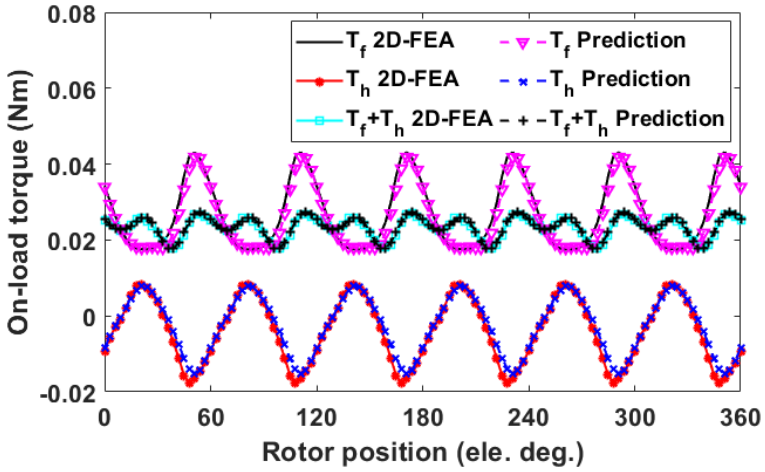

(b) I_1+I_{5th}

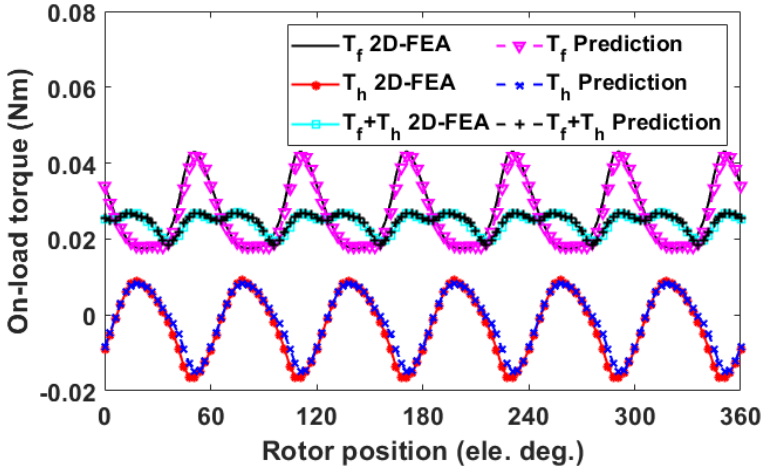

(c) I_1+I_{7th}

Fig. 2.18 Comparison of between FE and analytical predictions. 1Arms current is supplied.

Fig. 2.19 shows the spectra of DS-SRM with current harmonic injection method. It is obvious that 6^{th} order torque harmonic can be significant suppressed. The torque performance improvement can be concluded in TABLE 5.4.

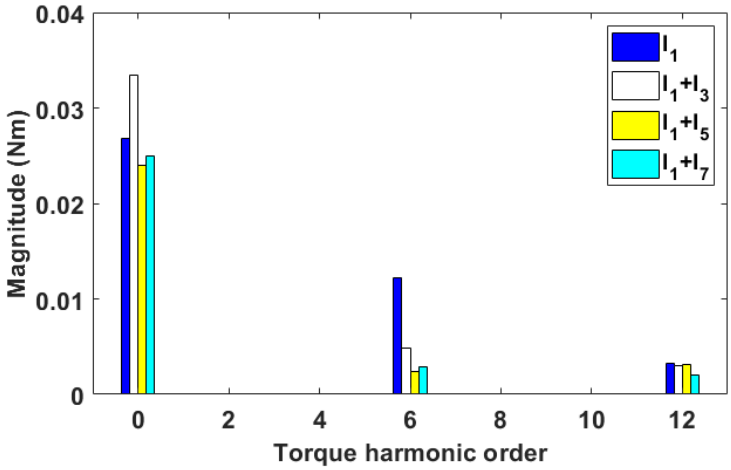

Fig. 2.19 Torque spectra of DS-SRM with current harmonic injection. 1Arms current is supplied.

TABLE 2.5 TORQUE PERFORMANCE IMPROVEMENT AFTER INJECTION

Harmonic (mag, phase)	Average (%)	Ripple (%)
3rd (30%, 53.6°)	+13.1	-55.9
5th (20%, 143.6°)	-11.6	-72.0
7th (20%, 233.4°)	-6.9	-65.3

2.4.2 EVEN ORDER CURRENT HARMONIC INJECTION

The proposed analytical model can also be used to analyze the torque contribution of even order current harmonic injection. For example, Fig. 2.20 shows the average torque and torque ripple coefficient versus current harmonic phase angle with the 2nd order current harmonic injection. Overall a good agreement can be observed between 2D-FE and analytical predictions. It is found that the variation of average torque for different current harmonic angle can be negligible. Based on previous investigations, when the 2nd order current harmonic is injected, the 1st and 3rd order inductance harmonics ($v \pm 1$) will contribute to the average torque. However, the magnitudes of odd order inductance harmonics are too small to contribute meaningfully to the torque for such machines. Moreover, in order to reduce the 6th order torque harmonic, based on (2.11), the four active inductance harmonics must be odd order inductance harmonics (e.g. 3rd, 5th,7th and 9th when $v = 2$) when even order current harmonic is injected. As a result, it is impossible to reduce the torque ripple by injecting even order current harmonics with any phase angle.

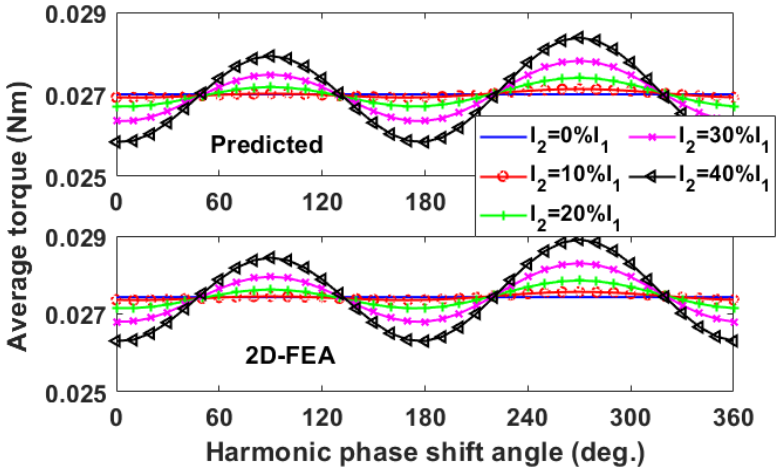

(a) Average torque

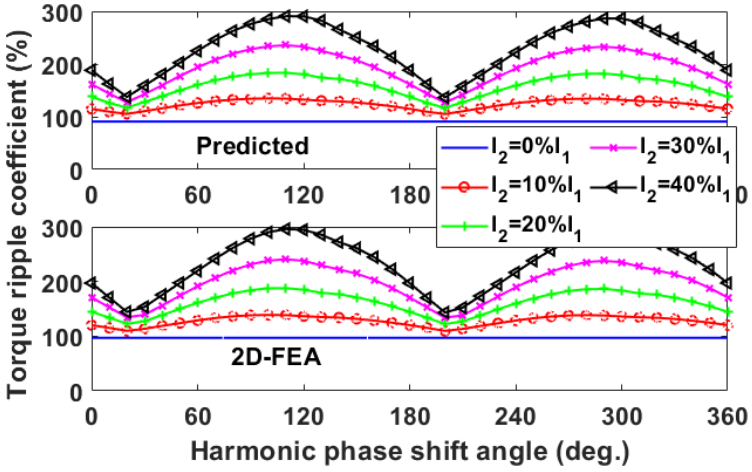

(b) Torque ripple coefficient

Fig. 2.20 FEA results of torque production for DS-SRM with the 2nd order current harmonic injection. The machines are supplied with 1A RMS current.

However, the even order current harmonic injection can modulate other unwanted torque harmonic, such as, the 3rd and 9th, etc. order torque harmonic, as shown in Fig. 2.21. It can be easily obtained by (4.17) that for the 2nd order current harmonic injection, the 2nd, 4th and 6th order inductance harmonics will contribute to the 3rd order torque harmonic, while the 6th, 8th, 10th and 12th order inductance harmonics will contribute to the 9th order torque harmonic. It can be concluded that the even order inductances (higher magnitude) will only produce the unwanted torque ripple when even order current harmonic injected. The active inductances to produce the average torque and torque ripple for even order current harmonic injection have been listed in TABLE 2.6.

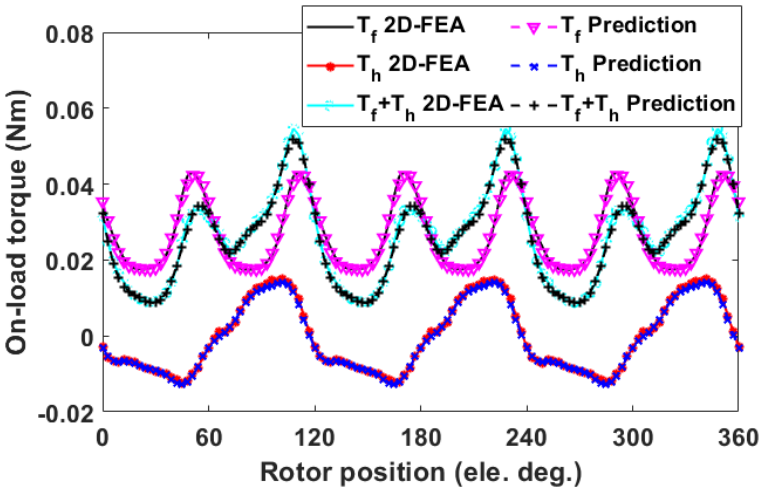

(a) On-load torque

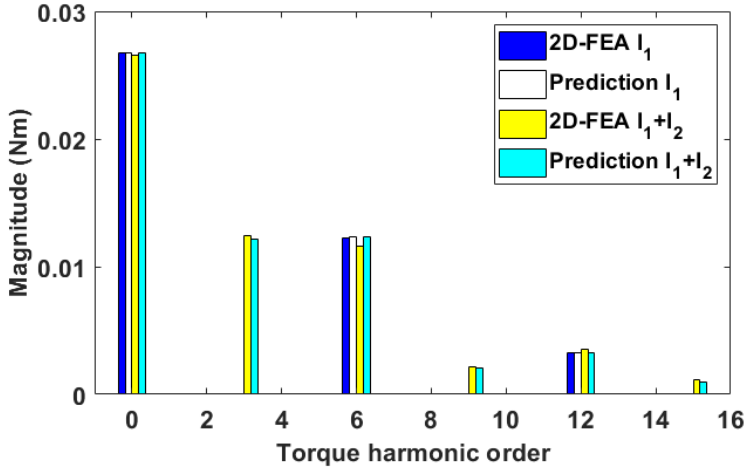

(a) Torque spectra

Fig. 2.21 On-load torque of DS-SRM with the 2nd order current harmonic injection. 1Arms current is supplied.

TABLE 2.6 ACTIVE INDUCTANCE ORDER SELECTION FOR EVEN ORDER CURRENT HARMONIC INJECTION

Current Components	Average torque	3rd torque ripple	6th torque ripple
2nd harmonic	1st and 3rd	2nd, 4th, 6th	3rd, 5th, 7th, 9th
4th harmonic	3rd and 5th	2nd, 6th,8th	1st, 3rd, 9th, 11th-
6th harmonic	5th and 7th	2nd,4th,8th 10th	1st, 11th, 13th

To sum up, there are three points showing that the even order harmonic is not good for current harmonic injection. Firstly, the even order current harmonics cannot generate extra average torque but they can reduce the fundamental current (for constant RMS current), leading to reduced average torque. Secondly, the desired torque ripple (6th) can only be produced by the

odd order inductance harmonics (low magnitude), which means it is difficult to be used to suppress the torque ripple due to fundamental current. Finally, the even order inductance harmonies (high magnitude) will contribute significantly to unwanted torque harmonics. Therefore, the proposed method will not focus on the even order current harmonic.

2.5 CONCLUSION

This chapter proposed an analytical solution for armature current harmonic injection in order to improve the average torque while reducing the torque ripple for doubly salient synchronous reluctance machines. The analyses are based on the instantaneous torque equation of the machine in question. It shows that for a 12s/8p combination, the average torque is mainly produced by the 2nd order inductance harmonic. It is also found that if a v^{th} current harmonic is injected, the $(v \pm 1)^{th}$ inductance will contributed to average torque. Although accuracy of proposed analytical model might be affected by magnetic saturation due to increased phase current, the effect of current harmonic injection on torque ripple reduction is not compromised.

Compared to other current harmonics, the 3rd order current harmonic injection exhibits the best performance, which can increase the average torque by 13% while reducing the torque ripple coefficient by 56%. The other odd order current harmonic injection, e.g. 5th and 7th can still be used to reduce the torque ripple. However, due to the characteristics of the self- and mutual-inductances, even order current harmonic injections have little effect on average torque and generally increase the torque ripple of the investigated machines. Therefore, they will not be investigated further in this thesis.

The proposed method not only predicts which current harmonic should be injected but also their amplitude and phase angle in order to achieve higher average torque and/or lower torque ripple. Although only the 12s/8p machine has been investigated as an example, the method introduced in this chapter can be extended to cover other slot/pole number combinations and also winding structures as will be detailed in next chapter. It is worth mentioning that the experimental validation will be carried out in Chapter 6.

Chapter 3 COMPARATIVE STUDIES OF THREE TYPICAL TYPES OF 3-PHASE DS-SRMS WITH CURRENT HARMONIC INJECTION

Three types of doubly salient synchronous reluctance machines (DS-SRMs) have been comparatively studied in this chapter to improve the torque performance using the current harmonic injection methods. These machines are derived from the switched reluctance machines (SRMs) with different winding configurations, such as the double/single DS-SRMs and fully pitched SRMs (FPSRMs), by supplying them with sinewave current. Such current supply mode can lead to higher torque/power density, lower vibrations and acoustic noise compared to the conventional rectangular current supply. The proposed torque analytical model can predict the instantaneous torque of the doubly salient SRMs with sinewave current excitation and the current harmonics also can be selected in order to reduce the torque ripple and/or increase the average torque. It has been found that the 3^{rd} current harmonic injection shows the best performance for single-layer DS-SRMs and FPSRMs because it improves the average torque and reduces the torque ripple at the same time. However, it has little influence on doubly-layer DS-SRMs. To improve the torque performance of such machines, other harmonic currents, e.g. 5^{th} and 7^{th}, need to be used.

This chapter comes from the author's own paper [137].

3.1 INTRODUCTION

As mentioned previously, many researchers investigated the possibility of reducing the vibrations and acoustic noise of conventional SRMs by using sinewave current supply rather than the classic rectangular wave current supply (120 electrical degrees conduction for 3-phase SRMs). This in effect makes SRMs become the doubly salient synchronous reluctance machines, as investigated in [6],[7]. However, the torque capability with sinewave current supply is reduced compared with the rectangular wave current supply [67]. In order to increase the average torque, the researchers in [24],[25] have proposed a new class of SRMs with fully pitched windings, namely fully pitched SRMs (FPSRMs). The torque generation of FPSRMs is entirely due to the rate of change of mutual-inductances between phases. It was verified that with sinewave current supply, FPSRMs can produce a torque twice as high as that of conventional SRMs. However, their longer end-winding compared with the short pitched winding of conventional SRMs results in higher copper loss at the same current level.

To combine the advantages of both conventional SRMs (short end-winding) and FPSRMs (high torque capability), the mutually coupled SRMs (MCSRMs) with double layer windings have been proposed in [26],[135]. For consistent, all the SRMs (doubly salient structure) with sinewave current supplied in this thesis is called DS-SRMs. It has been established that the double layer DS-SRMs generate torque via variation of both the self- and mutual-inductances, and are less sensitive to the magnetic saturation. As a result, the double layer DS-SRMs can operate at higher phase current and achieve higher overload capability [67],[138]. Apart from the aforementioned benefits, the double layer DS-SRMs can also achieve lower vibration and acoustic noise compared to conventional SRMs [4]. However, due to the nature of the self-and mutual-inductance variations, the torque ripple of double layer DS-SRMs is also higher. In order to mitigate this issue, researchers in [67] proposed some DS-SRMs with single layer windings (SL). They exhibit better performance, e.g. higher average torque and also lower torque ripple, at low current conditions compared to their double layer counterparts. However, these advantages diminish with increasing saturation level.

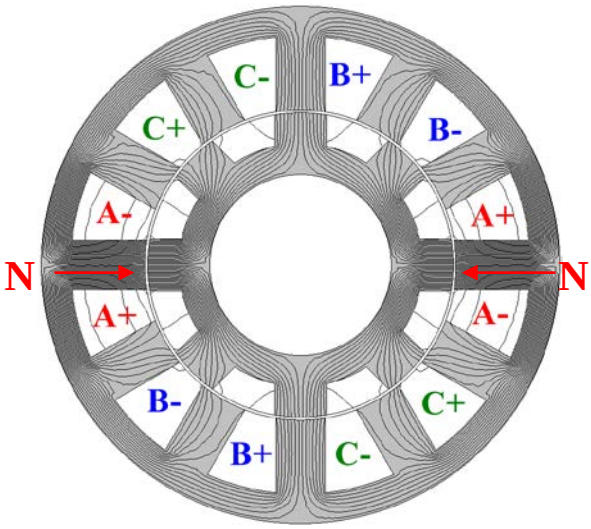

(a) Single layer DS-SRMs (b) FPSRMs

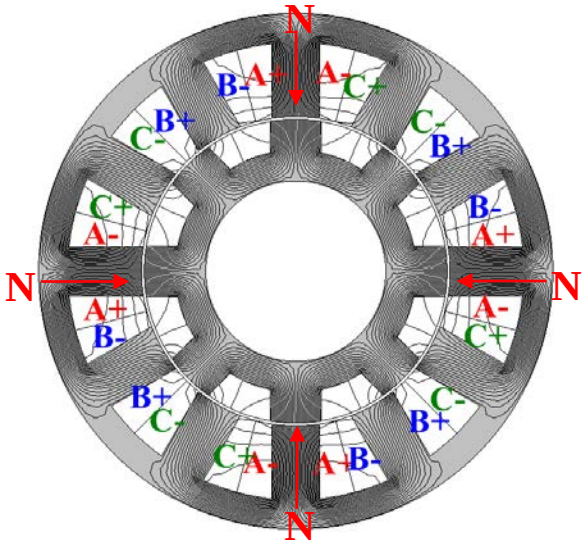

(c) double layer DS-SRMs

Fig. 3.1 Flux distributions at aligned position with phase A supplied by a 1A dc current.

In Chapter 2, a current harmonic injection method has been proposed to improve the torque performance of the single layer DS-SRMs. In order to justify the generality of the proposed current harmonic injection method, the comparative investigations between the doubly salient synchronous reluctance machines that evolved from the aforementioned SRMs with three different winding configurations, as shown in Fig. 3.1, are carried out in this chapter. The machine parameters are given in TABLE 2.1. It is worth noting that the single/double layer conventional SRMs will not be investigated due to their poor performance when supplied with sinewave current.

Due to different winding configurations, the self- and mutual-inductances for single/double layer DS-SRMs and FPSRM are different as well, which result in different electromagnetic

torque contribution, as shown in TABLE 3.1. Since the self-inductance of single layer DS-SRMs is much larger than the mutual-inductance, the torque due to the self-inductance is the most dominant component. However, the torque generation of FPSRMs is entirely due to the mutual-inductances because the variation of the self-inductances can be neglected. Moreover, the double layer DS-SRMs combines both the benefits of the self- and mutual-inductances.

TABLE 3.1 ELECTROMAGNETIC TORQUE COMPONENTS FOR DIFFERENT DS-SRMS

	Torque Components	
	Dominant	Subordinate
SL DS-SRM	Self-torque	Mutual-torque
DL DS-SRM	Self-/Mutual-torque	-
FPSRM	Mutual-torque	Self-torque

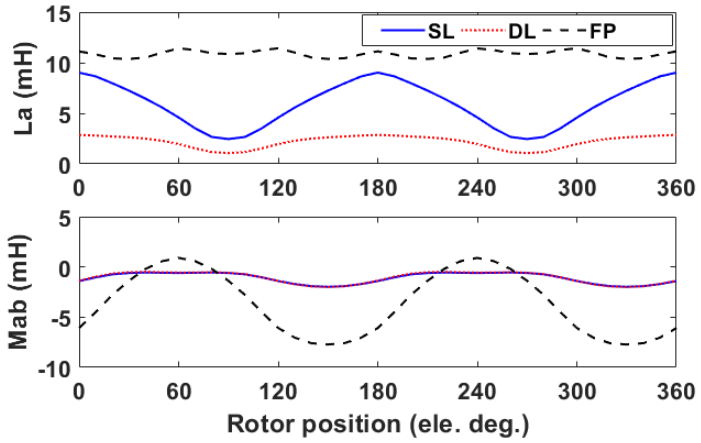

(a) Inductances waveform

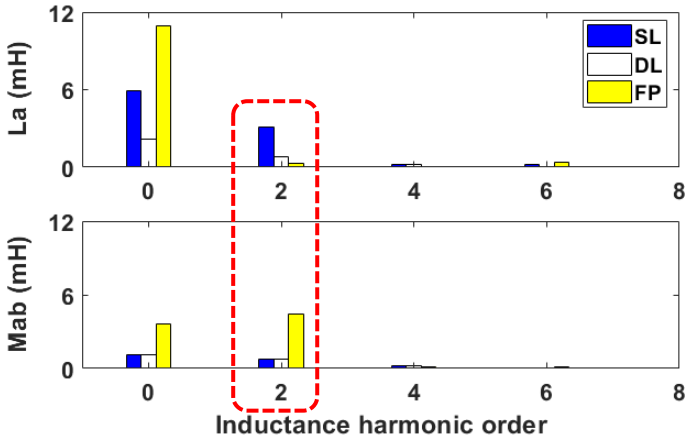

(b) Inductances spectra

Fig. 3.2 Comparison of self- and mutual-inductances for three winding configurations. The phase a is supplied with a 1A dc current.

Due to the nature of the inductances, the odd order inductance harmonics can be neglected as shown in Fig. 3.2. Based on the previous study, for all SRMs, the dc inductance component has no contribution to the torque, and hence can be neglected as well. The average torque produced by the fundamental current only depends on the 2nd order inductance harmonic. However, other even order inductance harmonics contribute to the torque ripples, in which the dominant one, i.e. the 6th order torque harmonic, is produced by the 4th, 6th and 8th order inductance harmonics. As a result, in order to reduce the torque ripple, as in Chapter 2, this chapter is focused on reducing the 6th order torque harmonic for different SRMs.

The same current harmonic injection method has been applied to the three aforementioned SRMs. The magnitudes and phase angles of different current harmonics for different types of machines have been predicted and compared, as shown in TABLE 3.2.

TABLE 3.2 CHARACTERISTICS OF CURRENT HARMONIC FOR ACHIEVING MINIMUM TORQUE RIPPLE

	3rd harmonic		5th harmonic		7th harmonic	
	Mag.	Phase	Mag.	Phase	Mag.	Phase
SL DS-SRM	30%	53.6°	20%	143.6°	20%	233.4°
DL DS-SRM	30%	45.2°	30%	113.3°	30%	205.7°
FPSRM	30%	270.6°	20%	180.5°	20%	270.5°

Fig. 3.3 shows the prediction of on-load torque with and without current harmonic injection for the three aforementioned SRMs. It shows a generally good agreement between the FEA and analytically predicted results for a phase root-mean-square (RMS) current of 1A. Moreover, it can be proven that the 3rd order current harmonic injection could reduce the torque ripples while increasing the average torque for both single layer DS-SRMs and FPSRMs, but it has little effect on double layer DS-SRMs. However, other harmonic currents, e.g., 5th and 7th, can be utilized to improve the torque performance. These conditions will be investigated further in the following section.

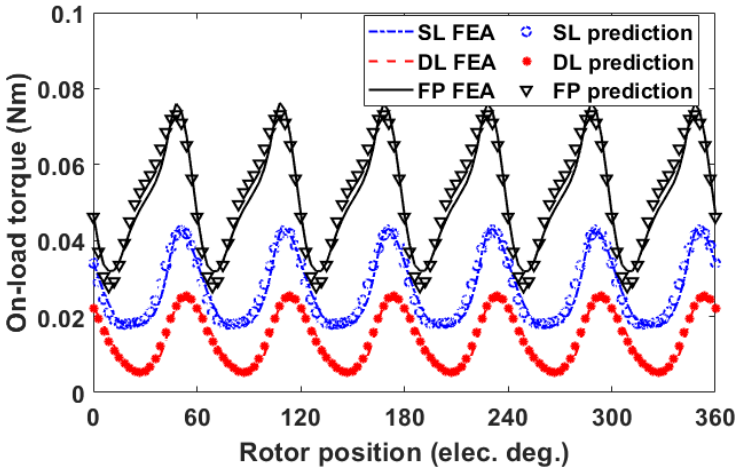

(a) I_1

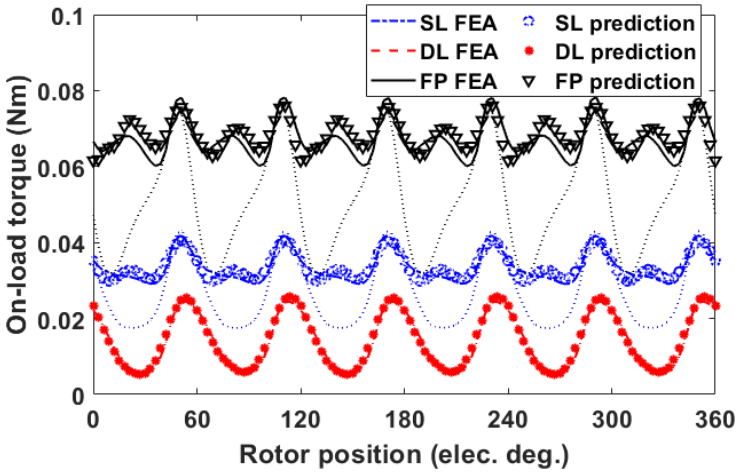

(b) I_1+I_{3rd}

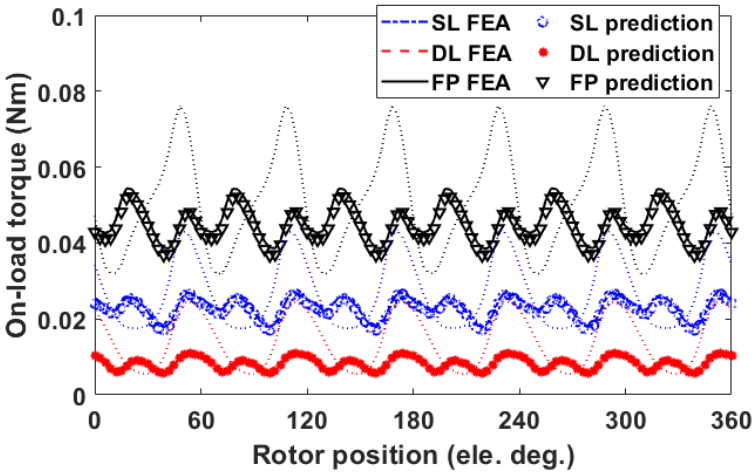

(c) I_1+I_{5th}

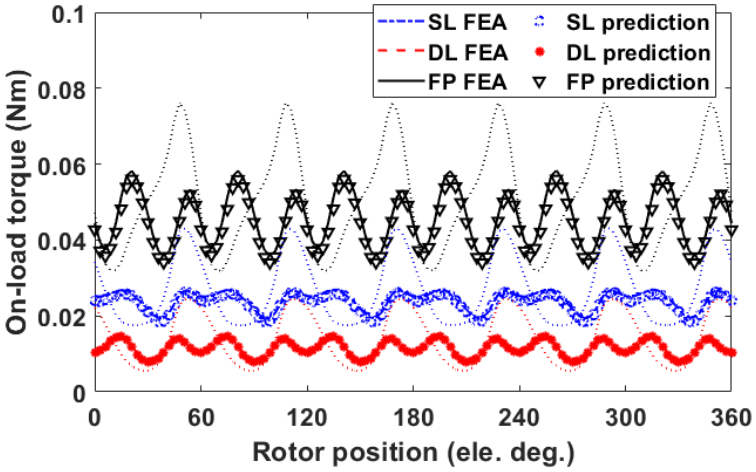

(d) I_1+I_{7th}

Fig. 3.3 Comparison of FEA and analytically predicted torque waveforms for the three SRMs when 1A RMS current is supplied.

3.2 Comparison of Torque Contribution with the 3rd Current Harmonic Injection

Based on the initial results in Fig. 3.3, it is surprising to see that although 3rd order current harmonic injection can improve the torque ripple and average torque for both single layer DS-SRMs and FPSRMs, but it has no influence on double layer DS-SRMs. In order to understand the reason behind, comparative studies for three SRMs with the 3rd order current harmonic injection have been carried out in this section.

3.2.1 Torque Contribution for Single/Double Layer DS-SRMS

Using the analytical torque models derived in Chapter 2, the torque produced by both the fundamental and harmonic currents can be reliably predicted without considering heavy magnetic saturation. According to T_{h0} in (2.14), the average torque, due to current harmonics, is a function of current harmonic phase angle β_v and can be simplified by (3.1) based on the trigonometric function transformation.

$$T_{h0}(\beta_v) = T_{H0}\sin(\beta_v + \varphi_{H0}) \tag{3.1}$$

where T_{H0} and φ_{H0} are the resultant torque magnitude and phase angle, respectively. φ_{res} is a constant and can be calculated using the inductance magnitude and also phase angle. It is 1.3° and 6.1° for the single/double layer DS-SRMs, respectively. It is obvious that the maximum average torque occurs when $\sin(\beta_v + \varphi_{res}) = 1$. Hence, the predicted β_v where the maximum

torques can be achieved for the single/double layer DS-SRM can be easily calculated as 88.7° and 83.9°, respectively, as shown in Fig. 3.4 (a).

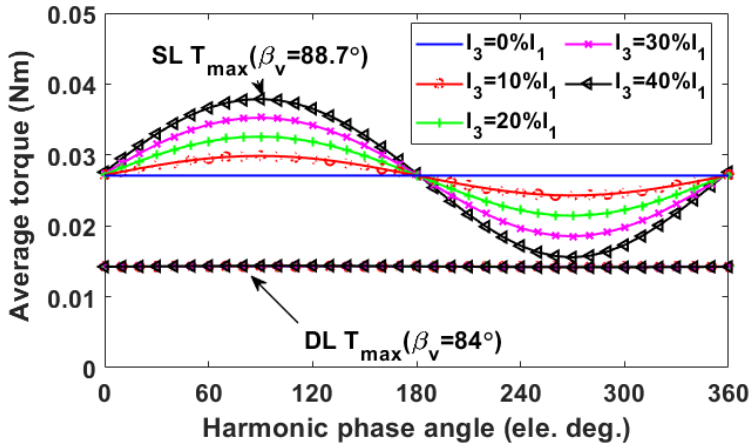

(a) Average torque

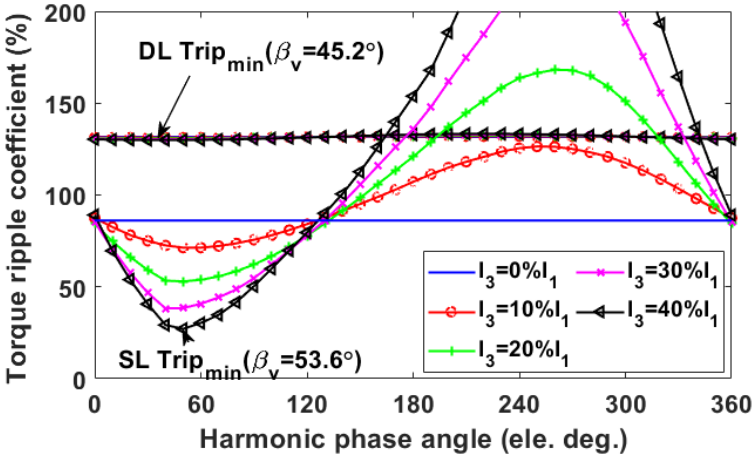

(b) Torque ripple coefficient

Fig. 3.4 FEA results of torque production for single/double layer DS-SRM with the 3rd order current harmonic injection. The machines are supplied with 1A RMS current.

As aforementioned in section 2.4, the 6th order torque ripple is the most dominant one, which is due to the fundamental and harmonic currents and can be simplified by (3.2) and (3.3).

$$T_{frip} = T_{Frip}\sin\left(6\theta_e + \varphi_{Frip}\right) \tag{3.2}$$

$$T_{hrip}(\beta_v, I_v) = T_{Hrip}(I_v)\sin\left(6\theta_e + \varphi_{Hrip} + \beta_v\right) \tag{3.3}$$

Therefore, the minimum torque ripple occurs when (3.2) and (3.3) have the same magnitude but π phase difference between them. This leads to (3.4)-(3.5).

$$T_{Frip} = T_{Hrip}(I_v) \tag{3.4}$$

$$\varphi_{Hrip} + \beta_v - \varphi_{Frip} = (2d+1)\pi \tag{3.5}$$

where d is an integer. Based on (2.5), (2.9) and (2.10), φ_{Frip} and φ_{Hrip} can be calculated as $143.5°$ and $-90.1°$, respectively, for the single layer DS-SRM. Therefore, the phase angle to achieve the minimum torque ripple can be obtained as $\beta_v = 53.6°$. It is the same for the double layer DS-SRM, β_v of which is $45.2°$. Fig. 3.4 (b) shows how the 3rd order current harmonic affects the torque ripple coefficients for both the single/double layer DS-SRM. It can be seen that for the single layer DS-SRM, the 3rd order current harmonic can reduce the torque ripple coefficient by 56% while increasing the average torque by 10%. However, whatever the 3rd order current harmonic is injected, it has little effect on both the average torque and the torque ripple coefficient of the double layer DS-SRM.

In order to study the reason why this is happening, the harmonic torques due to the self- and mutual-inductances are investigated separately by using (2.9)-(2.11). The active inductance harmonics (e.g. 2nd and 4th) for the 3rd order current harmonic injection listed in TABLE 2.4 are taken into account. By way of example, T_{hrip_2nd} produced by the 2nd order inductance harmonic with the 3rd order current harmonic injected [n=2, v=3 in (2.11)] can be simplified as (3.6).

$$\begin{aligned} T_{hrip\_2nd} = \frac{3p}{2} I_1 I_3 \Big[& L_2 \sin(6\theta_e + \beta_1 + \beta_3 + \alpha_2) \\ & + M_2 \sin\Big(6\theta_e + \beta_1 + \beta_3 + \alpha'_2 - \frac{\pi}{3}\Big)\Big] \end{aligned} \tag{3.6}$$

From the observation of the inductances, it is found that α_2 leads α'_2 by around $2\pi/3$ for both the single/double layer DS-SRM, which means $\alpha_2 - \alpha'_2 \approx 2\pi/3$ is always valid. As a result, the harmonic torque components in T_{hrip_2nd} due to the self- and mutual-inductances will produce a π phase difference for any 3rd order current harmonic injections as shown in (3.7).

$$\begin{aligned} T_{hrip\_2nd} &\approx \frac{3p}{2} I_1 I_3 [L_2 \sin(6\theta_e + \beta_1 + \beta_3 + \alpha_2) \\ &\quad + M_2 \sin(6\theta_e + \beta_1 + \beta_3 + \alpha_2 - \pi)] \\ &\approx \frac{3p}{2} I_1 I_3 (L_2 - M_2) \sin(6\theta_e + \beta_1 + \beta_3 + \alpha_2) \end{aligned} \tag{3.7}$$

Together with the similar magnitudes of L_2 and M_2 for the double layer DS-SRM, T_{h0_2nd} will be cancelled to a negligible level. The elimination happens on both average torque and torque ripple, which can be clearly shown in Fig. 3.5 (b). For comparison, Fig. 3.5 (a) shows the harmonic torque composition for the single layer DS-SRM. Even though its self- and

mutual-torques still have opposite signs, the larger difference between L_2 and M_2 leads to the considerable contribution in both the average torque and the torque ripple. This explains why the 3rd order current harmonic injection has little effect on the double layer DS-SRM but can improve the torque performance for the single layer DS-SRM.

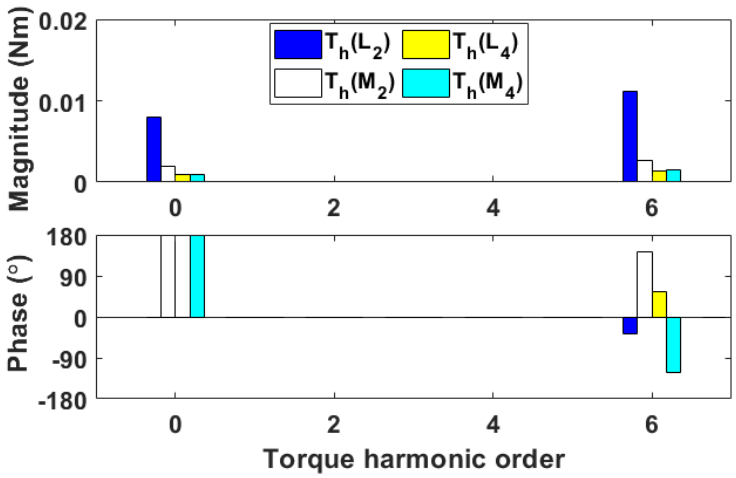

(a) Single layer DS-SRM

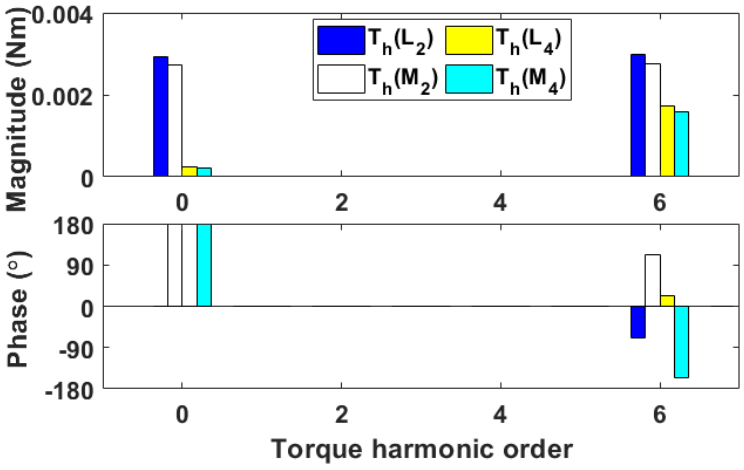

(b) Double layer DS-SRM

Fig. 3.5 Spectra of the harmonic torque produced by the active inductances with 30% 3rd current harmonic injection. The machines are supplied with 1A RMS current.

As well-established in [24] [26] and [28], the torque generation of the FPSRM depends entirely on the mutual inductance variation. This is the same case for the harmonic torque generation. The 2nd order self-inductance harmonic of the FPSRM is too small to produce any meaningful average torque, which can be predicted by (2.9)-(2.11), also shown in Fig. 3.6. However, due to a significant 2nd order mutual-inductance harmonic, there is a good potential

for the FPSRM to improve its torque performance (increased average torque and reduced torque ripple) by injecting the 3rd order current harmonic.

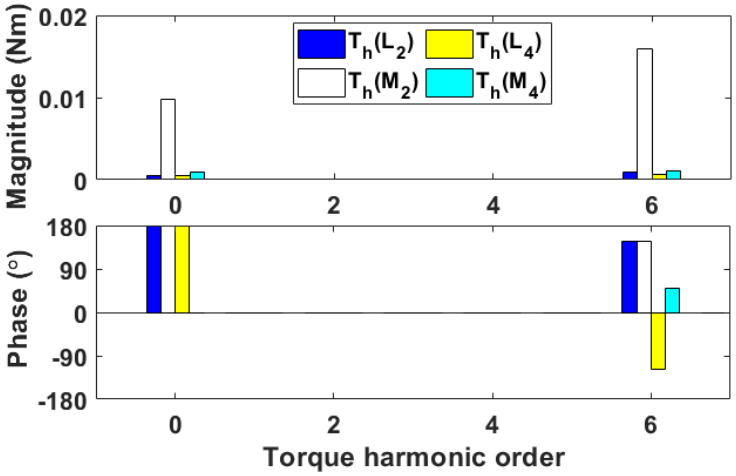

Fig. 3.6 Spectra of the harmonic torque produced by the active inductance harmonics with 30% 3rd order current harmonic injection for the FPSRM. The machines are supplied with 1A RMS current.

By using the same analytical torque model, the average torque and torque ripple coefficient against current harmonic phase angle for the FPSRM can be obtained, as shown in Fig. 3.7. The optimization of average torque and torque ripple can be carried out by applying the same equations (3.1)-(3.5) and the optimal 3rd order current harmonic phase angles are selected as 268.7° and 270.6°, respectively.

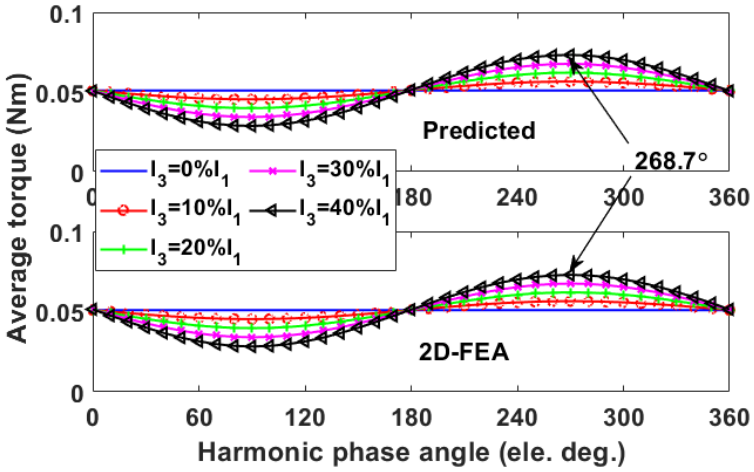

(a) Average torque

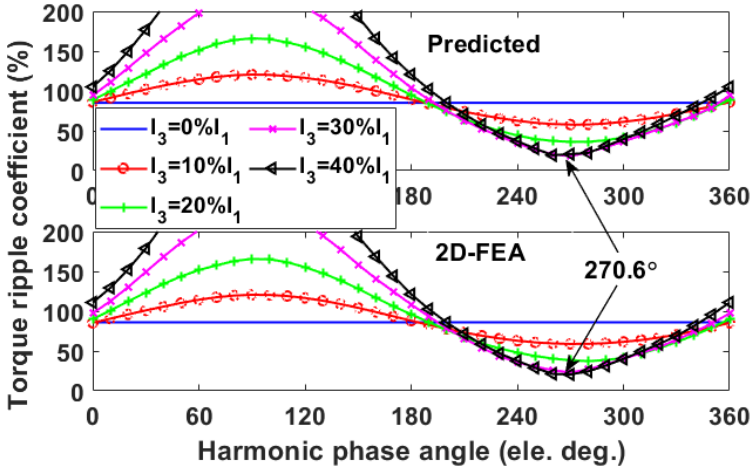

(b) Torque ripple coefficient

Fig. 3.7 Comparison between the 2D-FEA results and the analytical predictions for the FPSRM with the 3rd order current harmonic injection when three phases are supplied with 1A RMS currents.

3.2.2 Torque Performance with Saturation Considered

The machine inductances can vary nonlinearly with respect to phase RMS currents due to magnetic saturation. Therefore, this section investigates the influence of magnetic saturation on the effectiveness of the 3rd order current harmonic injection for different electric loadings. The comparison in terms of average torque and torque ripple coefficient against phase RMS current have been calculated by FEA, as shown in Fig. 3.8.

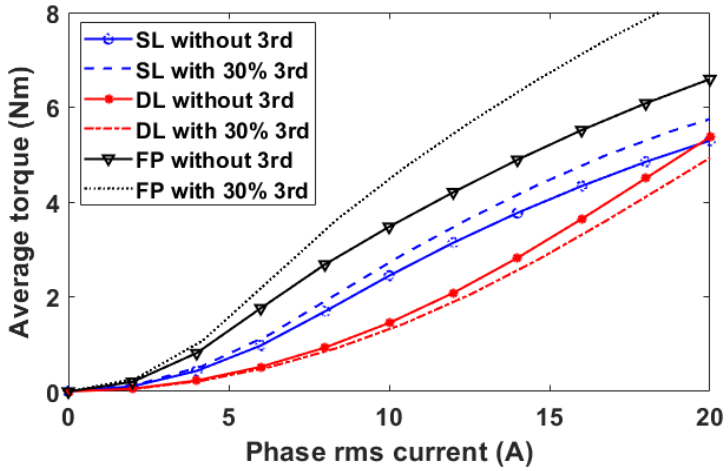

(a) Average torque

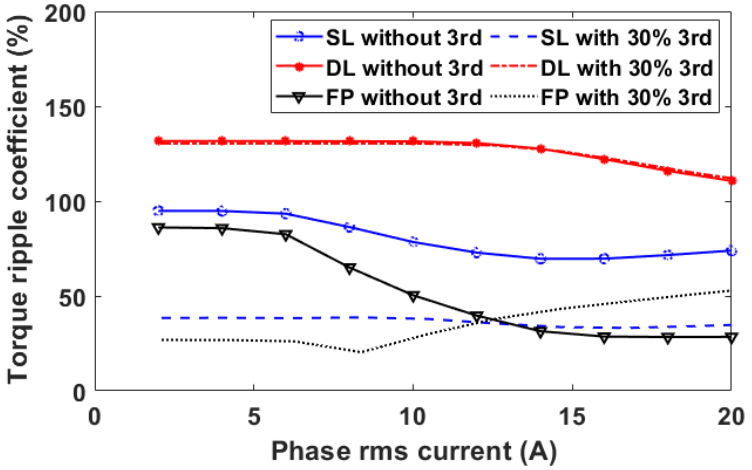

(b) Torque ripple coefficient

Fig. 3.8 Comparison of on-load torque *vs* phase RMS current with/without the 3rd order current harmonic injection. Current harmonic is selected to achieve minimum torque ripple, which is listed in TABLE 3.2.

As can be found, for both the single layer DS-SRM (dominant self-torque) and the FPSRM (pure mutual-torque), the 3rd order current harmonic could minimize the torque ripple and increase the average torque at lower current level. With increasing phase current, the 3rd order current harmonic can still increase the average torque for the FPSRM by about 25% but it loses the benefit in torque ripple reduction. One of the important reasons is that the machine inductances cannot be calculated accurately under magnetic saturation condition without using frozen permeability [135], [136]. This means that the current harmonics can no longer be properly selected by the proposed analytical torque model. Moreover, the 3rd order current harmonic injection has little effect on the double layer DS-SRM (self- and mutual torques) as investigated previously. The slight reduction in the average torque is due to the fact that for the

same RMS current, the additional injected 3rd order harmonic current leads to a reduced fundamental current.

3.3 5TH AND 7TH ORDER HARMONIC CURRENT INJECTIONS

The proposed analytical torque model could also be implemented to other orders of current harmonic injections, such as the 5th and 7th order current harmonics. It is worth mentioning that the even order current harmonics always present undesirable torque performance (reduced average torque and increased torque ripple), hence will not be detailed in this section.

In order to investigate the torque contribution for the 5th and 7th order current harmonics, the analytical method for the 3rd order current harmonic has been implemented for the three investigated machines as well. By way of example, for the double layer DS-SRM, when the 5th order current harmonic (v=5) is injected, according to (2.9)-(2.11) and TABLE 2.4, the dominant 6th order torque ripple ($|D|$=1-v-n=6), produced by the 2nd order inductance harmonic (n=2), can be expressed as (3.8).

$$T_{hrip\_2nd} = \frac{3p}{2} I_1 I_5 \left[L_2 \sin(-6\theta_e + \beta_1 - \beta_5 - \alpha_2) + 2M_2 \sin\left(-6\theta_e + \beta_1 - \beta_5 - \alpha'_2 - \frac{2\pi}{3}\right)\right] \tag{3.8}$$

As aforementioned, $\alpha_2 - \alpha'_2 \approx 2\pi/3$ for the double layer DS-SRM is again valid. Substituting it into (3.8) leads to

$$\begin{aligned} T_{hrip\_2nd} &\approx \frac{3p}{2} I_1 I_5 [L_2 \sin(-6\theta_e + \beta_1 - \beta_5 - \alpha_2) + 2M_2 \sin(-6\theta_e + \beta_1 - \beta_5 - \alpha_2)] \\ &\approx \frac{3p}{2} I_1 I_5 (L_2 + 2M_2) \sin(-6\theta_e + \beta_1 - \beta_5 - \alpha_2) \end{aligned} \tag{3.9}$$

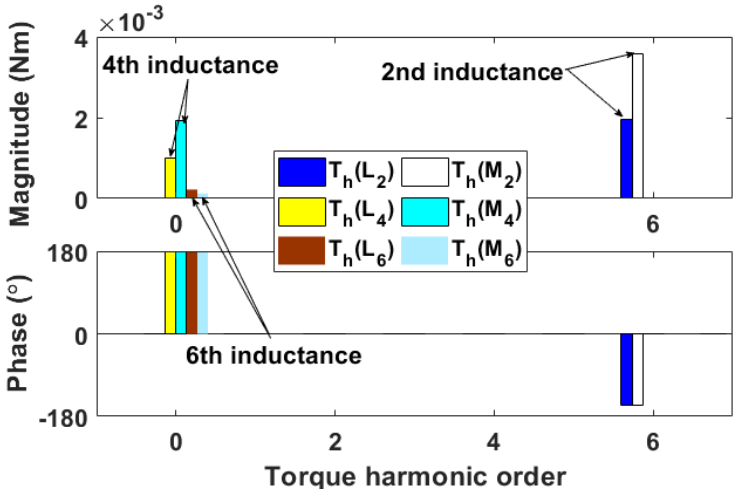

Fig. 3.9 Spectra of the harmonic torques produced by active inductance harmonics with 30% 5th order current harmonic injection. The double layer DS-SRM are supplied with 1A RMS current.

It is obvious that the self- and mutual-torque ripples due to the 5th order current harmonic will always have the same phase angle. This is different from that of the 3rd order current injection, and they will add together to compensate the torque ripple produced by the fundamental current, leading to an overall reduced torque ripple. As shown in Fig. 3.9 and Fig. 3.10, it will happen for both 5th and 7th order current harmonic injection. As a result, the 5th and 7th order current harmonics can achieve much more significant torque ripple reduction than that of the 3rd order current harmonic for the double layer DS-SRM.

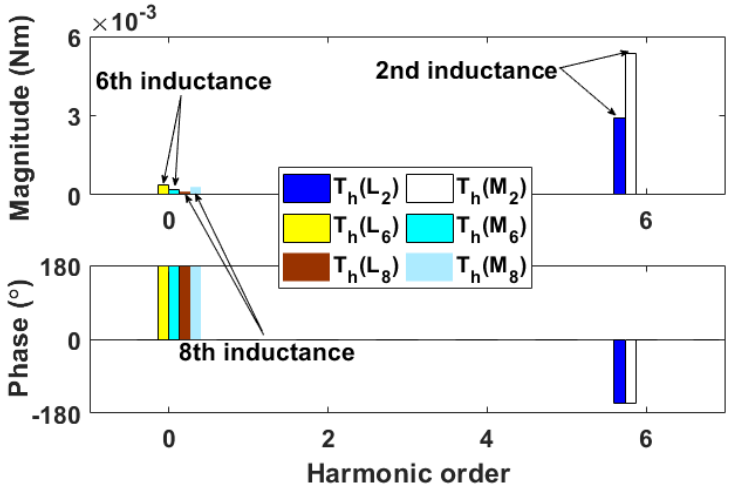

Fig. 3.10 Spectra of the harmonic torques produced by active inductance harmonics with 30% 7th order current harmonic injection. The double layer DS-SRM are supplied with 1A RMS current.

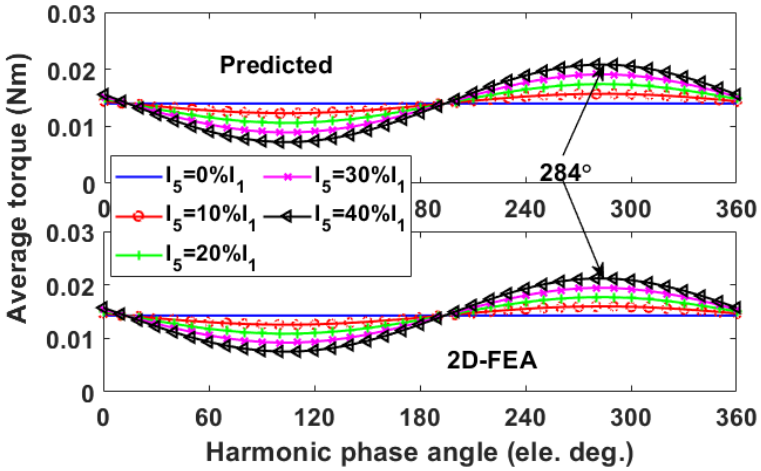

(a) Average torque

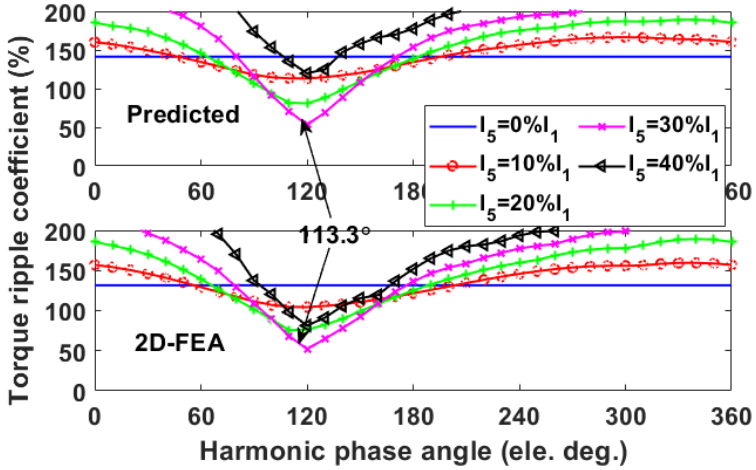

(b) Torque ripple coefficient

Fig. 3.11 Comparison between the FEA results and the analytical prediction for the double layer DS-SRM with the 5th order current harmonic injection when three phases are supplied with 1A RMS current.

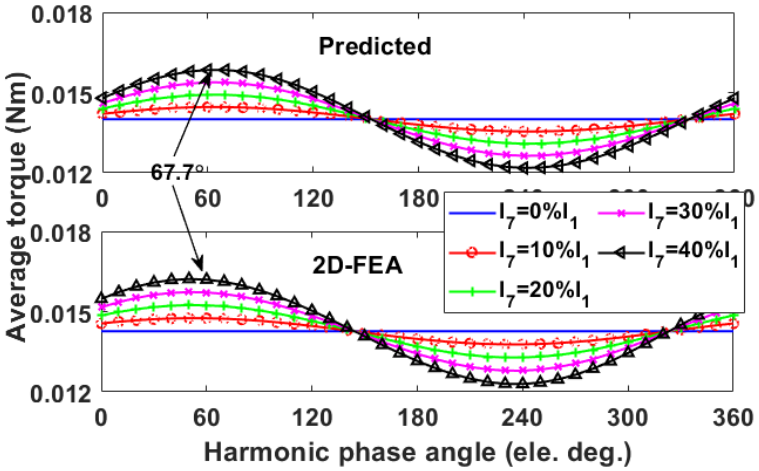

(a) Average torque

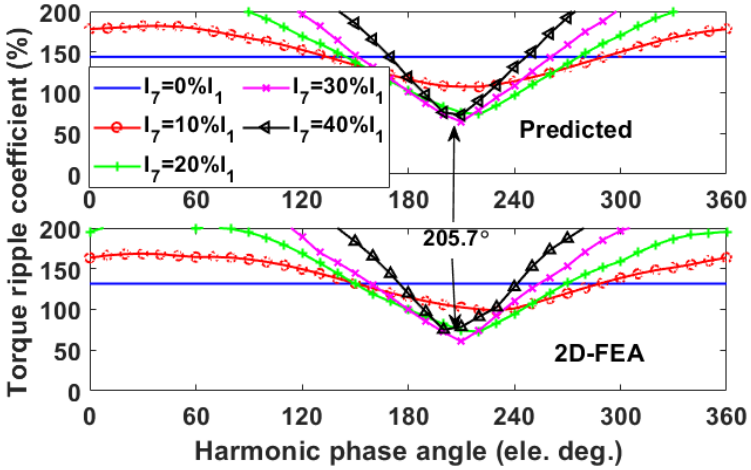

(b) Torque ripple coefficient

Fig. 3.12 Comparison between the FEA results and the analytical prediction for the double layer DS-SRM with the 7th order current harmonic injection when three phases are supplied with 1A RMS current.

Moreover, the torque production improvement with respect to the 5th and 7th order current harmonic phase angles for the double layer DS-SRM is shown in Fig. 3.11 and Fig. 3.12, respectively. It is apparent that the torque behavior with the 5th and 7th order current harmonic injection can also be reliably predicted. The phase angles for achieving the maximum average torque and minimum torque ripple have been calculated, being 284° and 113.3° for the 5th order current harmonic; 67.7° and 205.7° for the 7th order current harmonic, respectively. However, different from the 3rd order current harmonic injection used for the single layer DS-SRM and the FPSRM, the torque ripple and the average torque cannot be improved at the same time.

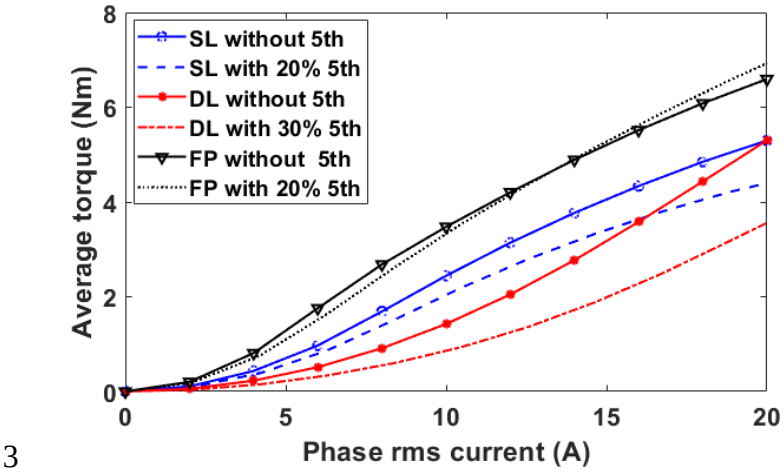

3

(a) Average torque

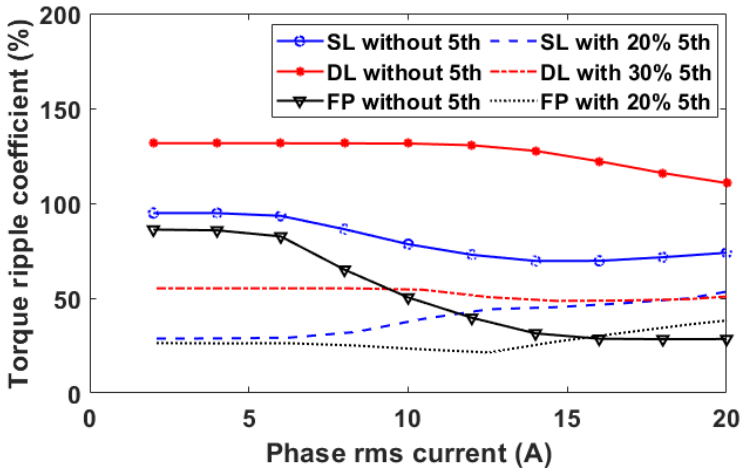

(b) Torque ripple coefficent

Fig. 3.13 Comparison of on-load torque *vs* phase rms current with/without the 5th order current harmonic injection. Current harmonic is selected to achieve minimum torque ripple, which is listed in TABLE 3.2.

By injecting the predicted current harmonic in TABLE 3.2, the FE results with the desired magnitude and also phase angle for achieving minimized torque ripple by the 5th order current harmonic injection are shown in Fig. 3.13. As can be seen, the FPSRM shows the best performance with the 5th order current harmonic injection, which reduces the torque ripple by around 69% without heavy magnetic saturation. Its average torque is only marginally influenced. There are also 70% and 58% reductions in the torque ripples for the single/double layer DS-SRM, respectively. However, the average torques for these two DS-SRMs are also reduced by about 15% and 35%, respectively.

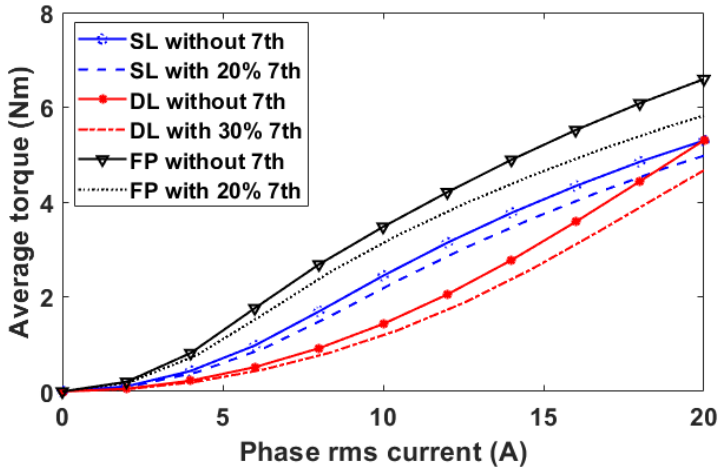

(a) Average torque

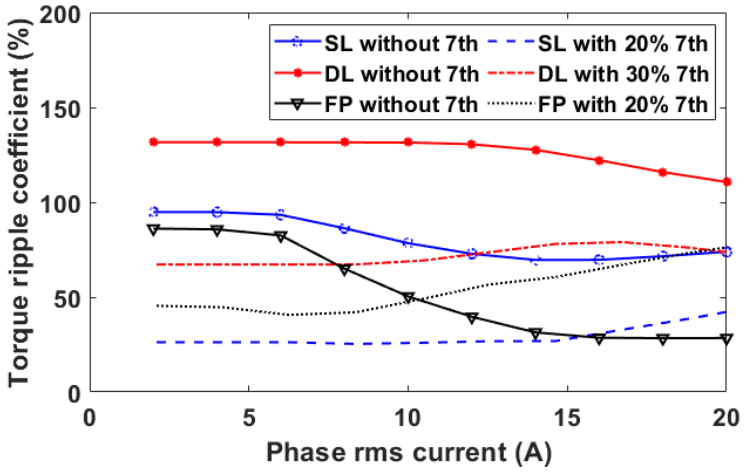

(b) Torque ripple coefficent

Fig. 3.14 Comparison of on-load torque *vs* phase rms current with/without the 7th order current harmonic injection. Current harmonic is selected to achieve a minimum torque ripple, which is listed in TABLE 3.2.

Similarly, the results for the 7th order current harmonic injections are shown in Fig. 3.14. It shows that there is around 10% reduction in average torque for all three types of machines. However, the torque ripple coefficient of the single layer DS-SRM has been significantly reduced by around 72%, and the reduction is not really compromised with the increasing phase current. For the double layer DS-SRM, the torque ripple coefficient can also be reduced by around 50%. Moreover, although there are 50% reduction in torque ripple coefficient for the FPSRM at low current, the benefits are compromised with increasing phase current due to magnetic saturation. The reason lies in the inaccurate calculation of machine inductances at high phase current.

3.4 CONCLUSION

This chapter comparatively studied the torque performance improvement for three types of doubly salient synchronous reluctance machines with different windings by current harmonic injections. The proposed methods could clearly quantify the torque contribution for each inductance harmonic. Based on the analytical model, the torque behaviours after injecting current harmonics can be predicted and verified by FEA and experiments.

It has been found that the 3rd order current harmonic injection for the single layer DS-SRM and the FPSRM exhibits the best performance, which can increase the average torque by 10% and 22%, respectively, while reducing the torque ripple coefficient by more than 55%. However, it has little effect on the double layer DS-SRM. This is mainly because the harmonic torques due to the self- and mutual-inductances have cancelled each other, leading to a negligible resultant harmonic torque.

The 5th and 7th order current harmonic injections are also implemented. The results showed that they can reduce the torque ripple coefficient of the double layer DS-SRM by 56% and 50%, respectively. For the single layer DS-SRM, the 7th order current harmonic injection presents better performance, which reduces the average torque by 10% but achieves 72% reduction in torque ripple coefficient. It is worth noting that all the current harmonic injection methods proposed in this section can reduce the torque ripple for the FPSRM under light load conditions. However, due to magnetic saturation, the effect in torque ripple coefficient reduction might be compromised but average torque could still be increased. Again, the analytical and numerical results will be validated by experiments in Chapter 6.

Chapter 4 TORQUE PRODUCTION MECHANISM FOR MULTI-PHASE DS-SRMS

This chapter investigates the contribution of each order inductance harmonic to the torque (both average torque and torque ripple) of multiphase doubly salient synchronous reluctance machines (DS-SRMs). First, a general analytical torque model based on Fourier Series analysis of inductances has been built for machines with different phase numbers, slot/pole number combinations and also winding configurations. The instantaneous torque for DS-SRMs with any given phase number can then be accurately predicted. Using such model, contribution of each order inductance harmonic to torque can be investigated separately. It is found that the torque ripple frequency of the DS-SRM only depends on phase number. For example, for a multi-phase machine, there will be $m \times k^{th}$ order torque ripple if $mod(mk, 2) = 0$, where m is phase number and k is a natural number. This study also explains why certain phase numbers inherently produce lower torque ripple than others. Moreover, this chapter attempts to further reduce the torque ripple of DS-SRMs by combining the multi-phase winding and current harmonic injection methods. For this purpose, analytical torque model have been extended for multi-phase DS-SRMs with current harmonic injection. It has been found that with current harmonic injection, the torque ripple of both the 5-phase and 6-phase DS-SRMs can be significantly reduced and the average torque can be improved, while it always has negative impact for the 4-phase machine.

This chapter comes from the author's own paper [139].

4.1 INTRODUCTION

Previous chapters investigate the current harmonic injection method for 3-phase doubly salient synchronous reluctance machines (DS-SRMs). It can quantify the torque contribution due to each inductance harmonic with and without current harmonic injection. As a result, it allows an appropriate selection of current harmonics (order, magnitude, phase angle) to improve the torque performance of the 3-phase DS-SRMs. Since the current shaping or harmonic current injection will introduce higher order harmonic currents, it could potentially increase losses in the machines, and hence lead to reduced efficiency.

Therefore, another one of the effective and simple ways to reduce the torque ripple is to increase the phase number. This method can be applicable not only to SRMs but also to synchronous (reluctance) machines and induction machines. Multiphase machines provide additional benefits apart from the torque ripple reduction because the machines with higher phase numbers (m>3) can also have higher torque density and better fault-tolerant capability compared with 3-phase machines [140],[141]. Additionally, different winding configurations for multi-phase machines can be selected to achieve even better torque performance [17],[142].

To reduce the modeling complexity, simple analytical torque model based on self- and mutual-inductances has been proposed for the investigated multi-phase DS-SRMs. Although the inductances can be calculated according to winding function theories [145],[146], for simplicity they are calculated by 2D-FEA in this chapter. The proposed model can be applied for all kinds of DS-SRMs with different slot/pole combinations and wining configurations, e.g. double-layer (DL), single-layer (SL) and fully-pitched (FP). Through harmonic analysis, the torque ripple frequency and magnitude for DS-SRMs with different phase numbers can be reliably predicted. In addition, the torque contribution due to each inductance harmonic can also be accurately quantified. As a result, the mechanism about why certain phase numbers can have inherently lower torque ripple while others cannot, can be investigated. This will be helpful for researchers to find optimal measures in order to reduce torque ripple of DS-SRMs either from machine design or machine control perspectives.

Moreover, some research has been done to combine the multi-phase machines with harmonic current injection to further reduce the torque ripple [147],[148]. However, these methods are for permanent magnet machines and no such research has been carried out for multi-phase DS-SRMs. The latter have significant different characteristics compared to permanent magnet machines due to their doubly salient structure, and also the fact that their torque is generated

by the variations of self- and mutual-inductances rather than the PM generated back-EMF. The researches in this chapter will reveal that the multi-phase DS-SRM also have different characteristics, e.g. more different types of mutual-inductances, compared to their 3-phase counterparts with sinewave current supply [139]. So if harmonic current is injected, it is highly likely that the multi-phase DS-SRMs will behave differently compared to the 3-phase counterpart. To investigate the impact of current harmonic injection on multi-phase DS-SRMs, in this chapter, a general analytical torque model has been developed based on Fourier Series analysis as well. The characteristics of injected current harmonic, such as order, magnitude and phase angle, where maximum average torque or minimum torque ripple will occur, can be predicted. A range of phase numbers (up to 6-phase) with different slot/pole number combinations and winding configurations, e.g. double-layer (DL) and single-layer (SL), will be considered. Therefore, the main contribution of this chapter is to establish some general guidelines for performance improvement of multi-phase DS-SRMs using current harmonic injection.

4.2 Analytical Torque Model without Current Harmonic Injection of Multi-Phase DS-SRMs

This section covers the DS-SRMs with various slot/pole number combinations and different phase numbers, e.g., 4s/4p 2-phase, 6s/4p 3-phase, 8s/6p 4-phase, 10s/8p 5-phase, 12s/8p 6-phase and 12s/10p 6-phase. Fig. 4.1 shows the cross sections and winding configurations for above multi-phase double layer DS-SRMs. The main specifications for all the topologies are listed in TABLE 4.1. It is worth noting that single layer winding machines have the same key dimensions and also the same number of turns per phase as their double layer counterparts. However, the number of turns per coil of the single layer machines will be doubled with the number of coils per phase being halved. In order to achieve optimal performance for the multi-phase DS-SRMs, the winding configurations have been designed according to classic winding theory for synchronous machines (fractional slot and also integer slot) [149],[150]. The stars of slots for double layer multi-phase DS-SRMs have been shown in Fig. 4.2

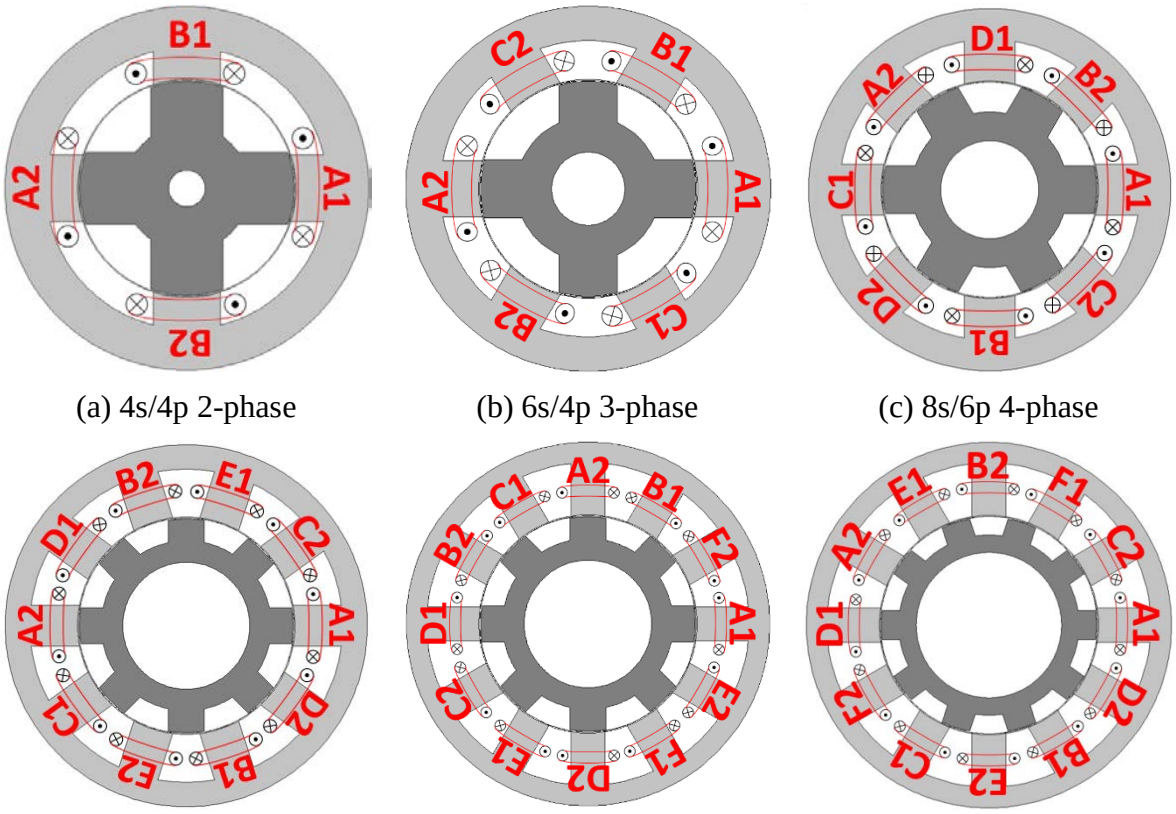

(a) 4s/4p 2-phase (b) 6s/4p 3-phase (c) 8s/6p 4-phase

(d) 10s/8p 5-phase (e) 12s/8p 6-phase (f) 12s/10p 6-phase

Fig. 4.1 Common double layer multi-phase DS-SRMs topologies.

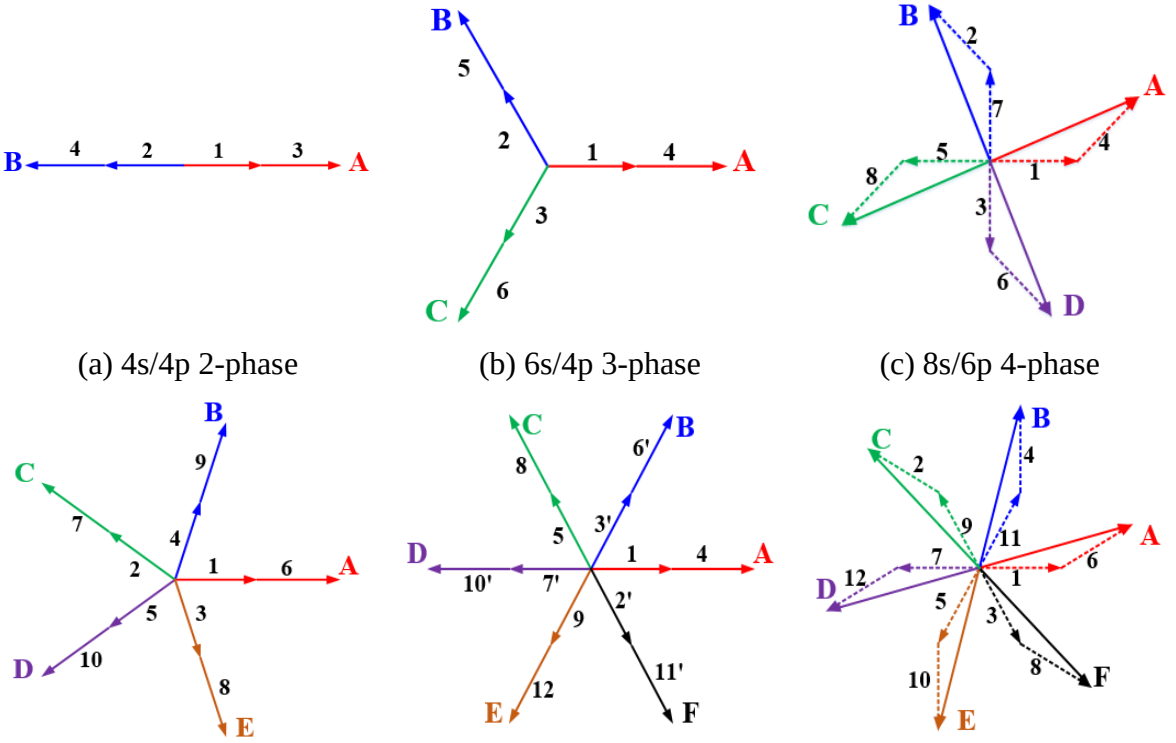

(a) 4s/4p 2-phase (b) 6s/4p 3-phase (c) 8s/6p 4-phase

(d) 10s/8p 5-phase (e) 12s/8p 6-phase (f) 12s/10p 6-phase

Fig. 4.2 Stars of slots double layer multi-phase DS-SRMs.

TABLE 4.1 MACHINE KEY DIMENSIONS AND DESIGN FEATURES

Stator outer radius (mm)	45
Split ratio	0.6
Air gap length (mm)	0.5
Active length (mm)	60
Number of turns per phase	132
Slot fill factor	0.37
Rated RMS current (A)	5

According to literature, the instantaneous torque equation of SRMs can be obtained based on the phase inductances (self and mutual) and phase currents [10],[96]. Assuming the magnetic saturation can be neglected, the on-load torque of a multi-phase SRM is given by

$$T_e = \frac{1}{2}[i_m]^T \frac{d[L_m]}{d\theta}[i_m] \tag{4.1}$$

where m represents the phase number, $[i_m] = [i_1, i_2, \cdots i_m]^T$. $[L_m]$ is a $m \times m$ inductance matrix. This equation can also be applicable for DS-SRMs and will be used to investigate the torque performance in this chapter. Assuming no harmonic current is injected, the general current equation for phase x can be written as

$$i_x = I_p \sin\left(\theta_e + \beta_1 - \frac{2\pi}{m}(x-1)\right) \text{ with } x = 1, 2, \cdots m \tag{4.2}$$

where I_p is the amplitude of phase current, θ_e is the electric rotor position, β_1 is the current phase angle.

It is worth noting that for a multi-phase DS-SRMs, the phase self-inductances have the same magnitude but have a $\frac{2\pi}{m}$ phase shift between them. However, the number of mutual-inductances between phases is a function of phase number m, which can be calculated by $m \times (m-1)$. By way of example, Fig. 4.3 (a) and (b) show the relative phase order in space for 5- and 6-phase machines, respectively. The mutual-inductances between two phases with the same distance in space will have the same waveform but with a $\frac{2\pi}{m}$ phase shift between them. The distance 1 means two phases are adjacent to each other, such as M_{ab}, M_{bc}, …; the distance 2 means two phases are not adjacent and have an interval of one phase between them, such as M_{ac}, M_{bd}, …Similarly, the distance 3 has an interval of two phases as shown in Fig. 4.3 (b), such as M_{ad}, M_{be}, … To be more generic, 'Z' can be employed to express the number of

different distances between phases for an multi-phase DS-SRMs. It is the minimum integer not less than $\frac{C_m^2}{m}$, as shown in (4.3)

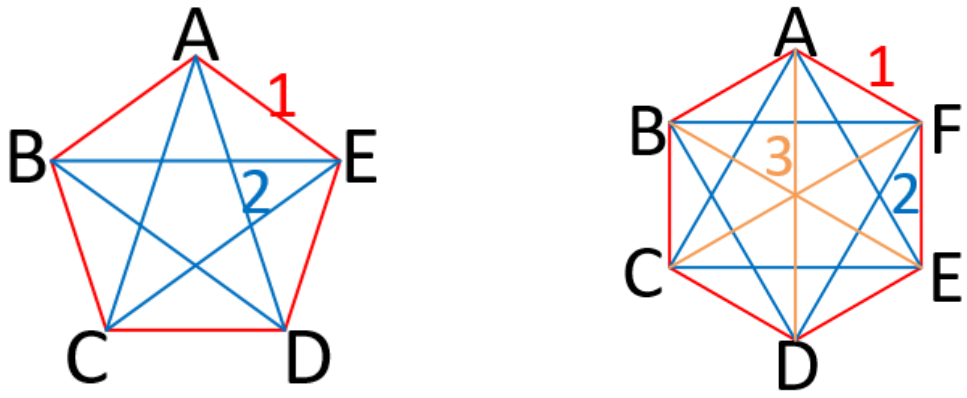

(a) 5-phase (b) 6-phase

Fig. 4.3. Relative phase order in space for DS-SRMs.

$$Z \geq \frac{C_m^2}{m} = \frac{m!}{2!\,(m-2)! \times m} = \frac{m-1}{2} \tag{4.3}$$

By way of example, for the 12s/8p double layer 6-phase DS-SRM, there are 3 types of mutual-inductances due to $\frac{C_6^2}{6} = 2.5$. The inductance waveforms and their spectra are shown in Fig. 4.4.

In order to identify the contribution of inductance harmonics to the average torque and torque ripple, the self- and mutual-inductances are expressed using Fourier Series analysis as shown in (4.4) and (4.5):

$$L = L_0 + \sum_{n=1}^{\infty} L_n \cos(n\theta_e + \alpha_n) \tag{4.4}$$

$$M_a = M_{a0} + \sum_{n=1}^{\infty} M_{an} \cos(n\theta_e + \alpha'_{an}) \tag{4.5}$$

where L and M_a represent the self- and mutual-inductances. α_n and α'_{an} are the phase angles of the n^{th} self- and mutual-inductances, respectively. The subscript '0' represents the dc component of inductances. 'a' represents the distance between two phases and $a \in (1, 2 \cdots Z)$. For example, M_{10} is the dc component of mutual-inductance with the distance 1 in Fig. 4.3.

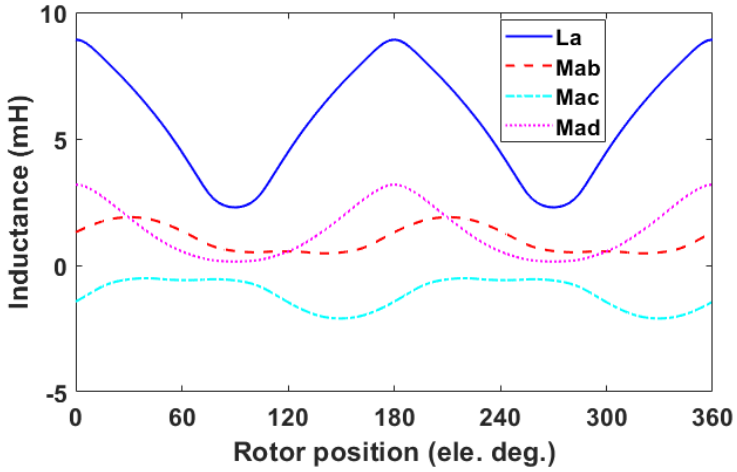

(a) Waveforms

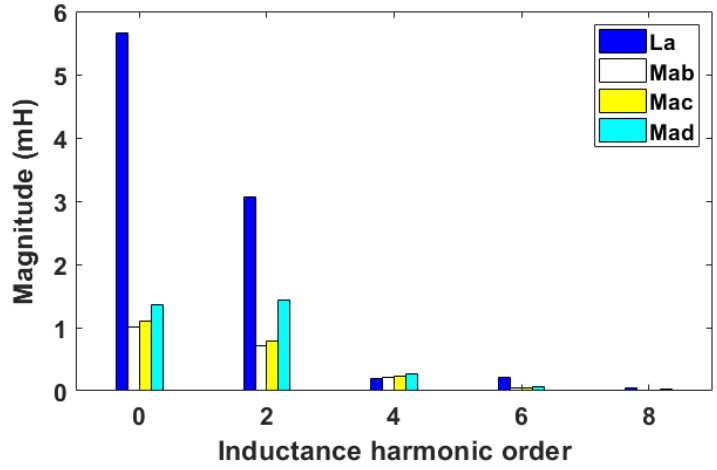

(b) Spectra

Fig. 4.4. Self- and mutual-inductances of a double layer 6-phase DS-SRM. Calculated by FEA when phase A is supplied with a 1A dc current.

Substituting (4.2), (4.4) and (4.5) into (4.1) gives

$$T_f = T_{fsel} + T_{fmut} \tag{4.6}$$

with

$$\begin{aligned} T_{fsel} = \frac{mp}{2}\sum_{k=0}^{\infty}\Big\{ & -\frac{mk}{2}L_{mk}I_p^2\sin(mk\theta_e + \alpha_{mk}) \\ & + \frac{mk-2}{4}I_p^2 L_{mk-2}\sin(mk\theta_e + 2\beta_1 + \alpha_{mk-2}) \\ & + \frac{mk+2}{4}I_p^2 L_{mk+2}\sin(mk\theta_e - 2\beta_1 + \alpha_{mk+2})\Big\} \end{aligned} \tag{4.7}$$

and

$$T_{fmut} = \frac{mp}{2}\sum_{k=0}^{\infty}\sum_{a=1}^{Z} c\left\{-\frac{mk}{2}I_p^2 M_{amk}\sin(mk\theta_e + \alpha'_{amk})\right.$$
$$+\frac{mk-2}{2}I_p^2 M_{a(mk-2)}\sin\left(mk\theta_e + 2\beta_1 + \alpha'_{a(mk-2)} - \frac{2\pi}{m}a\right) \quad (4.8)$$
$$\left.+\frac{mk+2}{2}I_p^2 M_{a(mk+2)}\sin\left(mk\theta_e - 2\beta_1 + \alpha'_{a(mk+2)} + \frac{2\pi}{m}a\right)\right\}$$

with

$$c = \begin{cases} 0.5 & \mathrm{mod}(m,2) = 0 \text{ and } a = Z \\ 1 & \text{otherwise} \end{cases} \quad (4.9)$$

where T_{fsel} and T_{fmut} are the torques produced by the self- and mutual-inductances, respectively. p is the pole-pair number, and k is a natural number. It can be seen that the average torque can be obtained when k is equal to '0'. Moreover, only the interaction between the fundamental current and the 2nd order harmonic inductance can produce the average torque, which can be rewritten as

$$T_{f0} = \frac{mp}{4}I_1^2 L_2\sin(-2\beta_1 + \alpha_2) + \frac{mp}{2}\sum_{a=1}^{Z} cI_1^2 M_{a2}\sin\left(-2\beta_1 + \alpha'_{a2} + \frac{2\pi}{m}a\right) \quad (4.10)$$

According to (4.6)-(4.8), it can be proven that for multi-phase DS-SRMs, in general, there will be mk^{th} order torque harmonics when sinewave current is supplied. This is due to the interaction between the fundamental current and the mk^{th}, $(mk \pm 2)^{th}$ order inductance harmonics. The contributions of each order inductance harmonic to the torque ripple harmonic are listed in TABLE 4.2. It is worth noting that from the above conclusion, the 3-phase machine will in theory produce triplen order torque harmonics. However, due to the fact that the odd order inductances are equal to zero, therefore the odd order torque harmonics, such as 3rd, 9th, 15th etc., do not exist. This is the same for the 5-phase machine, in which the 5th, 15th, 25th… order torque harmonics do not exist. Moreover, it can be predicted that the 2-phase and 4-phase machines present the worst performance in terms of torque ripple when sinewave current is supplied. The reason is that all orders of inductance harmonics will contribute to the torque ripple for both types of machine. Even the 2nd order inductance (with the highest magnitude, and normally contributes to average torque) will produce the 2nd and 4th order torque harmonics for the 2-phase machine while produce the 4th order torque harmonic for the 4-phase machine. This can explain why certain phase numbers generate higher torque ripple while others do not.

TABLE 4.2 ACTIVE INDUCTANCE HARMONICS FOR CERTAIN ORDER TORQUE HARMONICS

k / m		1	2	3
2	Torque	mk=2nd	mk=4th	mk=6th
	Inductance	2nd, 4th	2nd, 4th, 6th	4th, 6th, 8th
3	Torque	mk=3rd	mk=6th	mk=9th
	Inductance	1st, 3rd, 5th	4th, 6th, 8th	7th ,9th, 11th
4	Torque	mk=4th	mk=8th	mk=12th
	Inductance	2nd, 4th, 6th	6th, 8th, 10th	10th, 12th, 14th
5	Torque	mk=5th	mk=10th	mk=15th
	Inductance	3rd, 5th, 7th	8th, 10th, 12th	13th, 15th, 17th
6	Torque	mk=6th	mk=12th	mk=18th
	Inductance	4th, 6th, 8th	10th, 12th, 14th	16th, 18th, 20th

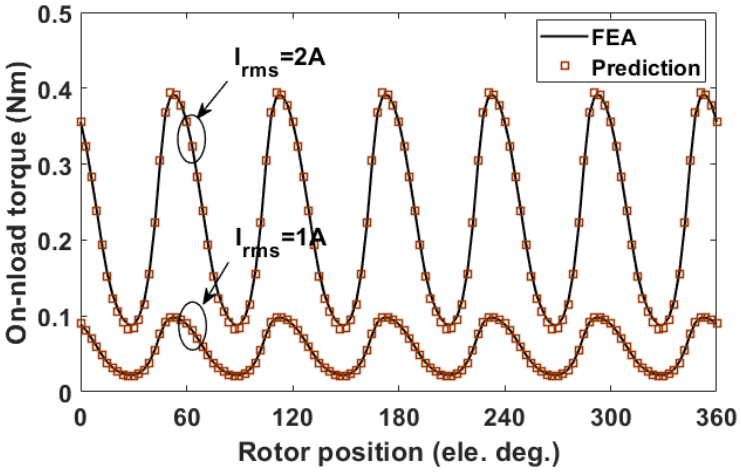

Fig. 4.5. Comparison of on-load torques between 2D-FEA and analytical prediction for a double layer 12s/8p 6-phase DS-SRM at I_{rms}= 1A and 2A.

Fig. 4.5 shows the comparison results between 2D-FEA and analytical prediction for a double layer 12s/8p 6-phase DS-SRM at 1A and 2A phase RMS currents. A generally good agreement can be observed, which validates the accuracy of the proposed analytical torque model. Therefore, only the prediction results of instantaneous torques and spectra are presented for other topologies, as shown in Fig. 4.6 and Fig. 4.7, respectively. As expected, the on-load torque of multi-phase machines will contain the mk^{th} torque order harmonic if $\mathrm{mod}(mk, 2) = 0$ is valid. However, it is worth noting that for the 12s/10p double layer 6-phase machine, the

6^{th} (k=1) order torque ripple can be ignored, which is different from other types of 6-phase machine. This will be investigated further in Section 4.3.

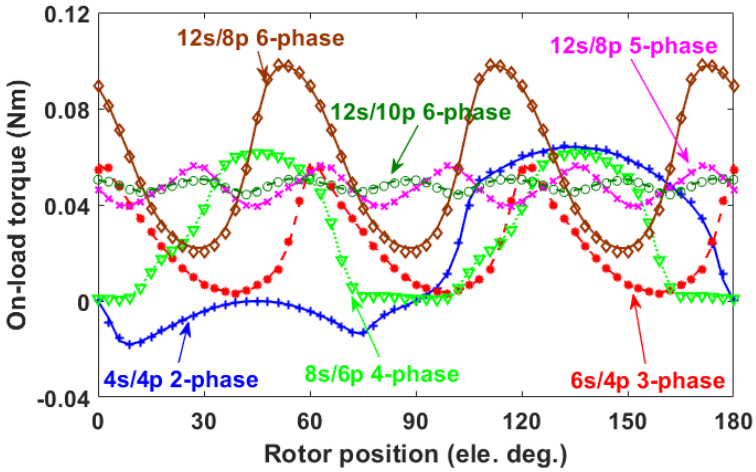

(a) Waveforms (Line: 2D-FEA; Mark: prediction)

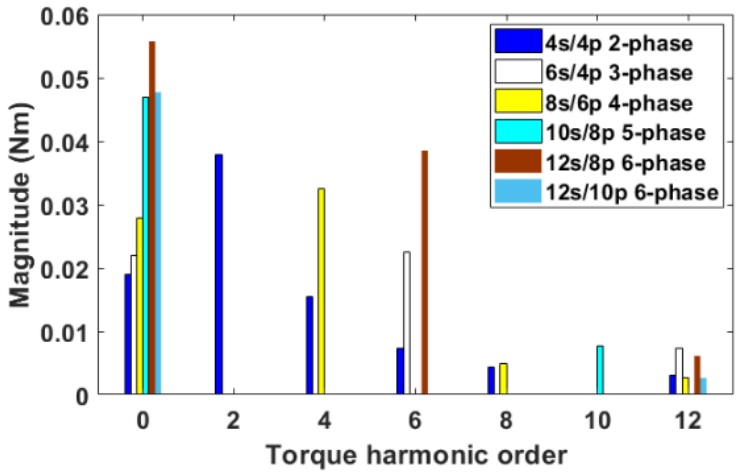

(b) Spectra

Fig. 4.6. Predicted on-load torques for multi-phase double layer DS-SRMs. The machines are supplied with 1A rms current.

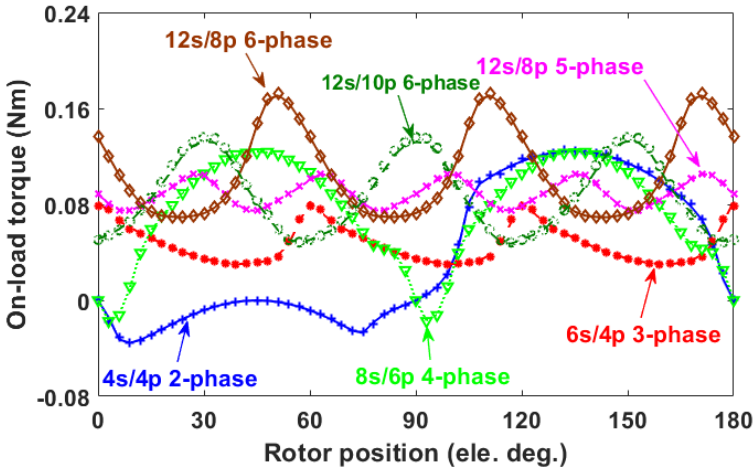

(a) Waveforms (Line: 2D-FEA; Mark: prediction)

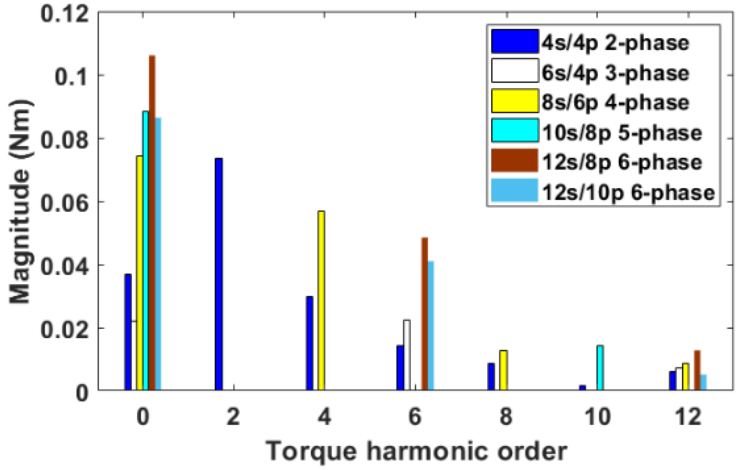

(b) Spectra

Fig. 4.7. Predicted on-load torques for multi-phase single layer DS-SRMs. The machine is supplied with 1A rms current.

4.3 Comparison Study Of Six-Phase Topologies

This section will further investigate the influence of machine topologies and winding configurations on torque ripple of the 6-phase machines. Several 6-phase machines (12s/4p, 12s/8p and 12s/10p) with different winding configurations (concentrated and distributed winding) have been considered.

4.3.1 Short Pitched Concentrated Winding

By way of example, the two single layer 12s/8p and 12s/10p 6-phase DS-SRMs have been shown in Fig. 4.8.

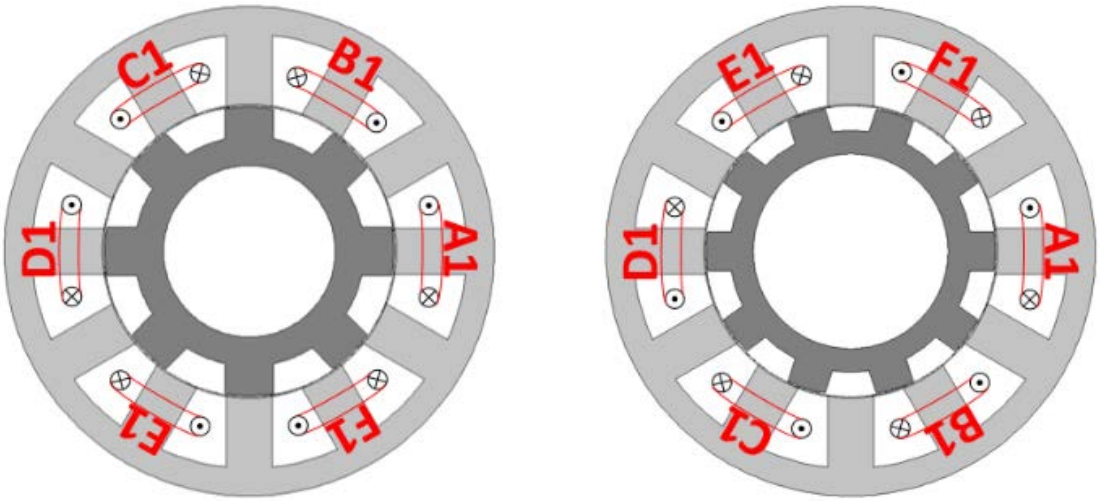

(a) 12s/8p (b) 12s/10p

Fig. 4.8. Two types of 6-phase single layer DS-SRMs.

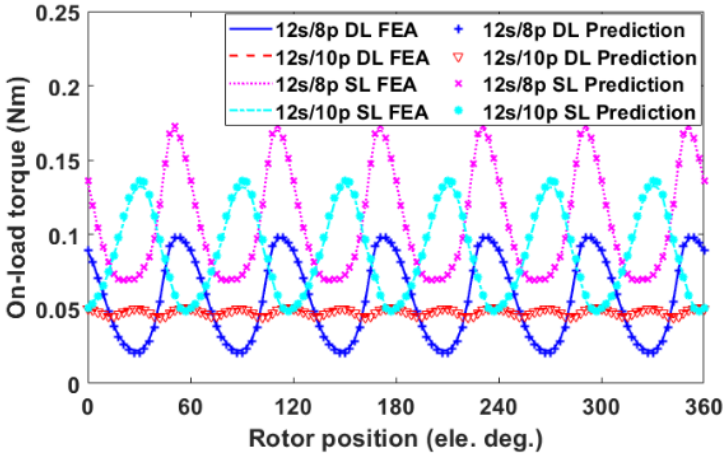

(a) Waveforms

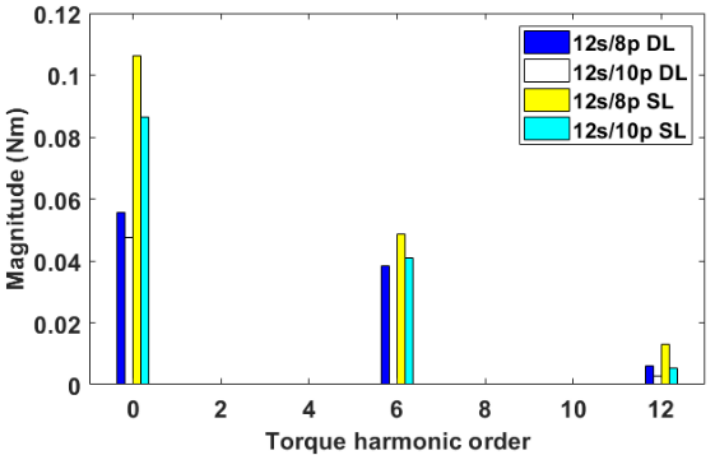

(b) Spectra

Fig. 4.9. Comparison in terms of on-load torque of four different 6-phase DS-SRMs. The machines are all supplied with 1A rms current.

According to (4.6)-(4.8), the comparison in terms of on-load torque for the four types of machines are given in Fig. 4.9. For different slot/pole number combinations of 6-phase machines, the 6^{th}, 12^{th}, 18^{th}… order torque harmonics will always exist. However, it is obvious from Fig. 4.9 that the 6^{th} order torque harmonic for the 12s/10p double layer machine can be neglected, which is different from other 6-phase machines. In order to figure out the reason behind, the 12s/8p and 12s/10p double layer machines have been further studied. The inductance spectra are shown in Fig. 4.10. It can be seen that for the two topologies, their inductance harmonic magnitudes have little difference, but the phase angles are significantly different. This will dramatically influence the torque contribution of each inductance harmonic. The torque produced by each inductance harmonic can be predicted by using the proposed torque models (4.6)-(4.8), and the results are shown in Fig. 4.11 and Fig. 4.12.

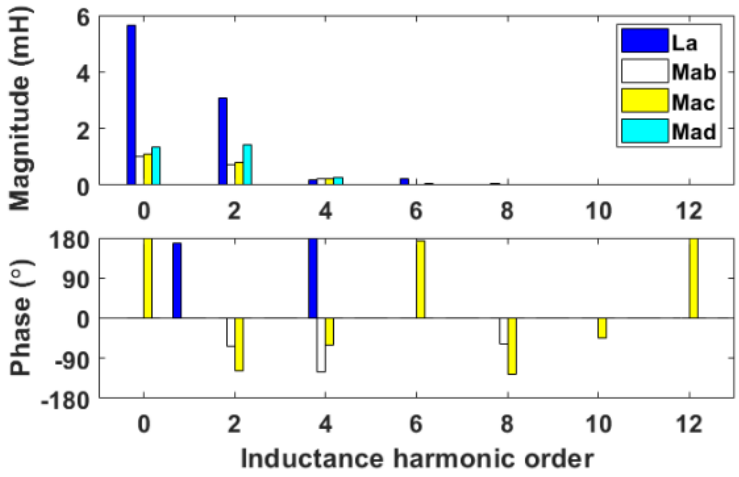

(a) 12s/8p

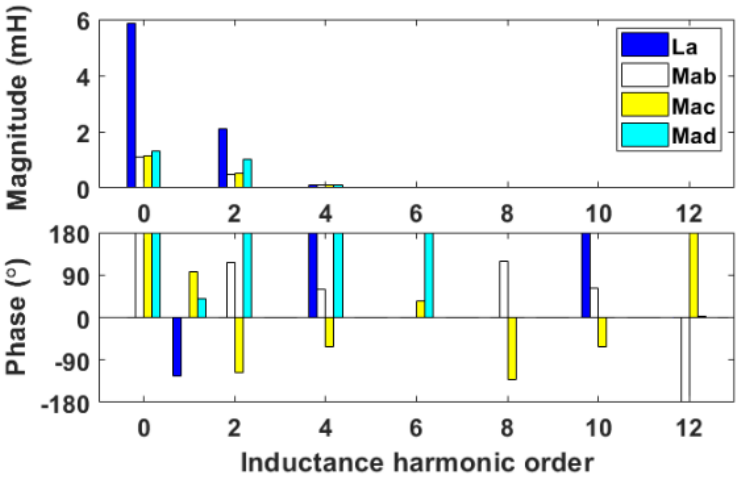

(b) 12s/10p

Fig. 4.10. Magnitudes and phases of inductance harmonics for double layer DS-SRMs.

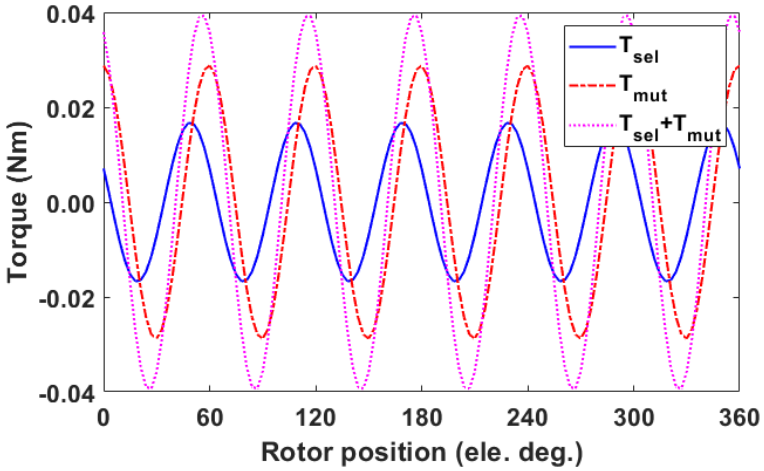

(a) Resultant torque

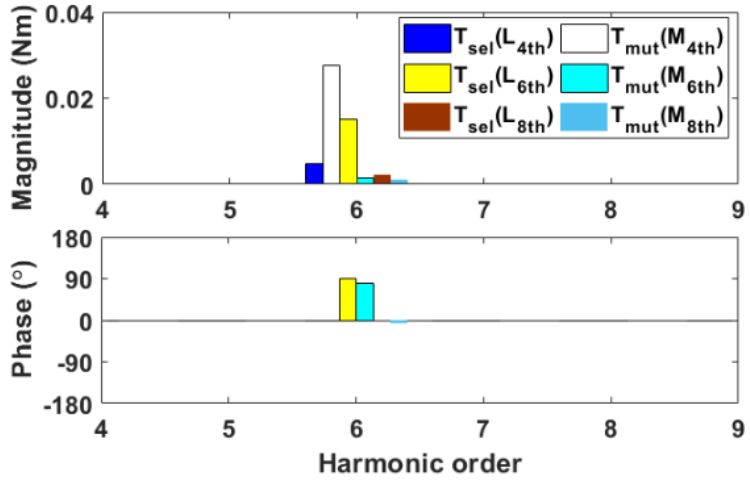

(b) Self- and mutual-torques due to each inductance harmonic

Fig. 4.11. 6th order torque harmonics of the 12s/8p double layer DS-SRMs. The phase RMS current is 1A.

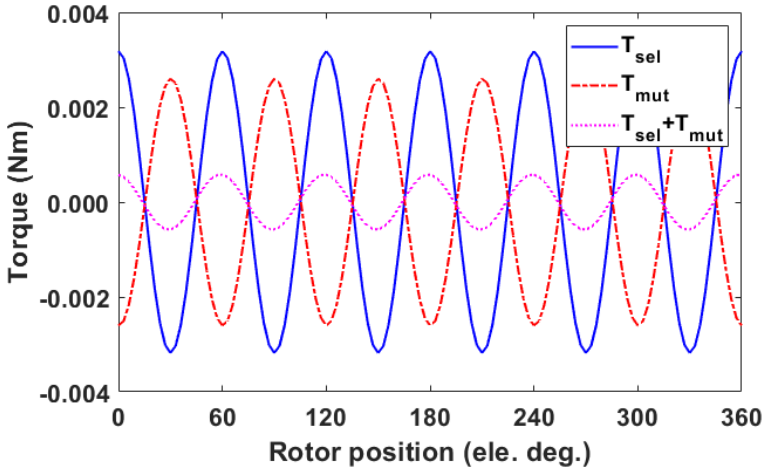

(a) Resultant torque

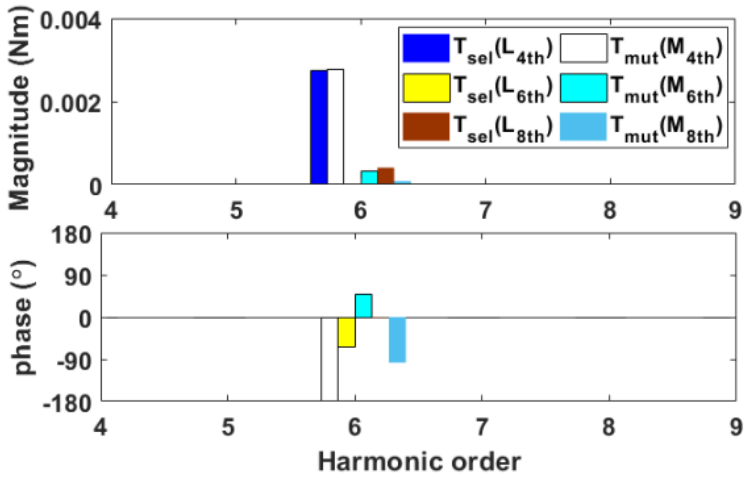

(b) Self- and mutual-torques due to each inductance harmonic

Fig. 4.12. 6th order torque harmonics of the 12s/10p double layer DS-SRMs. The phase RMS current is 1A.

From Fig. 4.11 and Fig. 4.12, it can be observed that the 12s/8p machine has much higher magnitudes in torque harmonics for every inductance harmonic than that of the 12s/10p. Moreover, for the 12s/8p machine, the self- and mutual-torques produced by the inductance harmonics have similar phase angles. As a result, the 6th order torque harmonics due to the self- and mutual-inductances are additive, leading to higher overall torque ripple level. In contrast, the self- and mutual-torques of the 12s/10p machine have almost 180 elec. deg. phase difference. This is particularly the case for the self- and mutual-torques due to the 4th order inductance harmonics. As a result, the 6th order torque harmonics for the double layer 6-phase 12s/10p DS-SRMs cancel one another, leading to much lower overall torque ripple level.

It is worth noting that the proposed torque model is based on the phase inductances calculated at relatively low electric loading. With the increasing phase current, the machines become saturated and there is an increasing discrepancy between the results obtained by FEA and the analytical torque models. The average torque and torque ripple coefficient versus phase root-mean-square (RMS) current, are shown in Fig. 4.13. It shows that the torque ripple benefit of the 12s/10p machine is not compromised at high saturation level compared with the 12s/8p machine.

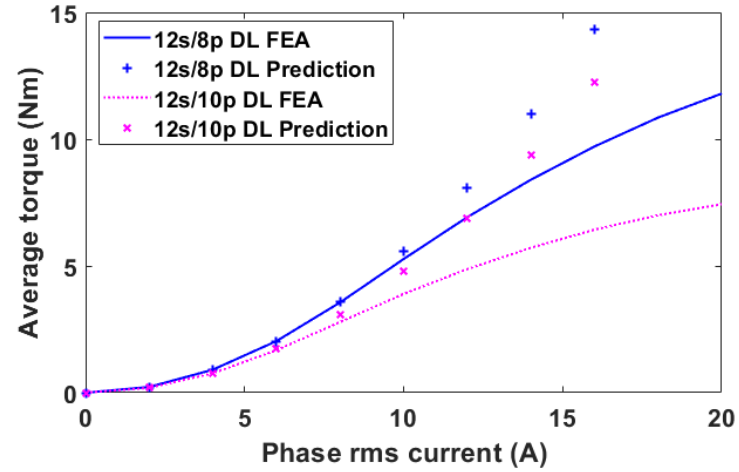

(a) Average torque

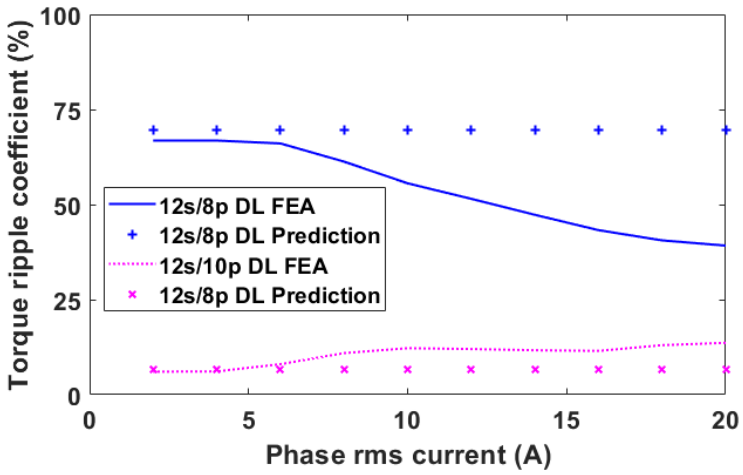

(b) Torque ripple coefficient

Fig. 4.13. Comparison of torque production for two slot/pole number combinations.

4.3.2 Fully Pitched Distributed Winding

For completeness, apart from the concentrated winding configurations, 6-phase fully-pitched DS-SRMs with distributed windings have also been investigated in this chapter. Their cross-sections and winding configurations are shown in Fig. 4.14. It is worth noting that the single

layer 12s/4p fully-pitched DS-SRMs have exactly the same torque performance as its double layer counterpart. However, the double layer winding does not work for the 12s/8p fully-pitched machines due to negligible torque capabilities. This is because the coil magneto-motive forces of each two opposite phases, e.g. phases A and D, have exactly the same polarity (NN for phase A and NN for phase D as well) at each rotor position, there will be no return path for the armature flux. As a result, the airgap flux density is almost zero, leading to very low output torque. Therefore, only single layer winding topologies have been selected for investigation in this section.

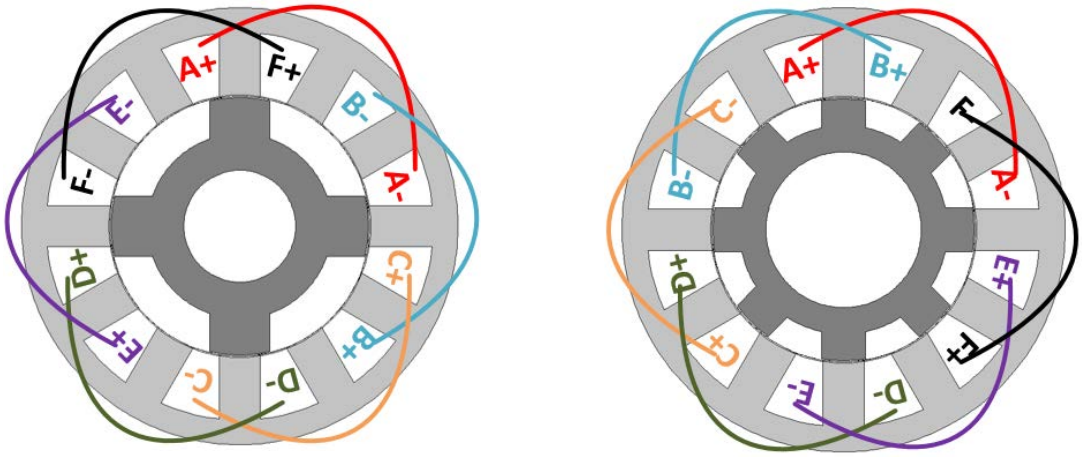

(a) 12s/4p (b) 12s/8p

Fig. 4.14. 6-phase fully-pitched DS-SRMs.

The same analyses as in sections 4.2 have been performed for these two machines and the comparison results are shown in Fig. 4.15. Again, the proposed torque model provides reliable prediction in terms of on-load torque and there are 6^{th}, 12^{th}, 18^{th}, etc. order torque harmonics as expected.

After comparative studies of different phase numbers, slot/pole number combinations and also winding configurations, one can confirm that for any multi-phase DS-SRMs, the torque harmonics due to fundamental current only depend on the phase number '*m*' and their orders are equal to *mk* when $\mathrm{mod}(mk, 2) = 0$. However, without quantifying the contribution of each order inductance harmonic (magnitude) to torque, it is hard to identify which torque harmonic is the most dominant one.

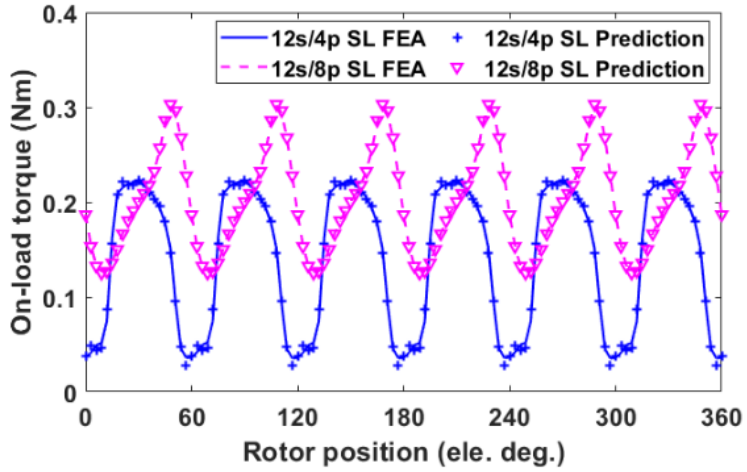

(a) Waveform

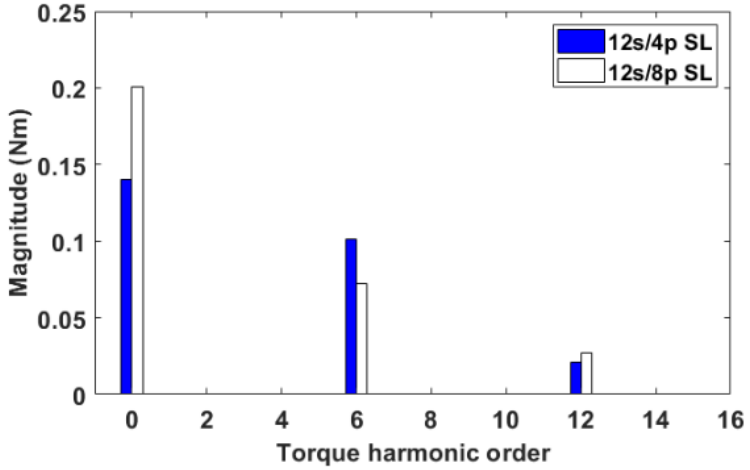

(b) Spectra

Fig. 4.15. Comparison in terms of on-load torque for fully-pitched 6-phase DS-SRMs with 1A rms phase current.

4.4 Copper Losses for Multi-Phase Machine

The investigated machines all have the same number of turns per phase so as to maintain similar phase voltage level. This means that for the same phase current, the copper losses will be different for different phase numbers. To be specific, higher phase number will have higher copper loss ($P_{cop} = mI_{rms}{}^2R$, where R is the phase resistance and I_{rms} is the phase rms current). In order to achieve fairer comparison, the average torque and torque ripple coefficient versus copper loss have been investigated in this section.

Due to concentrated winding, the DL and SL machines have much shorter end-windings than the FP machines if the number of turns per phase is the same for all machines. As a result, the

phase resistances of the DL and SL machines are much smaller than that of the FP machine. The average value of end-winding for different winding configuration is assumed as shown in Table 4.3. The Dimensions of end-winding are shown in Fig. 4.16.

TABLE 4.3 CALCULATION OF END-WINDING LENGTH FOR DIFFERENT WINDING CONFIGURATION

Winding configuration	End-winding
Short pitched	$\frac{1}{2}z\pi W_s + W_t$
Fully pitched	$\frac{1}{2}z\pi W_s + 2\pi(S_i + \frac{1}{2}h_s) \times \frac{360°/N_s \times a - \gamma}{360°}$

where the W_s is average stator slot width (trapezoidal), W_t is stator tooth width, S_i represents the stator inner radius, h_s is the tooth height, N_s is the number of slots, γ is the slot opening width in mechanical degree, and a is the slot number that each coil covers. The coefficient z depends on the double-layer (z=0.5) or single-layer (z=1) winding configuration.

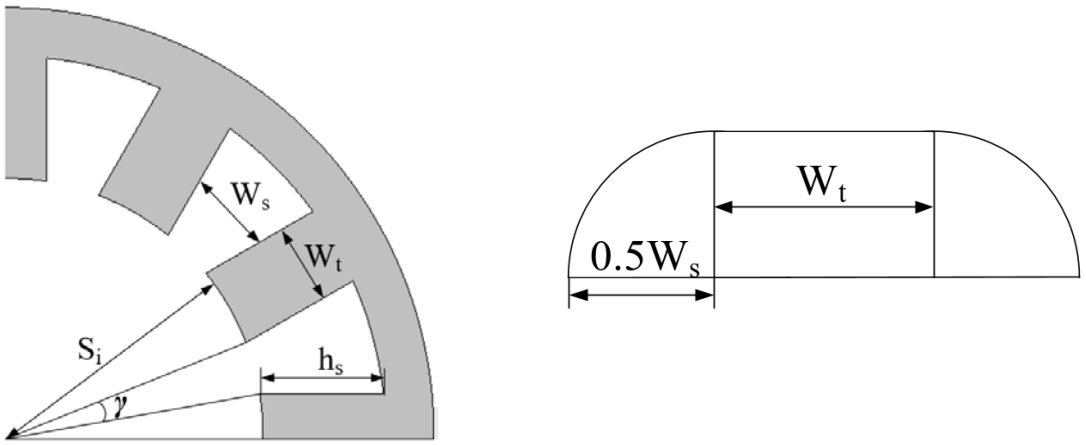

(a) Cross-section (b) Ideal shap of end-winding

Fig. 4.16. Dimensions of end-winding for DS-SRMs.

Once average end-winding length has been calculated, the phase resistance R of the multi-phase machines can be given by:

$$R = \rho N \frac{L}{S} \tag{4.11}$$

where ρ is the resistivity of copper, N represents the number of turns per phase, L is the copper length per turn, and S is the cross-section area of the copper wire. By using the equation (4.11), the phase resistances for different multi-phase machines are listed in TABLE 4.4.

TABLE 4.4 PHASE RESISTANCES ACCOUNTING FOR END-WINDINGS FOR DIFFERENT TOPOLOGIES @ 20 ℃

Machine topologies	DL (Ω)	SL (Ω)	FP (Ω)	Slot area (cm^2)	NT per slot
3-phase 12s/8p	0.51	0.558	0.809	1.171	66
2-phase 4s/4p	0.638	0.789	-	2.492	132
3-phase 6s/4p	0.766	0.893	-	1.835	132
4-phase 8s/6p	0.993	1.111	-	1.313	132
5-phase 10s/8p	0.985	1.089	-	1.259	132
6-phase 12s/8p	1.02	1.116	1.617	1.171	132
6-phase 12s/10p	1.02	1.116	-	1.171	132
6-phase 12s/4p	-	-	1.522	1.171	132

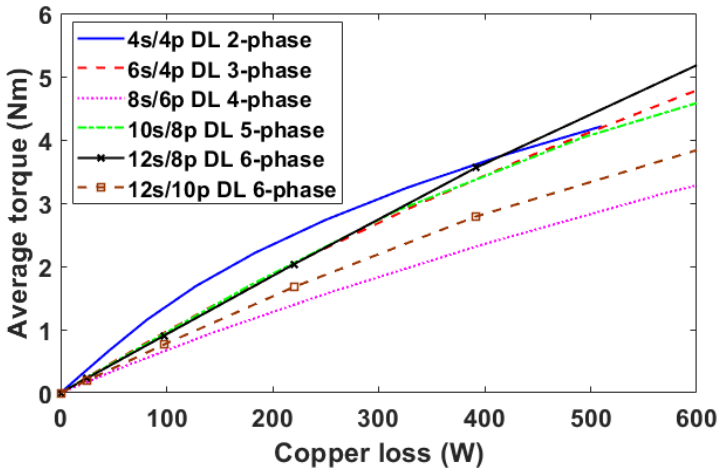

(a) Average torque

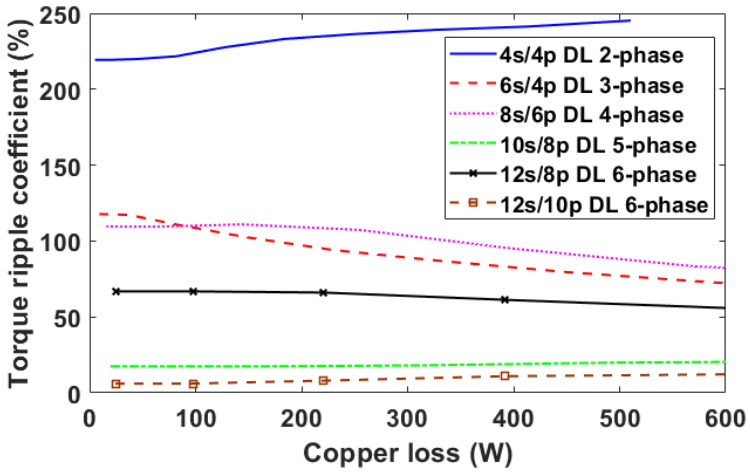

(b) Torque ripple coefficient

Fig. 4.17. Torque performance *vs* copper loss for double layer multiphase machines.

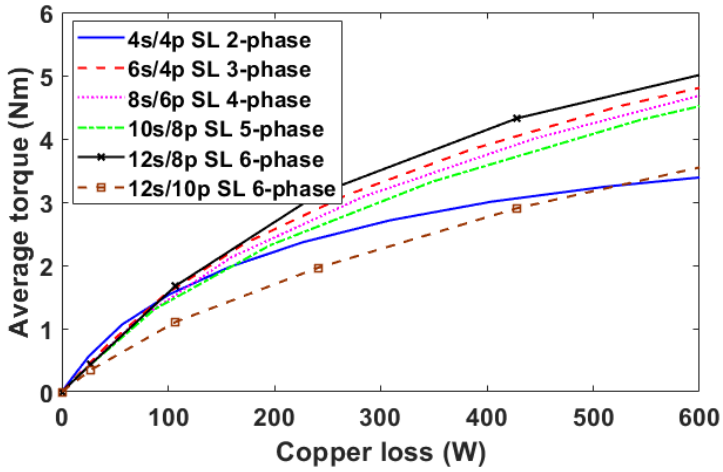

(a) Average torque

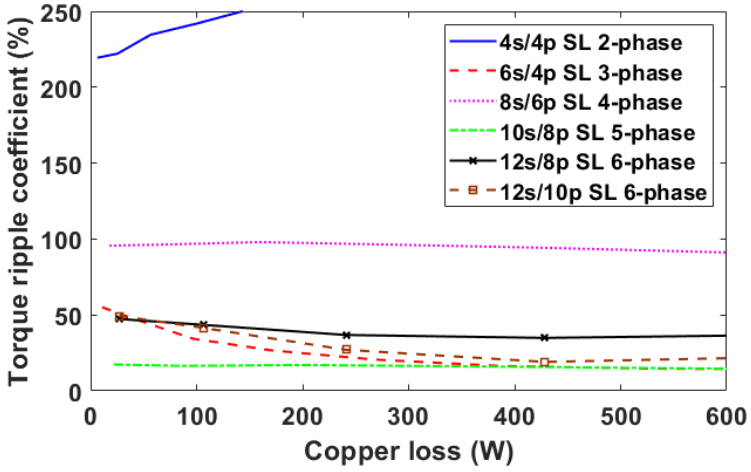

(b) Torque ripple coefficient

Fig. 4.18. Torque performance *vs* copper loss vs copper loss for single layer multiphase machines.

Fig. 4.17 and Fig. 4.18 show the average torque and torque ripple coefficient versus copper loss for the double layer and single layer DS-SRMs, respectively. It is found that for both double and single layer winding structures, the 2-phase machines produce higher average torque than other phase numbers at low copper loss. With increasing phase current (or copper loss), the 2-phase machines loss their benefit in terms of average torque, while the 12s/8p 6-phase DS-SRMs will produce the highest average torque at higher copper loss (>400W). 5-phase machines show similar torque capability as the 12s/8p 6-phase machine at lower copper loss, while they have almost the smallest torque ripple coefficient compared with other machines except the 12s/10p double layer 6-phase machine. In addition, the benefit in terms of torque ripple for the 5-phase machine will not be compromised with increased copper loss. It

is also worth noting that the double/single layer 2-phase and 4-phase DS-SRMs have shown much worse torque ripple performance, as expected.

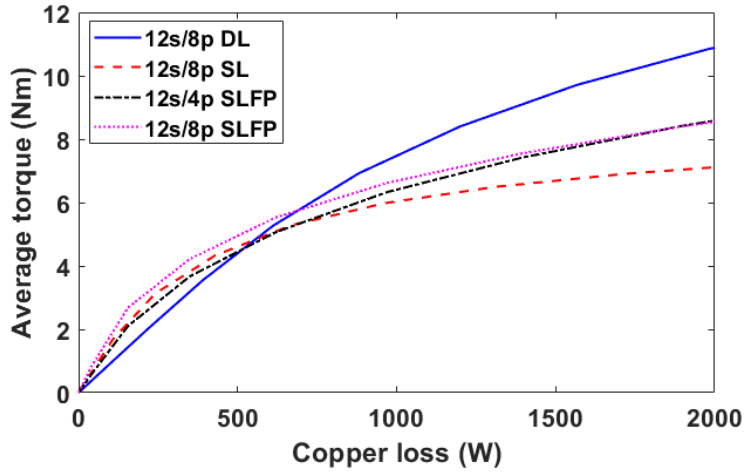

(a) Average torque

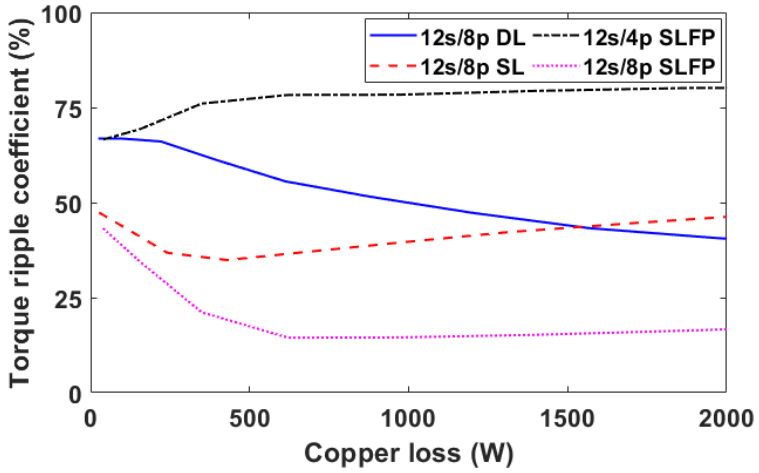

(b) Torque ripple coefficient

Fig. 4.19. Torque performance vs copper loss for 6-phase topologies.

The 12s/8p double/single layer 6-phase machines have also been compared with two types of fully-pitched machines and the results are shown in Fig. 4.19. It shows when the copper loss is less than 600W, the double layer machines exhibit the lowest average torque compared with other three machines. When the phase current increases, so does the copper loss, the benefit of double layer machines are increasingly evident. It is because they are less sensitive to magnetic saturation due to less flux concentrated in the stator yoke [67]. It is also apparent that the two fully-pitched machines show similar torque capability. However, the 12s/8p fully-pitched machines always achieve the lowest torque ripple compared with other machines, while the 12s/4p fully-pitched machines being the highest. Moreover, it is worth noting that the torque

ripple of single layer machines are generally lower than that of double layer machines for lower current (copper loss < 1600W). However, with increasing phase current, this advantage diminishes.

4.5 Analytical Torque Model with Harmonic Current for Multi-phase DS-SRMs

Similar to the three-phase machine, the stator current with single current harmonic injection can be described by (4.12). It is worth noting that only phase 'a' is given here because other phases will have the same magnitude while with a $2\pi/m$ phase shift.

$$I_a = I_1 \sin(\theta_e + \beta_1) + I_v \sin(v\theta_e + \beta_v) \tag{4.12}$$

Substituting (4.12), (4.4) and (4.5) into (4.1) and the instantaneous torque equation can be transformed as below:

$$T_e = T_f + T_h \tag{4.13}$$

with

$$\begin{cases} T_f = T_{fsel} + T_{fmut} = T_{f0} + T_{frip} \\ T_h = T_{hsel} + T_{hmut} = T_{h0} + T_{hrip} \end{cases} \tag{4.14}$$

Furthermore, the torque produced by the interaction between current harmonics and self-/mutual-inductances can be decoupled into two terms: $T_h(I_1 I_v)$ and $T_h(I_v^2)$. This chapter will first investigate harmonic torque term $T_h(I_1 I_v)$ (highest magnitude) as shown in (4.15) and (4.16) in order to improve torque performance. It has been given:

$$\begin{aligned} T_{hsel} = \frac{mp}{2} \sum_{n=1}^{\infty} \frac{nL_n}{2} I_1 I_v \{ & \sin(A\theta_e + \beta_1 + \beta_v + \alpha_n) \\ & - \sin(B\theta_e + \beta_1 + \beta_v - \alpha_n) \\ & - \sin(C\theta_e + \beta_1 - \beta_v + \alpha_n) \\ & + \sin(D\theta_e + \beta_1 - \beta_v - \alpha_n) \} \end{aligned} \tag{4.15}$$

And

$$
\begin{aligned}
T_{hmut} = \frac{mp}{2}\sum_{n=1}^{\infty}\sum_{x=1}^{\mathrm{Z}} c\frac{nM_{xn}}{2} I_1 I_v \\
&\left\{\sin\left(A\theta_e + \beta_1 + \beta_v + \alpha'_{xn} - \frac{2\pi}{m}vx\right)\right. \\
&-\sin\left(B\theta_e + \beta_1 + \beta_v - \alpha'_{xn} - \frac{2\pi}{m}vx\right) \\
&-\sin\left(C\theta_e + \beta_1 - \beta_v + \alpha'_{xn} + \frac{2\pi}{m}vx\right) \\
&+\sin\left(D\theta_e + \beta_1 - \beta_v - \alpha'_{xn} + \frac{2\pi}{m}vx\right) \\
&+\sin\left(A\theta_e + \beta_1 + \beta_v + \alpha'_{xn} - \frac{2\pi}{m}x\right) \\
&-\sin\left(B\theta_e + \beta_1 + \beta_v - \alpha'_{xn} - \frac{2\pi}{m}x\right) \\
&-\sin\left(C\theta_e + \beta_1 - \beta_v + \alpha'_{xn} - \frac{2\pi}{m}x\right) \\
&\left.+\sin\left(D\theta_e + \beta_1 - \beta_v - \alpha'_{xn} - \frac{2\pi}{m}x\right)\right\}
\end{aligned} \tag{4.16}
$$

and

$$
\begin{cases} A = 1 + v + n \\ B = 1 + v - n \\ C = 1 - v + n \\ D = 1 - v - n \end{cases} \tag{4.17}
$$

$$
c = \begin{cases} 0.5 & mod(m,2) = 0 \; and \; x = \mathrm{Z} \\ 1 & otherwise \end{cases}
$$

$\mathrm{A, B, C, D} = mk$ where k is 0, 1, 2, 3…

According to (4.15)-(4.17), it can be seen that the frequency of T_h is related to the order of injected current harmonic v and inductance harmonic n. Generally, T_h will only contain the multiple of m order torque harmonic, which is the same as that of T_f. As a result, it is possible to compensate torque ripple due to fundamental current by that produced by current harmonic. Moreover, it is proven that the average torque due to the injected current harmonic can be produced when the factor of θ_e (A, B, C or D) is equal to 0. Which means when the v^{th} order current harmonic is injected, the $(v \pm 1)^{th}$ order inductance will contribute to average torque, as described by (4.18).

$$T_{h0} = -\frac{mp(v \mp 1)}{4} I_1 I_v \{L_{v\mp 1} \sin(\beta_1 \mp \beta_v \pm \alpha_{v\mp 1}) + \sum_{x=1}^{z} cM_{x(v\mp 1)} \left[\sin\left(\beta_1 \mp \beta_v \pm \alpha'_{x(v\mp 1)} \pm \frac{2\pi}{m} xv\right) + \sin\left(\beta_1 \mp \beta_v \pm \alpha'_{x(v\mp 1)} - \frac{2\pi}{m} x\right)\right]\} \quad (4.18)$$

Moreover, pure harmonic torque term $T_{hv}(I_v^2)$ is also investigated and described by (4.19)-(4.21), which is quite small and has little influence on the torque produced by the fundamental current. However, the consideration of this torque term will lead to more accurate instantaneous torque prediction after harmonic injection. It is worth noting that $T_{hv}(I_v^2)$ only contains the mk^{th} order torque harmonic.

$$T_{hv} = T_{hvsel} + T_{hvmut} \quad (4.19)$$

and

$$T_{hvsel} = \frac{mp}{2} \sum_{k=0}^{\infty} \left\{-\frac{n}{2} L_n I_v^2 \sin(n\theta_e + \alpha_n) + \frac{n}{4} I_v^2 L_n \sin\big((2v+n)\theta_e + 2\beta_v + \alpha_n\big) + \frac{n}{4} I_v^2 L_n \sin\big((n-2v)\theta_e - 2\beta_v + \alpha_n\big)\right\} \quad (4.20)$$

$$T_{hvmut} = \frac{mp}{2} \sum_{k=0}^{\infty} \sum_{x=1}^{\Delta} cnM_{xn} I_v^2 \left\{-\cos\left(\frac{2\pi}{m} xv\right) \sin(n\theta_e + \alpha'_{xn}) + \frac{1}{2} \sin\left((2v+n)\theta_e + 2\beta_v + \alpha'_{xn} - \frac{2\pi}{m} xv\right) + \frac{1}{2} \sin\left((n-2v)\theta_e - 2\beta_v + \alpha'_{xn} + \frac{2\pi}{m} xv\right)\right\} \quad (4.21)$$

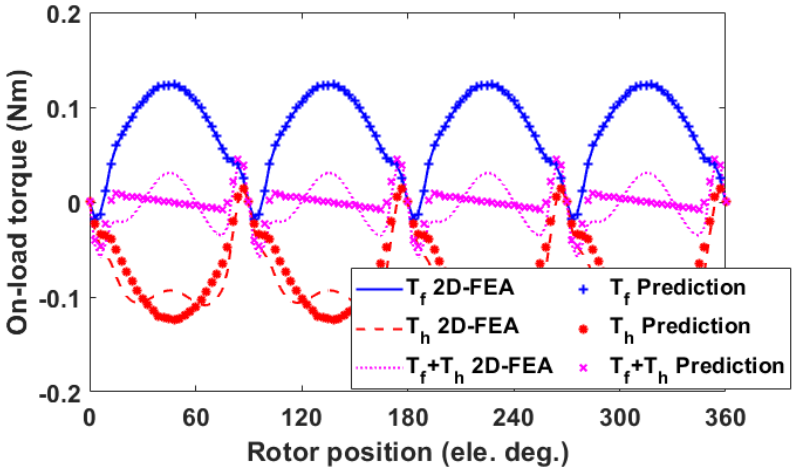

(a) Torque prediction without pure harmonic terms

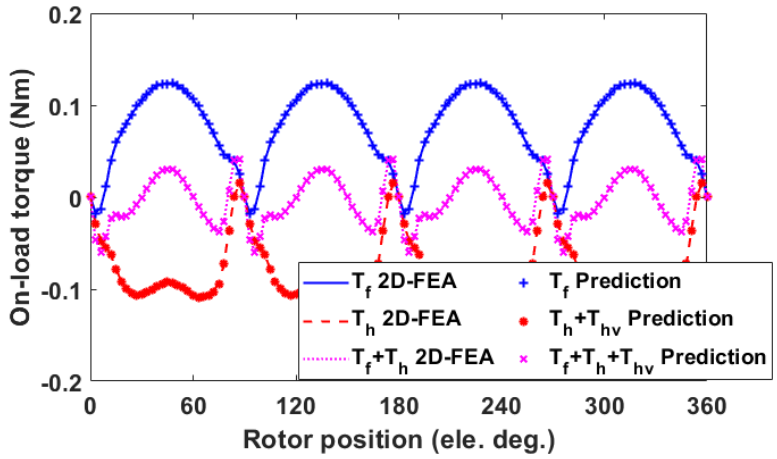

(b) Torque prediction with pure harmonic terms

Fig. 4.20. Comparison of 2D-FEA and analytically predicted instantaneous torque with I_1=1 Arms ($I_3 = 50\%I_1$, $\beta_3 = 266.1°$) for single layer 4-phase DS-SRMs.

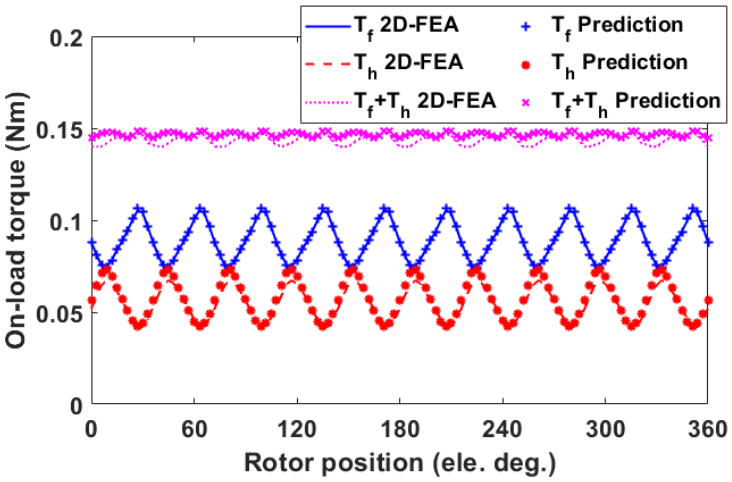

(a) Torque prediction without pure harmonic terms

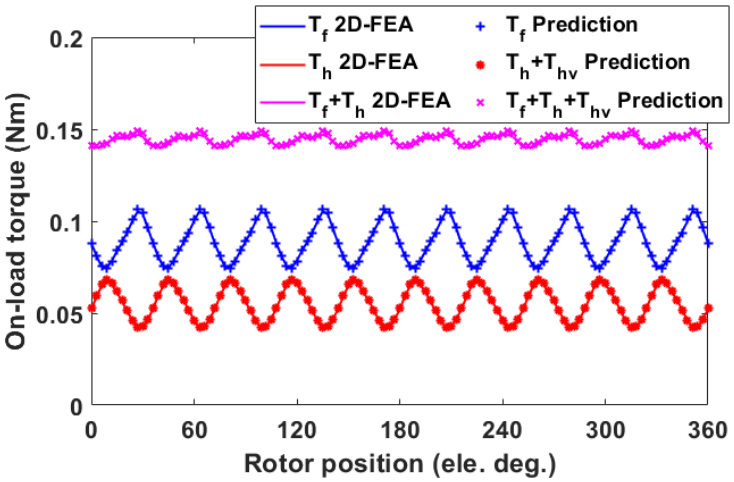

(b) Torque prediction with pure harmonic terms

Fig. 4.21. Comparison of 2D-FEA and analytically predicted instantaneous torque with I_1=1 Arms ($I_3 = 32.3\%I_1$, $\beta_3 = 78.6°$) for single layer 5-phase DS-SRMs.

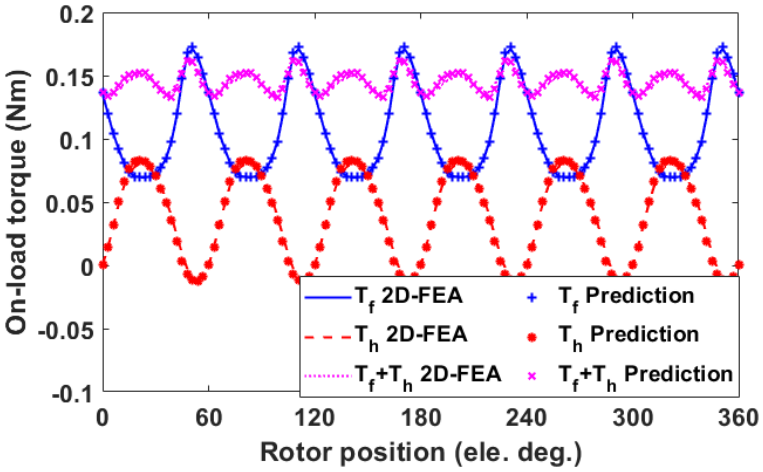

(a) Torque prediction without pure harmonic terms

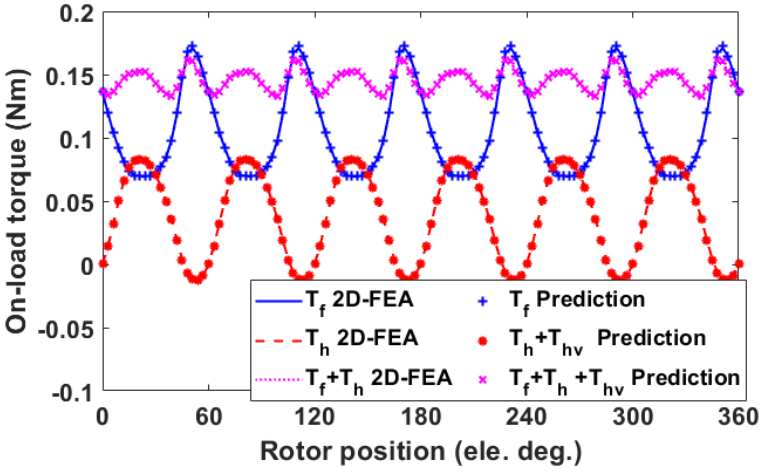

(b) Torque prediction with pure harmonic terms

Fig. 4.22. Comparison of 2D-FEA and analytically predicted instantaneous torque with I_1=1 Arms ($I_3 = 47.7\%I_1$, $\beta_3 = 45.1°$) for single layer 6-phase DS-SRMs.

Fig. 4.10, Fig. 4.11 and Fig. 4.22 shows the comparison between 2D-FEA and analytical results for a 4-phase, 5-phase and 6-phase single layer machine with the 3rd order current harmonic injection, respectively. It can be seen that considering the pure harmonic torque terms, the analytical prediction can be more accurate. Therefore, the pure harmonic torque terms will be considered for other order current harmonic injection as well. As an example, Fig. 4.23 shows the comparison between 2D-FE and analytical instantaneous torques for the SL 6-phase machine with different current harmonic injections. A generally good agreement can be observed between 2D-FE and analytical predictions at low phase rms current condition. It has been found that the proposed current harmonic injection method is able to suppress the torque ripple for the multi-phase DS-SRMs, if the current harmonic is properly selected.

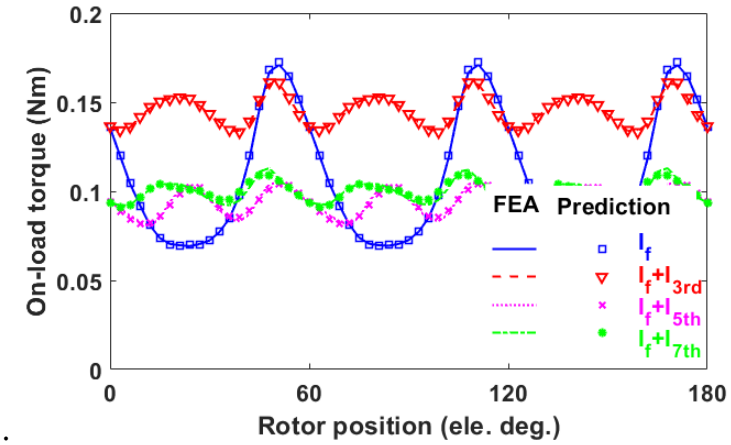

Fig. 4.23. Comparison of 2D-FE and analytically predicted instantaneous torques for the SL 6-phase DS-SRMs with current harmonic injections. The fundamental current I_1 is 1Arms and the characteristics of current harmonic are listed in TABLE 4.5.

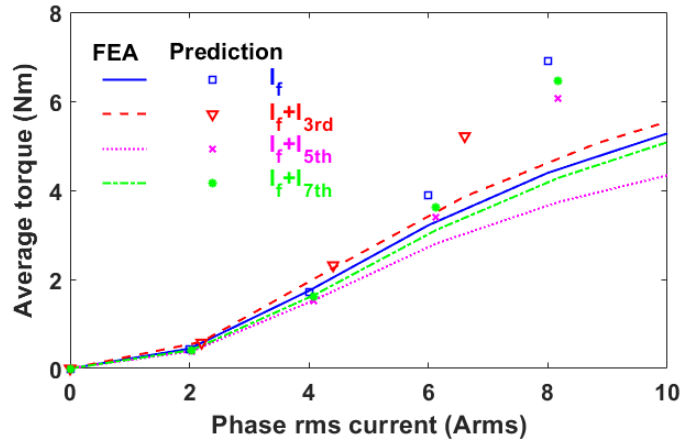

(a) Average torque

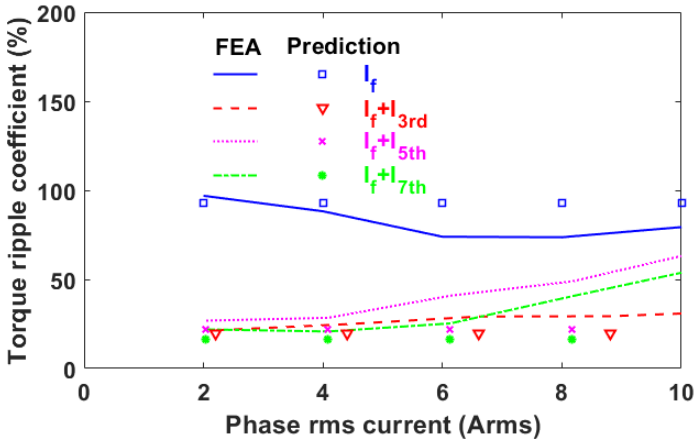

(b) Torque ripple coefficient

Fig. 4.24. Comparison torque performance *vs* phase rms current for the SL 6-phase DS-SRMs with current harmonic injections. Characteristics of current harmonic are listed in TABLE 4.5.

Fig. 4.24 illustrates the average torque and torque ripple coefficient versus phase rms current after current harmonic injection for the SL 6-phase DS-SRM. At a modest phase current (<4Arms), the proposed model can accurately predict the average torque and torque ripple. However, with increasing phase current, machine becomes saturated and there is an increasing discrepancy between the 2D-FE and analytical predictions. This would be the limitation of the developed analytical torque models. However, although the accuracy of the torque equation is reduced at high phase current, the effect of current harmonic injection on torque ripple reduction is not seriously compromised.

Once the accuracy of the analytical torque models has been validated by 2D-FEA, the prediction of on-load torque for multi-phase double layer counterparts with current harmonic injection can be shown in Fig. 4.25. The selection of magnitude and phase angle for the 3^{rd} order current harmonic has been investigated and listed in TABLE 4.5 (Chapter **4.6**). It is found that the 3^{rd} order current harmonic has little effect on the double layer 6-phase DS-SRMs, which is due to the fact that the harmonic torque produced by the self- and mutual-inductances cancelled each other similar to what has been observed for a 3-phase machine investigated in Chapter 3. The same condition will occur for the double layer 5-phase DS-SRMs when they are injected with the 5^{th} order current harmonic as shown in Fig. 4.25 (b). However, the other current harmonic injections (3^{rd} and 7^{th} for 5-phase machine; 5^{th} and 7^{th} for 6-phase machine) can still improve the average torque or reduce the torque ripple for such machines.

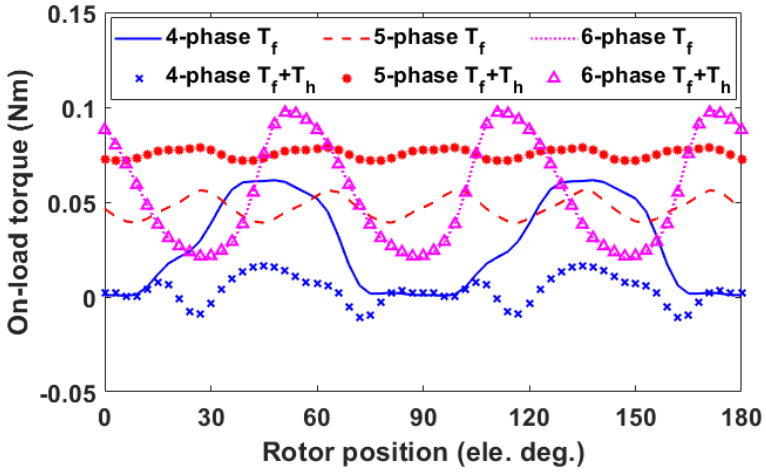

(a) I_1+I_{3rd}

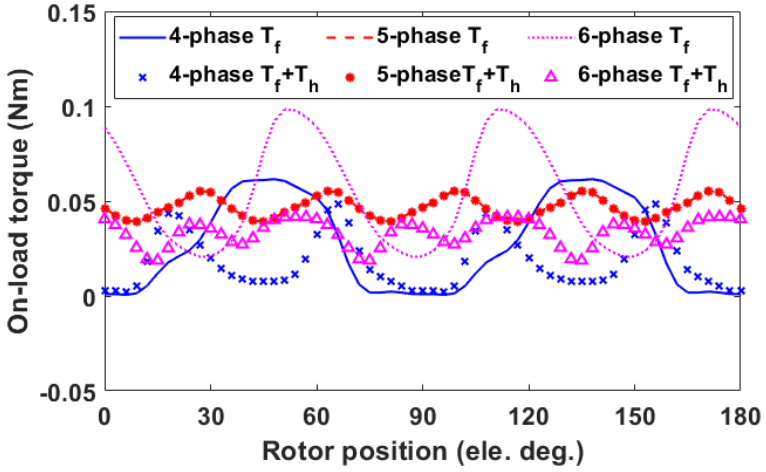

(b) I_1+I_{5th}

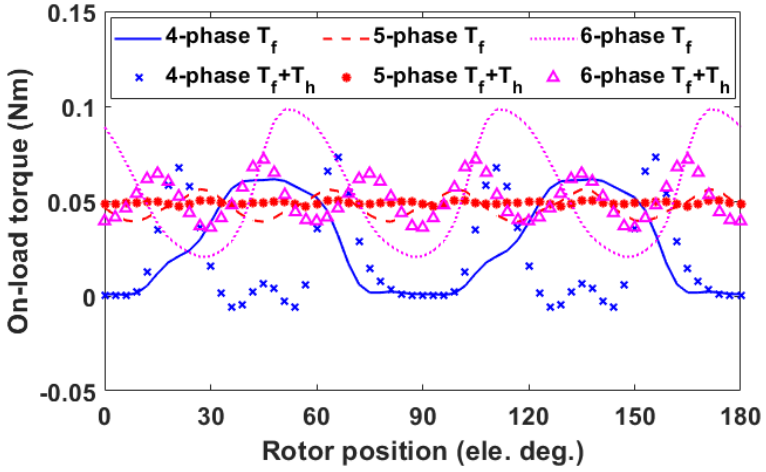

(c) I_1+I_{7th}

Fig. 4.25. Prediction of on-load torque with or without current harmonic injection for double layer multi-phase machine (I_1=1 Arms).

4.6 Analytical Solution for Optimal Torque Performance

Based on the analytical torque models for both fundamental and harmonic currents, the methods to predict the current harmonic magnitude and phase angle to achieve maximum torque or minimum torque ripple can be developed. The machines are always operating under the maximum torque per ampere (MTPA) conditions, which means that the phase advance angle β_1 is kept at 45° (largely true if saturation is negligible). It is worth mentioning that although the pure harmonic term $T_h(I_v^2)$ is taken into account for more accurate instantaneous torque prediction, considering it in predicting the current harmonic (order, magnitude and phase angle) will significantly increase the complexity with only little benefit (due to lower magnitude). Therefore, in this section only torque term $T_h(I_1 I_v)$ is considered to improve torque performance (average torque and/or torque ripple).

4.6.1 Maximum Average Torque

According to foregoing investigation, when the v^{th} order current harmonic is injected, the average torque produced by current harmonic for multi-phase machine can be expressed as (4.18). Moreover, only $v \mp 1^{th}$ order inductance harmonic will contribute to extra average torque, i.e. only the torque terms with factor *B* or *C* are considered in average torque due to the fact that *B* and *C* in (4.17) are equal to 0. It is worth noting that once *n* and *v* are confirmed there will be 2Z+1 torque terms in total (including both self- and mutual-torques), which have the same factor (*B* or *C*).

After applying trigonometric function, the average torque can be simplified as

$$\begin{aligned} T_{h0}(\beta_v) &= \sum_{i=1}^{2Z+1} T_{Bi} \sin(\varphi_{Bi} + \beta_v) + \sum_{i=1}^{2Z+1} T_{Ci} \sin(\varphi_{Ci} + \beta_v) \\ &= T_{H0} \sin(\beta_v + \varphi_{H0}) \end{aligned} \tag{4.22}$$

with

$$\begin{cases} \tan(\varphi_{H0}) = \dfrac{y}{x} \\ T_{H0} = \sqrt{x^2 + y^2} \end{cases} \tag{4.23}$$

$$\begin{cases} x = \sum_{i=1}^{2Z+1} T_{Bi}\cos(\varphi_{Bi}) + T_{Ci}\cos(\varphi_{Ci}) \\ y = \sum_{i=1}^{2Z+1} T_{Bi}\sin(\varphi_{Bi}) + T_{Ci}\sin(\varphi_{Ci}) \end{cases} \tag{4.24}$$

where T_{Bi}, T_{Ci}, φ_{Bi} and φ_{Ci} are all constants, which represent the magnitude and phase angle for each torque term with the same factors (B or C) when β_v is equal to 0, and $i \in (2Z+1)$. This will be used throughout this chapter. T_{H0} and φ_{H0} are the magnitude and phase angle of resultant torque produced by current harmonic injection. They can be easily calculated. Therefore, it is apparent that if the harmonic magnitude is kept unchanged, the torque equation will be a function of the phase angle β_v of the current harmonics. In this case, there must be a phase angle β_{v_Tmax} that can produce the maximum average torque and it can be calculated by (4.25).

$$\beta_{v\_Tmax} = \frac{\pi}{2} - \varphi_{res} \tag{4.25}$$

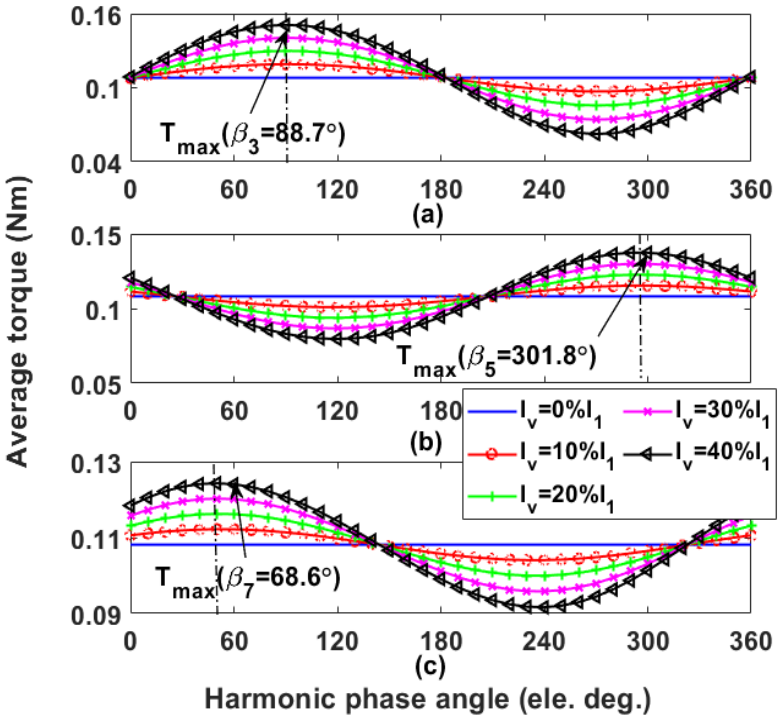

Fig. 4.26. 2D-FEA average torque versus harmonic phase angle for a single layer 6-phase DS-SRMs with different order harmonic injections. The fundamental current I_1 is equal to 1A. (a) 3rd harmonic, (b) 5th harmonic and (c) 7th harmonic. (Dashed line: Peak value of 2D-FEA, Arrow: Predicted phase angle)

Fig. 4.26 shows the 2D-FEA results of average torque against the phase angle with different current harmonic injection for single layer 6-phase DS-SRMs. It is worth noting that the phase angles shown in Fig. 4.26 are the predicted values, where the maximum average torque can be achieved, rather than the real peak values from the 2D-FEA results. The minor discrepancy between the prediction and 2D-FEA results is because only torque term $T_h(I_1 I_v)$ is considered to predict the current harmonics (order, magnitude and phase angle). But this discrepancy is largely acceptable.

In theory, without magnetic saturation, the torque could be increased continuously by increasing harmonic current magnitude. However, the current harmonic will generate extra copper losses at the same time. So in order to maintain the same copper loss, the root-mean-square (RMS) current is kept unchanged, i.e. $I_{RMS} = \sqrt{{I_{1rms}}^2 + {I_{vrms}}^2}$. Fig. 4.27 shows the average torque profile for a single layer 6-phase DS-SRMs, in which the 3rd order current harmonic ($\beta_3 = 88.7°$) is injected. It can be found that the maximum average torque can be obtained when $I_3 \approx 40\% I_1$.

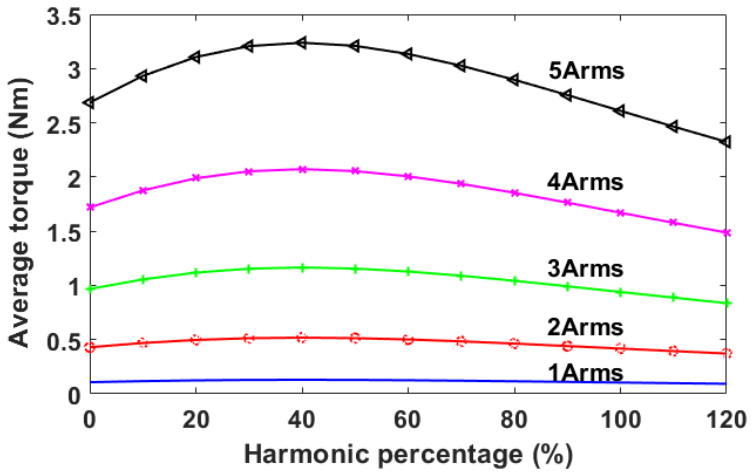

Fig. 4.27. Average torque against phase RMS current with different percentages of 3rd order current harmonic injection for the single layer 6-phase DS-SRM ($\beta_3 = 88.7°$).

4.6.2 Minimum Torque Ripple

After the investigation in section 0, the contribution in torque from each order inductance harmonic can be predicted for any multi-phase DS-SRMs. In order to cancel out dominant order torque ripple produced by fundamental current listed in TABLE 4.2, the torque due to

harmonic current, with the same frequency, the same magnitude but a phase shift of π, is required.

According to (4.7) and (4.8), the dominant order torque ripple (*mk*) due to fundamental current can be expressed by (4.26).

$$T_{frip\_mkth} = T_{Frip}\sin\left(mk\theta_e + \varphi_{Frip}\right) \tag{4.26}$$

In addition, according to (4.15) and (4.16), the frequency of torque ripple due to harmonic current is controlled by injected current order and inductance harmonic order, which is described by

$$|1 \pm v \pm n| = mk \tag{4.27}$$

when the injected current harmonic order is selected, the active inductance harmonic order related to the desired torque harmonic can be determined at the same time as

$$n = |mk \pm v \pm 1| \tag{4.28}$$

By way of example, if one wants to reduce the 6th (*mk*=6) order torque harmonic in 6-phase machines by injecting the 3rd order current harmonic (*v*=3), there will be four active inductances that contribute to the 6th order torque harmonic, such as, 2th, 4th, 8th and 10th, respectively. It is worth noting that the self- and mutual-torque terms due to the same active inductance harmonic have the same factor (A, B, C or D). Moreover, the torque terms due to two active inductances ($|mk - v \pm 1|$) show the same sign between θ_e and β_v, while other two ($|mk + v \pm 1|$) present different signs. Therefore, the torque ripple performance after current harmonic injection can be simply written as

$$\begin{aligned} T_{hrip}(\beta_v) &= \sum_{i=1}^{(2Z+1)\times 2} T_{Xi}\sin(mk\theta_e + \varphi_{Xi} + \beta_v) + T_{Yi}\sin(mk\theta_e + \varphi_{Yi} - \beta_v) \\ &= T_{Xrip}\sin\left(mk\theta_e + \varphi_{Xrip} + \beta_v\right) + T_{Yrip}\sin\left(mk\theta_e + \varphi_{Yrip} - \beta_v\right) \\ &= T_{Hrip}(\beta_v)\sin\left(mk\theta_e + \varphi_{Hrip}(\beta_v)\right) \end{aligned} \tag{4.29}$$

with

$$\begin{cases} \tan\left(\varphi_{Hrip}(\beta_v)\right) = \dfrac{B(\beta_v)}{A(\beta_v)} \\ T_{Hrip}(\beta_v) = \sqrt{A^2 + B^2} \end{cases} \tag{4.30}$$

$$\begin{cases} A = T_{Xrip}\cos\left(\varphi_{Xrip} + \beta_v\right) + T_{Yrip}\cos\left(\varphi_{Yrip} - \beta_v\right) \\ B = T_{Xrip}\sin\left(\varphi_{Xrip} + \beta_v\right) + T_{Yrip}\sin\left(\varphi_{Yrip} - \beta_v\right) \end{cases} \tag{4.31}$$

where X and Y $[X, Y \in (A, B, C, D)]$ represent the torque terms with the same or different sign between θ_e and β_v, respectively. T_{Xi}, T_{Yi}, φ_{Xi} and φ_{Yi} [i=1, 2 …$(2Z + 1) \times 2$] are all constant, representing the magnitude and phase angle for the relative torque terms, when β_v is 0. It can be observed that the resultant torque ripple harmonic can be controlled by β_v. It is worth noting that the resultant magnitude T_{Hrip} is also proportional to the injected current harmonic magnitude i_v. Therefore, in order to minimize the resultant torque ripple, as mentioned previously, (4.26) and (4.29) need to achieve the same magnitude and have a π phase difference, which leads to

$$\begin{cases} \varphi_{Hrip}(\beta_v) = \varphi_{Frip} + \pi \\ T_{Hrip}(I_v, \beta_v) = T_{Frip} \end{cases} \tag{4.32}$$

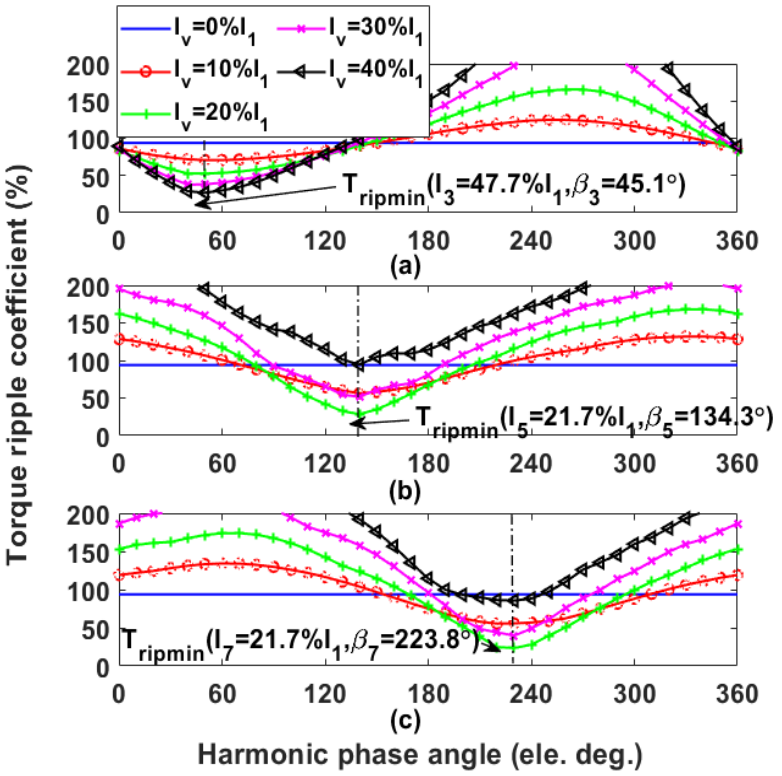

Fig. 4.28. 2D-FEA torque ripple *vs* harmonic current phase angle for a single layer 6-phase DS-SRMs with different harmonic current injections. The fundamental current I_1 is equal to 1A. (a) 3rd harmonic, (b) 5th harmonic and (c) 7th harmonic. (Dashed line: Peak value of 2D-FEA, Arrow: Predicted phase angle).

By solving (4.32), the harmonic magnitude and phase angle can be predicted at which the minimum torque ripple will occur. Fig. 4.28 shows the torque ripple coefficient ($\frac{T_{max}-T_{min}}{T_{ave}} \times$ 100%, where T_{max}, T_{min} and T_{ave} are the maximum, minimum and average torques during

one electrical period) versus harmonic phase angle when phase RMS current is 1Arms. It is proven that the prediction of harmonic magnitudes and phase angles are generally accurate where the minimum torque ripple will occur.

Proposed method can be implemented to different topologies. TABLE 4.5 shows the selection of different current harmonics based on the proposed method to suppress dominant torque ripple for several topologies. The phase RMS current is kept at 1A. After injecting these current harmonics, the predicted average torque and torque ripple variations have been shown in TABLE 4.6.

TABLE 4.5. CHARACTERISTICS OF CURRENT HARMONICS TO MINIMIZE TORQUE RIPPLE FOR DIFFERENT MACHINE TOPOLOGIES (PHASE RMS CURRENT IS 1ARMS)

Machine types		3rd		5th		7th	
		mag	phase	mag	phase	mag	phase
4	DL	48.4%	270.8°	64.9%	2.15°	67.2%	87°
	SL	50%	266.1°	35.7%	353.5°	35.3%	87.5°
5	DL	33.6%	71.3°	686%	196.9°	8.66%	90.9°
	SL	32.3%	78.6°	65%	177.7°	8.28%	89.1°
6	DL	1204%	0.06°	34%	113.4°	34.7%	202°
	SL	47.7%	45.1°	21.7%	134.3°	21.7%	223.8°

TABLE 4.6. AVERAGE TORQUE AND TORQUE RIPPLE COEFFICIENT AFTER CURRENT HARMONIC INJECTION WITH 1ARMS PHASE CURRENT

Machine types		3rd		5th		7th	
		Ave (%)	Rip (%)	Ave (%)	Rip (%)	Ave (%)	Rip (%)
4	DL	-94.2	+234.3	-50.4	+85.4	-52.3	+116.2
	SL	-99.7	+2045	+4.1	+12.2	+3.47	+2.0
5	DL	+43.7	-74.7	-98.2	-55.4	+3.0	-81.8
	SL	+45.9	-84.4	-38.7	-68.0	+3.1	-82.2
6	DL	-99.4	-69.5	-46.8	-50.2	-18.4	-49.7
	SL	+10.2	-78.0	-17.2	-72.2	-11.3	-77.8

Note: “+” means increased and “-” means reduced.

It is found that the 3rd order current harmonic shows the best performance for most machines, such as DL/SL 5-phase machines, SL 6-phase machines. It not only reduces the torque ripple by more than 70%, but also increases the average torque, especially, for the 5-phase machines.

However, it is ineffective in reducing the torque ripple or increasing the average torque for the DL 6-phase machine even when a 3rd order current harmonic of 1204% of the fundamental current is injected. This is mainly due to the fact that the harmonic torques due to the self- and mutual-inductances have cancelled each other. Similarly, the 5th order current harmonic will not be effective for the DL 5-phase machine. It is also found that, due to the special characteristics of the 4-phase machines, no harmonic current injection can be used for reducing their torque ripple regardless the SL or DL winding structure. However, the proposed methods can still be used to increase their average torque.

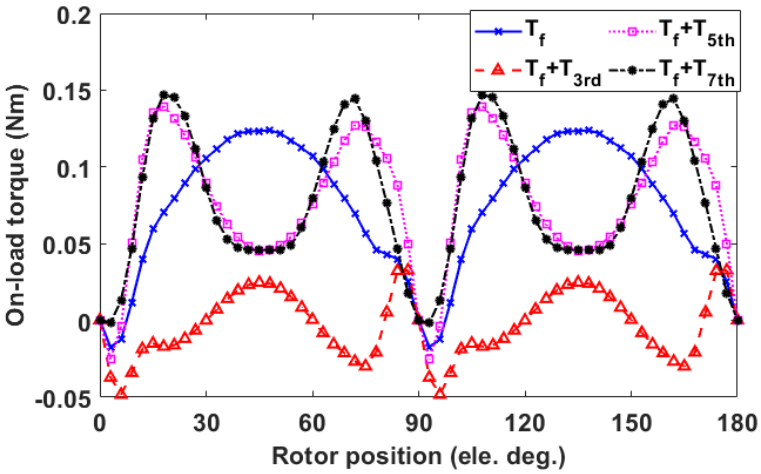

(a)

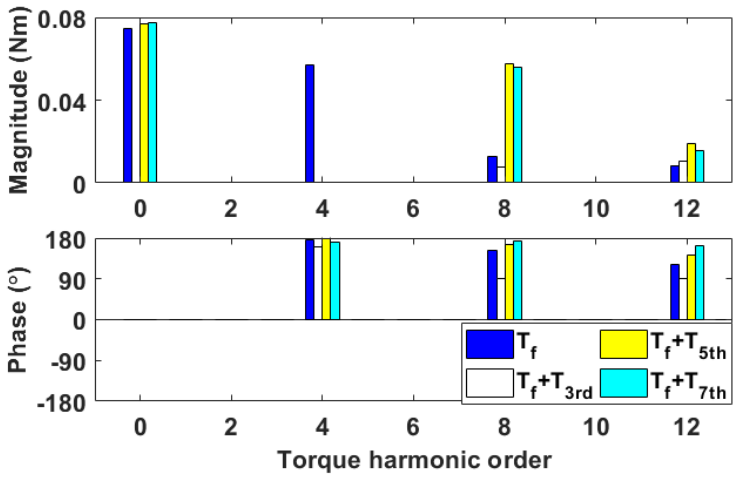

(b)

Fig. 4.29. (a) on-load torque and (b) spectra for single layer 4-phase DS-SRM with predicted current harmonics injected. Phase RMS current is 1A.

In order to find out the reason why the 4-phase machines are not performing well, the torques of a SL 4-phase DS-SRM with the injected current harmonic characterized in TABLE 4.5 are

shown in Fig. 4.29. It can be seen that after the 3rd order current harmonic is injected, the dominant 4th order torque ripple has been entirely suppressed, as expected. However, although this current harmonic injection has little effect on other harmonics such as the 8th and 12th order torque harmonics, the average torque is significantly reduced by 99.7%. This is mainly due to the fact that the 2nd order inductance harmonic (highest magnitude) is an active inductance harmonic ($v \pm 1$) interacting with the 3rd order current harmonic, which significantly reduces the average torque at the selected phase angle. It leads to an extremely high resultant torque ripple coefficient. The 5th and 7th order current harmonics can also suppress the 4th order torque harmonic, but different from the 3rd order current harmonic, the 8th order torque harmonic is significantly increased [see Fig. 4.29 (b)], due to the interaction between current harmonics and the 2nd order inductance harmonic ($|1 \pm v \pm n|$). Therefore, together with the reduction in the average torque, no obvious improvement is observed in the resultant torque ripple. This is similar for the double layer 4-phase DS-SRM, therefore its results have not been shown here to avoid repetition. It is worth noting that due to the nature of inductances for the 4-phase DS-SRMs, their instantaneous torques at some rotor positions, such as 0°, 90° and 180°, etc., are almost 0 and cannot be improved by the proposed methods as shown in Fig. 4.29 (a). Therefore, other methods such as the rotor pole shaping proposed in [10] might be needed to change the inductance profile so as to reduce the torque ripple.

4.7 CONCLUSION

This chapter proposes a general instantaneous torque prediction method for multiphase doubly salient synchronous reluctance machines (DS-SRMs). The torque produced by each inductance harmonic can be accurately predicted under linear condition. With increased magnetic saturation, the accuracy of the analytical prediction might be reduced. Based on the analytical torque equation, it is found that for the DS-SRMs, the torque harmonic frequency only depends on the phase number. Generally, there will be mk^{th} order torque harmonics for multi-phase machine if $\mathrm{mod}(mk, 2) = 0$ is valid, and they are due to the interaction between the fundamental current and the mk^{th}, $(mk \pm 2)^{th}$ order inductance harmonics. However, there is also a special case such as the 12s/10p double layer 6-phase machines which have self- and mutual- 6th order torque harmonics cancelled one another and inherently lead to much lower torque ripple.

Moreover, it is also found that the 2- and 4-phase machines will produce inherently higher torque ripple due to the fact that all the inductance harmonics contribute to torque ripple.

However, for the 5-phase machines, only certain inductance harmonics contribute to torque ripple. Other inductance harmonics, particularly some low order inductance harmonics (n<8), with relatively higher magnitudes, have no influence on torque ripple. As a result, the 5-phase machines generally achieve lower torque ripple than other phase numbers.

When the v^{th} order current harmonic is injected in a multi-phase machine, there will be two active inductance harmonics [$(v \pm 1)^{\text{th}}$] produce extra average torque. Compared with other current harmonic, the 3rd order current harmonic shows the best potential in average torque improvement. This is because the 2nd order inductance harmonic (highest magnitude) is often an active inductance harmonic for average torque production. Moreover, it is also found that the active inductances for torque ripple reduction [$(|mk \pm v \pm 1|)^{\text{th}}$] depends on the phase number *m* and the injected current harmonic order *v*. If the 2nd order inductance harmonic is one of the active inductance harmonics, when the v^{th} order current harmonic is injected, lower current harmonic (magnitude) is required to completely compensate the dominant torque harmonic due to fundamental current. The analytical and numerical results for multi-phase DS-SRMs will be validated by experiments in Chapter 6.

Chapter 5 ANALYSIS OF LOSSES AND DYNAMIC PERFORMANCE WITH CURRENT HARMONIC INJECTION

As investigated in previous chapters, a current harmonic injection method is adopted to improve the average torque and to reduce the torque ripple of DS-SRMs. However, the injected current harmonics will bring extra copper and iron losses. Moreover, the interaction between the inductance harmonics and the injected current harmonics will lead to non-negligible distortion in the phase voltage, which will influence machine's dynamic performance in the flux-weakening region. In order to fully evaluate the effectiveness and efficiency of the proposed harmonic current injection method, comprehensive studies of loss, efficiency and dynamic performance of the DS-SRMs with current harmonic injection will be investigated in this chapter. The analytical torque model in *dq0*-axis has been proposed in this chapter to investigate the dynamic performance such as torque speed curve and efficiency map with current harmonic injections. It has been found that, for the same RMS current, although the 3rd order current harmonic injection will cause extra losses, it can increase the average torque, reduce the torque ripple and slightly increase the efficiency at flux-weakening region. However, although the 5th and 7th order current harmonics can reduce the torque ripple, they also cause significant voltage distortion and lead to deteriorated dynamic performance.

This chapter comes from the author's own papers [151],[152].

5.1 INTRODUCTION

In order to reduce the torque ripple of DS-SRMs, a current harmonic injection methods have been proposed in previous chapters, which can suppress torque ripple and even further increase the average torque. The results showed that by properly selecting harmonic current order, its phase angle and also amplitude, machine average torque can be increased while its torque ripple can be significantly reduced. However, no study about the influence of current harmonic on machine losses (copper and iron) has yet been reported. In order to fill in this gap, this chapter will consider 3 types of 12s/8p DS-SRM with different winding configurations (single/double layer mutually coupled and fully pitched) as examples, to investigate the copper loss, iron losses, mechanical loss and efficiency after current harmonic injection.

Moreover, the interaction between the inductance harmonics and the injected current harmonics will lead to non-negligible distortion in the voltage, which will influence machine's dynamic performance in the flux-weakening region, particularly the efficiency maps of the DS-SRMs. As a result, the investigation of dynamic performance for DS-SRMs with current harmonic injection has been carried out as well. However, Due to the fact that the proposed electromagnetic model in Chapter 2 and Chapter 3 is in *abc*-axis frame, which is inconvenient for analysing the dynamic performance, the model in *dq0*-axis frame needs to be adopted. In the ideal electromagnetic model of synchronous reluctance machines, only the dc and 2nd order harmonics of the self- and mutual-inductances are considered. As a result, the *d*- and *q*-axis equivalents, such as, the *d*- and *q*-axis flux linkages and the electromagnetic torque become constants [153]-[104], which means that the influences of higher order inductance harmonics cannot be fully considered. Although some existing research papers consider the higher order harmonic inductances in the electromagnetic model of synchronous reluctance machines [155]-[156], they often neglect the influence of current harmonics on machine performances. Therefore, in order to account for both the higher order inductance and current harmonics, new electromagnetic models in *d*- and *q*-axis have been proposed in this chapter.

5.2 LOSSES OF 3-PHASE DS-SRMS

In Chapter 3, the comparative studies of three typical types of 3-phase DS-SRMs with current harmonic injection have been carried out. However, the injected current harmonic will leads to the extra loss due to higher frequency, particularly the iron losses. In order to fully investigate the effectiveness of the proposed method, this section will use these three typical DS-SRMs as

examples to investigate the copper, iron loss and overall machine efficiency after injecting the current harmonics. Similar study can be done for multi-phase machines, which will be part of our future works.

5.2.1 COPPER LOSSES

As mentioned in Chapter 4.4, the phase resistances of the DL and SL machines are much smaller than that of the FP machine, due to shorter concentrated winding. Using the same method as in Chapter 4.4, the phase resistances can be calculated, being 0.37Ω, 0.34Ω and 0.54Ω for DL, SL and FP, respectively. Therefore, copper loss can be calculated by $P_{cop} = mI_{rms}{}^2R$, It is worth noting that for a fairer comparison between different current harmonics, the phase rms current before and after injecting the harmonic currents is kept unchanged.

Fig. 5.1 and Fig. 5.2 show the average torque and torque ripple coefficient versus copper losses for foregoing 3-phase DS-SRMs. The same conclusion in Chapter 3 can be made that the 3rd order current harmonic shows the best performance for both the SL and FP 3-phase DS-SRMs. It could minimize the torque ripple and increase the average torque at lower current level (lower copper losses). With increasing phase current, the 3rd order current harmonic can still increase the average torque of the FP machine by 25% but it loses the benefit in torque ripple reduction with selected harmonic angle. Although the 3rd order current harmonic has little effect on the DL machine, the other order current harmonic injection can still be utilized to improve the torque ripple of such machine.

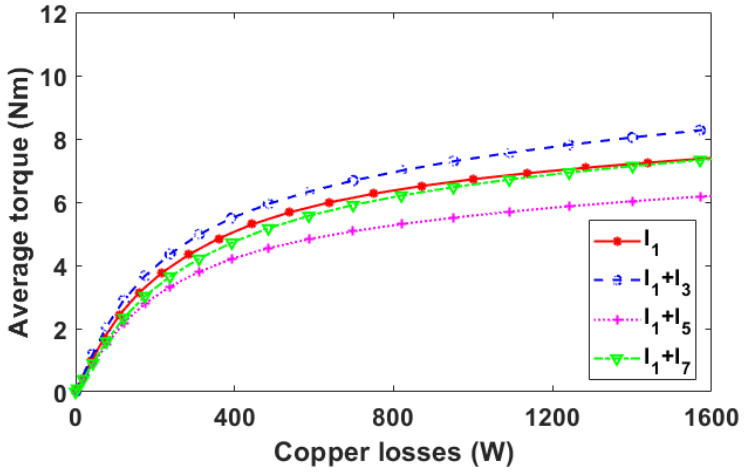

(a) SL

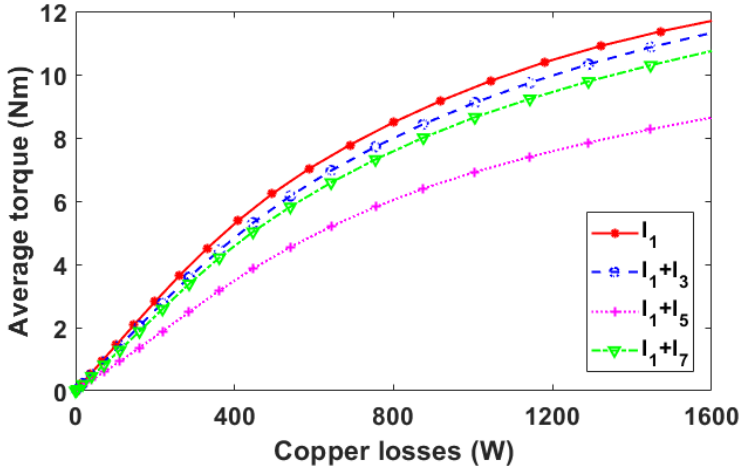

(b) DL

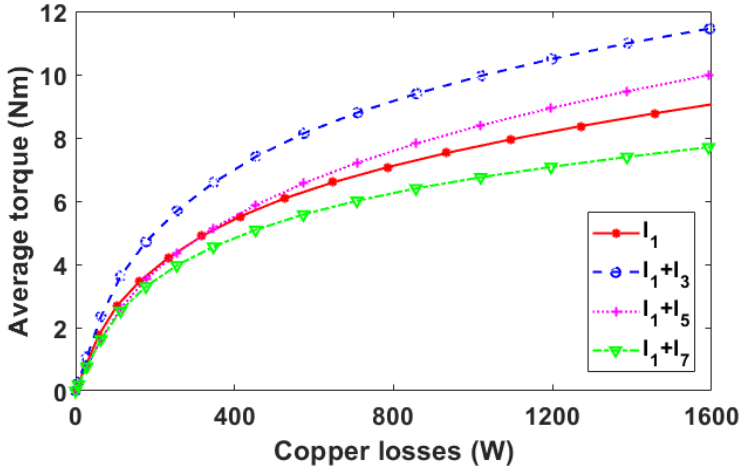

(c) FP

Fig. 5.1. Average torque *vs* copper losses for the 3-phase 12s/8p DS-SRMs with current harmonic injections.

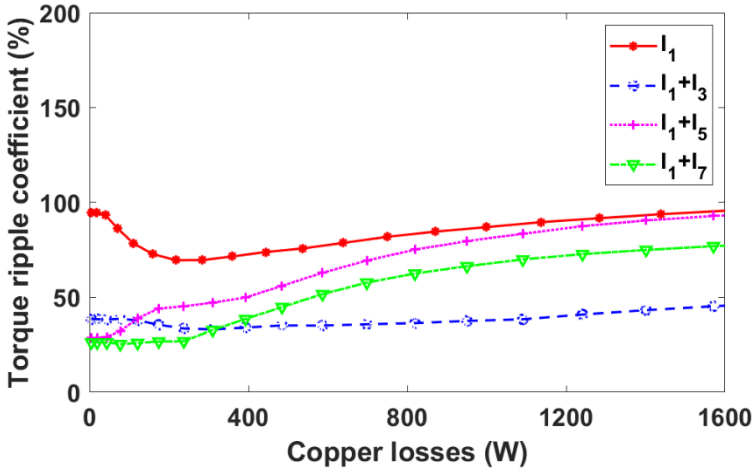

(a) SL

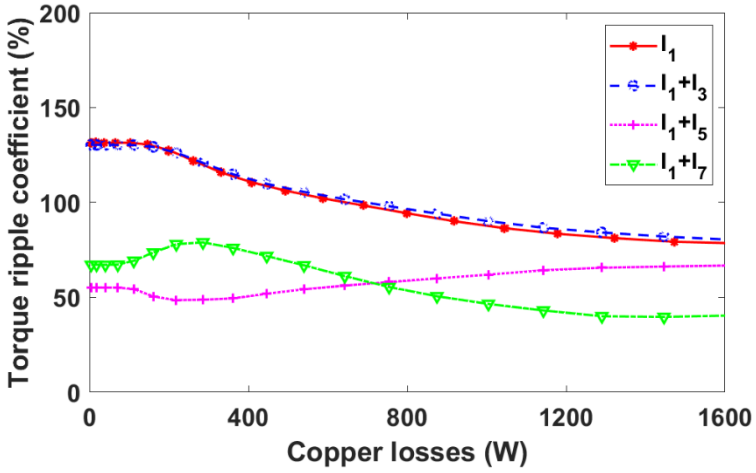

(a) DL

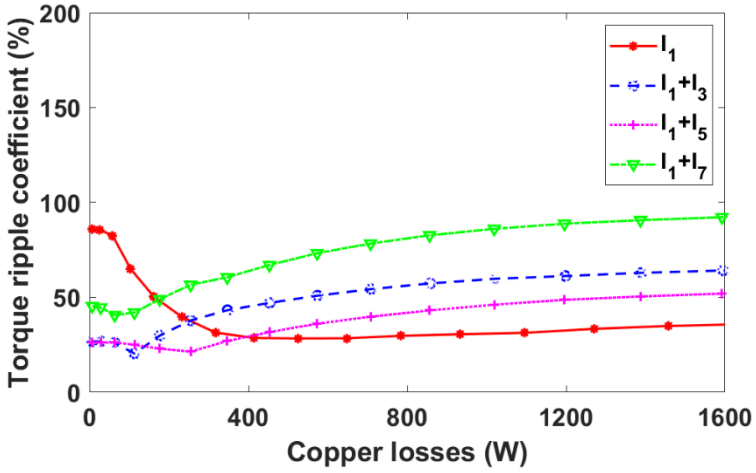

(a) FP

Fig. 5.2. Torque ripple coefficient *vs* copper losses for the 3-phase 12s/8p DS-SRMs with current harmonic injections.

5.2.2 IRON LOSSES

For the machine topologies considered in this section, although the sinewave excitation simplifies the process for estimating iron loss, non-sinusoidal localized flux densities still exist, especially after injecting current harmonics. In order to deal with this problem, the flux densities of each mesh element in the 2D finite element model have been analysed using Fourier Series analysis, and the iron loss density (W/Kg) due to each flux density harmonic can be predicted using (5.1) [157]-[159].

$$P_{Fe} = k_h(f, B_m) f B_m^2 + k_e(f, B_m) f^2 B_m^2 \tag{5.1}$$

where f is the stator or rotor flux-density frequency, B_m is the amplitude of the alternating flux density and k_h and k_e are the hysteresis and eddy current loss coefficients, respectively, which vary with frequency and flux density. The iron losses versus flux density for the investigated machines are shown in Fig. 5.3.

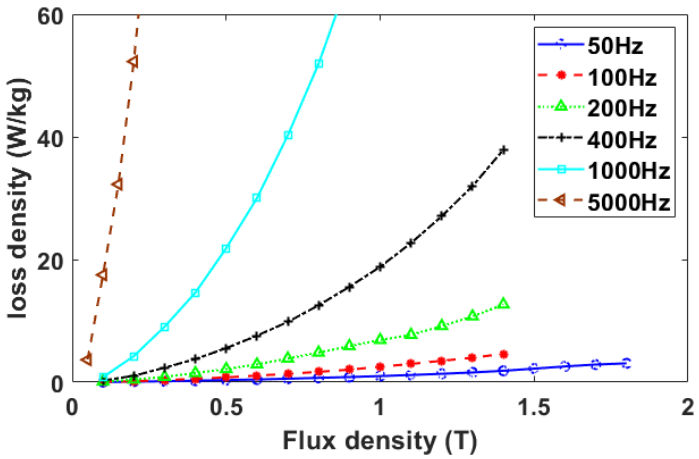

Fig. 5.3 Iron loss curves of investigated machines.

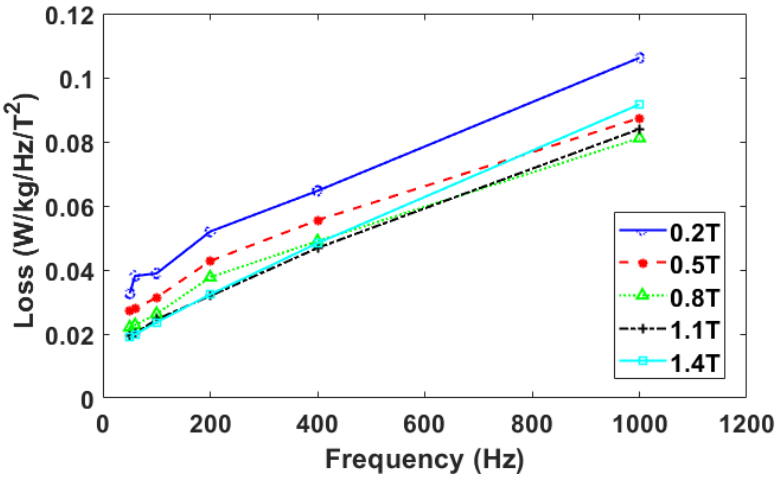

Fig. 5.4 Modified loss curves based on (5.2).

To work out k_h and k_e, (5.1) can be rewritten in the form of (5.2). It is obvious that a linear relationship between loss density and frequency can be achieved and shown in Fig. 5.4. The intersection between the curves and y-axis gives k_h and the slope of the curves indicates the value of k_e. Therefore, the coefficients of iron loss model used in this chapter can be obtained, as shown in Fig. 5.5.

$$\frac{P_{Fe}}{fB_m^2} = k_h(f, B_m) + k_e(f, B_m)f \tag{5.2}$$

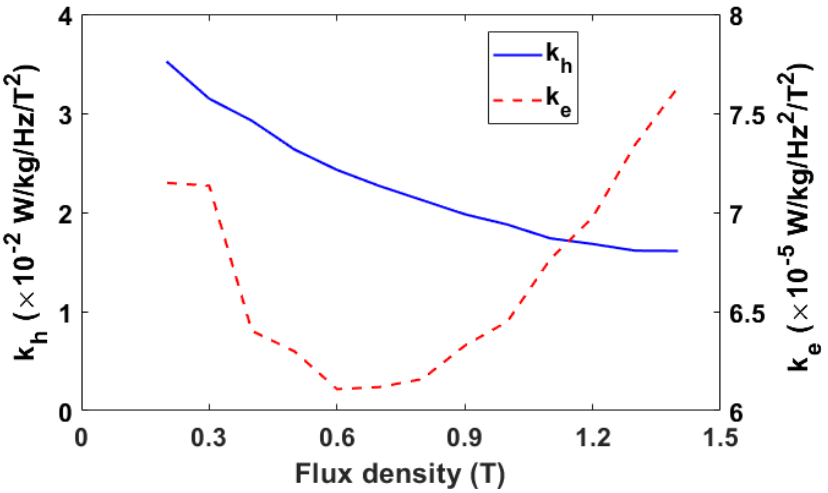

Fig. 5.5 Coefficients (k_h and k_e) of iron loss model of investigated machines.

In order to determine the frequencies of the stator and rotor flux density, a set of flux densities at four typical locations in the stator and rotor have been selected, as shown in Fig. 5.6. Points a and b, at stator tooth and yoke, have the largest flux density variation. This is the same for points c and d at rotor tooth and yoke, respectively. The flux density frequencies for different machine topologies have been given in TABLE 5.1. It is worth noting that the stator flux density frequency f_0 is the same as the fundamental electric frequency and can be calculated by $\frac{\omega p}{60}$, where ω is the rotor mechanical speed and p is the pole-pair number.

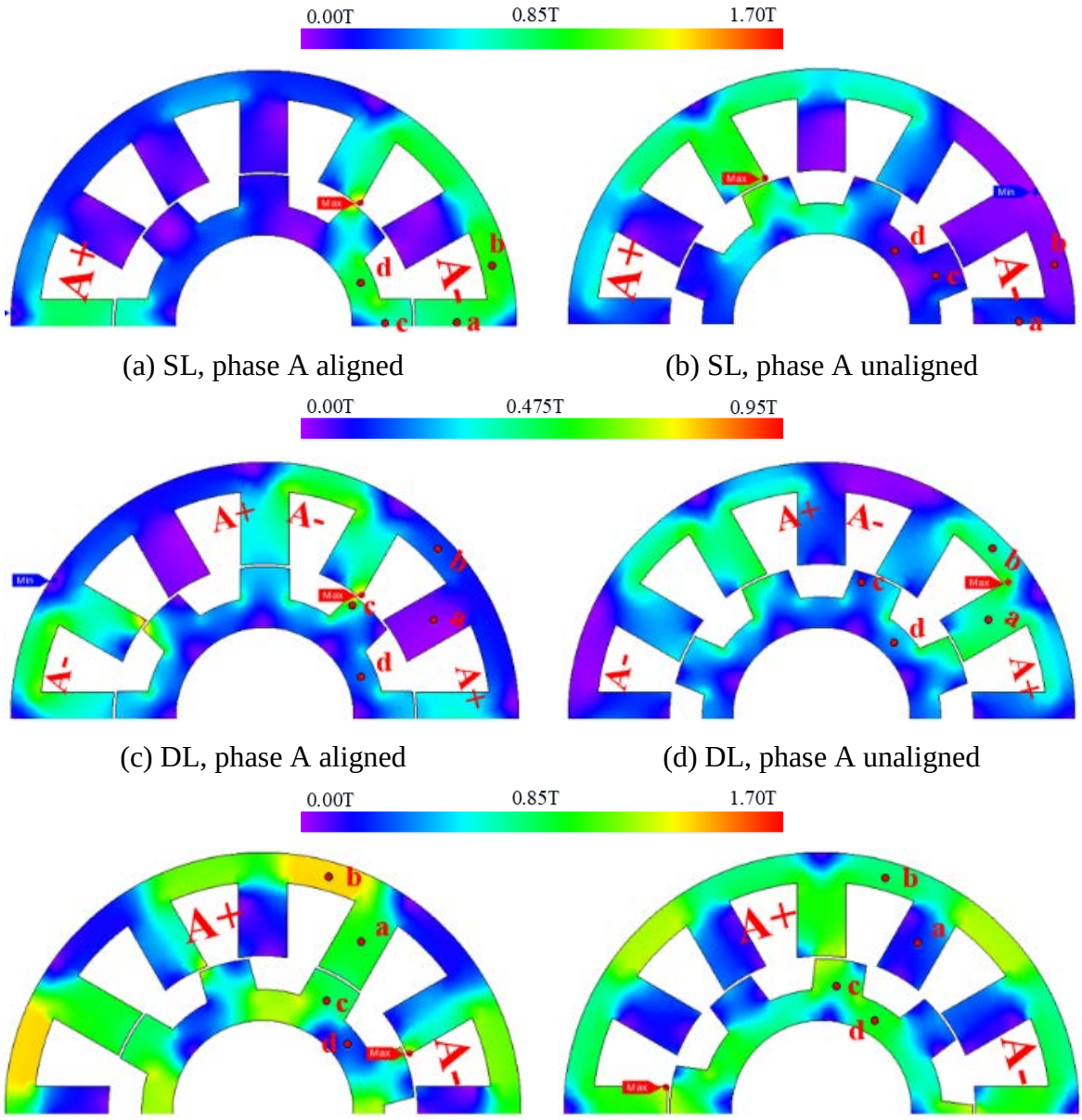

(a) SL, phase A aligned (b) SL, phase A unaligned

(c) DL, phase A aligned (d) DL, phase A unaligned

(e) FP, phase A aligned (f) FP, phase A unaligned

Fig. 5.6 Flux density distributions when machines are supplied by 5Arms 3-phase ac currents.

TABLE 5.1 FLUX DENSITY FREQUENCY

Machine Types	B_r/B_t frequency (Hz)	
	Stator	Rotor
SL	f_0	$1.5f_0$
DL	f_0	$3f_0$
FP	f_0	$1.5f_0$

Note: B_r and B_t are the radial and tangential components of flux density.

After implementing the above iron loss model, and by way of example, the iron losses of investigated machines (in Chapter 3) with different current harmonic injections were calculated at 5 Arms and at 400 rpm. The results are shown in TABLE 5.2. It can be found that for all the machine topologies, the iron losses in the stator are larger than that in the rotor. Moreover, it is also found that the FP machine has much higher iron loss compared with other types of winding configurations. This is mainly due to the fact that although all machines have the same f_0, the FP machine generally has the highest variation of flux density in both radial and tangential directions (B_r and B_t), as shown in Fig. 5.7.

TABLE 5.2 LOSSES OF DS-SRMS AT 5 ARMS, 400 RPM

Machine types	Current	Copper loss (W)	Iron loss (W)		
			Stator	Rotor	Total
SL	i_1	27.75	0.407	0.174	0.581
	$i_1 + i_3$	27.75	0.507	0.201	0.708
	$i_1 + i_5$	27.75	0.528	0.204	0.732
	$i_1 + i_7$	27.75	0.610	0.238	0.848
DL	i_1	25.5	0.167	0.020	0.187
	$i_1 + i_3$	25.5	0.155	0.019	0.174
	$i_1 + i_5$	25.5	0.271	0.054	0.325
	$i_1 + i_7$	25.5	0.320	0.062	0.382
FP	i_1	40.5	0.954	0.467	1.421
	$i_1 + i_3$	40.5	0.915	0.442	1.357
	$i_1 + i_5$	40.5	1.152	0.513	1.665
	$i_1 + i_7$	40.5	1.486	0.660	2.146

It has also been found that the 3rd order current harmonic injection has little effect on the DL machine due to cancelation effect between the self- and mutual-inductances [160]. As a result, the waveforms of flux density with and without the 3rd order harmonic current injection are quite similar [Fig. 5.7 (b)]. It is worth noting that the magnitude of flux density with the 3rd order harmonic current injection is slightly lower than that of the fundamental current supply, which is due to the fact that the phase RMS current has been kept constant. Therefore, the iron losses are slightly reduced after the 3rd order current harmonic injection.

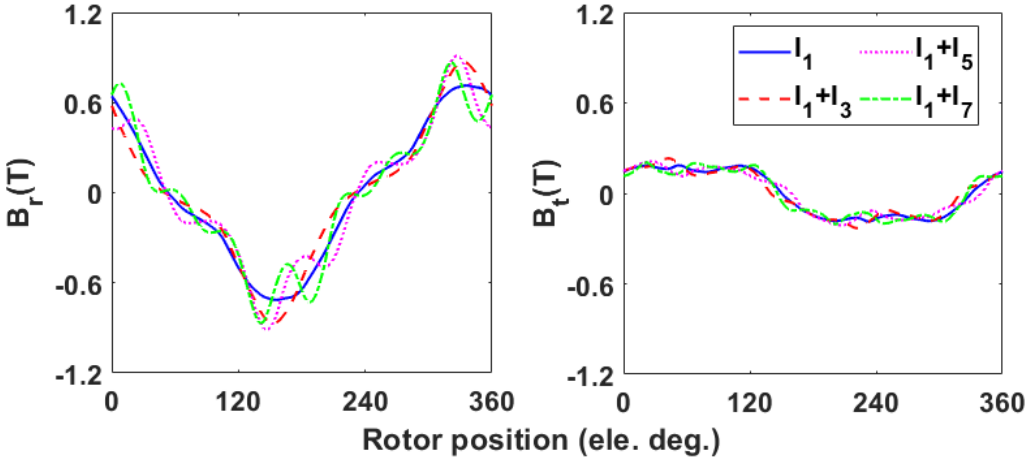

(a) SL

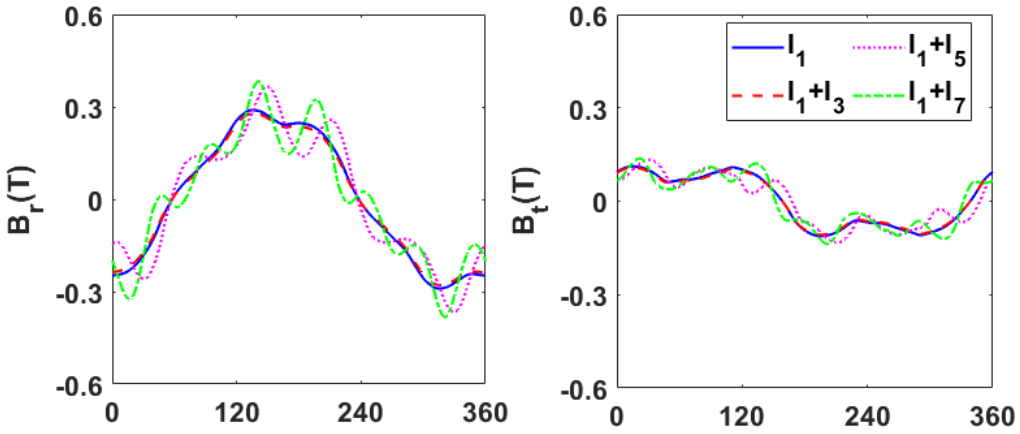

(b) DL

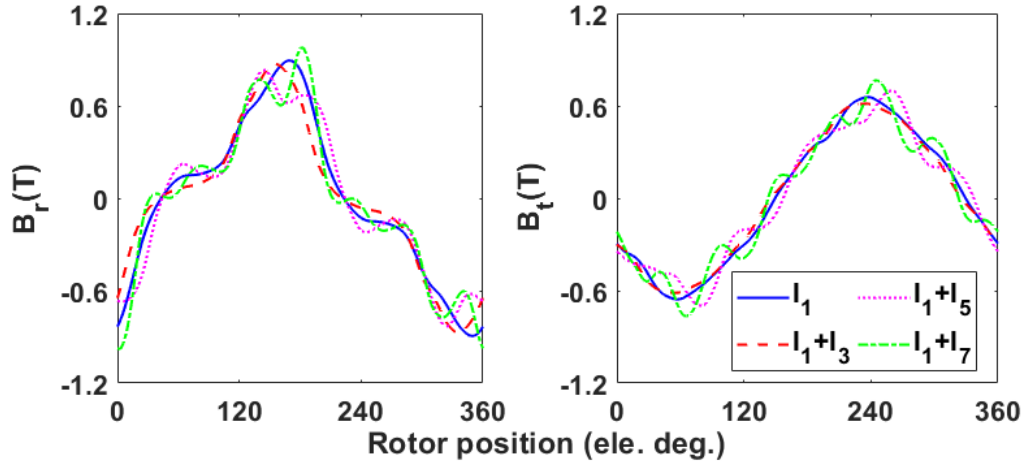

(c) FP

Fig. 5.7 Waveforms of B_r and B_t on the stator (at point b) of the DS-SRMs with current harmonic injections. Phase current is 5 Arms.

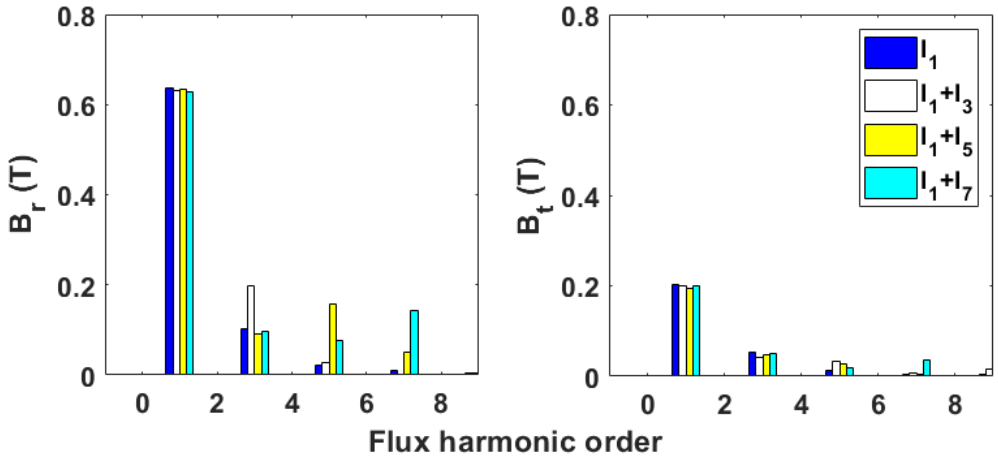

(a) SL

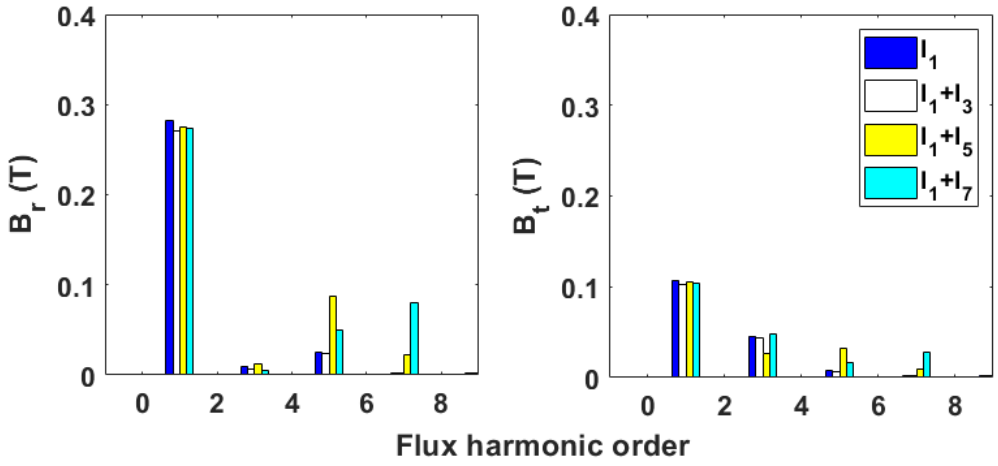

(b) DL

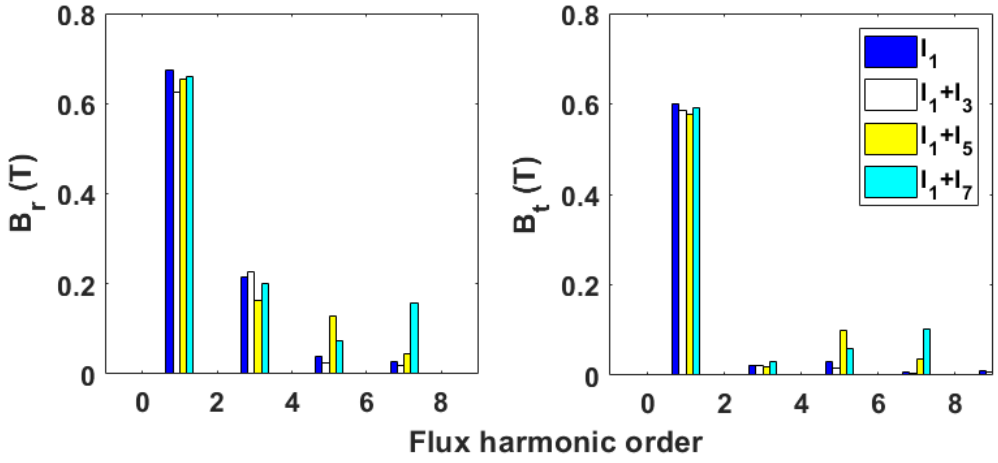

(c) FP

Fig. 5.8 Spectra of B_r and B_t on the stator (at point b) of the DS-SRMs with current harmonic injections. Phase current is 5 Arms.

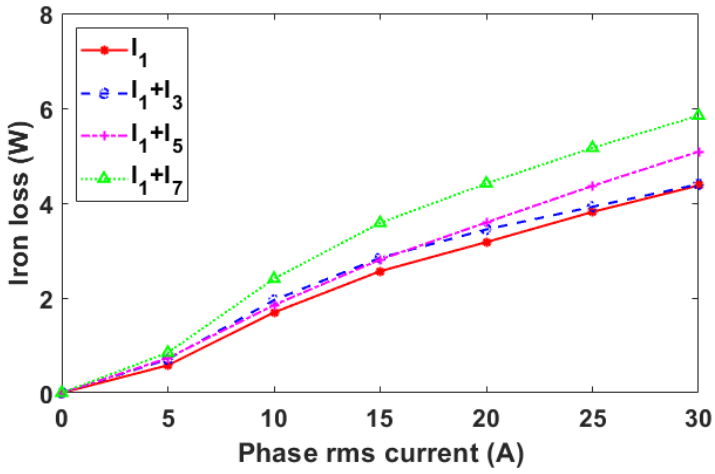

(a) SL

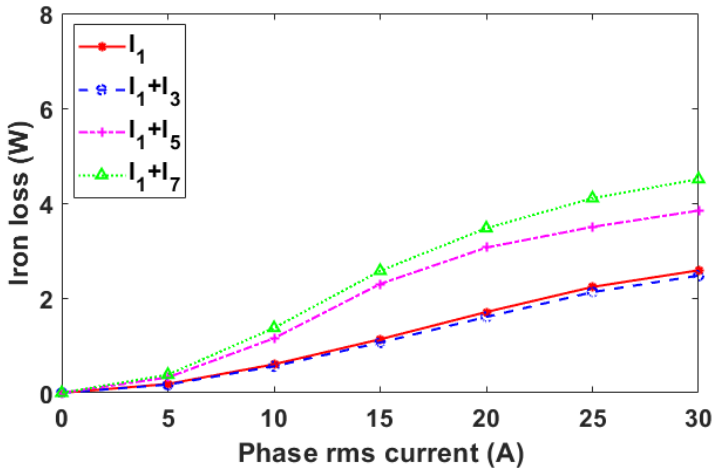

(b) DL

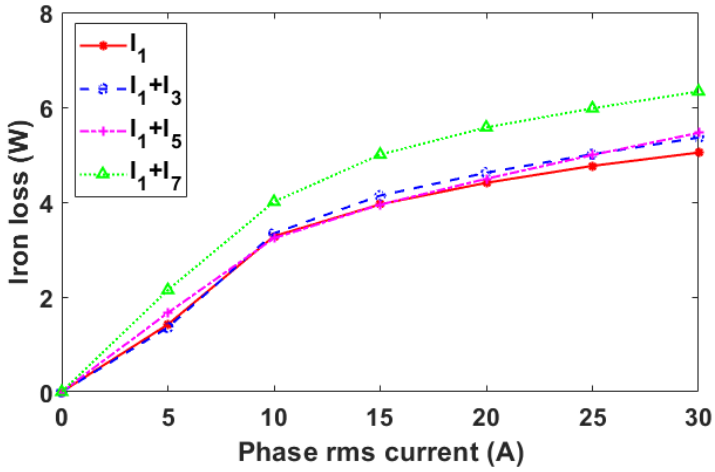

(c) FP

Fig. 5.9 Comparison of iron loss for 3-phase DS-SRMs at constant speed 400rpm with increasing phase rms current.

The spectra of B_r and B_t of the DS-SRMs with current harmonic injections are shown in Fig. 5.8. It can be found that although fundamental flux density is slightly reduced, the high order flux harmonics could be increased by the proposed method. Essentially, the k^{th} order current harmonic injection will increase the k^{th} order flux density harmonic.

Both the current level and current harmonic will influence the flux density of the machines and hence affect the iron loss. Therefore, the comparison of iron loss versus phase rms current has been investigated and the results are shown in Fig. 5.9. As can be seen that the 7^{th} order current harmonic injection always contributes to the highest iron loss for all the machine topologies. However, it is surprising to notice that for both the SL and FP machines, at modest current (<18A), the iron loss with the 3^{rd} order current harmonic injection is larger than that with the 5^{th} order current harmonic injection. In order to investigate this phenomenon, the stator eddy current loss and hysteresis loss at a phase current of 10Arms are shown in Fig. 5.10. Similar trend has been observed for the rotor losses, and therefore they are not shown here to avoid repetition. It has been found that when the machine is operating at this relatively low current level, both eddy current and hysteresis losses due to fundamental flux density are slightly reduced. This is mainly due to fact that the magnitude of fundamental current is reduced with current harmonic injection in order to maintain the same RMS current. However, the k^{th} order current harmonic injection will increase the losses due to the k^{th} order flux density harmonic. In this case, since larger 3^{rd} order current harmonic is injected (Chapter 3), its resultant iron loss could be higher than that with the 5^{th} order current harmonic injection. It is also found in the Fig. 5.9 that, at higher current level, the iron losses with the 3^{rd} order harmonic current injection can be lower than that of the 5^{th} order harmonic current injection. This is mainly due to the different effects of magnetic saturation on the different current harmonic injections. Moreover, for the DL machine, it is not surprising that the iron losses with the 3^{rd} order current harmonic have the same trend as that of fundamental current due to the fact that they have almost the same distribution of flux density, as shown in Fig. 5.7 (b).

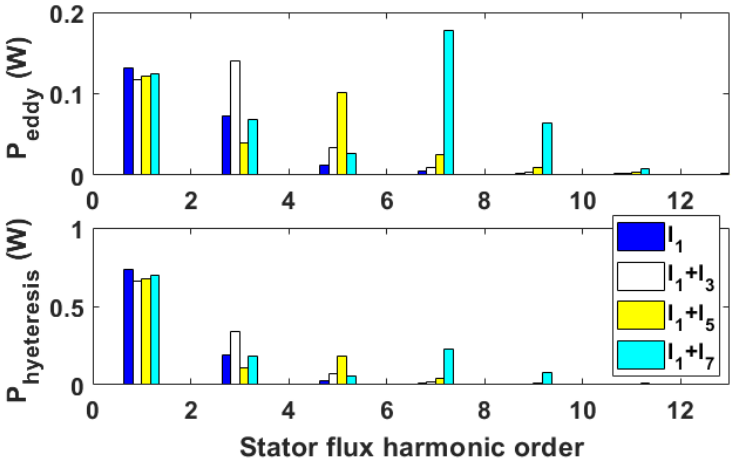

(a) SL

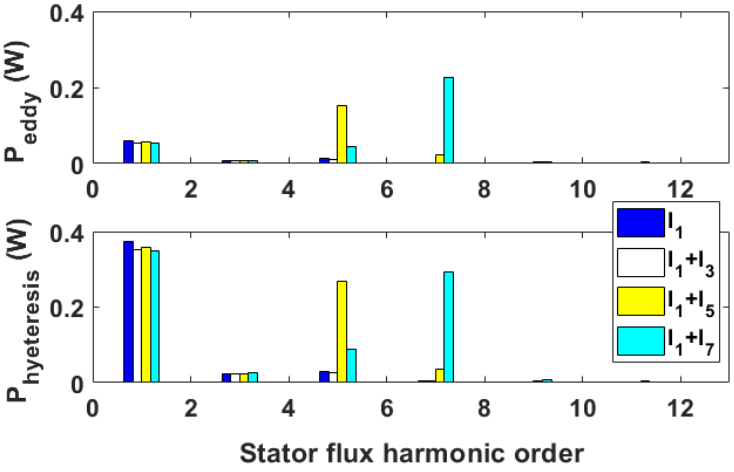

(b) DL

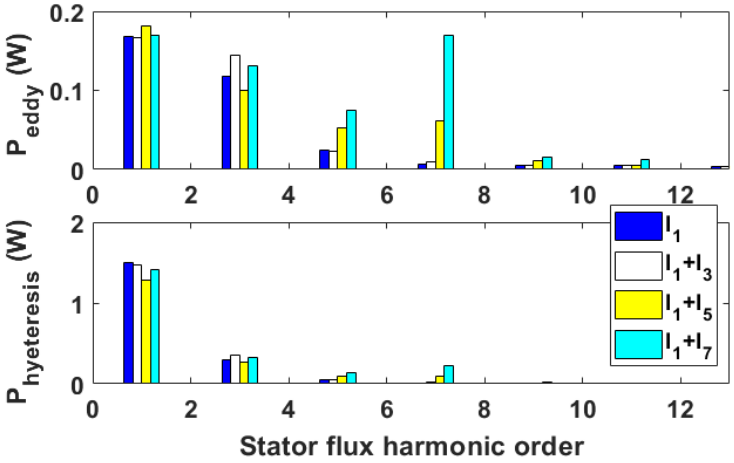

(c) FP

Fig. 5.10 Eddy current losses and hysteresis losses for 3-phase DS-SRMs. Phase current is 10Arms and rotor speed is 400rpm.

Fig. 5.11 shows the iron loss versus phase rms current of different machines with 3rd order current harmonic injection at 400rpm. The FP machine produces the highest iron losses while the DL machine always has the lowest iron loss. Moreover, with increasing phase rms current, the iron losses increase more slowly in FP machine, which can be attributed to the different phenomena in which magnetic saturation comes into play. It is worth noting that the same trend has been observed for other current harmonic injections. For completeness and by way of example, Fig. 5.12 shows the iron losses against the average torque for the SL machine with current harmonic injection. It can be found that the 3rd order current injection again shows the best performance compared with other current harmonics. At the same average torque level, the 3rd order current harmonic injection will produce similar or even lower iron loss than that of the fundamental current.

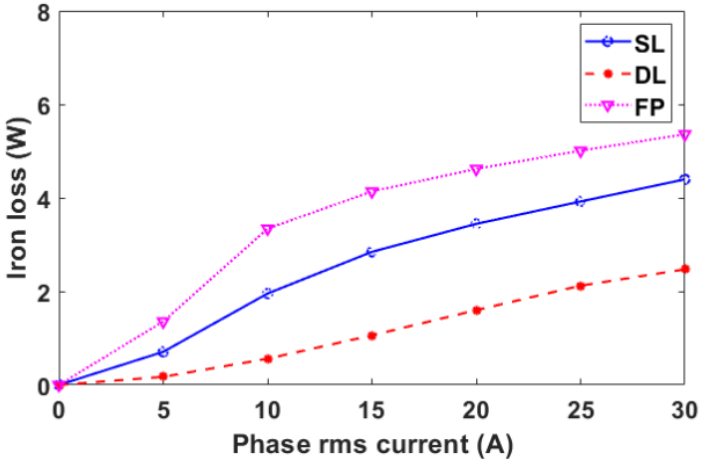

Fig. 5.11 Comparison of iron loss *vs* phase RMS current amongst different machines @ 400rpm with 3rd order current injection.

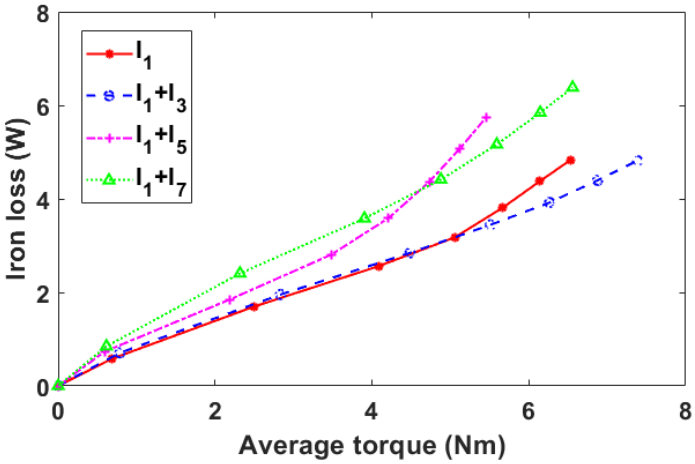

Fig. 5.12 Comparison of iron loss *vs* average torque @ 400 rpm with current harmonic injection for SL DS-SRMs.

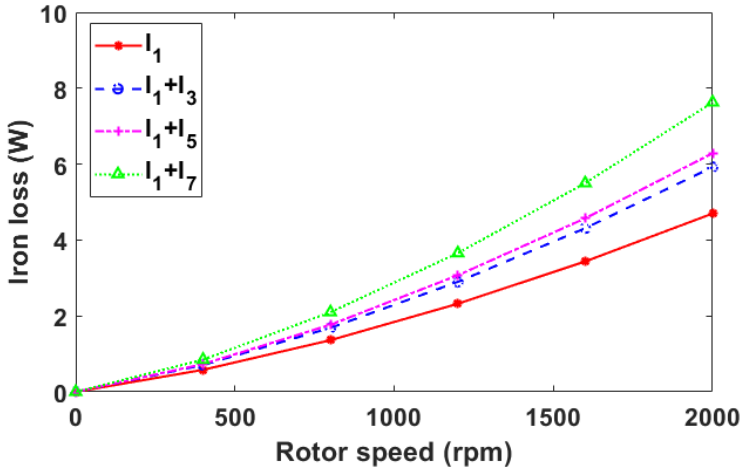

(a) SL

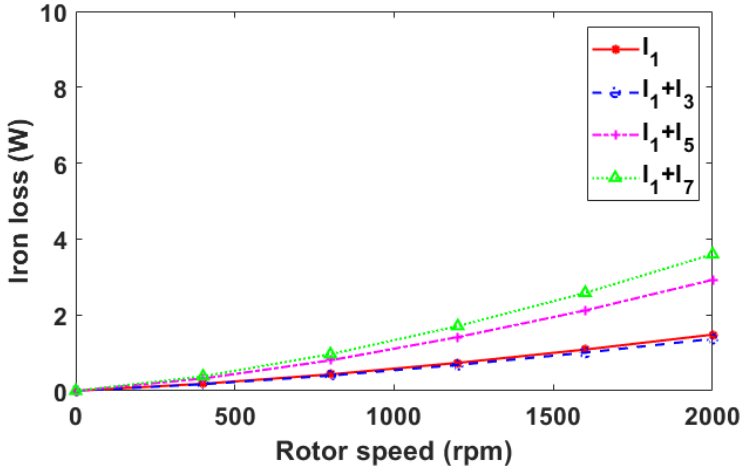

(b) DL

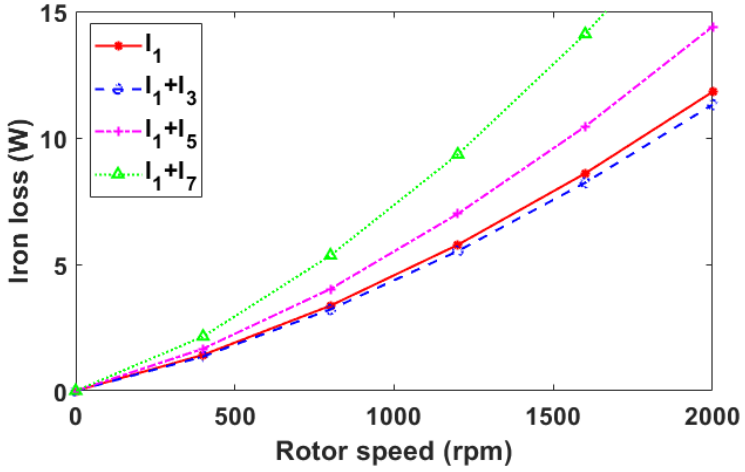

(c) FP

Fig. 5.13 Comparison of iron loss for 3-phase DS-SRMs at constant current 5Arms with increasing rotor speed.

Fig. 5.13 shows the iron loss for DS-SRMs at 5Arms current with increasing rotor speed. It is found that at 5Arms current, all the machines with the 7th order current harmonic injection will produce the highest iron loss for the full speed range. And the iron loss of the FP DS-SRMs with such current level is the highest as shown in Fig. 5.14. As can be expected, these relatively small machines operating at modest speeds, the absolute levels of iron losses in all the machine topologies with current harmonic injection are much smaller than the copper losses shown previously in TABLE 5.2. However, the relative magnitudes of the iron losses provide valuable, reasonable and scalable indicator for the relative performance in the different topologies with different current harmonic injections.

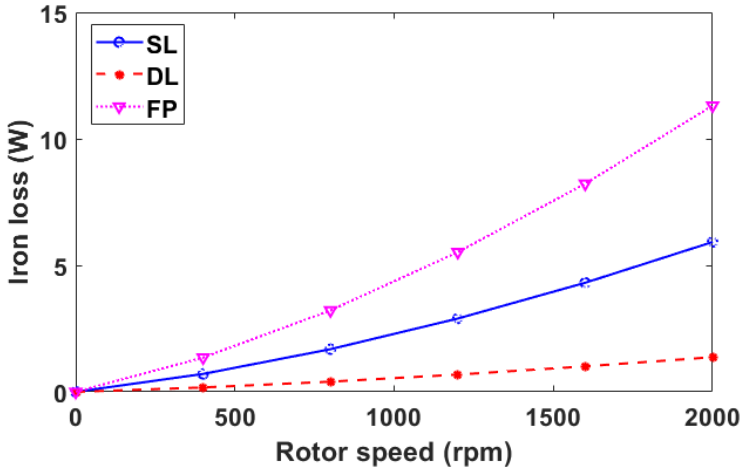

Fig. 5.14 Comparison of iron loss *vs* rotor speed amongst different machines with 3rd order current injection. Phase rms current is 5Arms.

5.2.3 EFFICIENCY

The machine efficiency can be calculated based on the output power and the machine losses as:

$$\eta = \frac{P_{out}}{P_{out} + P_{cop} + P_{Fe} + P_{mec}} \tag{5.3}$$

where P_{out} is the output power ($P_{out} = T_e \omega_m$) and P_{mec} represents the mechanical loss due to aerodynamic windage and bearing fraction. It has been calculated to be 2.64 W at 400 rpm for all the machines using the method introduced in [161]. Fig. 5.15 shows the average torque and efficiency versus total losses (copper loss + iron losses + mechanical loss) with current harmonic injections at a rotor speed of 400 rpm. Only the 3rd order current harmonic results have been given as example, since other harmonic current injections give the same trend for all

types of machines. It has been found that at low phase current region (low copper losses), the FP and SL machines have higher efficiency compared with the DL machine due to their higher output power. However, when the phase current increases (higher copper losses), the average torque of the DL machine exceeds that of the other two machines due to the fact that they are more sensitive to magnetic saturation.

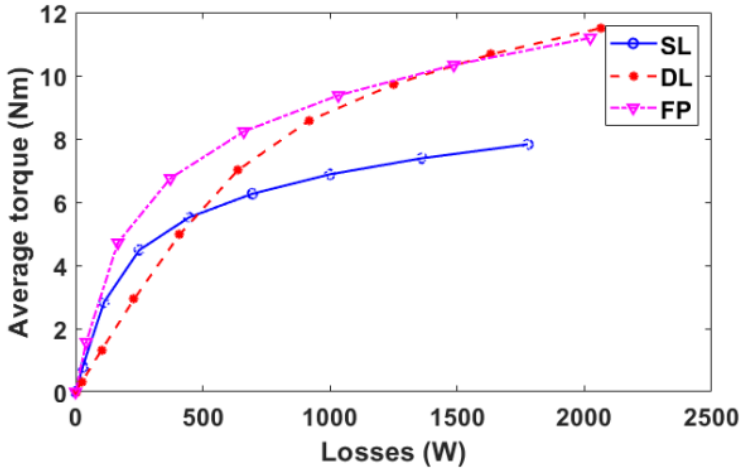

(a) Average torque *vs* total loss

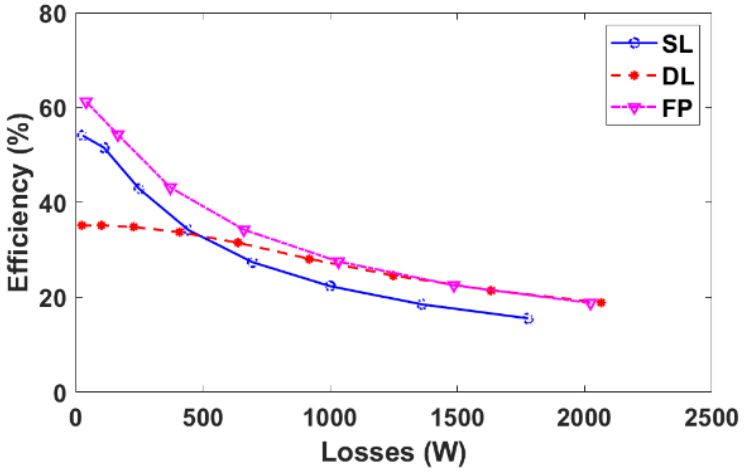

(b) Efficiency *vs* total losses

Fig. 5.15 Comparison of results for 3-phase DS-SRMs @ 400 rpm with 3rd order current injection.

TABLE 5.3 lists the efficiency results for all the machines before and after injecting harmonic current at 5Arms and 400rpm. The relatively low efficiency is mainly due to low speed and high copper losses. It is worth noting that for the relatively small size machines used in this thesis, the copper loss plays a dominant role in the machine losses therefore largely dominates the machine efficiency.

TABLE 5.3 EFFICIENCY OF DS-SRMS AT 5ARMS AND 400RPM

Machine types	Current	Output power (W)	Efficiency (%)
SL	i_1	28.7	50.3
	$i_1 + i_3$	33.0	53.7
	$i_1 + i_5$	24.7	46.5
	$i_1 + i_7$	25.8	47.4
DL	i_1	15.0	36.9
	$i_1 + i_3$	13.8	35.0
	$i_1 + i_5$	9.1	26.0
	$i_1 + i_7$	12.6	32.8
FP	i_1	54.2	56.4
	$i_1 + i_3$	65.9	61.2
	$i_1 + i_5$	48.7	53.6
	$i_1 + i_7$	48.6	53.3

For completeness, Fig. 5.16 shows the efficiency versus rotor speed at phase current of 5Arms. Generally, the DL machine has lower efficiency compared with the SL and FP machines. However, in terms of increasing rate of the efficiency, the DL machine has the best performance. By way of example, with only 3rd order current harmonic injection (see Fig. 5.17), the efficiency of the DL machine has increased by 100% (from 400 rpm to 2000 rpm) while for the SL and FP machines, it is only 66% and 49%, respectively. It is also found that except the DL machine, the 3rd order current harmonic injection can slightly increase the efficiency of the SL and FP machines by around 3-5%.

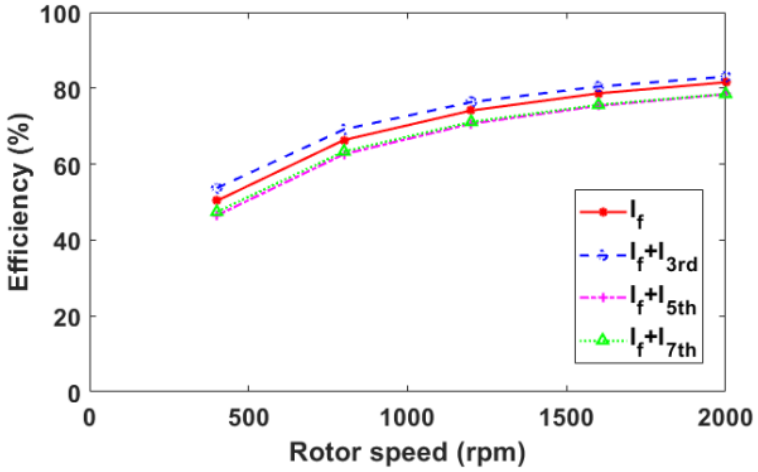

(a) SL

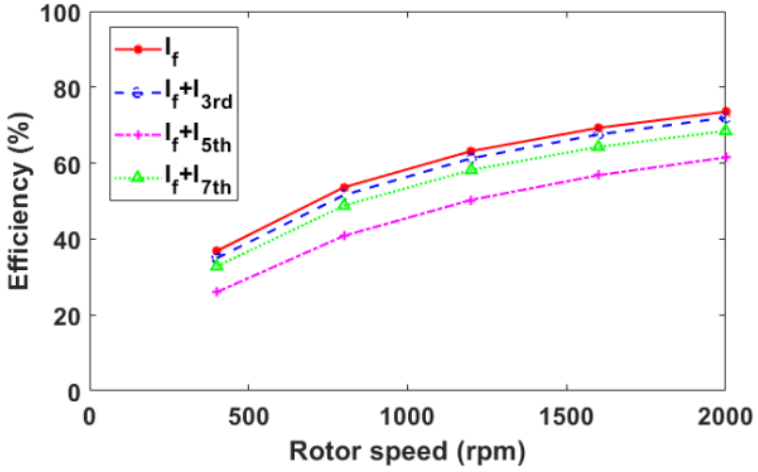

(b) DL

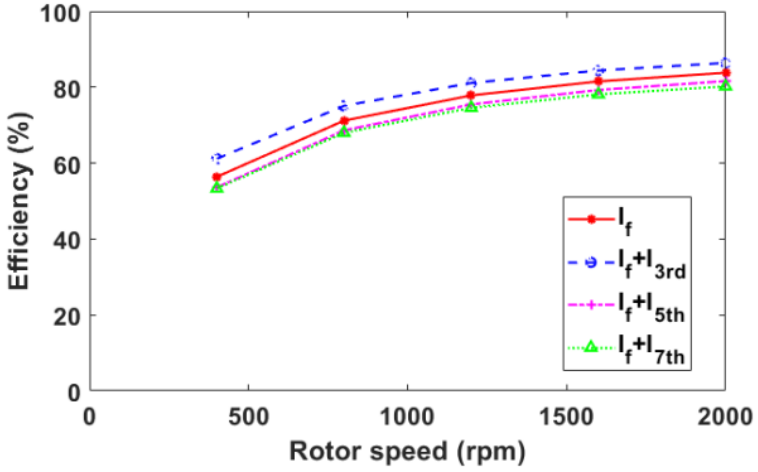

(c) FP

Fig. 5.16 Comparison of efficiency at phase current of 5Arms for DS-SRMs.

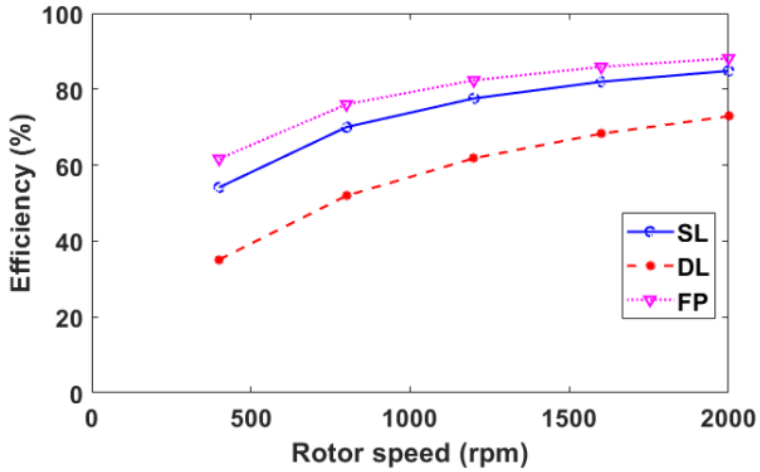

Fig. 5.17 Comparison of efficiency at phase current of 5Arms with 3rd order current harmonic injection.

Fig. 5.18 shows the efficiency versus phase rms current of DS-SRMs with current harmonic injection. It is found that the 5th and 7th order current harmonic injections will always reduce the efficiency at low phase current, due to lower output power and higher iron losses. However, with increasing phase current, the 5th and 7th order current harmonic injections may increase the efficiency of the DS-SRMs (7th for SL machine and 5th for FP machine). This is mainly due to the different effects of magnetic saturation on the different current harmonic injections, and the average torque might be increased by selected current harmonic. Moreover, it has also been found that the DL machine shows the highest efficiency when the phase current is larger than 20Arms as shown in Fig. 5.19, due to fact that the DL machine is less sensitive to magnetic saturation compared with the SL and FP counterparts.

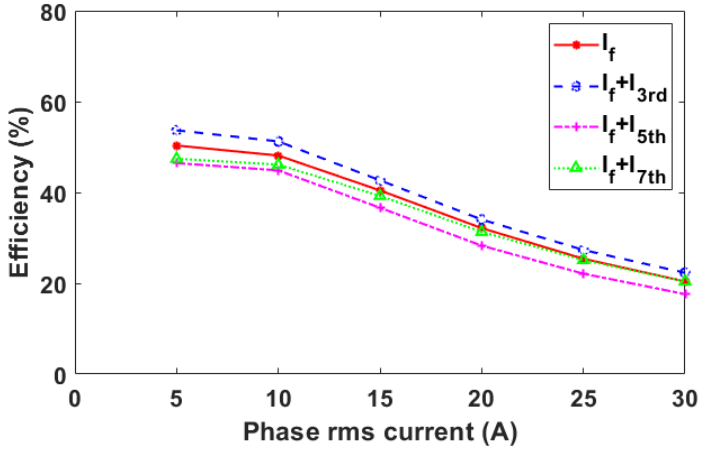

(a) SL

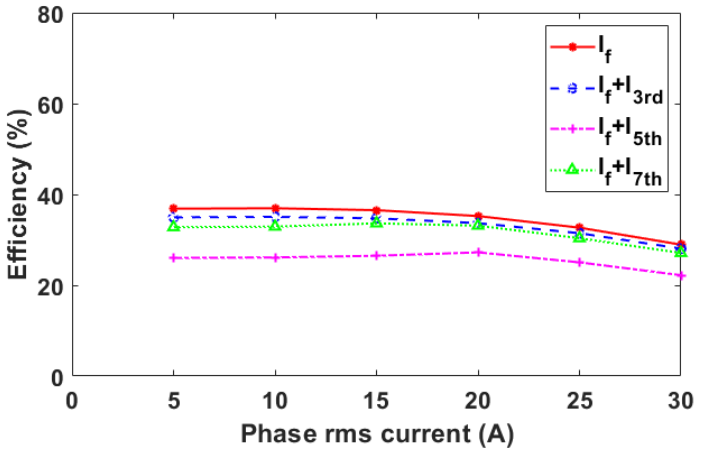

(b) DL

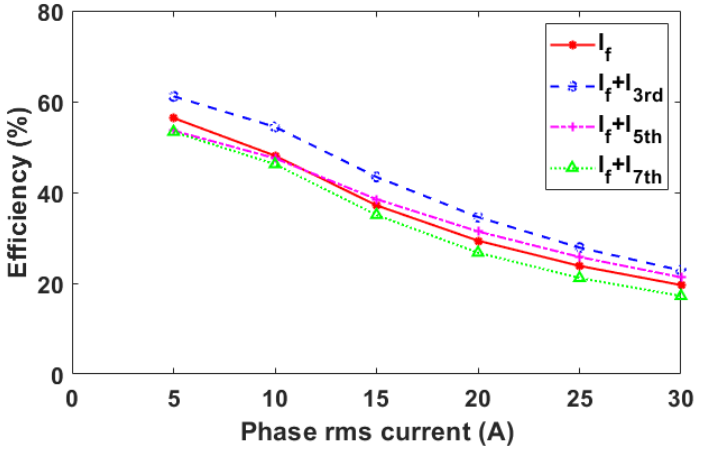

(c) FP

Fig. 5.18 Comparison of efficiency *vs* phase RMS current for DS-SRMs @ 400 rpm with current harmonic injection.

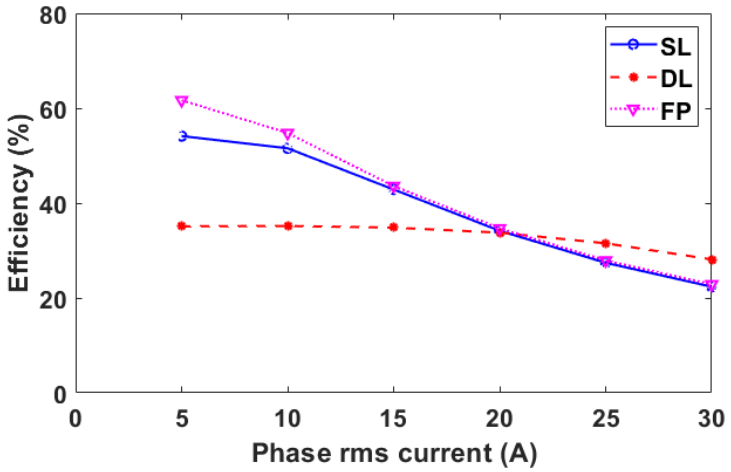

Fig. 5.19 Comparison of efficiency *vs* phase RMS current @ 400rpm with the 3rd order current harmonic injection.

5.3 Dynamic Performance with Current Harmonic Injection

Apart from losses, this chapter also investigates dynamic performances, such as, torque-speed curve and efficiency map, of 3-phase DS-SRMs with current harmonic injection. The interaction between the inductance harmonics and the injected current harmonics will lead to non-negligible distortion in the voltage, which will influence machine's dynamic performance in the flux-weakening region. In order to fully consider the effect of current harmonics on the dynamic performance, 2D-FE are often regarded as effective and straightforward tools. However, they are more time consuming. Therefore, in order to reduce modelling complexity, a new electromagnetic models in *dq*-axis, account for both the higher order inductance and current harmonics, have been proposed in this section.

5.3.1 Detailed Analytical Model of DS-SRMs in *dq0*-axis

General dynamic equation for a synchronous reluctance machine in the *abc*-axis frame given by (5.4) can also be employed for the DS-SRMs in this thesis [156].

$$[v]_{abc} = R[i]_{abc} + \frac{d[\psi]_{abc}}{dt} \tag{5.4}$$

$$[v]_{abc} = [L_s][i]_{abc} \tag{5.5}$$

where $[v]_{abc}$, $[i]_{abc}$ and $[\psi]_{abc}$ are stator voltages, currents and flux linkages, respectively. R and $[L_s]$ represent the stator resistance and 3-phase inductance matrix, respectively.

$$L_s = \begin{bmatrix} L_{aa} & M_{ab} & M_{ac} \\ M_{ba} & L_{bb} & M_{bc} \\ M_{ca} & M_{cb} & L_{cc} \end{bmatrix} \tag{5.6}$$

where *L* and *M* are the self- and mutual-inductances, respectively.

5.3.1.1 IDEAL ELECTROMAGNETIC MODEL

Generally, in an ideal synchronous machine, the spatial stator winding function distribution is assumed to be sinusoidal, leading to the fact that the self- and mutual-inductances only contain the dc component and the 2nd order harmonic component as shown as (5.7) and (5.8). As a result, the ideal torque model can only be used to derive the expression for average torque, while the torque ripple cannot be predicted.

$$L_{xx}(\theta_e) = L_{s0} + L_2\cos\big(2(\theta_e + \theta_{xx})\big) \tag{5.7}$$

$$M_{xy}(\theta_e) = M_{s0} + M_2\cos(2(\theta_e + \theta_{xy})) \tag{5.8}$$

where *x* and *y* indicate the phases a, b and c. L_{s0} and L_2 are the dc component and the magnitude of 2nd order harmonic self-inductance, while M_{s0} and M_2 are the dc component and the magnitude of the 2nd order harmonic mutual-inductance. θ_{xx} is the phase shift angle between three phases. For the investigated machines, it is equal to 0°, $-120°$ and $120°$, for phase a, b and c, respectively. However, θ_{xy} is equal to $120°$, 0° and $-120°$, between phases a and b, b and c and c and a, respectively.

After implementing the Park transformation (5.11) for (5.4)-(5.8), the ideal *dq0*-axis model can be derived as

$$\begin{bmatrix} v_d \\ v_q \\ v_0 \end{bmatrix} = R\begin{bmatrix} i_d \\ i_q \\ i_0 \end{bmatrix} + \begin{bmatrix} 0 & -\omega & 0 \\ \omega & 0 & 0 \\ 0 & 0 & 0 \end{bmatrix}\begin{bmatrix} \psi_d \\ \psi_q \\ \psi_0 \end{bmatrix} + \frac{d}{dt}\begin{bmatrix} \psi_d \\ \psi_q \\ \psi_0 \end{bmatrix} \tag{5.9}$$

The flux linkage in *dq0*-axis are given by:

$$\begin{bmatrix} \psi_d \\ \psi_q \\ \psi_0 \end{bmatrix} = L_{dq0}\begin{bmatrix} i_d \\ i_q \\ i_0 \end{bmatrix} \tag{5.10}$$

The L_{dq0} are calculated by $P^{-1}L_sP$, (where *P* is Park transformation matrix) and given by:

$$P = \begin{bmatrix} \cos\theta_e & -\sin\theta_e & 1 \\ \cos(\theta_e - 120°) & -\sin(\theta_e - 120°) & 1 \\ \cos(\theta_e + 120°) & -\sin(\theta_e + 120°) & 1 \end{bmatrix} \tag{5.11}$$

$$L_{dq0} = \begin{bmatrix} L_d & 0 & L_{0d} \\ 0 & L_q & L_{0q} \\ L_{d0} & L_{q0} & L_0 \end{bmatrix} \tag{5.12}$$

where

$$L_d = L_{s0} - M_{s0} + 0.5(L_2 + 2M_2) \tag{5.13}$$

$$L_q = L_{s0} - M_{s0} - 0.5(L_2 + 2M_2) \tag{5.14}$$

$$L_0 = L_{s0} + 2M_{s0} \tag{5.15}$$

$$L_{d0} = 0.5L_{0d} = 0.5(L_2 - M_2)\cos(3\theta_e) \tag{5.16}$$

$$L_{q0} = 0.5L_{0q} = -0.5(L_2 - M_2)\sin(3\theta_e) \tag{5.17}$$

For a balanced 3-phase system, there is no zero-sequence current. Therefore, only the contribution from *dq*-axis component is needed and the ideal electromagnetic torque for a DS-SRM is given by:

$$T_e = \frac{3}{2}p(L_d - L_q)i_d i_q \tag{5.18}$$

5.3.1.2 TORQUE DUE TO FUNDAMENTAL CURRENT

The DS-SRMs can be expressed by general dynamic voltage (5.4)-(5.6). The non-sinusoidal spatial MMF distribution causes the self- and mutual-inductances (neglecting the dc component) to be non-sinusoidal as well. In order to predict the torque contribution more accurately, the self- and mutual-inductances in (5.6) are rewritten as:

$$\begin{cases} L_{xx}(\theta_e) = L_{s0} + \sum_{n=2,4,6,\ldots}^{\infty} L_n \cos(n(\theta_e + \theta_{xx})) \\ M_{xy}(\theta_e) = M_{s0} + \sum_{n=2,4,6,\ldots}^{\infty} M_n \cos(n(\theta_e + \theta_{xy})) \end{cases} \tag{5.19}$$

where *x* and *y* indicate the phases a, b and c. L_{s0} and L_n are the dc component and the magnitude of the n^{th} order self-inductance harmonic, while M_{s0} and M_2 are the dc component and the magnitude of the n^{th} order mutual-inductance harmonic.

Transforming the inductance matrix in *abc*-axis such as (5.6) and (5.19) into *dq0*-axis yields:

$$L_{dq0} = \begin{bmatrix} L_d & L_{qd} & L_{0d} \\ L_{dq} & L_q & L_{0q} \\ L_{d0} & L_{q0} & L_0 \end{bmatrix} \tag{5.20}$$

The same method for calculating L_{dq0} as detailed in [156] has been adopted in this chapter. It is worth noting that the *dq0*-axis self-inductances, i.e. L_d, L_q and L_0, contain non-zero dc components and superimpose with the spatial harmonic components with order 6*k*, *k* = 1, 2, 3… However, the *dq0*-axis mutual-inductances do not have dc component and only contain harmonic components. For example, the harmonic orders are 6*k*, with *k* = 1, 2, 3… for L_{qd}, and 3*k* with *k* = 1, 3, 5… for L_{d0} and L_{q0}. Fig. 5.20 shows the waveform of *dq0*-axis self- and mutual-inductances. To simplify the analyses, the magnitude of the nth order inductance harmonic will be written as $L_{xx,n}$ in the following sections. For example, $L_{d,dc}$ represents the dc component of L_d, $L_{d,6}$ represents the magnitude of the 6th order L_d harmonic, etc.

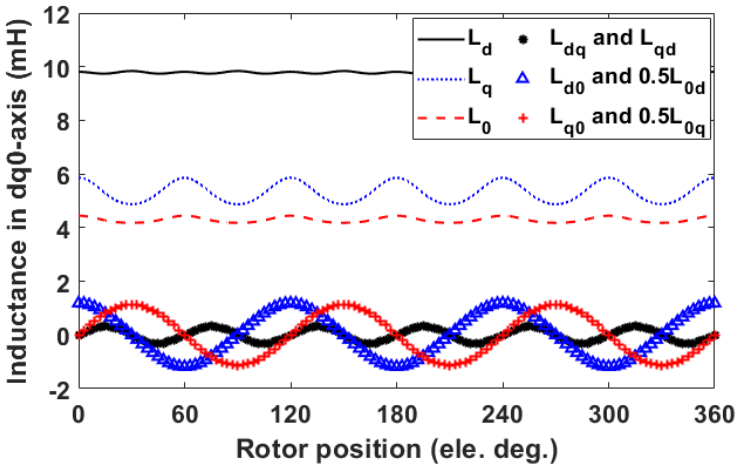

Fig. 5.20. *dq0*-axis inductances *vs* rotor position for the 3-phase 12s/8p SL DS-SRM.

The instantaneous power in the *dq0*-axis frame can be calculated as:

$$P_{in} = [v_a \quad v_b \quad v_c]\begin{bmatrix} i_a \\ i_b \\ i_c \end{bmatrix} = \left(P^{-1}\begin{bmatrix} v_d \\ v_q \\ v_0 \end{bmatrix}\right)^{-1} P\begin{bmatrix} i_d \\ i_q \\ i_0 \end{bmatrix} = \frac{3}{2}\left(v_d i_d + v_q i_q + 2v_0 i_0\right) \tag{5.21}$$

Therefore, the instantaneous torque T_e can be determined from the instantaneous power as:

$$\omega_m T_e = P_{in} - P_{cop} - \frac{dW_m}{dt} \tag{5.22}$$

where ω_m is the mechanical speed, P_{cop} represents the resistive loss. W_m is the stored energy in the machine, which can be calculated by flux-current map, and for the linear case, the stored magnetic energy can be calculated by [96]

$$W_m = \frac{1}{2}\sum_{i=a,b,c}\psi_i i_i = \frac{3}{2}\times\frac{1}{2}(\psi_d i_d + \psi_q i_q + 2\psi_0 i_0) \tag{5.23}$$

Substituting (5.9), (5.21) and (5.23) into (5.22), yields:

$$T_e = \frac{3}{2}p\left(\psi_d i_q - \psi_q i_d + \frac{1}{2}i_d\frac{d\psi_d}{d\theta_e} + \frac{1}{2}i_q\frac{d\psi_q}{d\theta_e} + i_0\frac{d\psi_0}{d\theta_e} - \frac{1}{2}\psi_d\frac{di_d}{d\theta_e} - \frac{1}{2}\psi_q\frac{di_q}{d\theta_e} - \psi_0\frac{di_0}{d\theta_e}\right) \tag{5.24}$$

Without considering the current harmonics in *abc*-axis, *dq*-axis currents will be constant as can be calculated by (5.25), and only the first four terms on right hand side of (5.24) will produce average torque and torque ripple.

$$\begin{bmatrix} i_d \\ i_q \\ i_0 \end{bmatrix} = \begin{bmatrix} I_{d,dc} \\ I_{q,dc} \\ 0 \end{bmatrix} \tag{5.25}$$

Therefore, the instantaneous torque due to fundamental current can be obtained:

$$T_f = T_{f,dc} + T_{f,rip} \tag{5.26}$$

In (5.26), the average torque $T_{f,dc}$ and torque ripple $T_{f,rip}$ can be calculated as:

$$T_{f,dc} = \frac{3}{2}p(L_{d,dc} - L_{q,dc})I_{d,dc}I_{q,dc} \tag{5.27}$$

and

$$\begin{aligned} T_{f,rip} = \frac{3}{2}p\Bigg\{ & \sum_{n=6,12,18,\dots}\left(L_{d,n} - L_{q,n} + nL_{dq,n}\right)I_{d,dc}I_{q,dc}\cos(n\theta_e) \\ & - \sum_{n=6,12,18,\dots}\frac{n}{2}(L_{d,n}I_{d,dc}^2 + L_{q,n}I_{q,dc}^2)\sin(n\theta_e) \\ & + \sum_{n=6,12,18,\dots}L_{dq,n}(I_{q,dc}^2 - I_{d,dc}^2)\sin(n\theta_e)\Bigg\} \end{aligned} \tag{5.28}$$

It can be found that the average torque is only produced by the dc components of *dq*-axis inductances. Moreover, the frequency of torque ripple is multiple of 6th order for the 3-phase DS-SRMs. And the nth order torque ripple is due to the interaction between the nth order *dq0*-axis inductance and the fundamental current (dc component in *dq*-axis). For accurate prediction and easy implementation, the 6th and 12th order inductance harmonics will be considered in this chapter, as show in Fig. 5.21. Although neglecting higher order inductance harmonics (n>12)

will lead to a slight discrepancy between the FE and analytical predictions, a generally good agreement between them can still be observed.

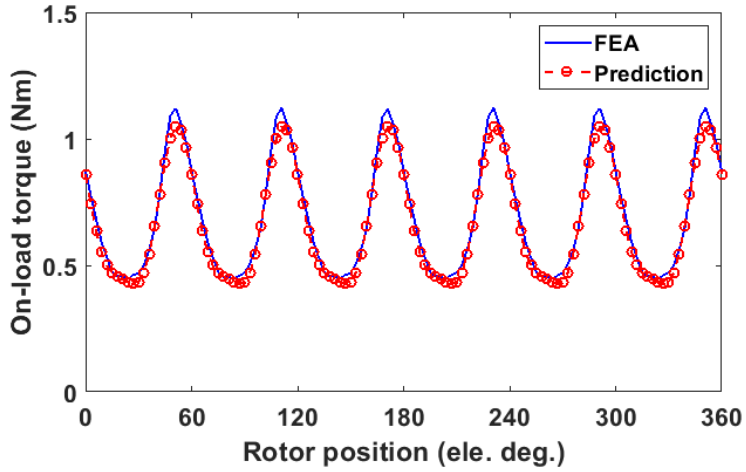

(a)

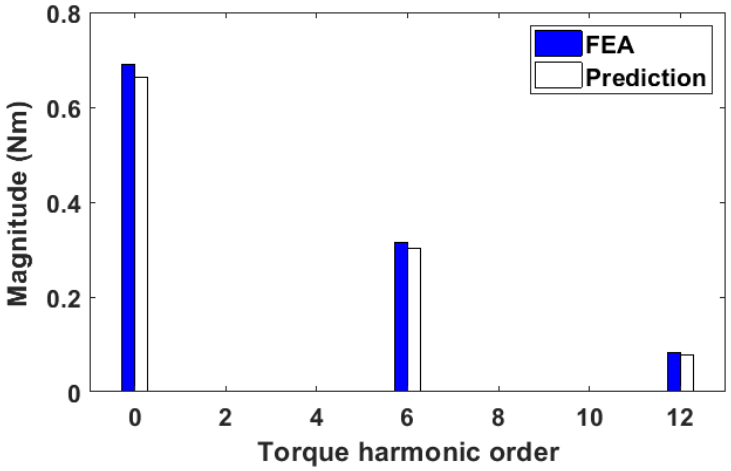

(b)

Fig. 5.21. Comparison of FEA and analytically predicted on-load torques. Three phases are supplied with 5 Arms ac currents. (a) Waveforms. (b) Spectra

5.3.1.3 TORQUE DUE TO CURRENT HARMONICS

In order to reproduce the current harmonic injection in *dq0*-axis frame, the investigation of Park Transformation has been carried out in Appendix A. Based on the study, it has been found that the single order current harmonic injection can be investigated for two separate cases, i.e. zero-sequence current harmonics in *dq0*-axis frame (3^{rd} order current harmonic in *abc*-axis frame) and non-zero-sequence current harmonic in *dq0*-axis frame (5^{th} and 7^{th} order current harmonic injection). And they will be discussed separately in this section.

A). TORQUE DUE TO ZERO-SEQUENCE CURRENT

The 3rd order current harmonic injection will bring extra zero-sequence current component for a balanced 3-phase system. This section will investigate the torque contribution due to the zero-sequence current. In order to inject the 3rd order current harmonic into phase current, assumptions about the *dq0*-axis current have to be made such that $I_{0,3} = I_v$ and $\varphi_0 = \beta_v$, and the current equation is given by:

$$\begin{bmatrix} i_d \\ i_q \\ i_0 \end{bmatrix} = \begin{bmatrix} I_{d,dc} \\ I_{q,dc} \\ I_{0,3}\cos(3\theta_e + \varphi_0) \end{bmatrix} \tag{5.29}$$

In this case, the coupling effect between zero-sequence and *dq*-axis current cannot be neglected. The flux linkage due to coupling effect can be written as (5.30).

$$\begin{bmatrix} \psi_d \\ \psi_q \\ \psi_0 \end{bmatrix}\Bigg|_{i_0} = \begin{bmatrix} 0 & 0 & L_{0d} \\ 0 & 0 & L_{0q} \\ L_{d0} & L_{q0} & L_0 \end{bmatrix} \begin{bmatrix} i_d \\ i_q \\ i_0 \end{bmatrix} \tag{5.30}$$

Putting (5.29) and (5.30) into (5.24), the torque due to zero-sequence current T_{zero} can be calculated by:

$$\begin{aligned} T_{zero} = \frac{3}{2}p\Bigg\{ & \sum_{n=3,9,15,\dots} \left(L_{d0,n} - nL_{q0,n}\right) I_{q,dc} I_{0,3} \cos\left((n-3)\theta_e - \varphi_0\right) \\ & + \sum_{n=3,9,15,\dots} \left(L_{q0,n} - nL_{d0,n}\right) I_{d,dc} I_{0,3} \sin\left((n-3)\theta_e - \varphi_0\right) \\ & + \sum_{n=3,9,15,\dots} \left(L_{d0,n} - nL_{q0,n}\right) I_{q,dc} I_{0,3} \cos\left((n+3)\theta_e + \varphi_0\right) \\ & + \sum_{n=3,9,15,\dots} \left(L_{q0,n} - nL_{d0,n}\right) I_{d,dc} I_{0,3} \sin\left((n+3)\theta_e + \varphi_0\right) \\ & - \sum_{n=6,12,18,\dots} \frac{n}{4} L_{0,n} {I_{0,3}}^2 \left(\sin\left((n+6)\theta_e + 2\varphi_0\right) + \sin\left((n-6)\theta_e - 2\varphi_0\right) + 2\sin(n\theta_e)\right)\Bigg\} \end{aligned} \tag{5.31}$$

It is obvious that once the zero-sequence current is not equal to zero, there will be multiple of 6th order torque harmonics in the resultant torque for a 3-phase DS-SRM. Moreover, when the coefficient of θ_e in (5.31) is equal to 0, i.e. n = 3 for the first two terms and n = 6 for the last term, an extra average torque can be obtained. Therefore, the first two terms and last term will contribute to average torque when the 3rd order current harmonic is injected, as shown below:

$$T_{zero,dc} = \frac{3}{2}p\left(L_{d0,3} - 3L_{q0,3}\right)I_{q,dc}I_{0,3}\cos(-\varphi_0) + \frac{3}{2}p\left(L_{q0,3} - 3L_{d0,3}\right)I_{d,dc}I_{0,3}\sin(-\varphi_0) - \frac{3}{8}pnL_{0,6}{I_{0,3}}^2\sin(-2\varphi_0) \tag{5.32}$$

Since the last term on the right hand side of (5.32) is much smaller than the other two terms, it can be neglected and the average torque can be rewritten as:

$$T_{zero,dc} = T\sin(\varphi_0 + \varphi) \tag{5.33}$$

where

$$T = \sqrt{A^2 + B^2} \tag{5.34}$$

$$\tan\varphi = \frac{B}{A} \tag{5.35}$$

with

$$\begin{cases} A = -\frac{3}{2}p\left(L_{q0,3} - 3L_{d0,3}\right)I_{d,dc}I_v \\ B = \frac{3}{2}p\left(L_{d0,3} - 3L_{q0,3}\right)I_{q,dc}I_v \end{cases} \tag{5.36}$$

Fig. 5.22 shows the comparison in terms torques versus I_d and I_q between 2D-FE and analytical predictions after injecting the 3rd order current harmonic in TABLE 5.4. It can be found that the proposed model can accurately predict average torque at relatively low phase current. However, with increasing current, there will be a marginal discrepancy between FEA and prediction due to magnetic saturation and W_m can no longer be accurately predicted using (5.23).

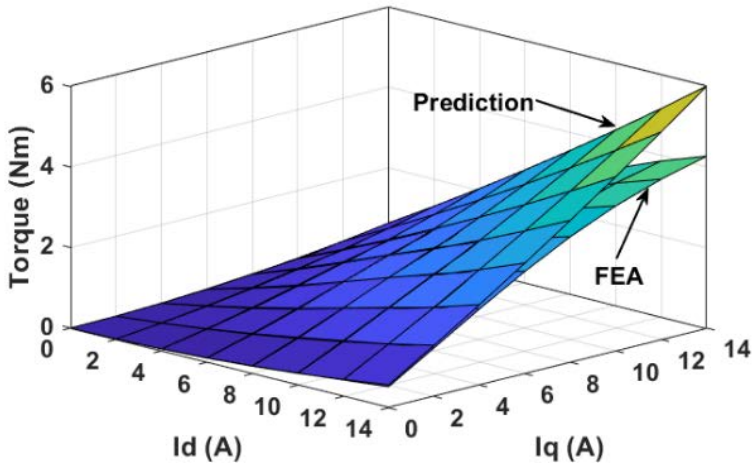

Fig. 5.22. Comparison of FEA and analytically predicted average torque [(5.27)+(5.33)] with the 3rd order current injection.

B). TORQUE DUE TO NON-ZERO-SEQUENCE CURRENT

This section will investigate the torque model due to a non-zero-sequence current. Base on the study in Appendix A.2, in order to inject the 5th or 7th order current harmonic in *abc*-axis frame, the 6th order current harmonic has to be injected in *dq0*-axis, as described by (5.37).

$$\begin{bmatrix} i_d \\ i_q \\ i_0 \end{bmatrix} = \begin{bmatrix} I_{d,dc} + I_{d,6}\cos(6\theta_e + \varphi_d) \\ I_{q,dc} + I_{q,6}\sin(6\theta_e + \varphi_q) \\ 0 \end{bmatrix} \tag{5.37}$$

Putting (5.10), (5.12) and (5.37) in (5.24), gives:

$$\begin{aligned} T_{non-zero} = \frac{3}{2}p\Big\{ & \frac{1}{2}(L_{d,dc} - L_{q,dc})I_{d,6}I_{q,6}\left(\sin(12\theta_e + \varphi_d + \varphi_q) - \sin(\varphi_d - \varphi_q)\right) \\ & + (L_{d,dc} - L_{q,dc})\left(I_{q,dc}I_{d,6}\cos(6\theta_e + \varphi_d) + I_{d,dc}I_{q,6}\sin(6\theta_e + \varphi_q)\right) \\ & + \sum_{n=6,12,18,\dots} \frac{1}{2}(L_{d,n} - L_{q,n})I_{d,n}I_{q,dc}\left(\cos((n+6)\theta_e + \varphi_d) + \cos((n-6)\theta_e - \varphi_d)\right) \\ & + \sum_{n=6,12,18,\dots} \frac{1}{2}(L_{d,n} - L_{q,n})I_{d,dc}I_{q,n}\left(\sin\left((n+6)\theta_e + \varphi_q\right) - \sin\left((n-6)\theta_e - \varphi_q\right)\right) \\ & - \sum_{n=6,12,18,\dots} L_{dq,n}I_{q,dc}I_{q,n}\left(\cos\left((n+6)\theta_e + \varphi_q\right) - \cos\left((n-6)\theta_e - \varphi_q\right)\right) \\ & - \sum_{n=6,12,18,\dots} L_{dq,n}I_{d,dc}I_{d,n}\left(\sin((n+6)\theta_e + \varphi_d) + \sin((n-6)\theta_e - \varphi_d)\right) \\ & - \sum_{n=6,12,18,\dots} \frac{n}{2}L_{d,n}I_{d,dc}I_{d,n}\left(\sin((n+6)\theta_e + \varphi_d) + \sin((n-6)\theta_e - \varphi_d)\right) \\ & + \sum_{n=6,12,18,\dots} \frac{n}{2}L_{q,n}I_{q,dc}I_{q,n}\left(\cos\left((n+6)\theta_e + \varphi_q\right) - \cos\left((n-6)\theta_e - \varphi_q\right)\right) \\ & + \sum_{n=6,12,18,\dots} \frac{n}{2}L_{dq,n}I_{d,dc}I_{q,n}\left(\sin\left((n+6)\theta_e + \varphi_q\right) - \sin\left((n-6)\theta_e - \varphi_q\right)\right) \\ & + \sum_{n=6,12,18,\dots} \frac{n}{2}L_{dq,n}I_{q,dc}I_{d,n}\left(\cos((n+6)\theta_e + \varphi_d) + \cos((n-6)\theta_e - \varphi_d)\right)\Big\} \end{aligned} \tag{5.38}$$

It has been found that if the 6th order current harmonic is injected in the *dq*-axis, there will be multiple of 6th order torque harmonics in the resultant instantaneous torque. Moreover, it is also found that the average torque can be obtained when *n* is 6. Therefore, the average torque due to the 6th order current harmonic can be calculated by:

$$T_{non-zero,dc} = T\sin(\varphi_d + \varphi) \tag{5.39}$$

where

$$T = \begin{cases} \sqrt{(A-D)^2 + (B-C)^2} & for\ \varphi_d = \varphi_q + \pi\ (5^{th}\ injection) \\ \sqrt{(A+D)^2 + (B+C)^2} & for\ \varphi_d = \varphi_q \qquad (7^{th}\ injection) \end{cases} \tag{5.40}$$

and

$$\tan\varphi = \begin{cases} \dfrac{A-D}{B-D} & for\ \varphi_d = \varphi_q + \pi\ (5^{th}\ injection) \\ \dfrac{A+D}{B+D} & for\ \varphi_d = \varphi_q \qquad (7^{th}\ injection) \end{cases} \tag{5.41}$$

with

$$\begin{cases} A = \left(\dfrac{(L_{d,6} - L_{q,6})}{2} + 3L_{dq,6}\right) I_{q,dc} I_v \\ B = \left(3L_{d,6} + L_{dq,6}\right) I_{d,dc} I_v \\ C = \left(\dfrac{\left(L_{d,6} - L_{q,6}\right)}{2} + 3L_{dq,6}\right) I_{d,dc} I_v \\ D = \left(-3L_{q,6} + L_{dq,6}\right) I_{q,dc} I_v \end{cases} \tag{5.42}$$

Fig. 5.23. shows the comparison of FEA and analytically predicted average torque with injecting current harmonic in TABLE 5.4.

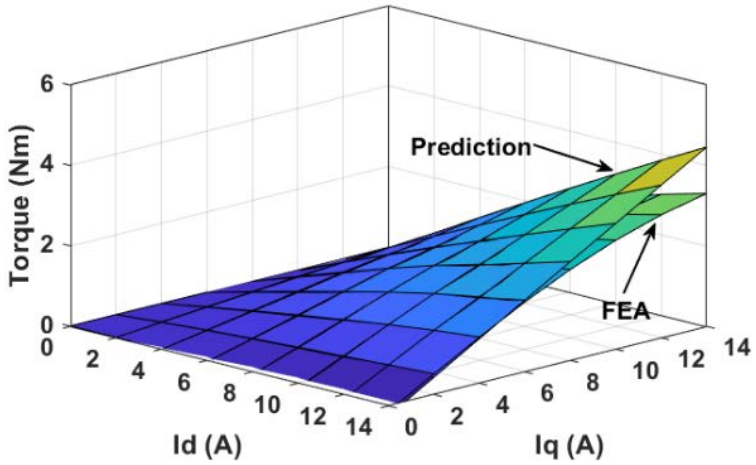

(a)

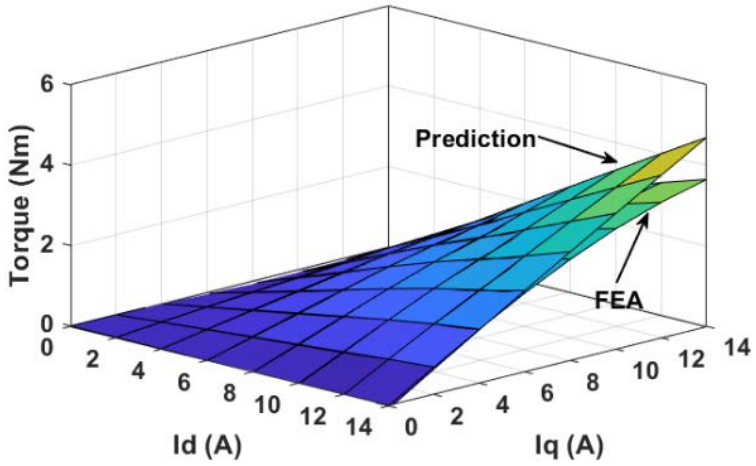

(b)

Fig. 5.23. Comparison of FEA and analytically predicted average torque [(5.27)+(5.39)]. (a) 5th order current injection ($\varphi_d = \varphi_q + \pi$) and (b) 7th order current injection ($\varphi_d = \varphi_q$).

5.3.1.4 CURRENT HARMONIC SELECTION

The analytical model in *dq0*-axis frame can also provide a powerful insight into the mechanism of torque generation, which allows for the optimum current harmonic to be injected to reduce the torque ripple and/or to improve the average torque.

A). CURRENT HARMONIC SELECTION FOR MAXIMIZING THE AVERAGE TORQUE

Proposed *dq0*-axis model can be used to optimize the torque production as well. Based on the developed torque equations, the average torque due to the 3rd, 5th and 7th order current harmonic injections can be calculated using (5.33) and (5.39), which can also be rewritten as:

$$T_{h,dc} = T\sin(\beta_v + \varphi) \tag{5.43}$$

where β_v is the phase angle [see 0] for the v^{th} order current harmonic in *abc*-axis frame. T and φ are magnitude and phase angle of the resultant torque. Both are constants and can be calculated by (5.34)-(5.36) and (5.40)-(5.42) depending on the injected current harmonics. Therefore, it is apparent that if the harmonic magnitude is kept unchanged, the average torque due to harmonic current will be a function of the harmonic phase angle β_v. In this case, when $\sin(\beta_v + \varphi)$ is equal to 1, the maximum average torque can be obtained. Therefore, the angles β_{v_Tmax}, which achieve maximum average torque, are $89°$, $302°$ and $70°$ for the 3rd, 5th and 7th order current harmonics, respectively.

B). CURRENT HARMONIC SELECTION FOR MINIMIZING TORQUE RIPPLE

The same idea can be used to minimize the torque ripple. Based on studies in the section 5.3.1.2, the dominant torque harmonic of the 12s/8p DS-SRMs can be expressed by (5.28)

$$T_{f,6} = T_{Frip} \sin\left(6\theta_e + \varphi_{Frip}\right) \tag{5.44}$$

According to (5.31), the 6th order torque harmonic due to zero-sequence current harmonic (3rd harmonic current injection) is produced by the interaction between $L_{d0,3}$ and $I_{0,3}$ as well as $L_{q0,3}$ and $I_{0,3}$, and can be calculated by

$$\begin{aligned} T_{\text{zero},6} = {} & \left(L_{q0,3} - 3L_{d0,3}\right) I_{d,dc} I_{0,3} \sin(6\theta_e + \varphi_0) \\ & + \left(L_{d0,3} - 3L_{q0,3}\right) I_{q,dc} I_{0,3} \cos(6\theta_e + \varphi_0) \end{aligned} \tag{5.45}$$

Similarly, for the non-zero-sequence harmonic current injection [see (5.38)], i.e. 5th and 7th harmonic current injections, the 6th order torque harmonic is mainly due to the interaction between $L_{d,dc}$ and $i_{dq,6}$ as well as $L_{q,dc}$ and $i_{dq,6}$. It can be simplified as:

$$T_{\text{non-zero},6} = \left(L_{d,dc} - L_{q,dc}\right)\left[I_{d,dc} I_{q,6} \sin\left(6\theta_e + \varphi_q\right) + I_{q,dc} I_{d,6} \cos(6\theta_e + \varphi_d)\right] \tag{5.46}$$

Therefore, for both the zero- and non-zero-sequence current injections, the 6th order torque harmonic due to current harmonic can be derived as

$$T_{h,6} = T \sin(6\theta_e + \beta_v + \varphi) \tag{5.47}$$

where

$$T = \sqrt{A^2 + B^2} \tag{5.48}$$

$$\tan\varphi = \frac{B}{A} \tag{5.49}$$

with

$$A = \begin{cases} \left(L_{q0,3} - 3L_{d0,3}\right) I_{d,dc} I_v & 3^{rd}\ injection \\ -\left(L_{d,dc} - L_{q,dc}\right) L_{d,dc} I_v & 5^{th}\ injection \\ \left(L_{d,dc} - L_{q,dc}\right) L_{d,dc} I_v & 7^{th}\ injection \end{cases} \tag{5.50}$$

$$B = \begin{cases} \left(L_{d0,3} - 3L_{q0,3}\right) I_{q,dc} I_v & 3^{rd}\ injection \\ \left(L_{d,dc} - L_{q,dc}\right) I_{q,dc} I_v & 5^{th}\ injection \\ \left(L_{d,dc} - L_{q,dc}\right) I_{q,dc} I_v & 7^{th}\ injection \end{cases} \tag{5.51}$$

As a result, in order to minimize the resultant torque ripple, (5.44) and (5.47) need to achieve the same magnitude but have a π phase shift angle. This leads to

$$\begin{cases} T_{F,6} = T(I_v) \\ \varphi + \beta_v - \varphi_{\mathrm{Frip}} = \pi \end{cases} \tag{5.52}$$

Using 3rd order current harmonic for example, φ_{Frip} and φ can be calculated as $135.5°$ and $224°$, respectively. Therefore, the phase angle to achieve the minimum torque ripple can be obtained as $\beta_v = 46.5°$. It is the same for the 5th and 7th order current harmonic injections, β_v of which are $135.5°$ and $225.5°$, respectively. After injecting these predicted current harmonics, the torque variations have been shown in TABLE 5.4.

TABLE 5.4 TORQUE PERFORMANCE IMPROVEMENT AFTER INJECTION

Harmonic (mag, phase)	Average torque (%)	Torque ripple (%)
3rd (30%, 46.5°)	+12.4	-60.1
5th (20%, 135.5°)	-15.4	-69.9
7th (20%, 225.5°)	-6.49	-77.1

The 2D-FE results have been utilized to validate the accuracy of the proposed analytical torque model. Fig. 5.24 shows the comparison of instantaneous torque calculated by FEA and analytical torque model with/without current harmonic injection. A good agreement has been observed at a phase rms current of 5A. Fig. 5.25 shows the average torque and torque ripple coefficient *vs* phase rms current. The same limitation as for the torque model in *abc*-axis frame is that with increasing phase current, marginal discrepancy will occur between the analytical and FEA predictions due to the fact that magnetic saturation has not been taken into account in the analytical torque equations.

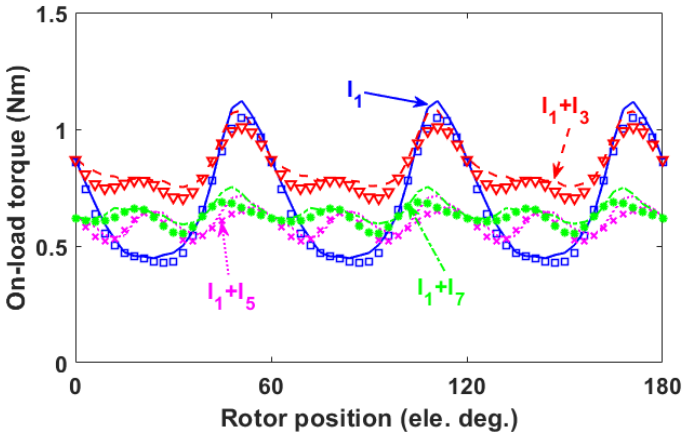

Fig. 5.24. Comparison of instantaneous torque by FEA and analytical predictions with/without current harmonic injection. Phase current is 5Arms. The phase angle selection for all the current harmonics is listed in TABLE 5.4 (Line: FEA; Mark: Analytical prediction).

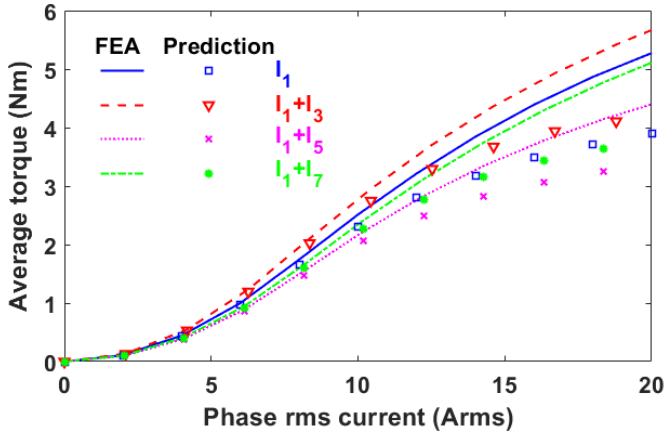

(a) Average torque

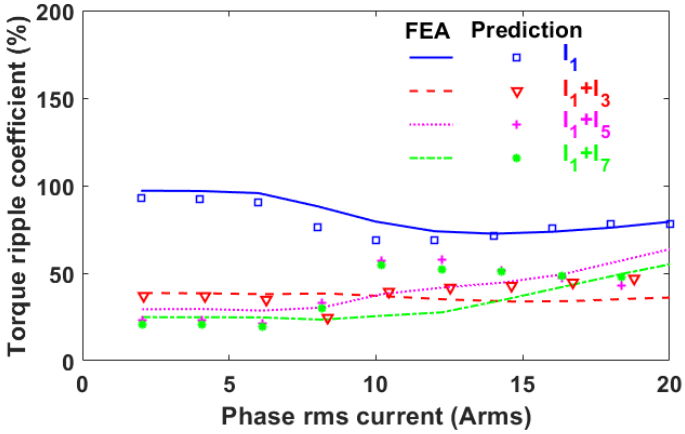

(b) Torque ripple coefficient

Fig. 5.25. Comparison of torque production of 12s/8p 3-phase SL DS-SRMs with/without current harmonic injection. The phase angle selection for all the current harmonics is listed in TABLE 5.4. (Line: FEA; Mark: Analytical prediction).

5.3.2 TORQUE-SPEED CURVE

5.3.2.1 TORQUE-SPEED CURVE WITHOUT VOLTAGE DISTORTION

Without considering voltage distortion, the voltage term $\frac{d\psi_{dq0}}{dt}$ is 0 at steady-state and the variations in L_d and L_q are ignored. Therefore, the phase current and voltage should satisfy the following conditions for the full range of speeds including constant torque region and also constant power region (flux weakening operation):

$$\sqrt{{v_d}^2 + {v_q}^2} \leq V_{max} = \frac{V_{dc}}{\sqrt{3}} \tag{5.53}$$

$$\sqrt{{i_d}^2 + {i_q}^2} \leq I_{max} \tag{5.54}$$

where V_{max} and I_{max} are the voltage and current constraints of the inverter. As an example, Fig. 5.26 shows the current waveform of the 3rd order current harmonic injection listed in TABLE 5.4. It has been found for the same rms current, the peak current is higher than that of the fundamental current. This means that the selected 3rd order current harmonic will reach the current limit earlier than the pure sinewave current supply. Therefore, the rms current should be reduced to keep the peak current at the same level after injecting the current harmonic. It will happen for the 5th and 7th order current harmonic injections as well. For completeness, the dynamic performance will be investigated in two cases, i.e. one is constant rms current condition (CRMS), while the other is constant peak current condition (CPC).

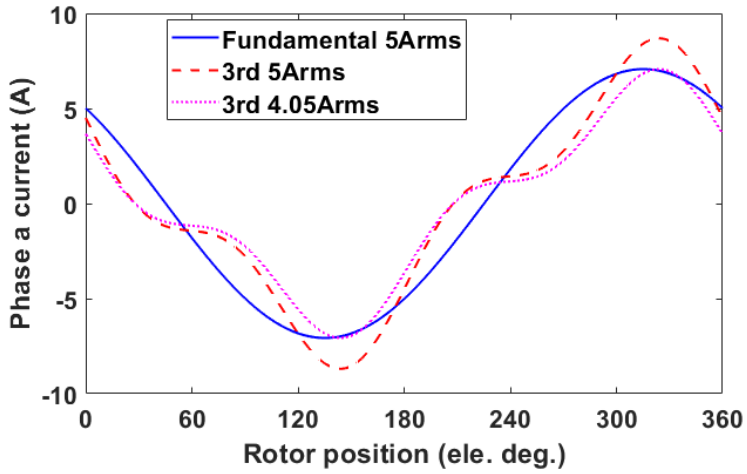

Fig. 5.26. Phase a current waveform with the 3rd order current harmonic injection.

The torque-speed curve has been calculated using the torque equations developed in this chapter and compared against the FEA results. Fig. 5.27 shows the results for CRMS condition (I_{rms}=5Arms), and the dc link voltage is 24V. Due to the fact that the voltage distortion has not

been considered, and the relatively low percentage of current harmonic has little effect on magnetic saturation, therefore the variation in average values of *dq*-axis inductances after injecting current harmonics is small. As a result, the current harmonic injection method presents only modest effect on the base speed. Moreover, without considering the voltage distortion, the 3rd order current harmonic can increase the average torque in both maximum torque per ampere (MTPA) region and flux weakening region. However, both the 5th and 7th order current injections, although effective in reducing torque ripple, degrade the dynamic performance for the full range of speeds.

Fig. 5.28 shows the torque-speed curves under constant peak current condition. Using the 3rd order current harmonic injection as example, due to the fact that the rms current is reduced by 19% (see Fig. 5.26), the average torque can be reduced to $(1-0.19)^2 \times 100 = 65.6\%$ of that of the CRMS condition. However, it is worth noting that the dynamic performance for the two cases (CRMS or CPC condition) are the same in flux weakening region. This is due to the fact that in the flux weakening region, machine is limited by the voltage rather than the current, together with the same machine parameters, the torque-speed performance of the two cases should be the same. This is also the case for other orders of harmonic current injection.

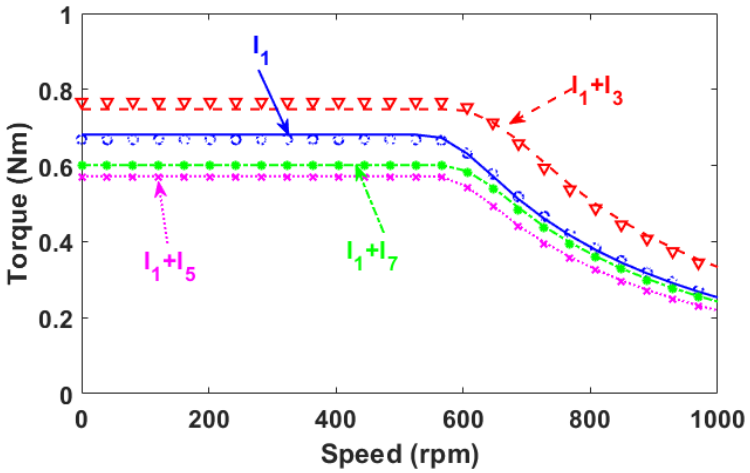

Fig. 5.27. Torque-speed curves after current harmonic injections without considering the voltage distortion. I_{rms} =5Arms and V_{dc}=24V. (Line: FEA; Mark: Analytical prediction).

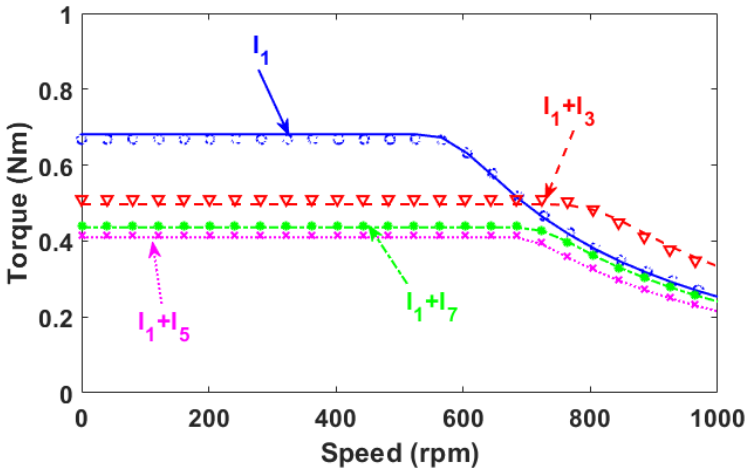

Fig. 5.28. Torque-speed curves after current harmonic injections without considering the voltage distortion. I_{peak}=7.07A and V_{dc}=24V. (Line: FEA; Mark: Analytical prediction).

5.3.2.2 TORQUE-SPEED CURVE WITH VOLTAGE DISTORTION

If the current harmonics and also the harmonics in self- and mutual-inductances are considered, the phase voltage will be distorted. By way of example, under CRMS condition, shows Fig. 5.29 the dynamic voltage variation with/without the 5th and 7th order current harmonic injections. For clarity, the voltages in $\alpha\beta$-axis frame instead of dq-axis frame have been used in this section. The rms current is 5Arms, the rotor speed is 200rpm and the dc voltage is 24V. It is obvious that if the inductance harmonics are considered for such machines, the distortion in the phase voltage is significant, especially when current harmonics are injected. And with increasing rotor speed, the peak voltage will reach the inverter's voltage limit earlier than the pure sinewave current supply. In order to avoid undesirable current harmonics, the machine has to enter into the flux-weakening region earlier. This will in theory reduce the flux weakening capability of the machine, which will be investigated in this section.

It is worth noting that, different from the 5th and 7th harmonic current injections, the 3rd order current harmonic injection will bring extra zero-sequence current. Therefore, it requires a special control strategy to control the injected zero-sequence current. This can be achieved using the 3-dimentional (3D) SVPWM [162]-[163] (Investigated in Chapter 6), in which the neutral point of a 3-phase machine is connected to an extra half bridge leg. It has been found that without considering over modulation, the voltage limit of the 3D-SVPWM can be calculated by $\frac{V_{dc}}{\sqrt{3}}$, as shown in (5.55). Similarly, the voltage distribution with the 3rd order current harmonic injection can be limited in a sphere with a radius of $\frac{V_{dc}}{\sqrt{3}}$, as shown in Fig. 5.30.

$$\sqrt{{v_d}^2 + {v_q}^2 + {v_0}^2} \leq V_{max} = \frac{V_{dc}}{\sqrt{3}} \tag{5.55}$$

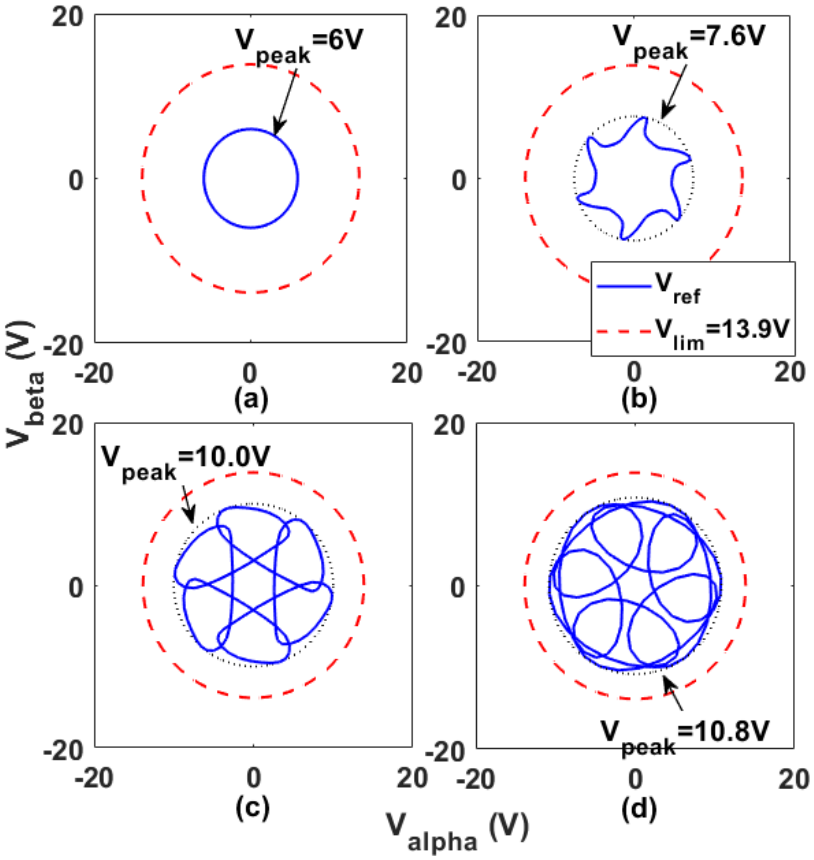

Fig. 5.29. *αβ*-axis voltages with a phase current of 5Arms, a speed of 200rpm and a DC link voltage V_{dc}=24V. (a) I_1 (without voltage distortion), (b) I_1 (with voltage distortion), (c) I_1+I_5 and (d) I_1+I_7.

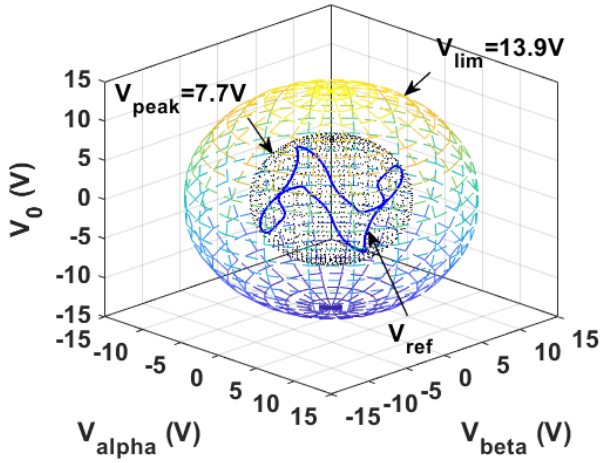

Fig. 5.30. *αβ0*-axis voltages with 3rd order current harmonic injection with a phase current of 5Arms, a speed of 200rpm and a DC link voltage V_{dc}=24V.

Similar as in section 5.3.2.1, the torque-speed curve considering the voltage distortion under CRMS condition has been calculated, as shown in Fig. 5.31. A good agreement can be observed between the FEA and analytical predictions. It is also found that, different from section 5.3.2.1, the base speed of the DS-SRM might be reduced after injecting the current harmonics, especially the 5th and 7th order current harmonics. It is mainly due to the fact that these current harmonics cause significant voltage distortion which limits the flux weakening capability. However, the 3rd order current harmonic can increase the average torque in constant torque region and maintain similar torque level as fundamental current supply in flux weakening region. Fig. 5.32 shows the torque-speed curves for the CPC condition. The same results have been obtained when the voltage distortion is considered. The output power is reduced under CPC condition and the dynamic performance for both CRMS and CPC conditions are the same.

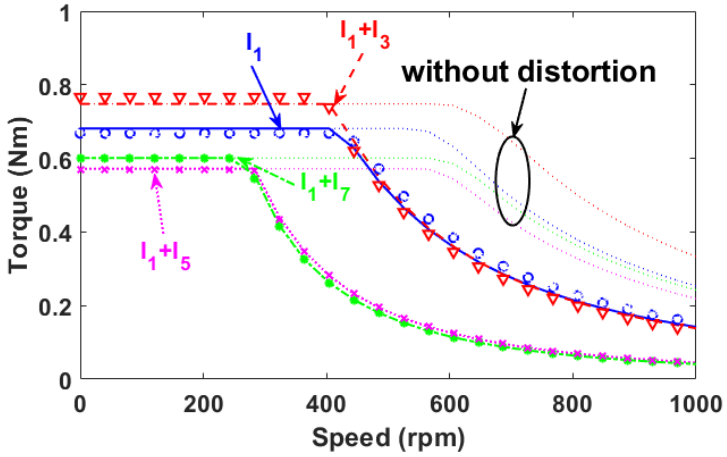

Fig. 5.31. Torque-speed curves after current harmonic injection with considering the voltage distortion. I_{rms}=5Arms and V_{dc}=24V. (Line: FEA; Mark: Analytical prediction).

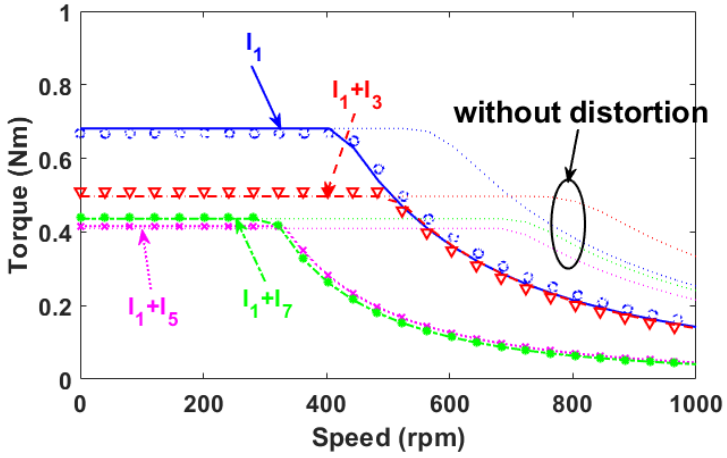

Fig. 5.32. Torque-speed curves after current harmonic injection with considering the voltage distortion. I_{peak}=7.07A and V_{dc}=24V. (Line: FEA; Mark: Analytical prediction).

5.3.3 EFFICIENCY MAP

Apart from torque-speed curves, the efficiency maps under the above two conditions (CRMS and CPC) have also been calculated using (5.3). The efficiency maps under CRMS condition with different current harmonic injections are compared in Fig. 5.33. It can be found that a maximum efficiency of 68% is achieved by the 3rd order current harmonic injection between 1000 and 1500rpm. It can also increase the efficiency under MTPA compared with that of fundamental current, due to the extra average torque that can be produced due to harmonic current injection. However, the 5th and 7th order current harmonic injections degrade the dynamic performance of the machine for the full speed range. For both harmonic current injections, a modest efficiency of 60% can be achieved at lower speed (around 700 rpm).

The efficiency maps under CPC condition have also been calculated, as shown in Fig. 5.34. It has been found that the dynamic performance of the machine with current harmonic injection in flux weakening region does not change. The only difference is that the output torque in MTPA region has been reduced. This is due to the fact that the peak current is maintained the same as fundamental current, and hence the rms current is reduced.

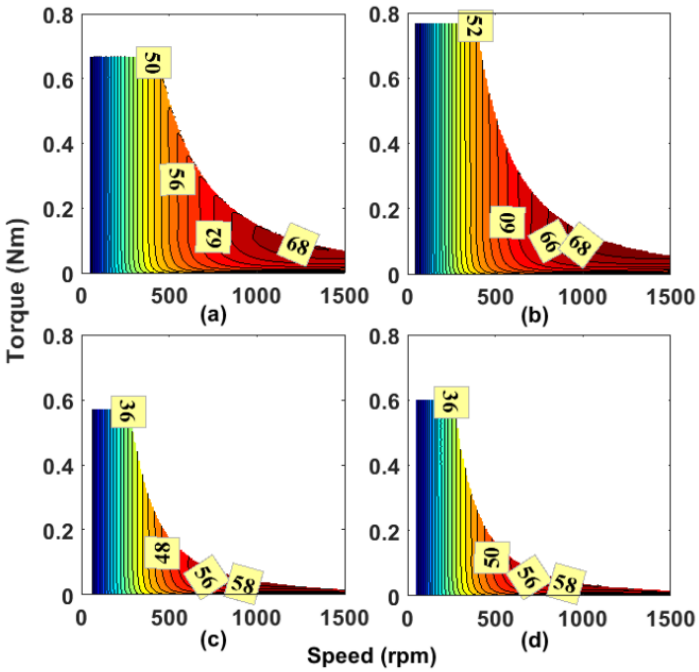

Fig. 5.33. Efficiency map with current harmonic injection when I_{rms}=5Arms and V_{dc}=24V. (a) I_1, (b) I_1+I_3, (c) I_1+I_5 and (d) I_1+I_7.

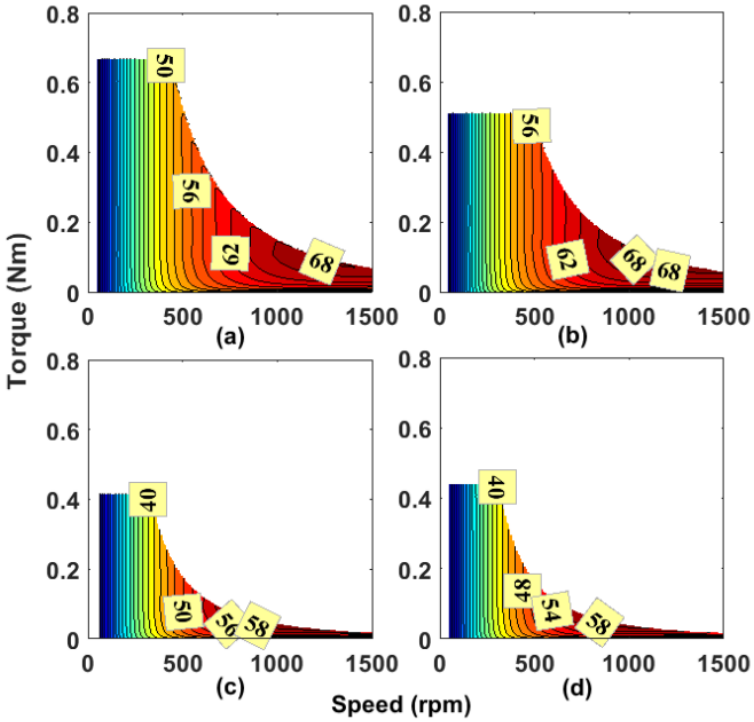

Fig. 5.34. Efficiency map with current harmonic injection when I_{peak}=7.07A and V_{dc}=24V. (a) I_1, (b) I_1+I_3, (c) I_1+I_5 and (d) I_1+I_7.

5.3.4 Case Study for Double Layer DS-SRM and FPSRM

Once the accuracy of analytical torque models has been validated by 2D-FE, it can be utilized to predict the dynamic performance for different topologies with current harmonic injection. Double layer (DL) DS-SRM and fully-pitched (FP) DS-SRM have been investigated in this section. For fair comparison, the dc link voltage is kept the same as that of SL machine (24V). The torque-speed curves under CRMS condition (5Arms) have been shown in Fig. 5.35. It is found that for both machines, the current harmonic injection will reduce their base speed significantly, especially, with the 5th and 7th order current harmonics. This is mainly due to significant voltage distortion. Therefore, the flux-weakening performances are always poorer after injecting the current harmonics. However, some current harmonic could increase the average torque and reduce the torque ripple at the same time, such as, the 3rd order current harmonic for SL DS-SRMs and FP DS-SRMs. For these cases, not only the output power in the constant torque region can be increased, but also the torque level in flux weakening region can be maintained at a similar level as the pure fundamental current supply. Moreover, it is worth noting that the torque reduction of DL machine with 3rd order current harmonic is mainly

due to the fact that magnitude of fundamental current is reduced to maintain a constant phase rms current.

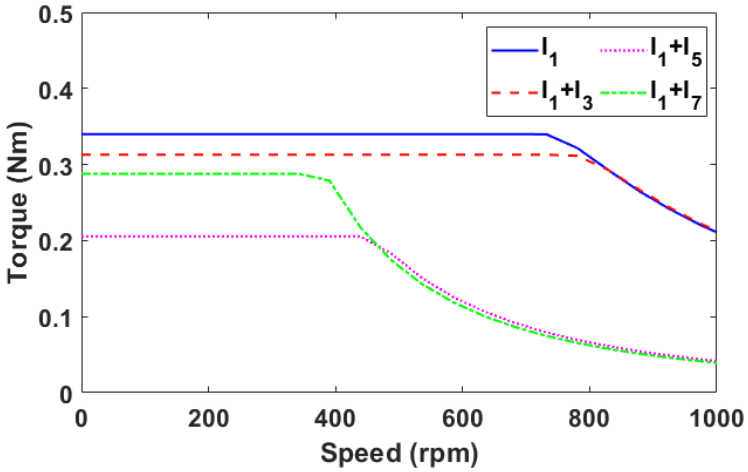

(a) DL DS-SRM

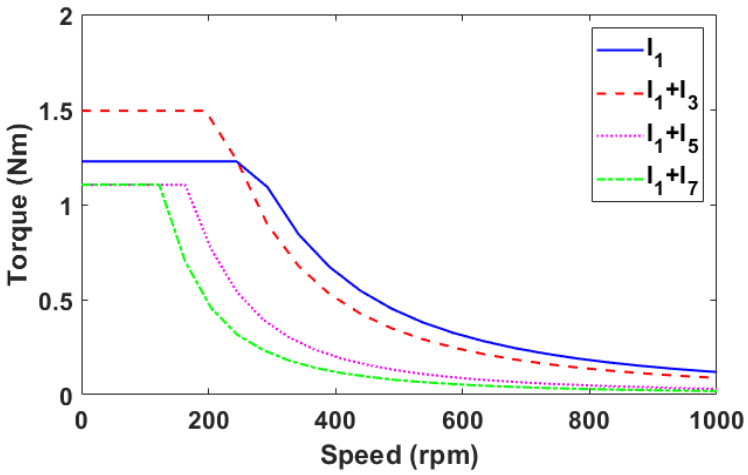

(b) FP DS-SRM

Fig. 5.35. Torque-speed curves after current harmonic injection for the 12s/8p 3-phase machines. I_{rms}=5Arms and V_{dc}=24V.

Fig. 5.36 shows the efficiency maps for DL DS-SRM under CRMS condition with different current harmonic injections. It can be found that a maximum efficiency of 54% is achieved by fundamental current supply between 1300 and 1500rpm. The 3rd order harmonic injection brings no benefit for such machine, and it increases the copper losses and reduces the efficiency. Moreover, although the 5th and 7th order current harmonic injections could reduce the torque ripple, they degrade the dynamic performance of the machine for the full speed range.

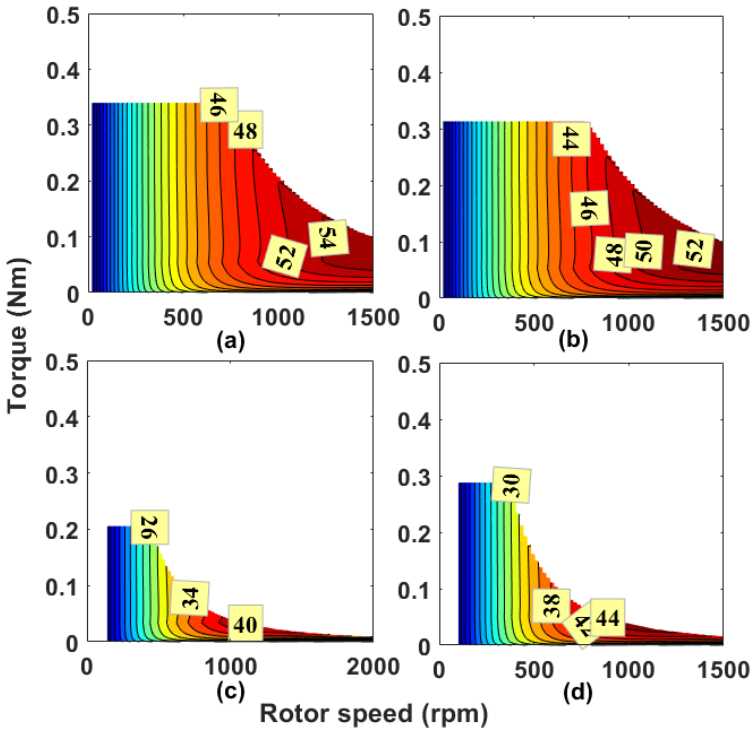

Fig. 5.36. Efficiency map with current harmonic injection for DL DS-SRM when I_{rms}=5Arms and V_{dc}=24V. (a) I_1, (b) I_1+I_3, (c) I_1+I_5 and (d) I_1+I_7.

Fig. 5.37 shows the efficiency maps for the DL DS-SRM under CRMS condition with different current harmonic injections. Compared with other winding configurations, the FP DS-SRM at a relatively low current level (5Arms) can achieve the highest efficiency (74%), which is achieved by the 3rd order current harmonic injection between 1000 and 1500rpm. However, due to the fact that higher MMF is concentrated in the stator yoke, the FP DS-SRM is much more sensitive to magnetic saturation. Together with the highest phase resistance, its benefit in efficiency will be compromised with increasing phase current. Moreover, the same as other DS-SRMs, with selected 5th and 7th order current harmonic injections, the dynamic performance of this machine will be reduced for the full speed range. A modest efficiency of 64% and 60% can be achieved by 5th and 7th order current harmonics, respectively. The comparison of dynamic performance for three DS-SRMs have been listed in TABLE 5.5.

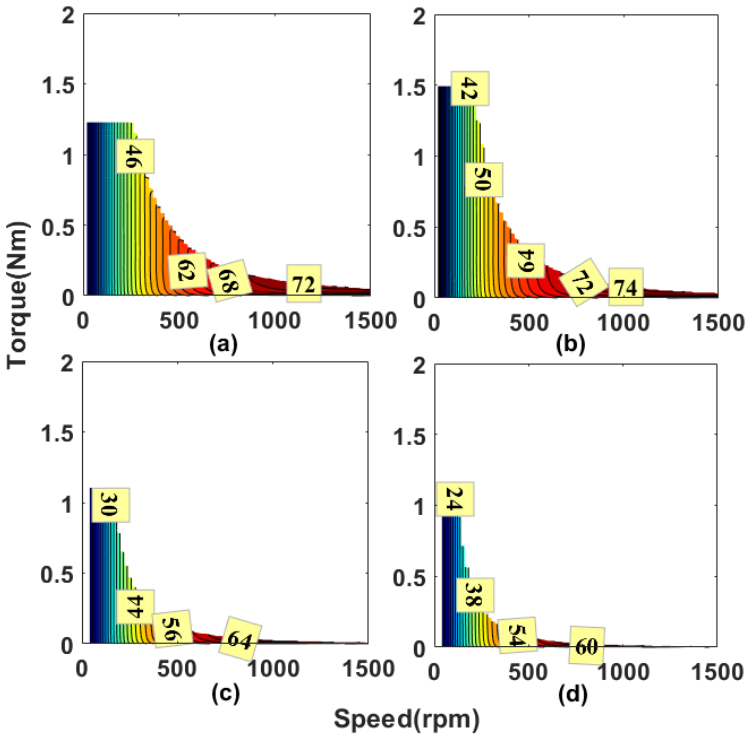

Fig. 5.37. Efficiency map with current harmonic injection for FPSRM when I_{rms}=5Arms and V_{dc}=24V. (a) I_1, (b) I_1+I_3, (c) I_1+I_5 and (d) I_1+I_7.

TABLE 5.5 COMPARISON RESULTS OF 3-PHASE DS-SRMS WITH CURRENT HARMONIC INJECTIONS (I_{RMS}=5ARMS AND V_{DC}=24V)

DS-SRMs	Harmonic	Base speed (rpm)	Peak torque (Nm)	Torque ripple	Maximum efficiency
SL	I_1	400	0.668	94.8%	68%
	I_1+I_3	400	0.766	38.5%	68%
	I_1+I_5	282	0.570	28.8%	58%
	I_1+I_7	260	0.600	26.2%	58%
DL	I_1	730	0.340	131.6%	54%
	I_1+I_3	780	0.313	130.3%	52%
	I_1+I_5	439	0.206	55.2%	40%
	I_1+I_7	390	0.288	67.2%	44%
FP	I_1	250	1.236	83.7%	72%
	I_1+I_3	195	1.493	26.8%	74%
	I_1+I_5	163	1.103	26.1%	64%
	I_1+I_7	122	1.105	42.5%	60%

5.4 Effectiveness of Current Harmonic Injection for Multi-phase DS-SRMs

Apart from the 3-phase DS-SRMs, the dynamic performances of multi-phase machines with the proposed harmonic current injection method have also been investigated in this section. As investigated in Chapter 4, although the harmonic current injection can reduce torque ripple and could even increase the average torque for some cases, the high order current harmonic will lead to extra losses due to higher frequency. This could deteriorate the dynamic performances, particularly the efficiency maps of the DS-SRMs. In order to fully investigate the effectiveness of the proposed method for multi-phase machines, this section will use SL 5-phase and 6-phase DS-SRMs as examples to investigate the losses and dynamic performance with current harmonic injection. It is worth noting that the I_{RMS} with/without current harmonic injection is always kept the same and the resistances of such machine is calculated in Chapter 4. Therefore, the copper loss does not change for each machine before/after current harmonic injection.

5.4.1 5-Phase DS-SRMs

5.4.1.1 Iron Losses

The comparison of iron loss versus phase rms current of a 5-phase SL DS-SRM has been investigated and the results are shown in Fig. 5.38. It has been found that the 5th order current harmonic produces the highest iron losses, which is mainly due to the fact that a significant magnitude (65%I_1) of current harmonic was injected (See Chapter 4). Similar to the 3-phase DS-SRMs, at modest current (<16 A) for the SL machine, the iron loss with 3rd order current harmonic injection is larger than that with 7th order harmonic injection. This is because higher percentage of harmonic current has been injected for a better torque performance (Chapter 4). However, with increasing phase rms current, the iron losses with the 7th order harmonic current injection exceed that of the 3rd order harmonic current injection. This is mainly due to the different effects of magnetic saturation on the different current harmonic injections. Fig. 5.39 shows the stator eddy current loss and hysteresis loss at a phase current of 5Arms. It is found that although the losses of fundamental current is reduced (the same RMS current is maintained), the k^{th} order current harmonic injection will increase the iron losses due to the k^{th} order flux density harmonic, which leads to an increase in the resultant iron losses.

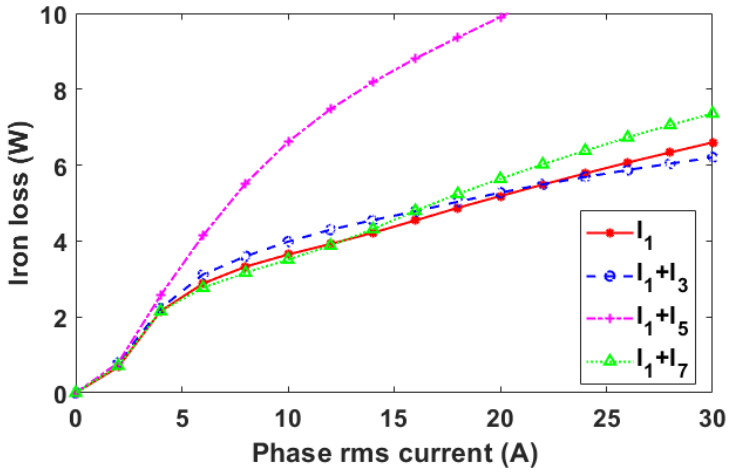

Fig. 5.38. Comparison of iron loss for 5-phase SL DS-SRM with current harmonic injection. Rotation speed is 400rpm.

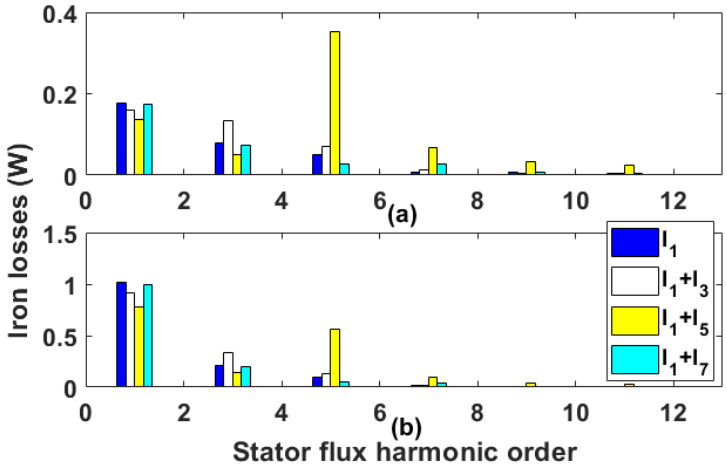

Fig. 5.39 Stator (a) eddy current losses and (b) hysteresis losses for the 5-phase SL DS-SRM. Phase current is 5Arms and rotor speed is 400rpm.

5.4.1.2 TORQUE-SPEED CHARACTERISTICS

In order to simplify the investigation of dynamic performance for the 5-phase machine, the rotating (*dq0*-axis) reference frame has been adopted in this section as well, which has been detailed in the Appendix A.3. It is well established that the machine electromagnetic equation can be expressed as (5.56). After applying the Park transformation for 5-phase machines as described by (5.57), (5.56) can be simplified in terms of flux linkages in *dq0*-axis frame, as expressed by (5.58).

Based on the study in [164]-[166], the Space Vector Pulse Width Modulation (SVPWM) for 5-phase synchronous reluctance machine has been investigated and the voltage limitation can

be calculated as $0.616V_{dc}$. The same as what has been done for 3-phase machine, where the voltage term $\frac{d\psi_{dq0}}{dt}$ will not be neglected. The peak voltage distortion, due to the interaction between inductance and current harmonics, will be utilized as the reference to compare with the voltage limitation. This section uses the 5-phase SL DS-SRM as an example to investigate the dynamic performance with proposed current harmonic injection method.

$$[v]_{abcde} = R[i]_{abcde} + \frac{d[\psi]_{abcde}}{dt} \tag{5.56}$$

and the Park Transformation for 5-phase machine is given by:

$$\frac{2}{5}\begin{bmatrix} \cos\theta_e & \cos\left(\theta_e - \frac{2\pi}{5}\right) & \cos\left(\theta_e - \frac{2\pi}{5}\right) & \cos\left(\theta_e - \frac{2\pi}{5}\right) & \cos\left(\theta_e - \frac{2\pi}{5}\right) \\ -\sin\theta_e & -\sin\left(\theta_e - \frac{2\pi}{5}\right) & -\sin\left(\theta_e - \frac{2\pi}{5}\right) & -\sin\left(\theta_e - \frac{2\pi}{5}\right) & -\sin\left(\theta_e - \frac{2\pi}{5}\right) \\ \cos 3\theta_e & \cos\left(3\left(\theta_e - \frac{2\pi}{5}\right)\right) & \cos\left(3\left(\theta_e - \frac{2\pi}{5}\right)\right) & \cos\left(3\left(\theta_e - \frac{2\pi}{5}\right)\right) & \cos\left(3\left(\theta_e - \frac{2\pi}{5}\right)\right) \\ -\sin 3\theta_e & -\sin\left(3\left(\theta_e - \frac{2\pi}{5}\right)\right) & -\sin\left(3\left(\theta_e - \frac{2\pi}{5}\right)\right) & -\sin\left(3\left(\theta_e - \frac{2\pi}{5}\right)\right) & -\sin\left(3\left(\theta_e - \frac{2\pi}{5}\right)\right) \\ \frac{1}{2} & \frac{1}{2} & \frac{1}{2} & \frac{1}{2} & \frac{1}{2} \end{bmatrix} \tag{5.57}$$

This yields

$$\begin{bmatrix} v_d \\ v_q \\ v_{d3} \\ v_{q3} \\ v_0 \end{bmatrix} = R\begin{bmatrix} i_d \\ i_q \\ i_{d3} \\ i_{q3} \\ i_0 \end{bmatrix} + \begin{bmatrix} 0 & -\omega & 0 & 0 & 0 \\ \omega & 0 & 0 & 0 & 0 \\ 0 & 0 & 0 & -3\omega & 0 \\ 0 & 0 & 3\omega & 0 & 0 \\ 0 & 0 & 0 & 0 & 0 \end{bmatrix}\begin{bmatrix} \psi_d \\ \psi_q \\ \psi_{d3} \\ \psi_{q3} \\ \psi_0 \end{bmatrix} + \frac{d}{dt}\begin{bmatrix} \psi_d \\ \psi_q \\ \psi_{d3} \\ \psi_{q3} \\ \psi_0 \end{bmatrix} \tag{5.58}$$

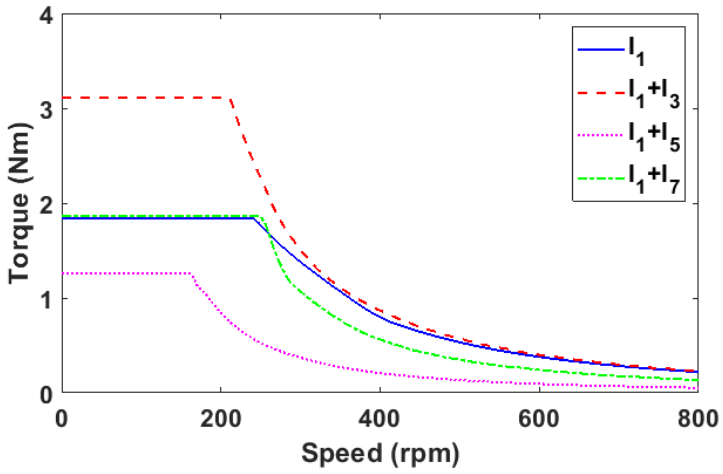

Fig. 5.40. Torque-speed curves of the 5-phase SL DS-SRM when $I_{rms} = 5Arms$ and V_{dc} = 24V.

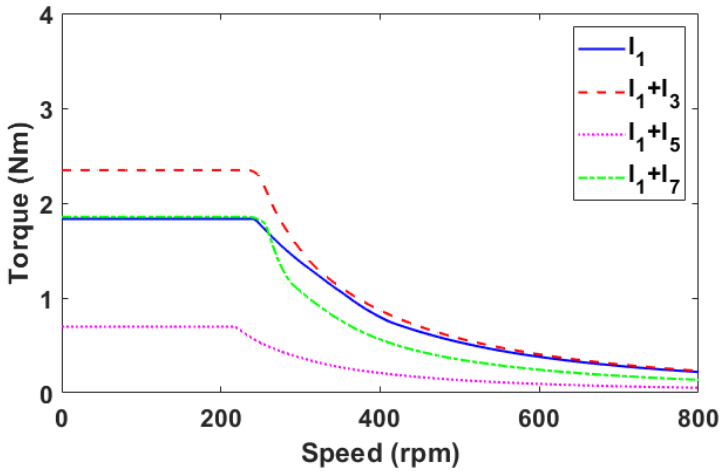

Fig. 5.41. Torque-speed curves of the 5-phase SL DS-SRM when $I_{peak} = 7.07A$ and V_{dc} = 24V.

Fig. 5.40 shows the torque-speed curves for the 5-phase SL DS-SRM under CRMS condition when the current limit is 5Arms and the dc-link voltage is 24V. It shows that the 3rd order current harmonic can increase the average torque by 60% in the constant torque region and present the same torque capability compared with the fundamental current supply in the flux weakening region. It is not surprising that the 5th order current harmonics will significantly reduce the dynamic performance in both constant torque and flux weakening regions. This is due to the fact that they reduce the output torque and increase the voltage distortion, leading to limited flux weakening capability. As investigated Chapter 4, the selected 7th order current harmonic injection could slightly increase the average torque. Therefore, it can maintain the torque capability at constant torque region, but due to the effect of voltage distortion, the performance in flux weakening region could be compromised.

Fig. 5.41 shows the torque-speed curves for the 5-phase SL DS-SRM under CPC condition. The dc link voltage is 24V. Similar to the investigation for the 3-phase machine (section 5.3.2.1), the phase rms current has to be reduced to ensure the peak current is not beyond 7.07A (see Fig. 5.26). Therefore, the output torque in constant torque region can be reduced. However, the dynamic performance in flux weakening region will not change. This is because that in the flux weakening region, machine is limited by the voltage rather than the current, together with the same machine parameters, the torque-speed performance of the two cases should be the same.

5.4.1.3 EFFICIENCY MAPS

The efficiency maps of CRMS condition have been calculated, as shown in Fig. 5.42. It can be found that the 3rd order current harmonic injection can significantly increase efficiency of 5-phase DS-SRMs in both constant torque and flux weakening region. The maximum efficiency of 72% can be achieved when speed is between 600rpm and 800rpm. The 7th order current harmonic injections can maintain the same level of efficiency as that of the fundamental current supply for the full speed range. However, the 5th order current harmonic will not be selected to suppress the torque ripple of 5-phase DS-SRM, since it degrades the efficiency for the full speed range and the modest efficiency can only achieve 44%.

Fig. 5.43 shows the efficiency maps under CPC condition for the 5-phase SL DS-SRM. It is not surprising that the dynamic performance of the machine with current harmonic injection in flux weakening region is the same as that of CRMS condition. The only difference is that the output torque in MTPA region has been reduced.

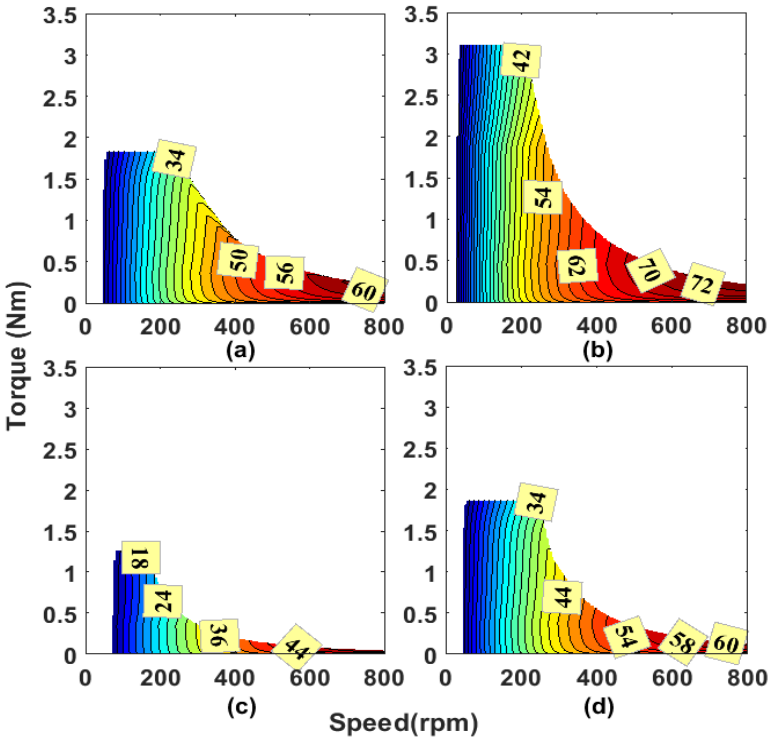

Fig. 5.42 Efficiency maps of the 5-phase SL DS-SRM with/without current harmonic injections. $I_{rms} = 5Arms$ and V_{dc} = 24V. (a) I_1, (b) I_1+I_3, (c) I_1+I_5 and (d) I_1+I_7.

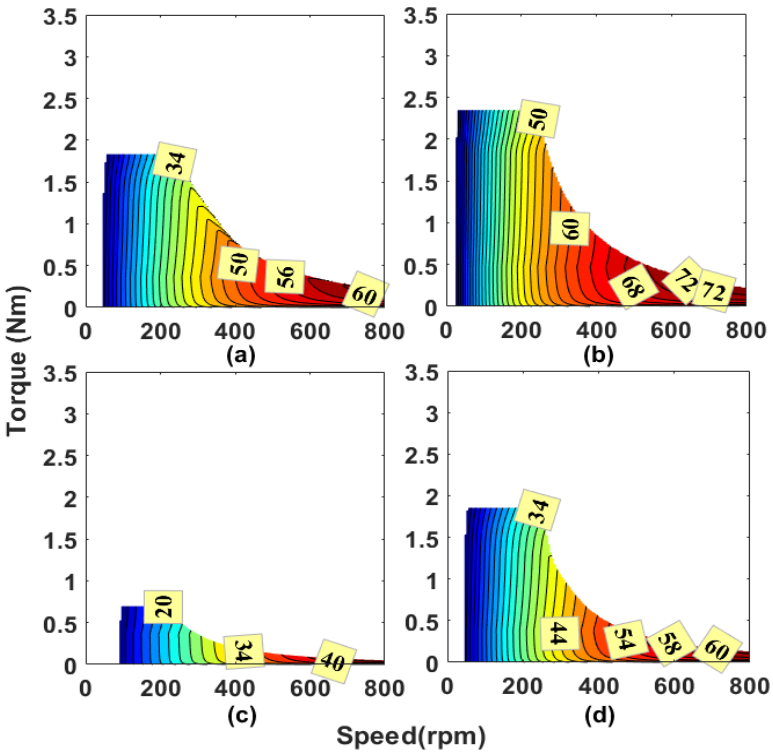

Fig. 5.43 Efficiency maps of the 5-phase SL DS-SRM with/without current harmonic injections. $I_{peak} = 7.07A$ and V_{dc} = 24V. (a) I_1, (b) I_1+I_3, (c) I_1+I_5 and (d) I_1+I_7.

5.4.2 6-PHASE DS-SRMS

5.4.2.1 IRON LOSSES

Similarly, the comparison of iron loss versus phase rms current of 6-phase DS-SRMs has also been investigated and the results are shown in Fig. 5.44. The same trend is presented that at low current level, the iron loss with 3rd order current harmonic injection is larger than that with 5th order harmonic injection, due to higher percentage of harmonic current has been injected for a better torque performance. With increasing phase current, the iron losses with the 5th order harmonic current injection exceed that of the 3rd order harmonic current injection. This is mainly due to the different effects of magnetic saturation on the different current harmonic injections. Fig. 5.45 clarifies iron loss distribution of each order flux harmonic with current harmonic injection. It shows that although the iron losses due to fundamental flux have been reduced, the injected current harmonic brings the extra losses in high order flux harmonic, leads to the resultant iron losses being increased.

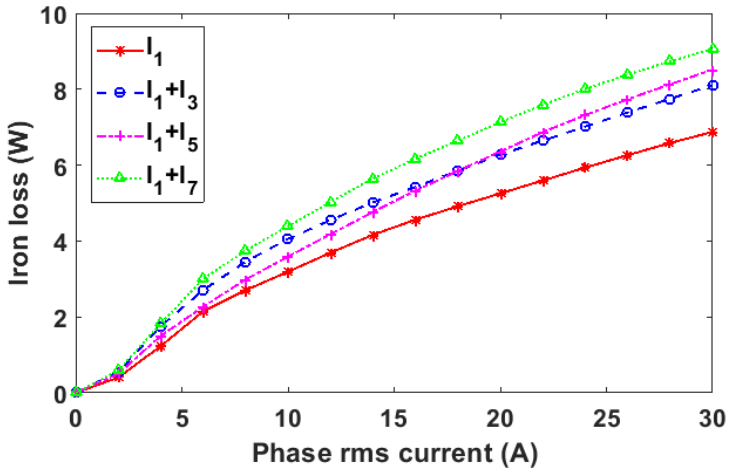

Fig. 5.44. Comparison of iron loss for 6-phase SL DS-SRM with current harmonic injection. Rotation speed is 400rpm.

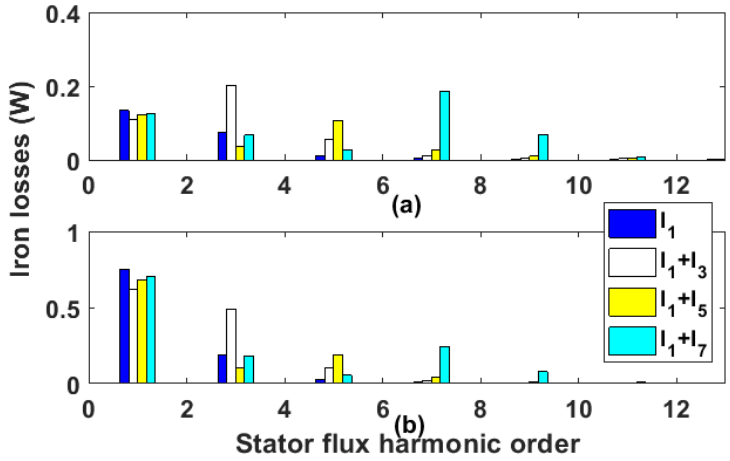

Fig. 5.45 Stator (a) eddy current losses and (b) hysteresis losses of for the 6-phase SL DS-SRM. Phase current is 5Arms and rot speed is 400rpm.

5.4.2.2 TORQUE-SPEED CHARACTERISTICS

It is worth noting that the 6-phase machine can be regarded as two 3-phase machines. As a result, the exactly same method in section 5.3.2 can be used to investigate the torque-speed characteristics of the 6-phase machine. The torque-speed curves for 6-phase SL DS-SRM under CRMS condition have been shown in Fig. 5.46. Again the 3rd order current harmonic shows the best performance in constant torque region but for this case, it slightly reduces the torque capability compared with the fundamental current supply in the flux weakening region. It is not surprising that the 5th and 7th order current harmonics will reduce the dynamic performance in both constant torque and flux weakening regions. This is due to the fact that they reduce the output torque and increase the voltage distortion, leading to limited flux weakening capability.

For CPC condition, as shown in Fig. 5.47, it is found that the current harmonic injection method will reduce the torque capability of such machine if the peak current is limited by the inverter.

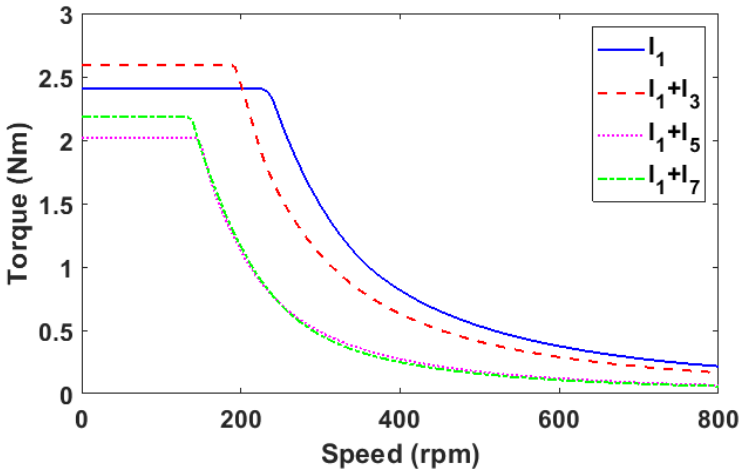

Fig. 5.46. Torque-speed curves of the 6-phase SL DS-SRM when $I_{rms} = 5Arms$ and V_{dc} = 24V.

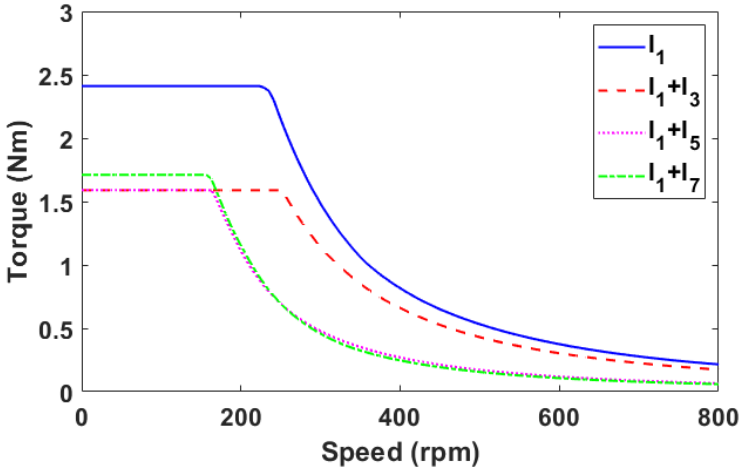

Fig. 5.47. Torque-speed curves of the 6-phase SL DS-SRM when $I_{peak} = 7.07A$ and V_{dc} = 24V.

5.4.2.3 Efficiency Maps

The efficiency maps of CRMS condition have been calculated, as shown in Fig. 5.48. It can be found that a maximum efficiency of 72% is achieved by the 3rd order current harmonic injection between 600rpm and 800rpm. Although the efficiency at base speed with the 3rd order current harmonic injection is reduced, it can still increase the efficiency in the lower speed region, due to extra torque production. However, the 5th and 7th order current harmonic injections degrade the efficiency for the full speed range. A modest efficiency of 64% can be

achieved at speeds ~600 rpm. The efficiency maps of CPC condition have also been shown in Fig. 5.49.

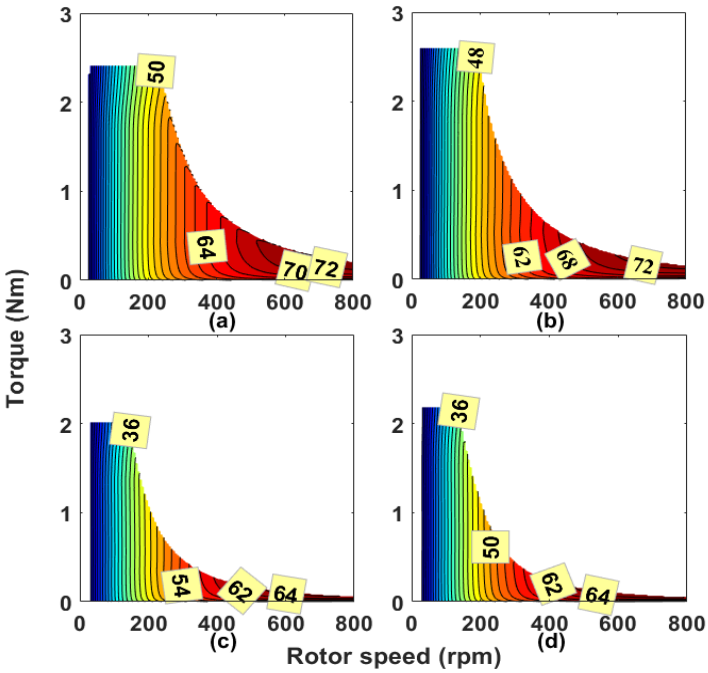

Fig. 5.48 Efficiency maps of the SL 6-phase DS-SRM with/without current harmonic injections. $I_{rms} = 5Arms$ and V_{dc} = 24V. (a) I_1, (b) I_1+I_3, (c) I_1+I_5 and (d) I_1+I_7.

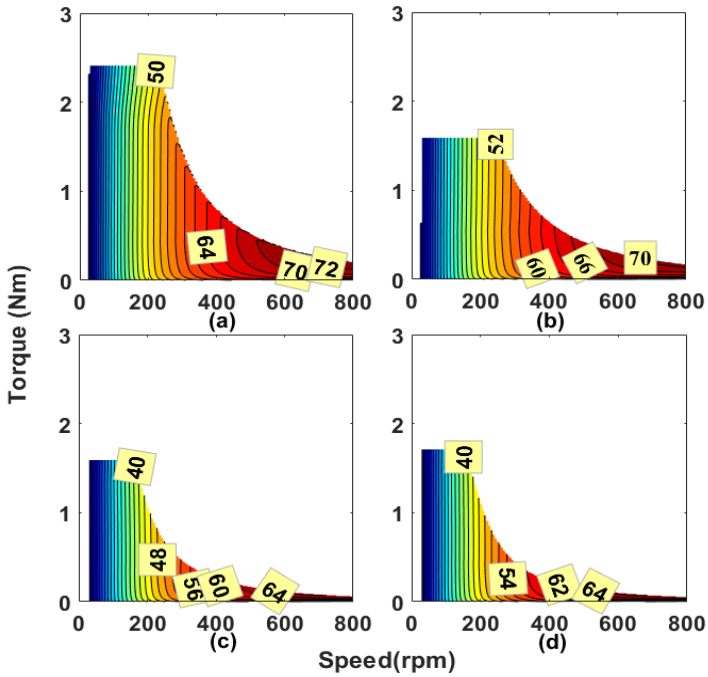

Fig. 5.49 Efficiency maps of the SL 6-phase DS-SRM with/without current harmonic injections. $I_{peak} = 7.07A$ and V_{dc} = 24V. (a) I_1, (b) I_1+I_3, (c) I_1+I_5 and (d) I_1+I_7.

5.5 CONCLUSION

After investigating the losses and efficiency of three typical types of 3-phase DS-SRMs, i.e. DL, SL and FP. It is found that at relatively low phase current, the FP DS-SRM can achieve the highest efficiency. Although the DL machine has the lowest efficiency, its increasing rate of efficiency is the fastest compared with other machines. Especially under high phase current condition, the efficiency of the DL machine exceeds that of the FP machine.

It is also found when higher order harmonic current is injected, the DS-SRM will generally produce higher iron losses. However, the 3rd order current harmonic has little influence on the flux density of the DL machine. As a result, the iron loss and torque performance have nearly no difference before and after injecting the 3rd order current harmonic. This is different for both the SL and FP machines. Even though the 3rd order current harmonic can bring extra losses, due to the significant improvement in average torque, the efficiency can still be increased by around 3-5%. Moreover, the 5th and 7th order current harmonics, although can be used to reduce the torque ripple, might contribute to extra losses and hence lead to reduced machine efficiency.

This chapter also investigates dynamic performances, such as torque-speed curves and efficiency maps, for 3-phase DS-SRMs with current harmonic injection. In order to simplify the investigation of dynamic performance, an analytical torque model based on the *dq0*-axis frame DS-SRMs with current harmonic injection is proposed. Similar to the model in *abc*-axis frame, such an analytical model can also provide a powerful insight into the mechanism of torque generation, which allows for the optimum current harmonic to be injected to reduce the torque ripple and/or improve the average torque.

When the current and inductance harmonics are both considered, the voltage distortion will be increased. As a result, for a given DC-bus voltage, the achievable base speed of the DS-SRMs will be reduced. However, if the phase rms current is kept constant, due to extra average torque that can be produced, the 3rd order current harmonic injection shows the best performance in constant torque region. In flux-weakening region, the 3rd order harmonic current injection can achieve similar torque performance as that supplied with fundamental current. Moreover, the 3rd order current harmonic can achieve the highest efficiency compared with other harmonic current injections.

However, the 5th and 7th order current harmonics, although can be effective in reducing the torque ripple, will lead to reduction in average torque and also high voltage distortion. If the phase peak current is limited by the inverter current constraint, the proposed current harmonic

injection method might have negative impact on the dynamic performance, since the phase rms current needs to be reduced for the same peak current.

Based on the investigation of 3-phase (i.e. SL, DL, FP) and multi-phase (SL 5- and 6-phase) DS-SRMs, the general conclusion of current harmonic injection can be drawn, i.e. the current harmonic injection will bring extra iron losses, generally, the k^{th} order current harmonic injection will increase the iron losses due to the k^{th} order flux density. However, once the injected harmonic current is properly selected, the efficiency at constant torque region could be improved and the same flux weakening capability as pure fundamental current supply could be maintained.

Chapter 6 EXPERIMENTAL VERIFICATION

Previous chapters proposed the current harmonic injection method to improve torque performances for several DS-SRMs with different winding structures, slot/pole number combinations and also phase numbers. The proposed methods have been validated by both analytical modelling and also 2D-FEA simulations. However, there are still some challenges left, for example, how to implement the proposed method under actual situation, especially to inject the 3rd order current harmonic with zero-sequence current. Therefore, this chapter will use four prototype DS-SRMs to evaluate the feasibility and effectiveness of the proposed method in practice. It is worth noting that both static and dynamic tests have been carried out in this chapter.

6.1 INTRODUCTION

Chapter 2-Chapter 4 proposed the current harmonic injection method to improve the average torque and to reduce the torque ripple of the DS-SRMs, and Chapter 5 also investigates the losses, efficiency and dynamic performance of proposed method. In order to validate the effectiveness of the proposed methods, two 12s/8p prototype DS-SRMs with different winding configurations, i.e. double layer (DL) and single layer (SL), have been adopted for experimental verifications. The design specifications are shown in TABLE 2.1. Fig. 6.1 (a) and (b) show the stator windings for SL and DL machines, respectively. The common rotor used for both the SL and DL machines is shown in Fig. 6.1 (c). It is worth noting that the existing prototype machines can be converted from 3-phase machine to 6-phase machine and vice versa by changing stator winding connections. When they are controlled as 6-phase, the number of turns per phase are reduced by half compared to the 3-phase version. This means that the 2D-FE and predicted results should be changed correspondingly. It is worth noting that only the 3-phase and 6-phase DS-SRMs have been tested. This is due to the fact that manufacturing machines can be time consuming and the existing prototype machines is enough for validating the proposed method. The experimental verification is separated into two parts, namely, static test and dynamic test.

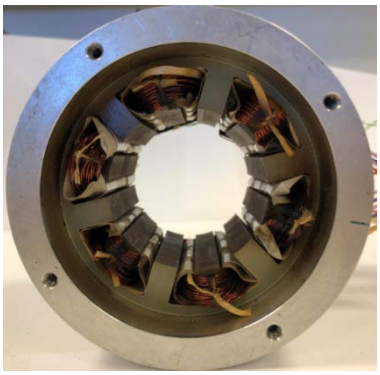

(a) SL stator

(b) DL stator

(c) Rotor

Fig. 6.1. 12s/8p prototype DS-SRMs.

6.2 STATIC TEST

6.2.1 METHODOLOGIES

The static test has been carried out in this section, the methodology to measure the static torque is detailed in the [167]. The equipment required for carrying out the tests are the power supplies, digital scale, balance beam and pre-load weight. Once equipment is set up as shown in Fig. 6.2, mass m^* at each rotor position with relative dc current can be measured by the digital scale. And the static torque at different rotor positons can be calculated by

$$T = (m^* - m)gL \tag{6.1}$$

where L is the length from the centre to the end of the balance beam, m is the pre-load weight added on the end of the balance beam and g is gravitational acceleration, i.e. $g = 9.81\text{m/s}^2$.

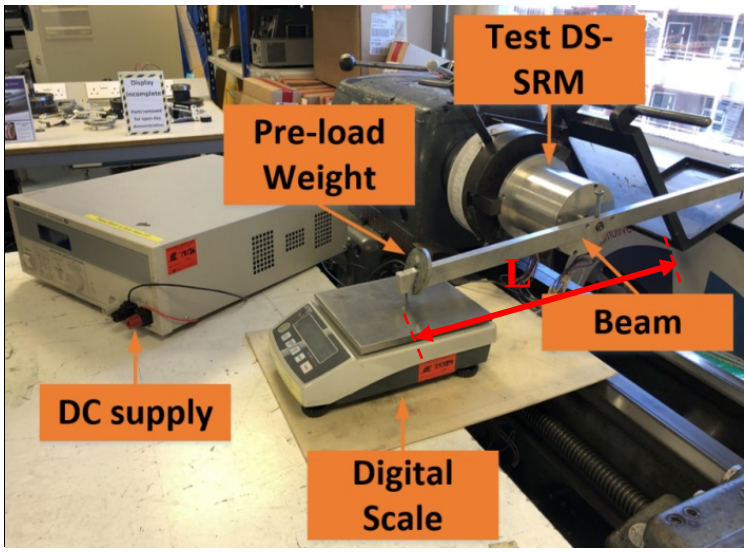

Fig. 6.2. Test rig and prototype machine for static tests.

6.2.2 TEST OF 3-PHASE DS-SRM

The fundamental characteristics of the 3-phase DS-SRMs such as self- and mutual-inductances, static torque with dc current, efficiency, etc. were tested in [67]. The static on-load torque with proposed harmonic current injection methods have been carried out in the following sections. To simulate the 3-phase AC current supply under static conditions and also to account for current harmonics, at each rotor position for one electrical period, 3-phase dc currents are supplied. These 3-phase dc currents are adjusted such that they are equal to the exact values of 3-phase AC currents at each rotor position. The phase rms current is 5A. The static on-load torques when current harmonic is injected to achieve the minimum torque ripple

can then be measured as shown in Fig. 6.3. Overall, a good agreement between the predictions and measurements can be observed.

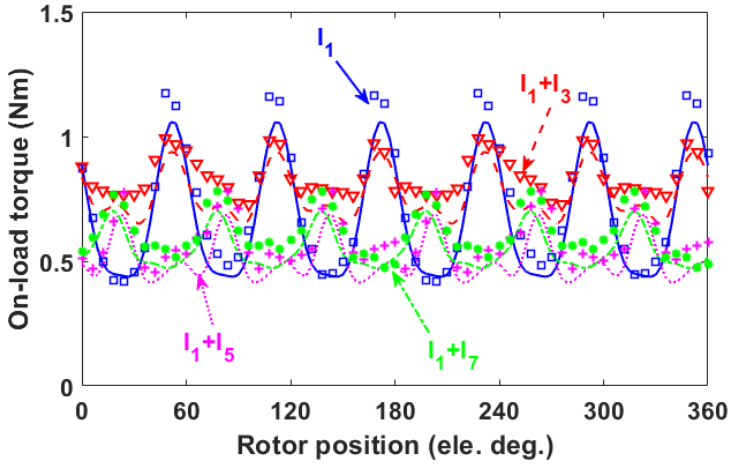

(a) SL

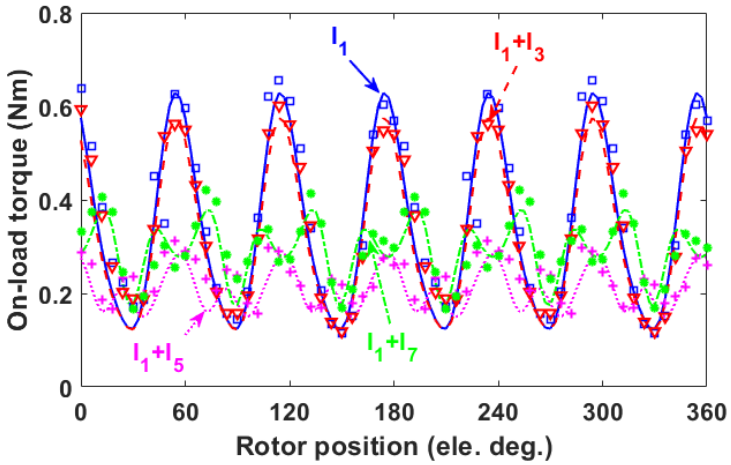

(b) DL

Fig. 6.3 Static on-load torque for 12s/8p 3-phase DS-SRMs with current harmonic injection for a phase current of 5Arm. (Lines: predicted results, marks: measured results).

Fig. 6.4 shows the torque spectra of two DS-SRMs with current harmonic injection. It is proved that the 3rd order current harmonic injection exhibits the best performance for the SL machine, which can increase the average torque by 13% while reducing the 6th order torque harmonic by 70% as investigated in Chapter 2. Although the torque ripple of the SL machine can be reduced by the 5th and 7th order current harmonic injections, the average torque is reduced by around 12% with the specific phase angles. Moreover, it is also validated that the 3rd order current harmonic has little effect on the DL machine which was investigated in Chapter 3. This is due to the fact that the harmonic torques due to the self- and mutual-

inductances are cancelled. For such a machine, the other order current harmonics, e.g. 5th and 7th, still can be utilized to reduce the torque ripple.

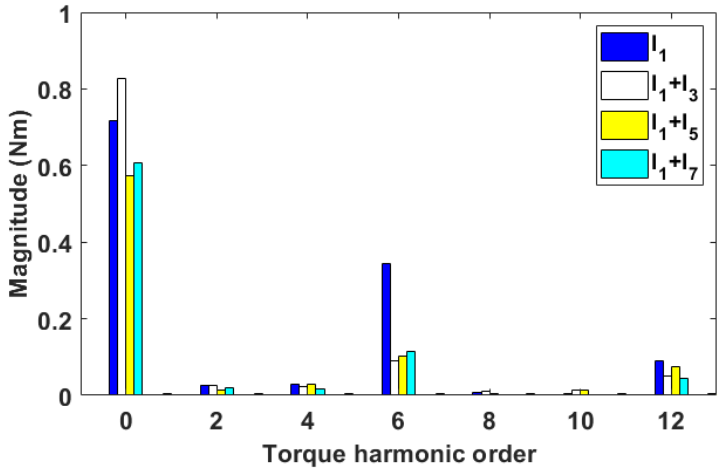

(a) SL

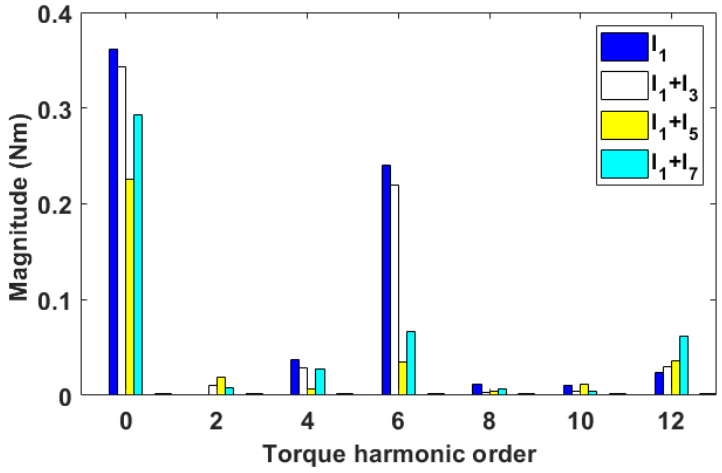

(b) DL

Fig. 6.4 Static torque spectra for 12s/8p 3-phase DS-SRMs with current harmonic injection for phase current of 5Arm.

6.2.3 TEST OF MULTI-PHASE DS-SRM

As mentioned in section 6.1, in order to validate the torque capability of proposed 6-phase SL and DL DS-SRMs (12s/8p), two 6-phase prototype DS-SRMs with SL and DL windings, have been tested. It is worth noting that all multi-phase SRMs in Chapter 4 have the same number of turns per phase (132). However, due to the fact that the tested 6-phase machines are converted from 3-phase machines, the number of turns per phase are reduced by half (66). This means that the inductance will in theory be reduced by four times. To be consistent with the prototype machines, in the experimental validation section, the number of turns per phase in

the FEA models is also reduced to 66. This test is relevant to the investigations carried out in Chapter 4.

6.2.3.1 SELF- AND MUTUAL-INDUCTANCES

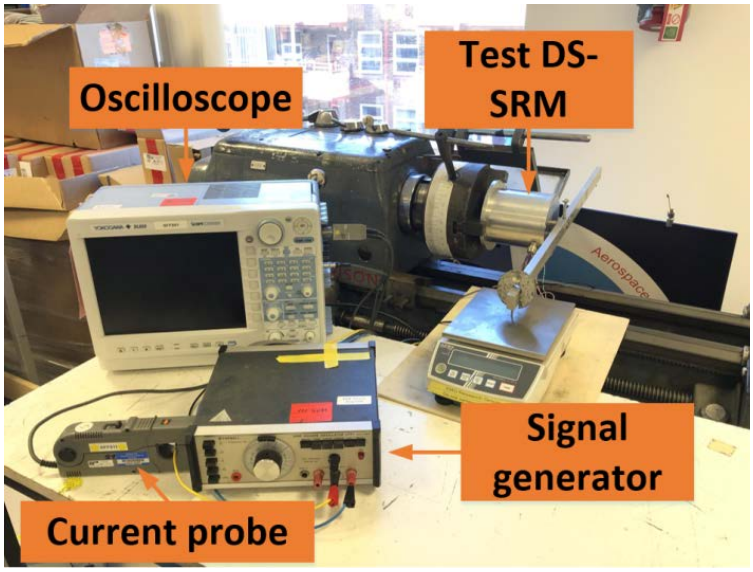

Fig. 6.5. Test rig and prototype machine for inductance measurement.

First of all, the inductance measurement of the 6-phase DS-SRMs has been carried out. The self-inductance L_a and mutual-inductance M_{aj} are measured according to (6.2) and (6.3) as detailed in [29].

$$L_a(\theta) = \frac{\sqrt{(V_a/I_a)^2 - {R_a}^2}}{2\pi f} \tag{6.2}$$

$$M_{aj}(\theta) = \frac{V_j}{2\pi f I_a} \tag{6.3}$$

where j can be phase b, c, d, e and f. V_a and V_j are the voltage of phase A and phase j, respectively. I_a is the magnitude of phase A current and f is the frequency of the injected phase voltage. Phase resistance R_a is measured as 0.7Ω and 0.8Ω for 6-phase SL and DL DS-SRMs, respectively.

The test rig for inductance measurement is shown in Fig. 6.5. During the test, the sinusoidal voltage source with a frequency of 100Hz and a magnitude of 2.5V has been injected into phase A by signal generator. And the phase A current and voltage can be measured and displayed on the oscilloscope. The self- and mutual-inductances can be obtained, as shown in Fig. 6.6 and Fig. 6.7, respectively. Overall, a good agreement in both the trend and magnitude can be

observed. It is worth noting that the slight discrepancy between 2D-FE and measurement is mainly due to the fact that the end-winding effect has not been taken into account in the simulations.

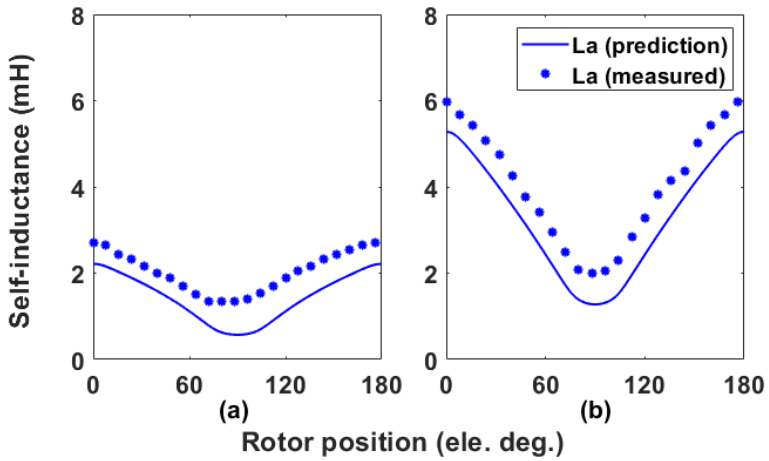

Fig. 6.6. FEA and measured self-inductance (L_a) for 12s/8p 6-phase DS-SRMs when phase A is supplied with a 2A dc current (FEA simulations). (a) DL and (b) SL.

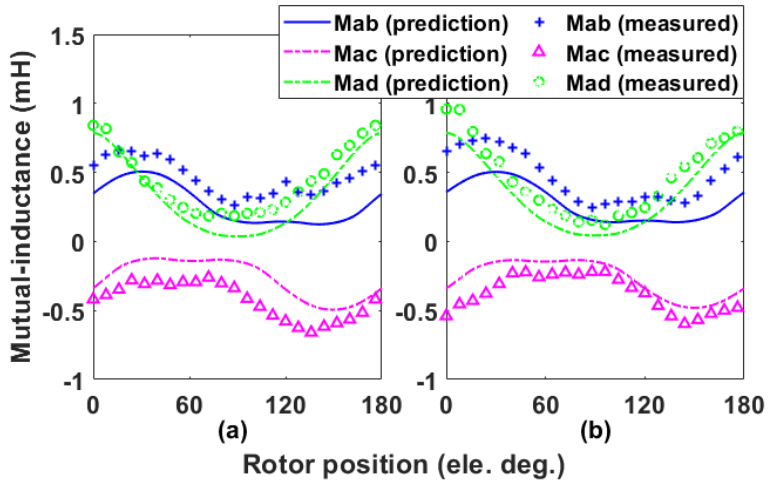

Fig. 6.7. FEA and measured mutual inductances with different distance (M_{ab}, M_{ac}, and M_{ad}) for 12s/8p 6-phase DS-SRMs when phase A is supplied with a 2A dc current (FEA simulations). (a) DL and (b) SL.

6.2.3.2 SELF- AND MUTUAL-TORQUES

Apart from the inductance measurement, the static torques due to self- and mutual-inductance have also been measured. The method of static torque measurement is introduced in section 6.2.1. The self-torque can be measured by supplying one single phase with a dc current. For example, 2A dc current is supplied to phase A, and the self-torque T_a can be

obtained as shown in Fig. 6.8. To measure the mutual-torque, firstly, the same level of dc current (2A) is supplied to two phases connected in series, e.g. phases A and B, the resultant torque (T_a + T_b + T_{ab}) can be measured for different rotor positions as shown Fig. 6.9. Then, the mutual torque (T_{ab}) can be easily obtained by subtracting self-torques of phases A and B, i.e. T_a and T_b, and the results are shown in Fig. 6.10. It shows that both double and single layer machines have similar level of mutual-torque.

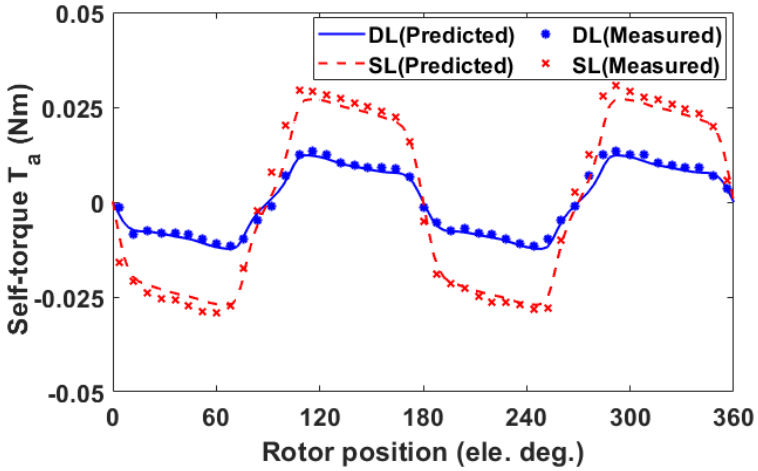

Fig. 6.8. FEA and measured resultant self-torques T_a for 12s/8p 6-phase DS-SRMs when phase A is supplied with a 2A dc current. (a) DL and (b) SL.

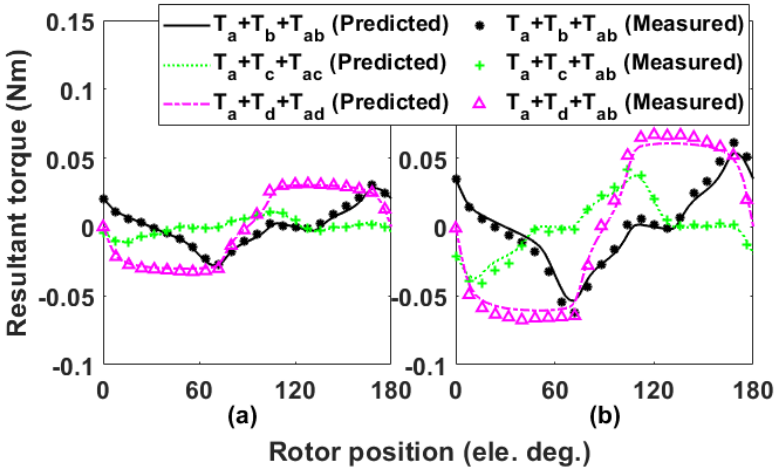

Fig. 6.9. FEA and measured resultant-torques with different distance (Detailed in Fig. 4.3) for 12s/8p 6-phase DS-SRMs when phase A and B are supplied with a 2A dc current. (a) DL and (b) SL.

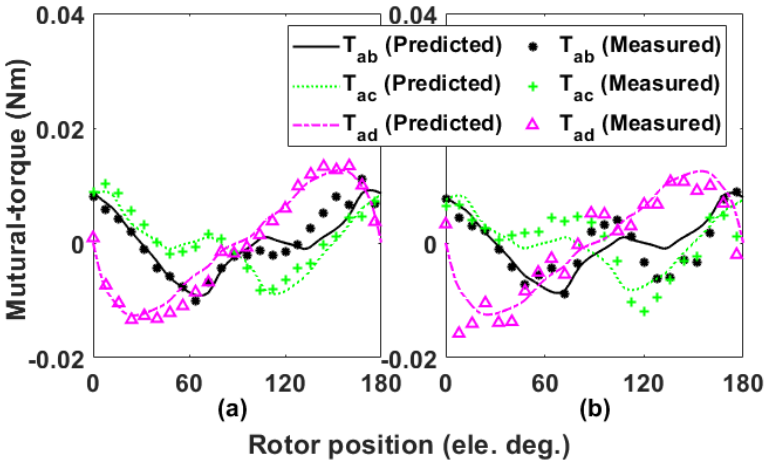

Fig. 6.10. FEA and measured mutual-torques with different distance (Detailed in Fig. 4.3) for 12s/8p 6-phase DS-SRMs when phase A is supplied with a 2A dc current. (a) DL and (b) SL.

6.2.3.3 STATIC TORQUE VS PHASE CURRENT

In this section, machines are tested under a pseudo sinewave current condition ($I_A = I$, $I_B = I/2$, $I_C = -I/2$, $I_D = -I$, $I_E = -I/2$, and $I_F = I/2$), where I is dc current which is 2.83A (2A RMS). The static torque at each rotor position (equivalent to current phase advance angle) can be measured as shown in Fig. 6.11.

After rotor is locked at the position where the maximum average torque can be achieved (phase advance angle of 45° for synchronous reluctance machines), the static torque against phase RMS current can be measured and compared with FEA results, as shown in Fig. 6.12. Overall, good agreement can be observed between the predicted and measured results.

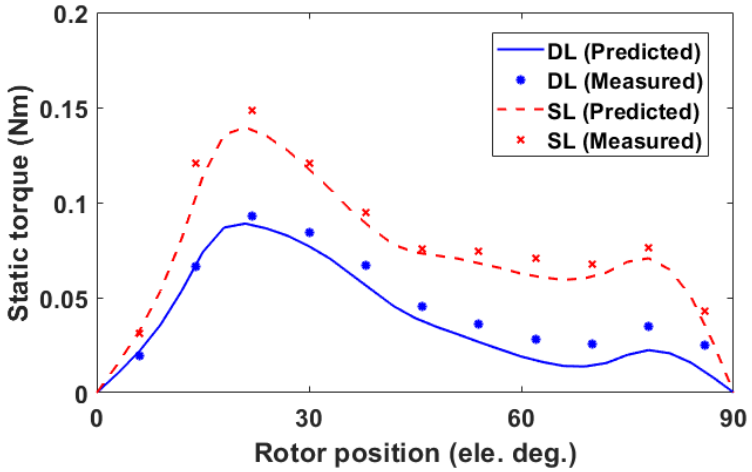

Fig. 6.11. FEA and measured static torques versus rotor position at 2A phase RMS current for 12s/8p 6-phase DS-SRMs.

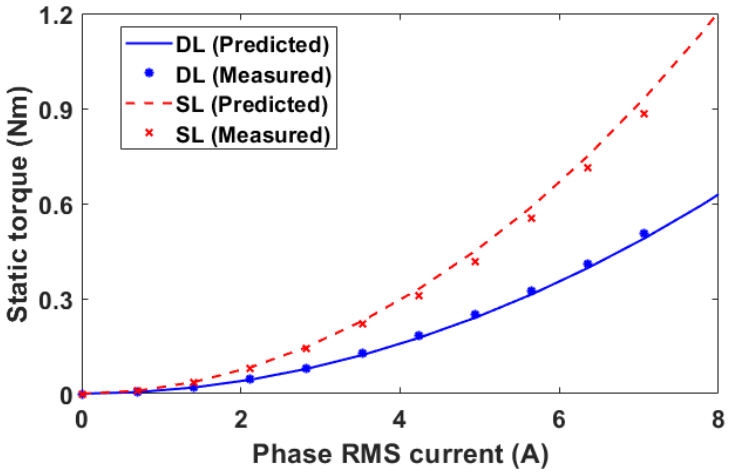

Fig. 6.12 FEA and measured static torques versus phase RMS current for 12s/8p 6-phase DS-SRMs.

6.2.3.4 ON-LOAD STATIC TORQUE

In order to measure on-load static torque versus rotor positions for 6-phase DS-SRMs under sinewave excitation, at least 4 current generators are required if using the same measurement methods as 3-phase machine. This is very inconvenient. However, it is much easier to use two 3-phase half-bridge inverters to control the 6-phase currents. During the test, the rotors are locked at different rotor positions. At each rotor position, 6-phase dc currents are supplied to the machines, and the amplitudes of these currents are chosen according to the values of 6-phase sinewave currents at different rotor positions. The torque can then be measured by torque transducer. The control method will be detailed in dynamic test parts. It is worth noting that due to the limitation of laboratory facilities, there is no extra half bridge inverter available which allows the zero-sequence current to pass through. Therefore, the 3^{rd} order current harmonic cannot been injected, and only the tests with the 5^{th} and 7^{th} order current injections have been carried out. It is worth noting that, due to the inaccuracy of the torque transducer, higher phase RMS current (5A) has been chosen in this test in order to improve the signal to noise ratio. Fig. 6.13 shows the predicted and measured on-load torques. It is proved that for both the SL and DL 6-phase DS-SRMs, the 5^{th} and 7^{th} order current harmonic injection can reduce the torque ripple significantly.

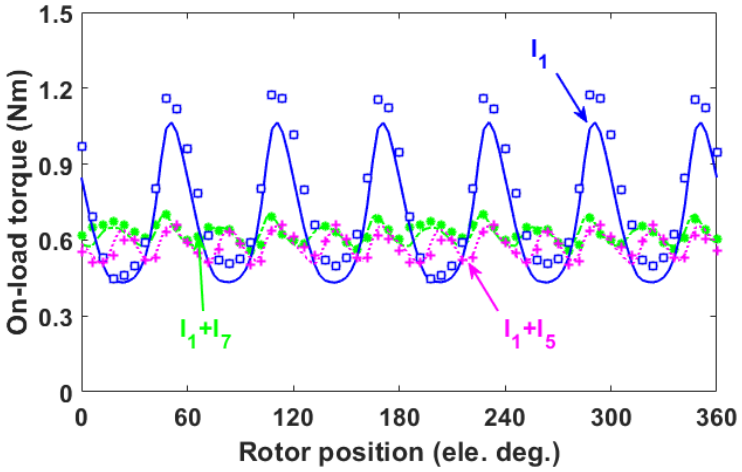

(a) SL

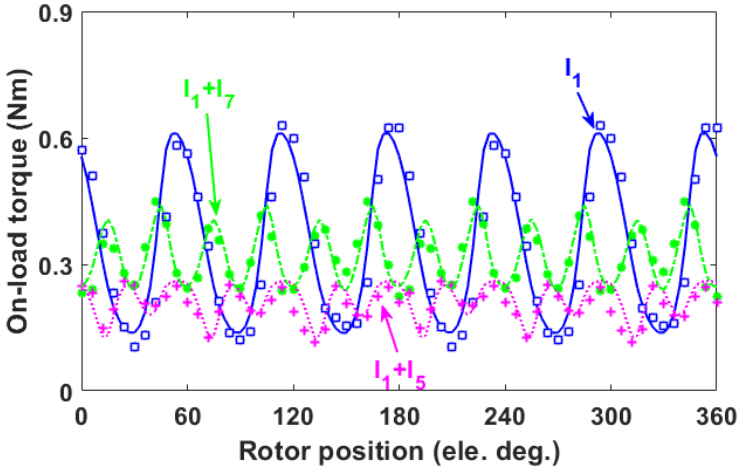

(a) DL

Fig. 6.13 FEA and measured on-load static torques for 12s/8p 6-phase DS-SRMs versus rotor position at 5A phase RMS current.

6.3 Dynamic Test

Dynamic test has been investigated in this section. Due to the fact that when the 3rd order current harmonic is injected, the current flow at neutral point is not equal to zero. The simplest way to deal with zero-sequence current is to use the three-phase H-bridge inverter, as shown in Fig. 6.14 (a), and control the three-phase currents separately. However, it will potentially increase the cost and losses in the inverter. In order to achieve zero-sequence current control in an economical and efficient way, at least one extra leg, compared with conventional three-phase voltage source inverter for synchronous machine, is required to provide the flow path for zero-sequence current. Hence, the three-phase four-leg inverter shown in Fig. 6.14 (b) will be utilized and investigated for injecting the current harmonics. For such inverter, the new pulse

width modulation (PWM) method introduced in [162],[163]has been reproduced to achieve current harmonic injection. Fig. 6.15 shows the test rig and prototype machine for dynamic test.

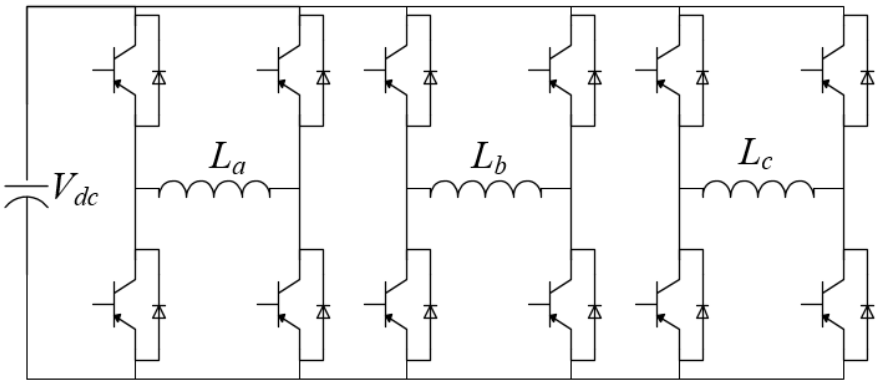

(a) H-bridge invester

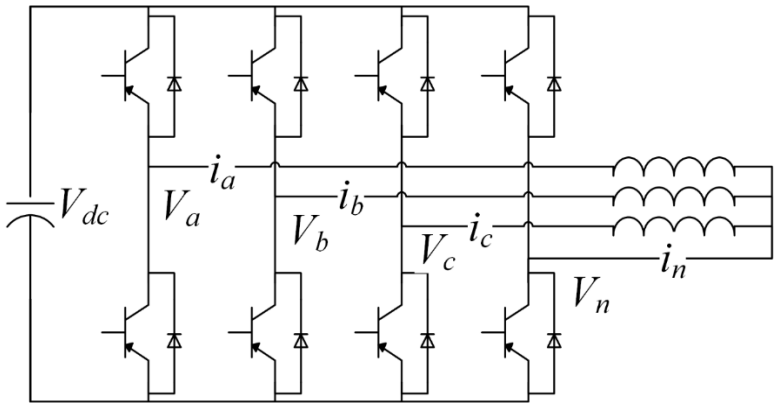

(b) Three-phase four-leg inverter

Fig. 6.14 Voltage source inverter for 3rd order current harmonic injection.

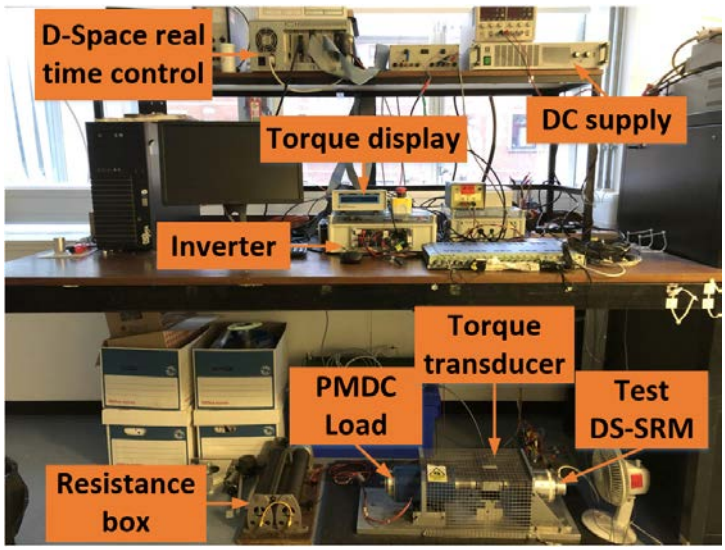

Fig. 6.15 Test rig and prototype machine for dynamic tests.

6.3.1 THREE-DIMENSIONAL SPACE VECTOR PULSE WIDTH MODULATION (3D SVPWM)

6.3.1.1 SWITCHING VECTORS IN THREE DIMENSIONAL SPACE

For the three-phase four-leg inverter, the system voltages are unbalanced as:

$$V_{an} + V_{bn} + V_{cn} \neq 0 \tag{6.4}$$

In this case the equivalent space voltage vector is moving in the space (three dimensional space). For the four wire networks, unbalanced three phase current can be obtained and the zero-sequence current can be defined by:

$$i_a + i_b + i_c = i_n \neq 0 \tag{6.5}$$

TABLE 6.1 SWITCHING COMBINATIONS AND PHASE TO NEUTRAL POINT VOLTAGE FOR EACH SWITCHING STATE.

Vector	S_a	S_b	S_c	S_n	V_{an}	V_{bn}	V_{cn}
V_1	0	0	0	0	0	0	0
V_2	0	0	0	1	$-V_{dc}$	$-V_{dc}$	$-V_{dc}$
V_3	0	0	1	0	0	0	V_{dc}
V_4	0	0	1	1	$-V_{dc}$	$-V_{dc}$	0
V_5	0	1	0	0	0	V_{dc}	0
V_6	0	1	0	1	$-V_{dc}$	0	$-V_{dc}$
V_7	0	1	1	0	0	V_{dc}	V_{dc}
V_8	0	1	1	1	$-V_{dc}$	0	0
V_9	1	0	0	0	V_{dc}	0	0
V_{10}	1	0	0	1	0	$-V_{dc}$	$-V_{dc}$
V_{11}	1	0	1	0	V_{dc}	0	V_{dc}
V_{12}	1	0	1	1	0	$-V_{dc}$	0
V_{13}	1	1	0	0	V_{dc}	V_{dc}	0
V_{14}	1	1	0	1	0	0	$-V_{dc}$
V_{15}	1	1	1	0	V_{dc}	V_{dc}	V_{dc}
V_{16}	1	1	1	1	0	0	0

As well established, for each leg of the inverter, there are two switching states, i.e. “1” and “0”, where “1” means the top switch in the leg is on and bottom switch is off, while “0” is the opposite. Therefore, in the three-phase four-leg inverter there are sixteen (2^4) different combination of switching states. Each of these switching states represents a certain space

vector. And two of them are zero switching vectors (ZSV) and the rest are fourteen non-zero switching vectors (NZSV). The phase to neutral point voltage for all switching states can be calculated by (6.6), as shown in TABLE 6.1

$$\begin{bmatrix} V_{an} \\ V_{bn} \\ V_{cn} \end{bmatrix} = \begin{bmatrix} 1 & 0 & 0 & -1 \\ 0 & 1 & 0 & -1 \\ 0 & 0 & 0 & -1 \end{bmatrix} \begin{bmatrix} S_a \\ S_b \\ S_c \\ S_n \end{bmatrix} \cdot V_{dc} \tag{6.6}$$

After implementing the Clarke transformation given in (6.7), the switching space vectors in $\alpha\beta\gamma$-axis can be obtained, as listed in TABLE 6.2. These space vectors can be plotted in space as shown in Fig. 6.16 (a). It is worth noting that $\alpha\beta$ plane is the plane in which $V_{an} + V_{bn} + V_{cn} = 0$ and γ-axis represents zero-sequence component. The top view of these vectors would form a regular hexagon as shown in Fig. 6.16 (b)

$$V_{ref} = \begin{bmatrix} V_\alpha \\ V_\beta \\ V_\gamma \end{bmatrix} = \frac{2}{3} \begin{bmatrix} 1 & \frac{-1}{2} & \frac{-1}{2} \\ 0 & \frac{\sqrt{3}}{2} & \frac{-\sqrt{3}}{2} \\ \frac{1}{2} & \frac{1}{2} & \frac{1}{2} \end{bmatrix} \begin{bmatrix} V_{an} \\ V_{bn} \\ V_{cn} \end{bmatrix} \tag{6.7}$$

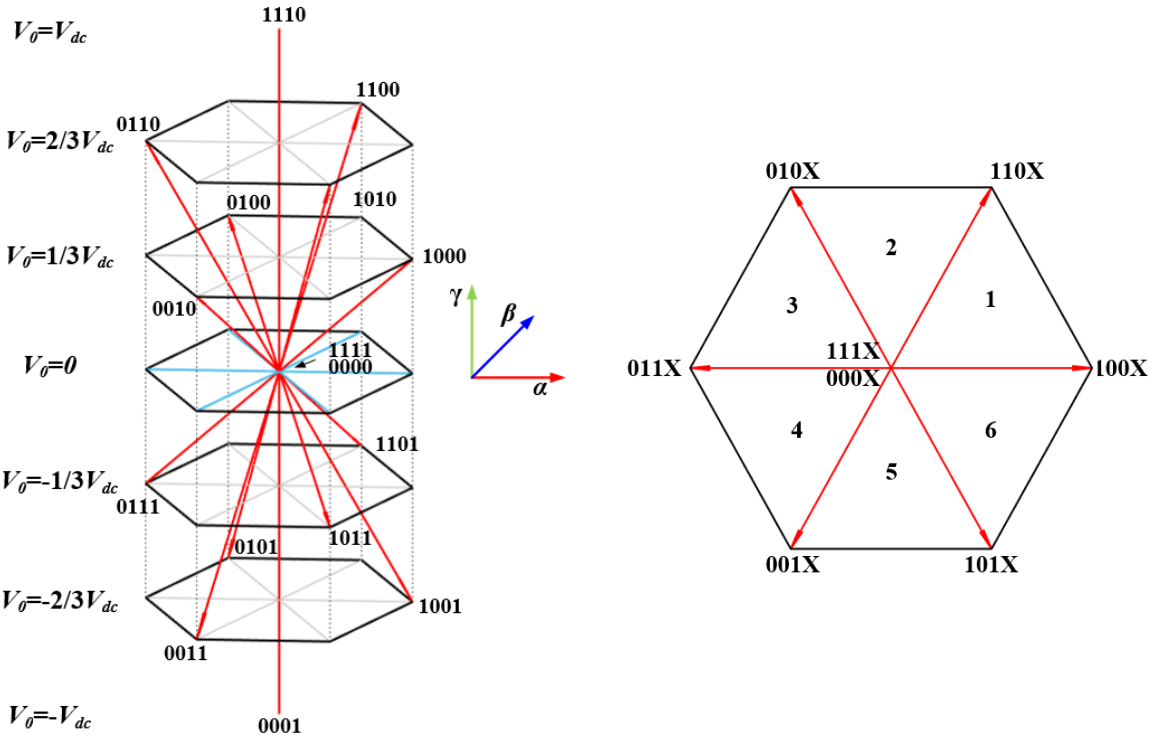

(a) Switching state vectors (b) Top view 6 sectors

Fig. 6.16 Switching vectors in $\alpha\beta\gamma$-axis frame.

TABLE 6.2 INVERTER VOLTAGES IN $\alpha\beta\gamma$-AXIS FOR SIXTEEN VOLTAGE VECTORS

Vector	V_α	V_β	V_γ
V_1	0	0	0
V_2	0	0	$-V_{dc}$
V_3	$-\frac{1}{3}V_{dc}$	$-\frac{\sqrt{3}}{3}V_{dc}$	$\frac{1}{3}V_{dc}$
V_4	$-\frac{1}{3}V_{dc}$	$-\frac{\sqrt{3}}{3}V_{dc}$	$-\frac{2}{3}V_{dc}$
V_5	$-\frac{1}{3}V_{dc}$	$\frac{\sqrt{3}}{3}V_{dc}$	$\frac{1}{3}V_{dc}$
V_6	$-\frac{1}{3}V_{dc}$	$\frac{\sqrt{3}}{3}V_{dc}$	$-\frac{2}{3}V_{dc}$
V_7	$-\frac{2}{3}V_{dc}$	0	$\frac{2}{3}V_{dc}$
V_8	$-\frac{2}{3}V_{dc}$	0	$-\frac{1}{3}V_{dc}$
V_9	$\frac{2}{3}V_{dc}$	0	$\frac{1}{3}V_{dc}$
V_{10}	$\frac{2}{3}V_{dc}$	0	$-\frac{2}{3}V_{dc}$
V_{11}	$\frac{1}{3}V_{dc}$	$-\frac{\sqrt{3}}{3}V_{dc}$	$\frac{2}{3}V_{dc}$
V_{12}	$\frac{1}{3}V_{dc}$	$-\frac{\sqrt{3}}{3}V_{dc}$	$-\frac{1}{3}V_{dc}$
V_{13}	$\frac{1}{3}V_{dc}$	$\frac{\sqrt{3}}{3}V_{dc}$	$\frac{2}{3}V_{dc}$
V_{14}	$\frac{1}{3}V_{dc}$	$\frac{\sqrt{3}}{3}V_{dc}$	$-\frac{1}{3}V_{dc}$
V_{15}	0	0	1
V_{16}	0	0	0

6.3.1.2 SYNTHESIS OF THE REFERENCE VECTOR

Similar to 2D SVPWM, the reference vector V_{ref} is synthesized by using different space vectors in different sectors. However, the 3D SVPWM will be more complex due to the fact that the number of space vectors is doubled and the dimension is upgraded. The synthesis of V_{ref} is divided into two steps:

1) Selection of space vectors;
2) Calculation of duty cycle.

Step 1: Selection of space vectors: In order to minimize the circulating energy and reduce the current ripple, the space vectors which adjacent to V_{ref} should be selected. Different from the 2D SVPWM, there are two steps required to determine the space vector for the 3D SVPWM, namely, sector identification and tetrahedron identification.

There are six sectors in the three-dimensional space, as shown in Fig. 6.16 (b). Similar to the sector identification for the 2D SVPWM, the sector number for the 3D SVPWM can be easily identified by using (6.8) and (6.9).

$$Sector\ No. \begin{cases} 1 & 0° \le \theta_{\alpha\beta} < 60° \\ 2 & 60° \le \theta_{\alpha\beta} < 120° \\ 3 & 120° \le \theta_{\alpha\beta} < 180° \\ 4 & 180° \le \theta_{\alpha\beta} < 240° \\ 5 & 240° \le \theta_{\alpha\beta} < 300° \\ 6 & 300° \le \theta_{\alpha\beta} < 360° \end{cases} \tag{6.8}$$

$$\theta_{\alpha\beta} = \tan^{-1}\frac{V_\beta}{V_\alpha} \tag{6.9}$$

Moreover, there are six NZSVs and two ZSVs in each sector, e.g. Sector 5 in Fig. 6.17, which divide the prism into four tetrahedrons. Numbering the tetrahedron from bottom to top would identify from tetrahedrons I and II at lower half of the cylinder and tetrahedrons III and VI at the upper half of the cylinder. The V_{ref} lies in one of these tetrahedrons and three space vectors of the tetrahedron together with two ZSVs are utilized to synthesise V_{ref}. It is worth noting that the line to neutral voltage polarities produced by each NZSV are different as shown in TABLE 6.1, which can be the way of selecting the tetrahedron in each sector. (6.10) expresses the determination of the tetrahedron. Finally, the space can be divided into 24 tetrahedrons by the space vectors as listed TABLE 6.3.

$$Tetrahedron\ No. = \sum_{1}^{3} x_i \tag{6.10}$$

and

$$x_i = \begin{cases} 1 & V_i \ge 0 \\ 0 & V_i < 0 \end{cases} \text{ with } i = a, b, c \tag{6.11}$$

Step 2: Calculation of duty cycle: As mentioned previously, V_{ref} is synthesised by using the three adjacent NZSVs and two ZSVs. And the duty cycle of each space vector can be easily

computed by projecting them to $\alpha\beta\gamma$-axis. By way of example, in T18 (Tetrahedron II, Sector 5) as shown in Fig. 6.17, the available vectors are V_3, V_4, V_{12} and $V_{1,16}$. The corresponding duty cycle can be given by (6.12).

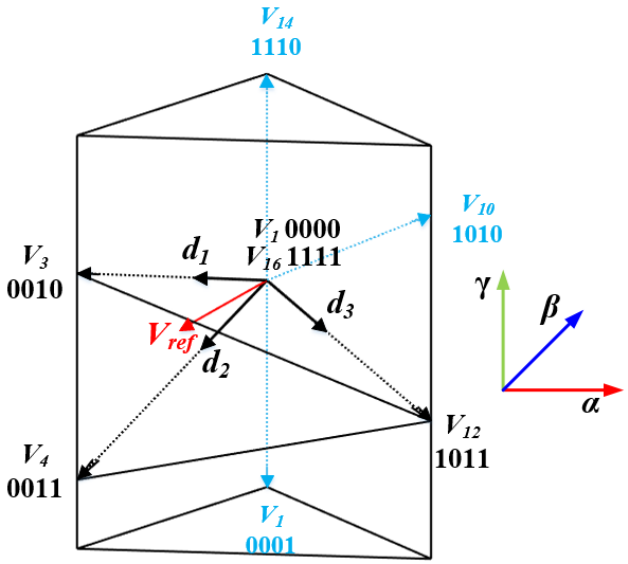

Fig. 6.17 Duty cycles for the active vector in T18 (Tetrahedron II, Sector 5).

$$\overrightarrow{V_{ref}} = d_1\overrightarrow{V_3} + d_2\overrightarrow{V_4} + d_3\overrightarrow{V_{12}} \tag{6.12}$$

Resolving into Cartesian coordinates:

$$\begin{bmatrix} V_\alpha \\ V_\beta \\ V_\gamma \end{bmatrix} = V_{dc} \begin{bmatrix} \frac{-1}{3} & \frac{-1}{3} & \frac{1}{3} \\ \frac{-\sqrt{3}}{3} & \frac{-\sqrt{3}}{3} & \frac{-\sqrt{3}}{3} \\ \frac{1}{3} & \frac{-2}{2} & \frac{-1}{3} \end{bmatrix} \begin{bmatrix} d_1 \\ d_2 \\ d_3 \end{bmatrix} \tag{6.13}$$

Therefore, the duty cycle for such tetrahedron can be calculated by (6.14) and (6.15). It is worth noting that for V_{ref} in other tetrahedrons, the only difference is to change the matrix in (6.14). The complete table for all 24 tetrahedrons is given TABLE 6.3.

$$\begin{bmatrix} d_1 \\ d_2 \\ d_3 \end{bmatrix} = \frac{1}{V_{dc}} \begin{bmatrix} \frac{-1}{3} & \frac{-1}{3} & \frac{1}{3} \\ \frac{-\sqrt{3}}{3} & \frac{-\sqrt{3}}{3} & \frac{-\sqrt{3}}{3} \\ \frac{1}{3} & \frac{-2}{2} & \frac{-1}{3} \end{bmatrix}^{-1} \begin{bmatrix} V_\alpha \\ V_\beta \\ V_\gamma \end{bmatrix} = \frac{1}{V_{dc}} \begin{bmatrix} \frac{-1}{2} & \frac{-\sqrt{3}}{2} & 1 \\ -1 & 0 & -1 \\ \frac{3}{2} & \frac{-\sqrt{3}}{2} & 0 \end{bmatrix} \begin{bmatrix} V_\alpha \\ V_\beta \\ V_\gamma \end{bmatrix} \tag{6.14}$$

$$d_0 = 1 - d_1 - d_2 - d_3 \tag{6.15}$$

TABLE 6.3 CORRESPONDING MATRICES TO COMPUTE THE DUTY RATIOS FOR ALL TETRAHEDRONS.

	Tetrahedron			
	I	II	III	IV
1	$T_1\ (V_2, V_{10}, V_{14})$ $\begin{bmatrix} -1 & 0 & -1 \\ \frac{2}{3} & \frac{-\sqrt{3}}{2} & 0 \\ 0 & -\sqrt{3} & 0 \end{bmatrix}$	$T_2\ (V_9, V_{10}, V_{14})$ $\begin{bmatrix} 1 & 0 & 1 \\ \frac{1}{2} & \frac{-\sqrt{3}}{2} & -1 \\ 0 & \sqrt{3} & 0 \end{bmatrix}$	$T_3\ (V_9, V_{13}, V_{14})$ $\begin{bmatrix} \frac{3}{2} & \frac{-\sqrt{3}}{2} & 0 \\ \frac{-1}{2} & \frac{\sqrt{3}}{2} & 1 \\ \frac{1}{2} & \frac{\sqrt{3}}{2} & -1 \end{bmatrix}$	$T_4\ (V_9, V_{13}, V_{15})$ $\begin{bmatrix} \frac{3}{2} & \frac{-\sqrt{3}}{2} & 0 \\ 0 & \sqrt{3} & 0 \\ \frac{-1}{2} & \frac{-\sqrt{3}}{2} & 1 \end{bmatrix}$
2	$T_5\ (V_2, V_6, V_{14})$ $\begin{bmatrix} \frac{1}{2} & \frac{-\sqrt{3}}{2} & -1 \\ \frac{-3}{2} & \frac{\sqrt{3}}{2} & 0 \\ \frac{3}{2} & \frac{\sqrt{3}}{2} & 0 \end{bmatrix}$	$T_6\ (V_5, V_6, V_{14})$ $\begin{bmatrix} \frac{-1}{2} & \frac{\sqrt{3}}{2} & 1 \\ -1 & 0 & -1 \\ \frac{3}{2} & \frac{\sqrt{3}}{2} & 0 \end{bmatrix}$	$T_7\ (V_5, V_{13}, V_{14})$ $\begin{bmatrix} \frac{-3}{2} & \frac{\sqrt{3}}{2} & 0 \\ 1 & 0 & 1 \\ \frac{1}{2} & \frac{\sqrt{3}}{2} & -1 \end{bmatrix}$	$T_8\ (V_5, V_{13}, V_{15})$ $\begin{bmatrix} \frac{-3}{2} & \frac{\sqrt{3}}{2} & 0 \\ \frac{3}{2} & \frac{\sqrt{3}}{2} & 0 \\ \frac{-1}{2} & \frac{-\sqrt{3}}{2} & 1 \end{bmatrix}$
3	$T_9\ (V_2, V_6, V_8)$ $\begin{bmatrix} \frac{1}{2} & \frac{-\sqrt{3}}{2} & -1 \\ 0 & \sqrt{3} & 0 \\ \frac{-3}{2} & \frac{-\sqrt{3}}{2} & 0 \end{bmatrix}$	$T_{10}\ (V_5, V_6, V_8)$ $\begin{bmatrix} \frac{-1}{2} & \frac{\sqrt{3}}{2} & 1 \\ \frac{1}{2} & \frac{\sqrt{3}}{2} & -1 \\ \frac{-3}{2} & \frac{-\sqrt{3}}{2} & 0 \end{bmatrix}$	$T_{11}\ (V_5, V_7, V_8)$ $\begin{bmatrix} 0 & \sqrt{3} & 0 \\ \frac{-1}{2} & \frac{-\sqrt{3}}{2} & 1 \\ -1 & 0 & -1 \end{bmatrix}$	$T_{12}\ (V_5, V_7, V_{15})$ $\begin{bmatrix} 0 & \sqrt{3} & 0 \\ \frac{-3}{2} & \frac{-\sqrt{3}}{2} & 0 \\ 1 & 0 & 1 \end{bmatrix}$
4	$T_{13}\ (V_2, V_4, V_8)$ $\begin{bmatrix} \frac{1}{2} & \frac{\sqrt{3}}{2} & -1 \\ 0 & -\sqrt{3} & 0 \\ \frac{-3}{2} & \frac{\sqrt{3}}{2} & 0 \end{bmatrix}$	$T_{14}\ (V_3, V_4, V_8)$ $\begin{bmatrix} \frac{-1}{2} & \frac{-\sqrt{3}}{2} & 1 \\ \frac{1}{2} & \frac{-\sqrt{3}}{2} & -1 \\ \frac{-3}{2} & \frac{\sqrt{3}}{2} & 0 \end{bmatrix}$	$T_{15}\ (V_3, V_7, V_8)$ $\begin{bmatrix} 0 & -\sqrt{3} & 0 \\ \frac{-1}{2} & \frac{\sqrt{3}}{2} & 1 \\ -1 & 0 & -1 \end{bmatrix}$	$T_{16}\ (V_3, V_7, V_{15})$ $\begin{bmatrix} 0 & -\sqrt{3} & 0 \\ \frac{-3}{2} & \frac{\sqrt{3}}{2} & 0 \\ 1 & 0 & 1 \end{bmatrix}$
5	$T_{17}\ (V_2, V_4, V_{12})$ $\begin{bmatrix} \frac{1}{2} & \frac{\sqrt{3}}{2} & -1 \\ \frac{-3}{2} & \frac{-\sqrt{3}}{2} & 0 \\ \frac{3}{2} & \frac{-\sqrt{3}}{2} & 0 \end{bmatrix}$	$T_{18}\ (V_3, V_4, V_{12})$ $\begin{bmatrix} \frac{-1}{2} & \frac{-\sqrt{3}}{2} & 1 \\ -1 & 0 & -1 \\ \frac{3}{2} & \frac{-\sqrt{3}}{2} & 0 \end{bmatrix}$	$T_{19}\ (V_3, V_{11}, V_{12})$ $\begin{bmatrix} \frac{-3}{2} & \frac{-\sqrt{3}}{2} & 0 \\ 1 & 0 & 1 \\ \frac{1}{2} & \frac{-\sqrt{3}}{2} & -1 \end{bmatrix}$	$T_{20}\ (V_3, V_{11}, V_{15})$ $\begin{bmatrix} \frac{-3}{2} & \frac{-\sqrt{3}}{2} & 0 \\ \frac{3}{2} & \frac{-\sqrt{3}}{2} & 0 \\ \frac{-1}{2} & \frac{\sqrt{3}}{2} & 1 \end{bmatrix}$
6	$T_{21}\ (V_2, V_{10}, V_{12})$	$T_{22}\ (V_9, V_{10}, V_{12})$	$T_{23}\ (V_9, V_{11}, V_{12})$	$T_{24}\ (V_9, V_{11}, V_{15})$

	$\begin{bmatrix} -1 & 0 & -1 \\ \frac{3}{2} & \frac{\sqrt{3}}{2} & 0 \\ 0 & -\sqrt{3} & 0 \end{bmatrix}$	$\begin{bmatrix} 1 & 0 & 1 \\ \frac{1}{2} & \frac{\sqrt{3}}{2} & -1 \\ 0 & -\sqrt{3} & 0 \end{bmatrix}$	$\begin{bmatrix} \frac{3}{2} & \frac{\sqrt{3}}{2} & 0 \\ \frac{-1}{2} & \frac{-\sqrt{3}}{2} & 1 \\ \frac{1}{2} & \frac{-\sqrt{3}}{2} & -1 \end{bmatrix}$	$\begin{bmatrix} \frac{3}{2} & \frac{\sqrt{3}}{2} & 0 \\ 0 & -\sqrt{3} & 0 \\ \frac{-1}{2} & \frac{\sqrt{3}}{2} & 1 \end{bmatrix}$

6.3.1.3 DETERMINATION OF SWITCHING VECTOR SEQUENCES

The sequencing of space vectors in each tetrahedron is to minimize the switching times and to reduce the switching loss. Therefore, symmetrically aligned sequence of space vector is used in the 3D SVPWM. Again using T18 (Tetrahedron II, Sector 5) for example, the active vectors are V_3 (0010), V_4 (0011) and V_{12} (1011). It is obvious that if it starts with ZSV V_1 the sequence of the active vectors will be given by: $V_1 \rightarrow V_3 \rightarrow V_4 \rightarrow V_{12} \rightarrow V_{16} \rightarrow V_{12} \rightarrow V_4 \rightarrow V_3 \rightarrow V_1$, as shown in Fig. 6.18.

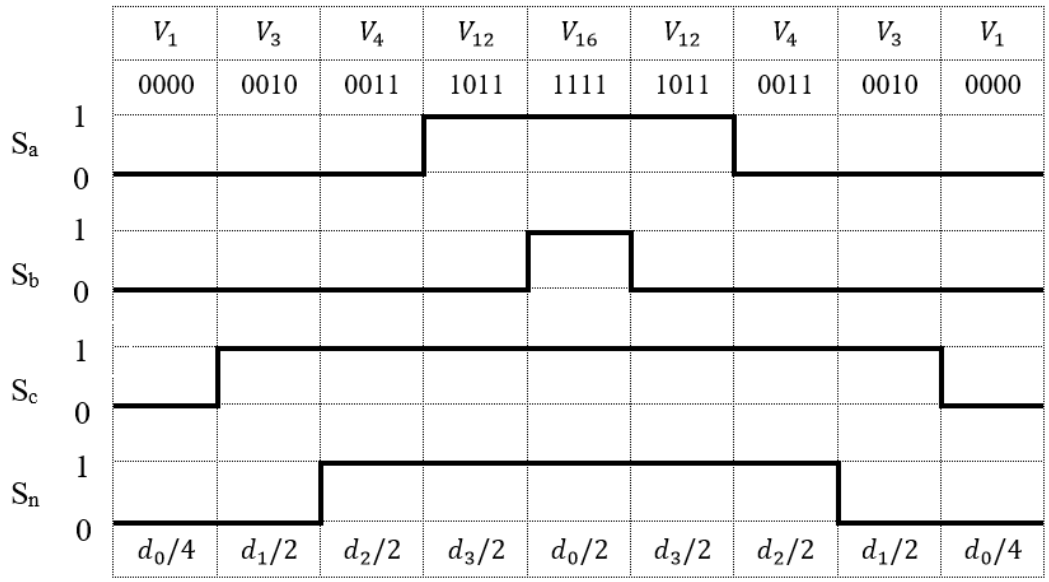

Fig. 6.18 Switching vector sequences for in T18 (Tetrahedron II, Sector 5).

6.3.1.4 MATLAB/SIMULINK MODELLING OF THE 3D SVPWM

Based on previous study, a Matlab/Simulink model for the 3D SVPWM has been built as shown in Fig. 6.19. Its subsystems include sector calculation module, the tetrahedron identification module (Fig. 6.20) and duty cycle calculation module (Fig. 6.11). The $V_{\alpha\beta\gamma}$ components should be provided as the input during each sampling.

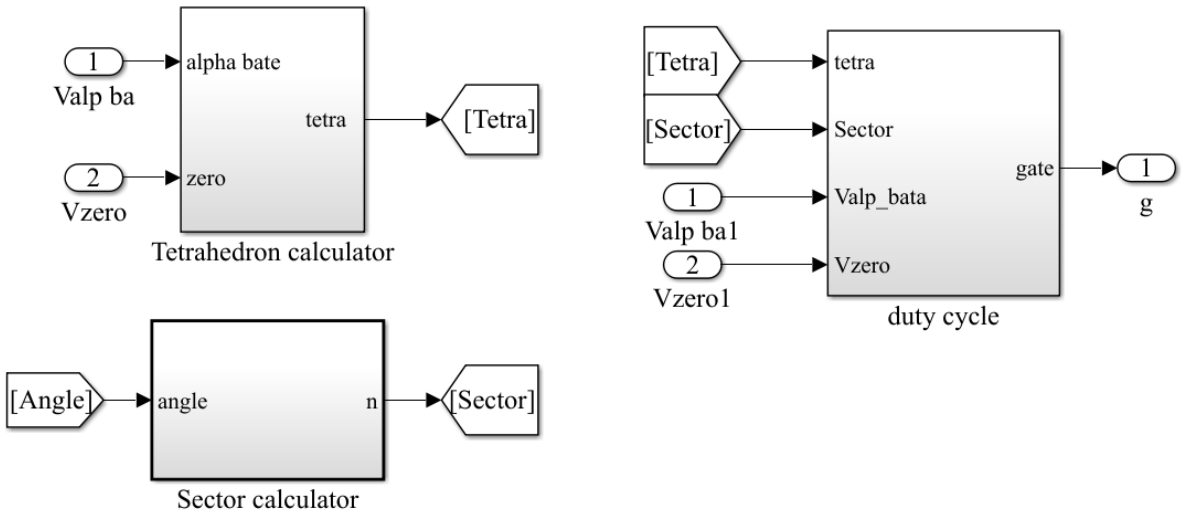

Fig. 6.19 Matlab/Simulink model for the 3D SVPWM.

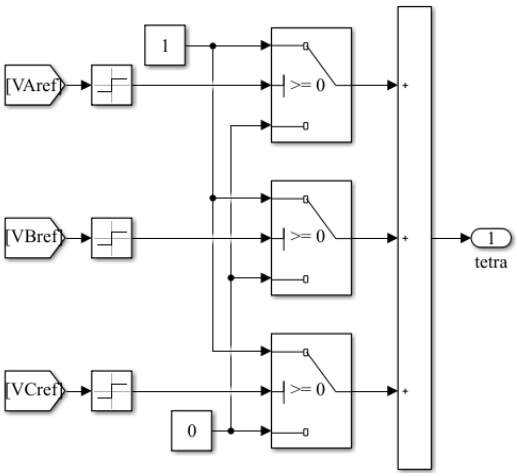

Fig. 6.20 Matlab/Simulink model for tetrahedron calculator [(6.10) and (6.11)]

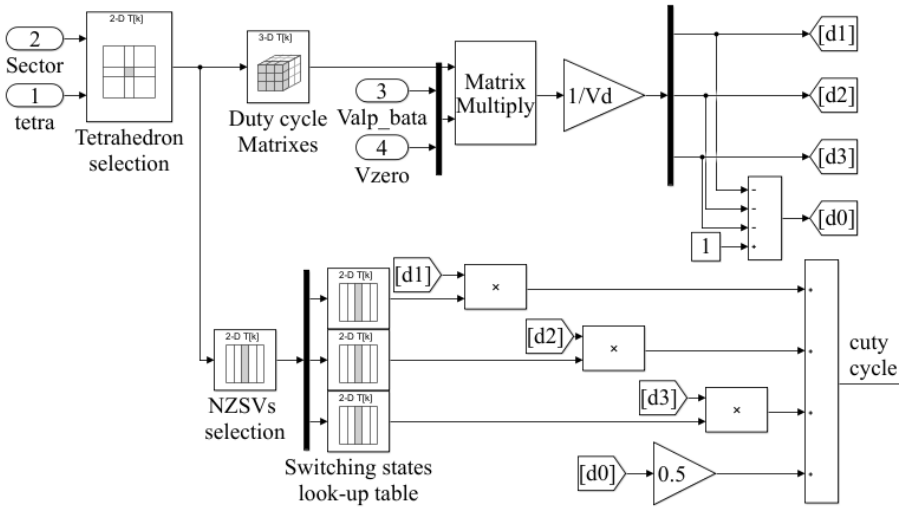

Fig. 6.21 Matlab/Simulink for duty cycle calculator (TABLE 6.1 and TABLE 6.3).

The resistor-inductor circuit as shown in Fig. 6.22 is used to validate the effectiveness of the built 3D SVPWM model. The dc bus voltage is 50 V and carrier wave frequency is 10kHz. The resistance is 1Ω, while the inductance is 8mH. The system is operating under current control and *dq*-axis current demands are kept at 1A. The 3rd, 5th and 7th order current harmonic are injected in sequence for one electric period, and their amplitudes are 30%I_1, where I_1 is the fundamental current. The method of implementing current harmonic injection has been detailed in Appendix A. The simulation results are listed through Fig. 6.24-Fig. 6.29.

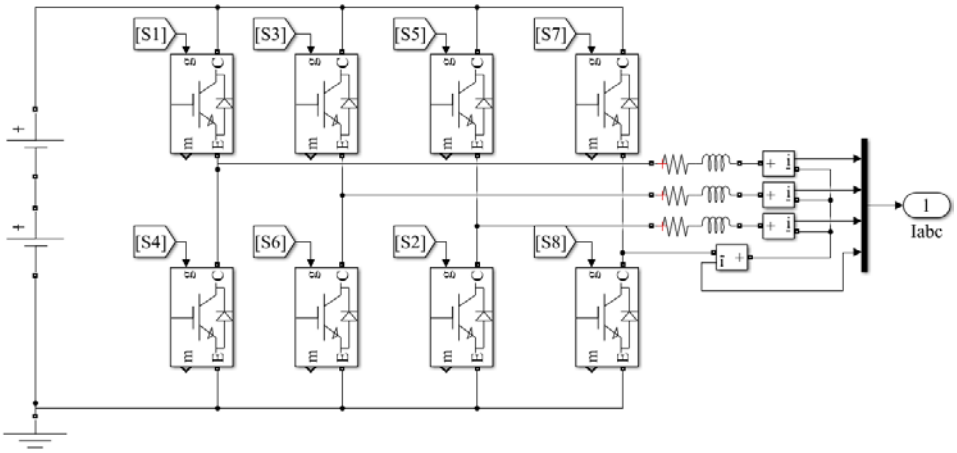

Fig. 6.22 Matlab/Simulink model for three-phase four-leg inverter.

Fig. 6.23 presents the comparisons between the reference current demand and inverter output current. It is shown that three-phase four-leg inverter controlled by 3D-SVPWM allows us to inject current harmonic into *dq0*-axis currents and the designed controller can fully track the reference current.

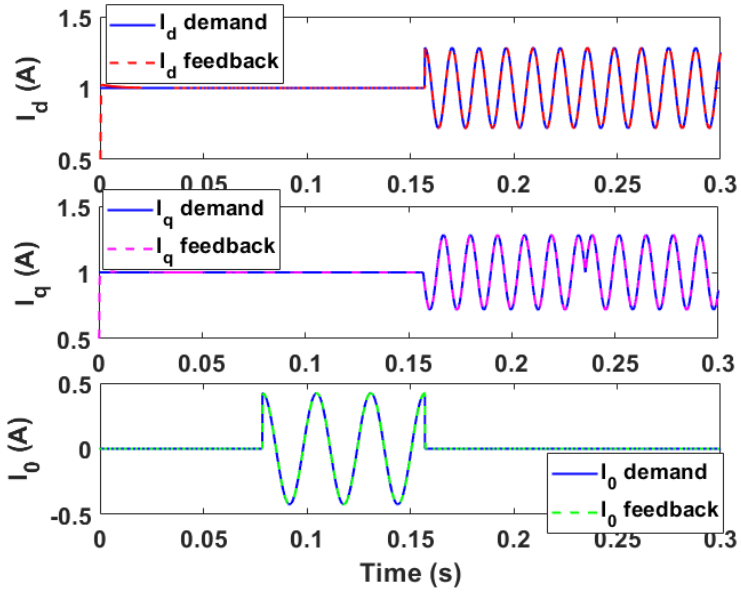

Fig. 6.23 Comparison between reference current and inverter output current.

Fig. 6.24 shows the reference voltage applied to the three-phase four-leg inverter, while Fig. 6.25 presents the output phase voltage of the inverter.

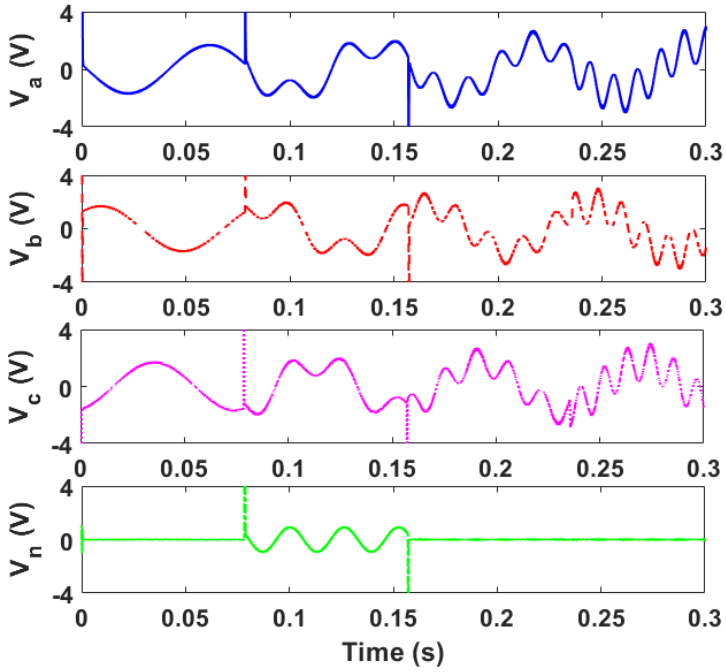

Fig. 6.24 Reference voltage applied to three phase four-leg inverter.

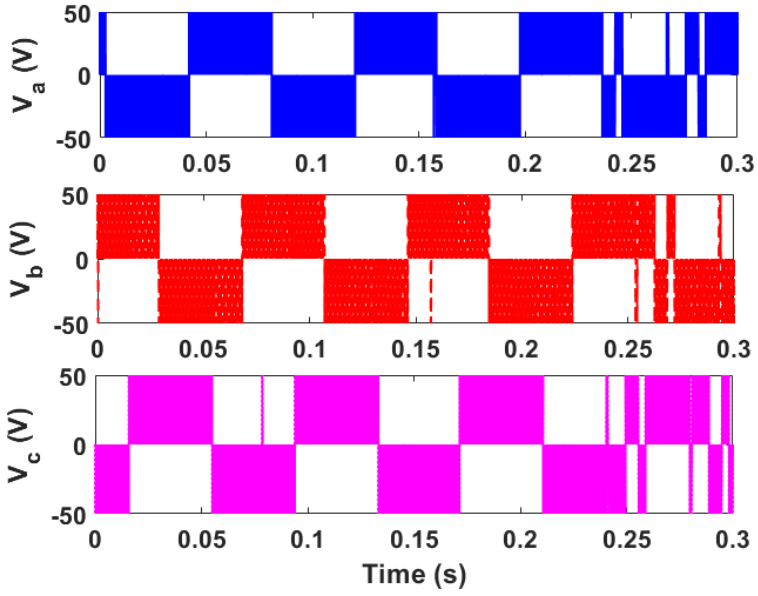

Fig. 6.25 Output phase voltage of three phase four-leg inverter.

In Fig. 6.26, the duty cycles for each inverter leg are shown, which corresponds to the symmetrical sequence mentioned previously. With current harmonic injection, the peak to peak value of duty cycle could be slightly larger than that with pure sinewave supply. Therefore, the

duty cycle with current harmonic injection potentially reach maximum value “1” earlier than that with pure sinewave supply. In other words, the machine will enter flux-weakening region in advance as have already been investigated in Chapter 5.3

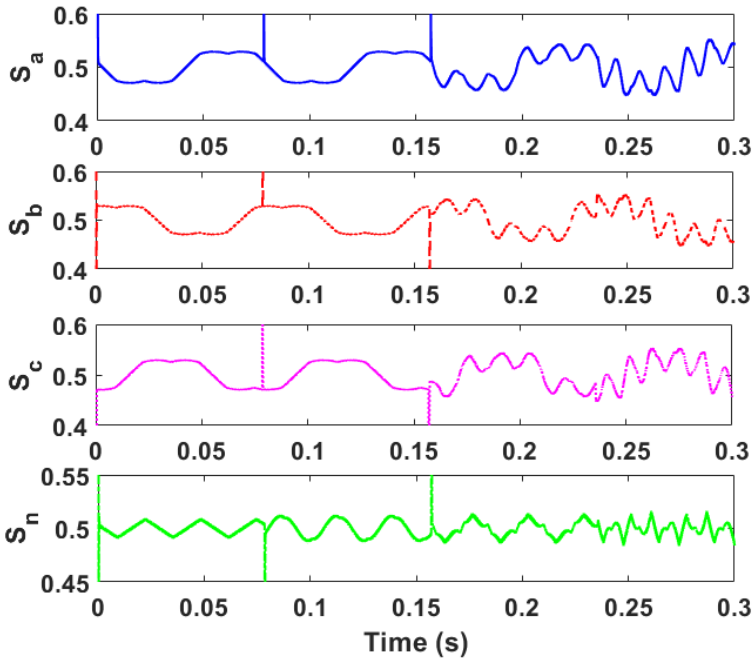

Fig. 6.26 Duty cycle of three phase four-leg inverter.

Fig. 6.27 shows the current waveforms for 3D SVPWM control. It confirms that the benefits of this type of inverters, which can operate under both balanced and unbalanced current conditions.

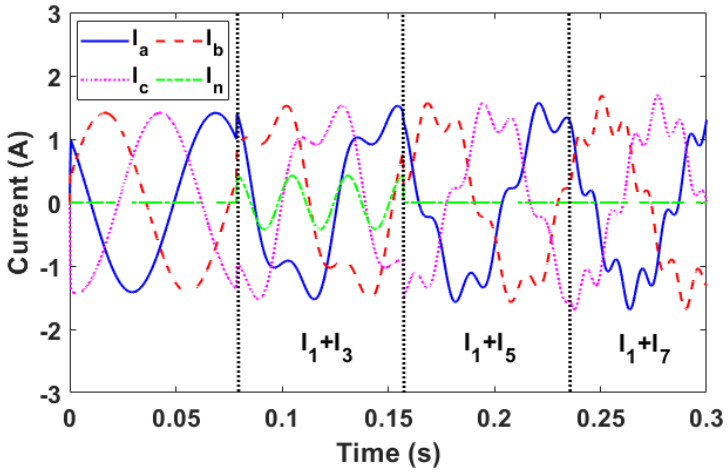

Fig. 6.27 Three phase currents with different current harmonic injection. The 3rd 5th and 7th order current harmonics are injected in sequence.

Fig. 6.28 and Fig. 6.29 show the selection of sectors and tetrahedrons in which voltage space vector passed.

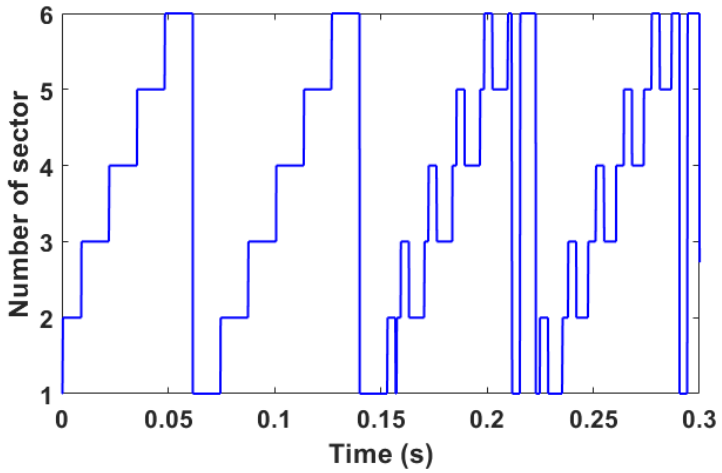

Fig. 6.28 Number of sectors in which the voltage space vectors passed.

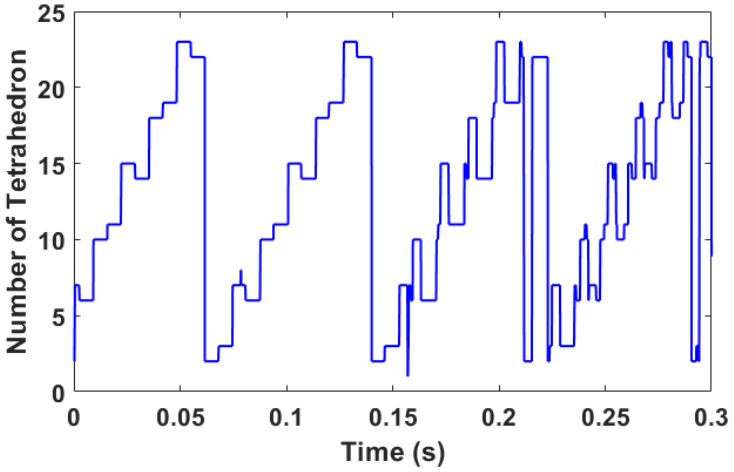

Fig. 6.29 Number of tetrahedrons in which the voltage space vectors passed

6.3.2 TEST OF 3-PHASE DS-SRMS

Once the effectiveness of the 3D SVPWM for three-phase four-leg inverter has been validated, the dynamic tests for the DS-SRMs with current harmonic injections can be carried out. Two 3-phase DS-SRMs are tested initially. The block diagram of implementing the harmonic current injections is shown in Fig. 6.30. Three types of dynamic tests including steady-state test, transient-state test as well as torque- and efficiency-speed curves are carried out.

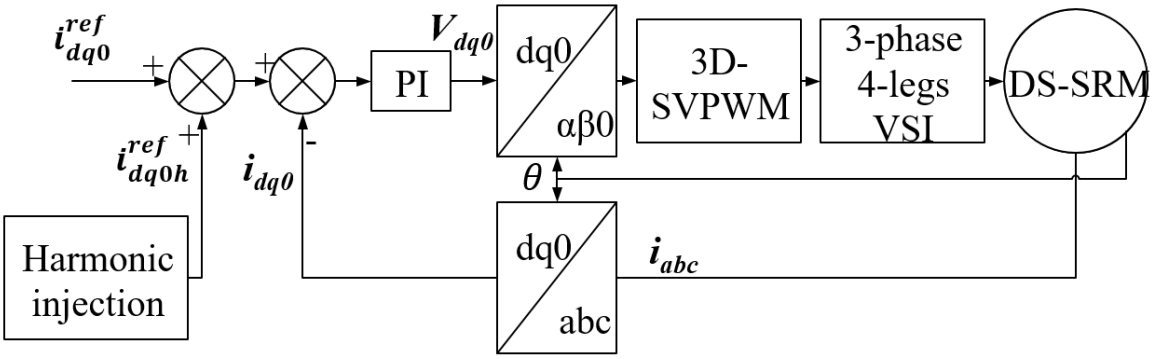

Fig. 6.30 Current control block diagram of the 3-phase DS-SRM with current harmonic injection.

6.3.2.1 STEADY-STATE TESTS

Firstly, the test machine is operating under current control and the phase rms current stays constant at 5A for all the conditions. The performance of the proposed harmonic current injection method at steady state is evaluated. The machine reached the steady state with only fundamental current within the first 3s. Then after every 3s, the 3rd, 5th and 7th order current harmonics are injected consecutively and each time only one harmonic current is injected.

A). SL DS-SRM

The experimental results for the SL DS-SRM are shown in Fig. 6.31. It can be seen that as predicted, all the harmonic current injections can effectively reduce torque ripple. The *dq*-axis currents reduce slightly after the harmonic current injections mainly because the phase RMS is kept constant.

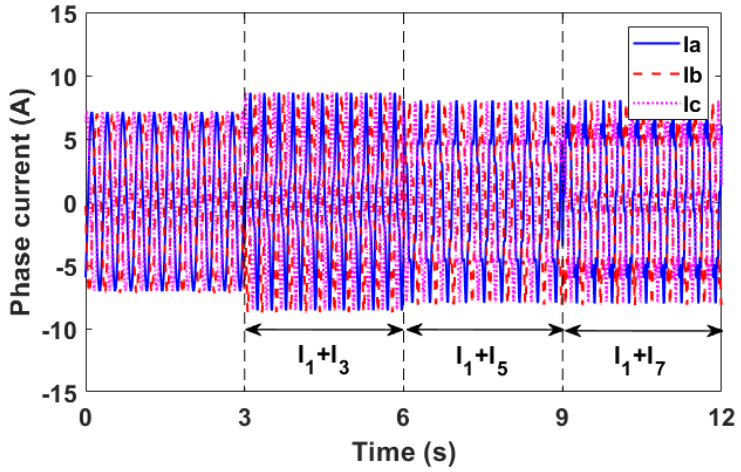

(a) Phase current

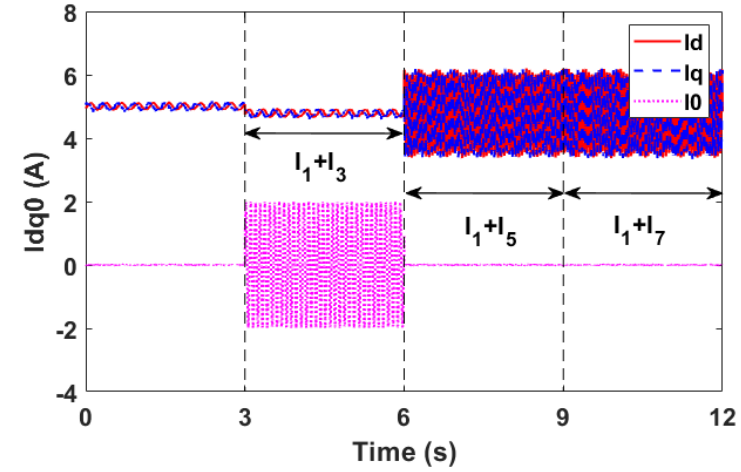

(b) *dq0*-axis current

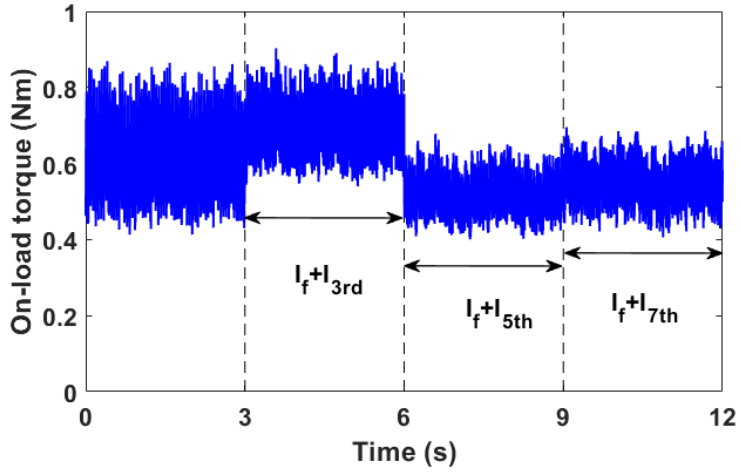

(c) On-load torque

Fig. 6.31. Measured currents, speed and torque for SL DS-SRM before and after current harmonic injections.

The torque spectra are shown in Fig. 6.32. It can be seen that after current harmonic injections, the 6th order torque harmonics have been effectively reduced by around 60%, as expected. However, it is also observed that there are some low frequency harmonics in the on-load torque. This is mainly due to the manufacturing tolerance of the prototype machine, the unavoidable imbalance in the test rig and also the torque ripple introduced by the load generator.

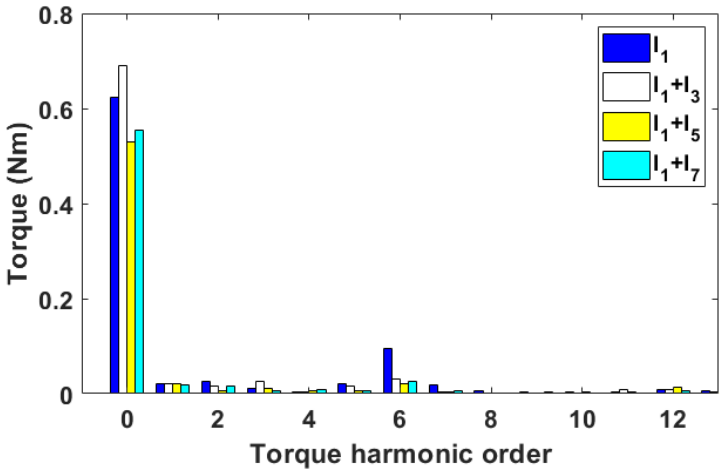

Fig. 6.32. Comparison of torque spectra for SL DS-SRM after various order current harmonic injections.

B). DL DS-SRM

Fig. 6.33 shows the current and torque waveforms at steady state after the 3rd, 5th and 7th order current harmonics individually injected into the test machine, respectively. It is obvious that for the DS-SRM, the 3rd order current harmonic has little effect on the torque production, as predicted. The slight reduction in *dq*-current and average torque, after the 3rd order current injection, is mainly due to the fact that the phase RMS current is kept constant. It also proves that the 5th and 7th order current harmonics can effectively reduce the speed and torque ripple.

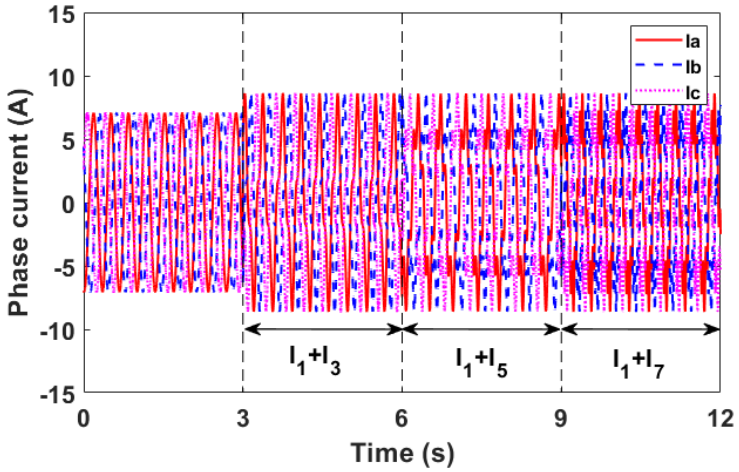

(a) Phase current

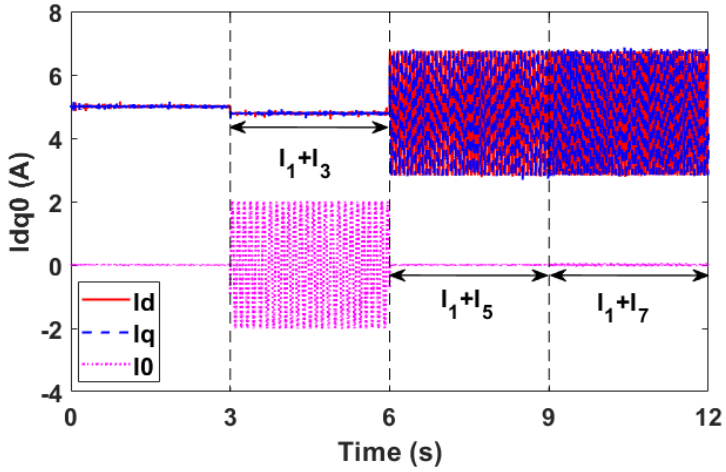

(b) *dq0*-axis current

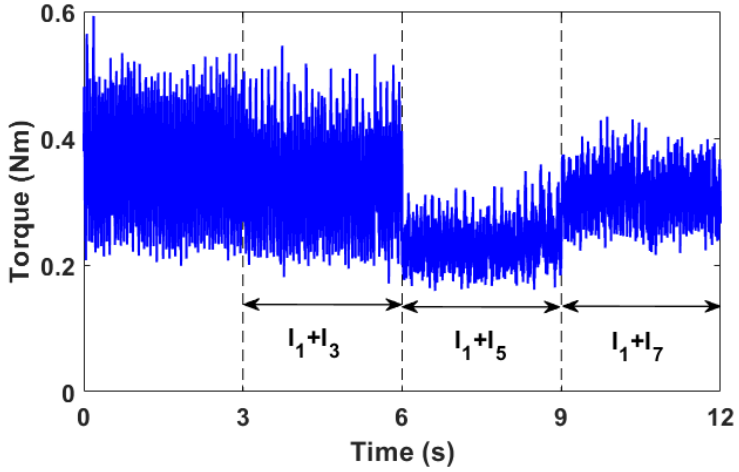

(c) On-load torque

Fig. 6.33. Measured currents, speed and torque for DL DS-SRM before and after current harmonic injections.

The torque spectra are also plotted, as shown in Fig. 6.34. The results show that the 5th and 7th current harmonic injections can reduce 66% and 70% of the 6th order torque harmonics, respectively. The 3rd current harmonic has negligible effect on the 6th order torque harmonic.

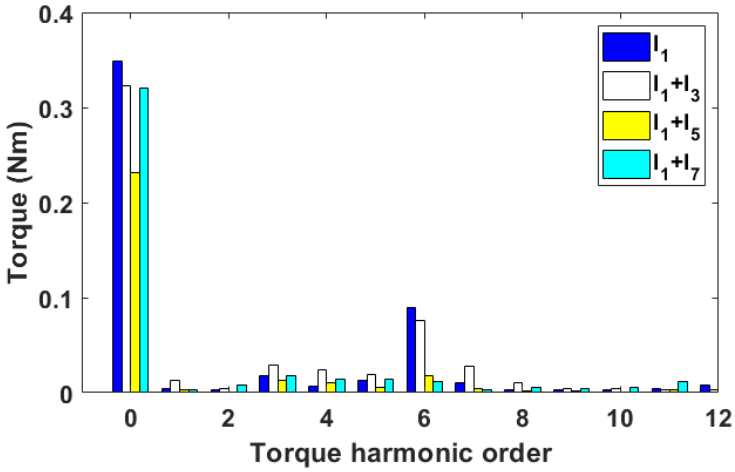

Fig. 6.34. Comparison of torque spectra for DL DS-SRM after various order current harmonic injections.

6.3.2.2 TRANSIENT-STATE TESTS

The second test evaluated the performance of the proposed current injection method at transient state. Therefore, the machine is operating under speed control, and a permanent magnet dc generator is utilized as the load. At the beginning, the test machine rotates at 50rpm and after 3s, the speed demand increases to 200rpm. The harmonic current can be injected into the *dq0*-axis directly, as investigated in Appendix A.

A). SL DS-SRM

The phase a currents are shown in Fig. 6.35 (a) and the speed and torque of the SL DS-SRM with and without the current harmonic injection are shown in Fig. 6.35 (b) and (c), respectively. It can be seen that the speed and torque ripple suppression by the proposed method is not compromised at transient-state. Moreover, the transient time from 50rpm to 200rpm can even be reduced by more than 10% after injecting the 3rd order current harmonic. This is due to the extra torque produced by such harmonic current injection. The transient time can be increased by around 17% and 15% after injecting the 5th and 7th order current harmonics, which is mainly due to the fact that the average torque is reduced by such harmonic current injections.

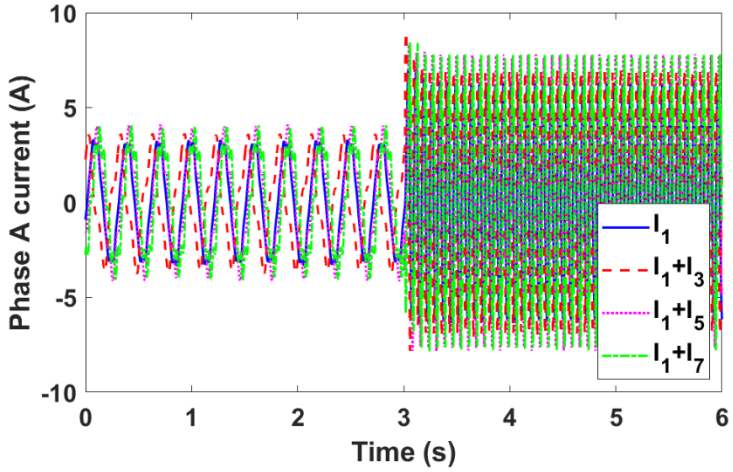

(a) Phase A current

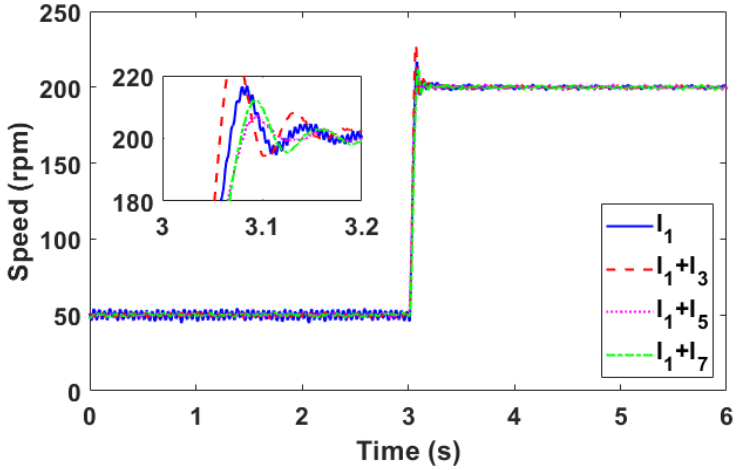

(b) Speed

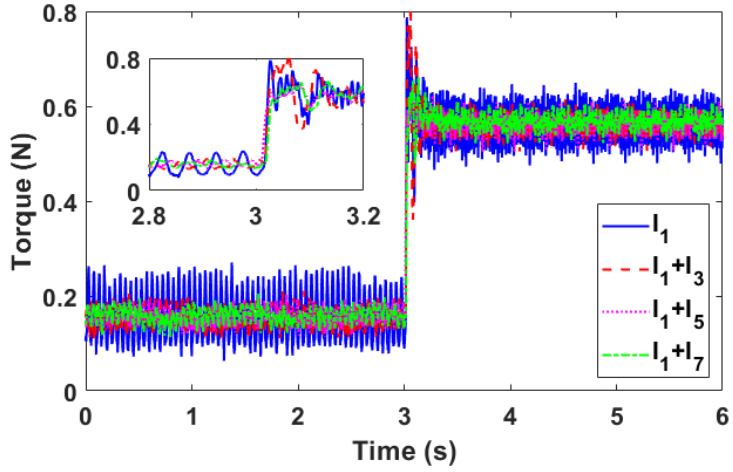

(c) Torque

Fig. 6.35. Transient state results with/without current harmonic injection. $I_{rms} = 5Arms$ and V_{dc}=24V

Fig. 6.36 shows the torque spectra at different speeds. A clear reduction in the 6th order torque ripple can be observed at both low and relatively higher speeds. However, it is also observed that there are some low frequency harmonics in the on-load torque. Again, this is due to the manufacturing tolerance of the prototype machine, the unavoidable imbalance in the test rig and also the torque ripple introduced by the load generator.

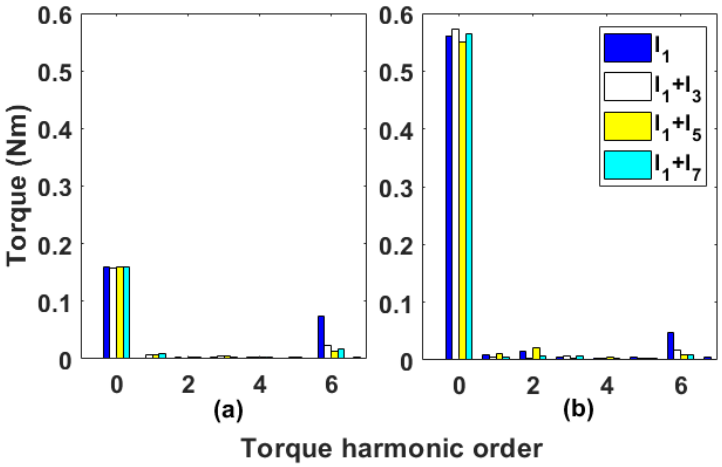

Fig. 6.36. Torque spectra at different speeds. (a) $\omega = 50rpm$ and (b) $\omega = 200rpm$.

B). DL DS-SRM

The same test in transient-state has been done for the DL DS-SRM. Fig. 6.37 shows the dynamic test results after current harmonic injection. As expected, the transient time from 50rpm to 200rpm is not changed after injecting the 3rd order current harmonic, while transient time after 5th and 7th order current harmonic is increased by about 20% and 10%, respectively. It is obvious that the torque ripple for the full time range can be reduced significantly. Fig. 6.36 shows the torque spectra for DL DS-SRM at different speeds. Again, the effectiveness of proposed current harmonic injection has been validated.

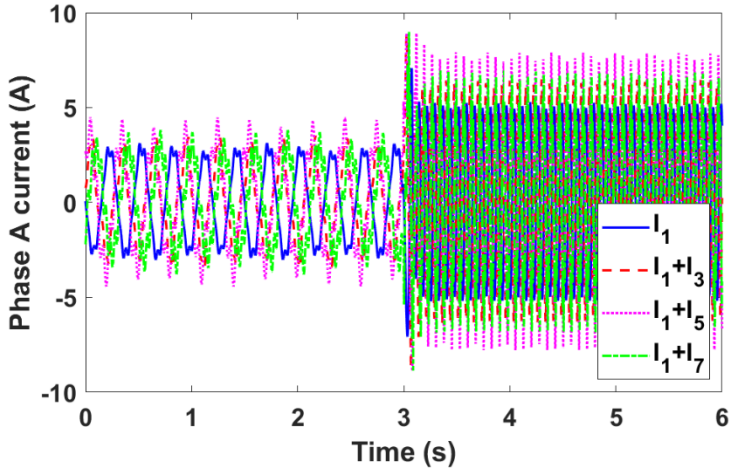

(a) Phase A current

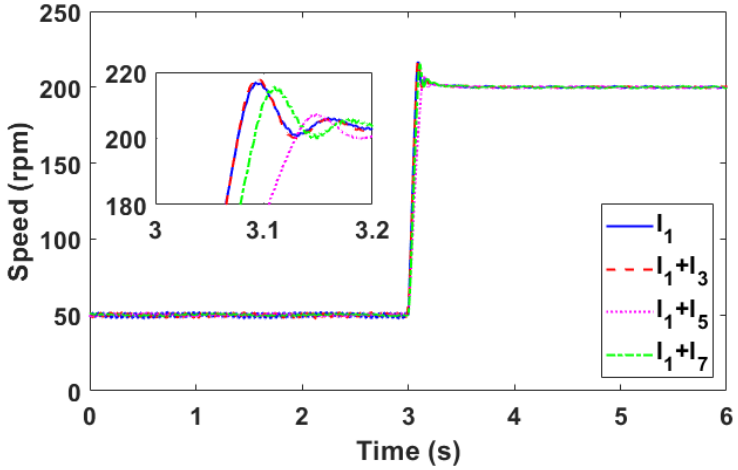

(b) Speed

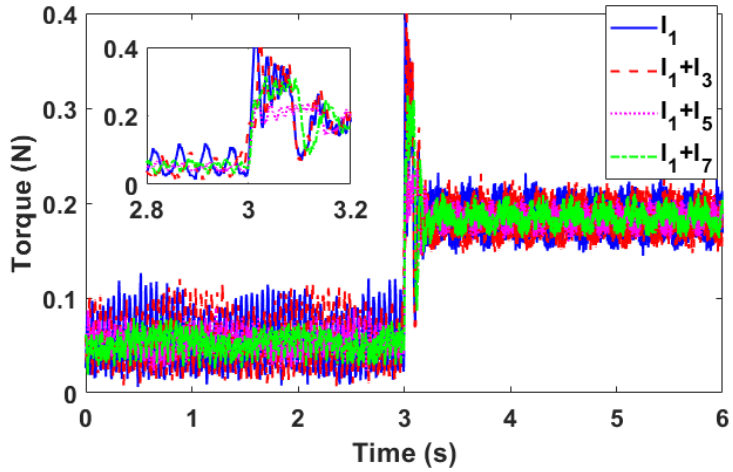

(c) Torque

Fig. 6.37. Transient state results with/without current harmonic injection. $I_{rms} = 5Arms$ and V_{dc}=24V.

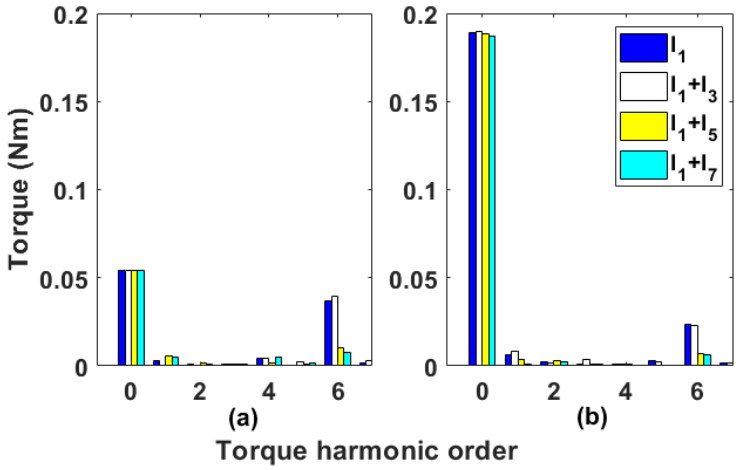

Fig. 6.38. Torque spectra at different speeds. (a) $\omega = 50rpm$ and (b) $\omega = 200rpm$.

6.3.2.3 TORQUE- AND EFFICIENCY-SPEED CURVES

Apart from the steady and transient-state tests, the torque- and efficiency-speed curves have also been measured. It is worth mentioning that in order to ease the winding process of the prototype machine, smaller copper wires ware deliberately used in the prototype machine, leading to higher phase resistance. As a result, if V_{dc} is still kept at 24V as in Chapter 5.3, there will be no constant torque region. Therefore, a higher V_{dc} of 40V has been used in this test.

Fig. 6.39 (a) and (b) show the torque-speed curves for the SL and DL DS-SRM, respectively. Overall, the measured torque-speed curves match well with the predictions. As expected, with the 3rd order current harmonic injection, the SL machine produces more than 10% extra torque at the constant torque region, and slightly higher torque during the flux-weakening operation. However, the 3rd order current harmonic has no benefit but extra losses for the DL machine. Moreover, the base speeds for both the SL and DL machines with the 5th and 7th order current harmonics are reduced by more than 50%, which corresponds to previous studies in Chapter 5.3.

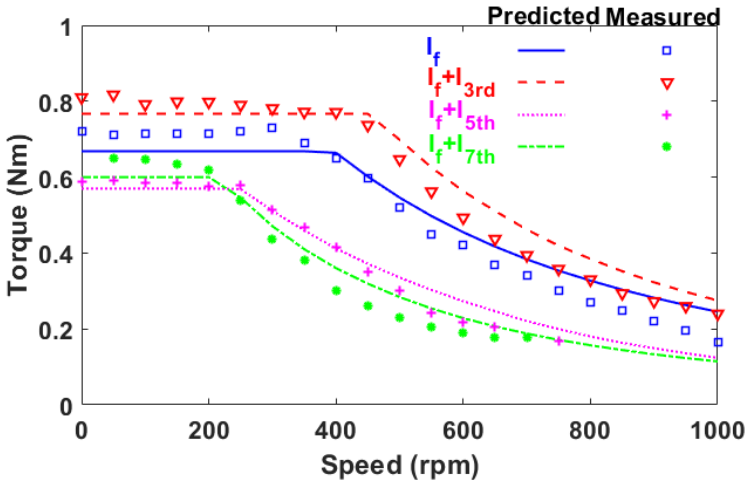

(a) SL

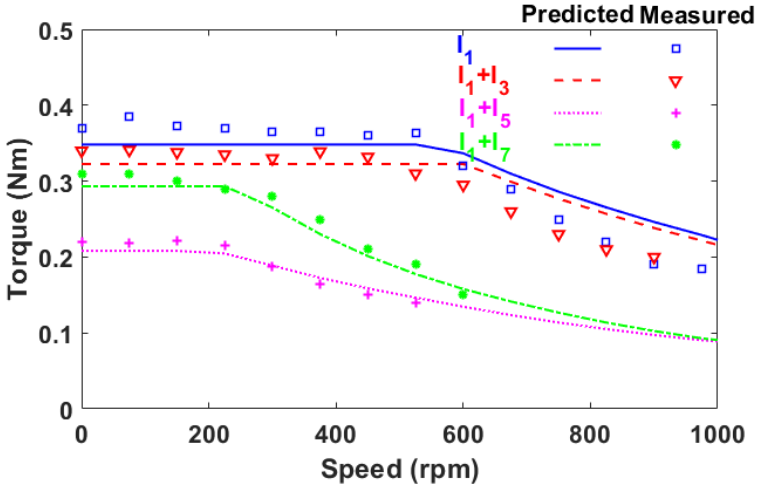

(b) DL

Fig. 6.39. Predicted and measured torque-speed curves for DS-SRMs with different winding structures. $I_{rms} = 5Arms$ and V_{dc}=40V.

Fig. 6.40 shows the efficiency-speed curves for the SL and DL DS-SRMs. It is not surprising that the 3rd order current harmonic injection can also improve the efficiency of the SL machine for the investigated speed range, while the 5th and 7th order current harmonic injections can only reduce the machine efficiency in the full speed range. Moreover, the efficiency of the DL machine with the 5th and 7th order current harmonic injections is also reduced. This is due to reduction in average torque and increase in losses. It is worth noting that the lower efficiency is mainly due to relatively higher phase resistance, which leads to higher copper loss.

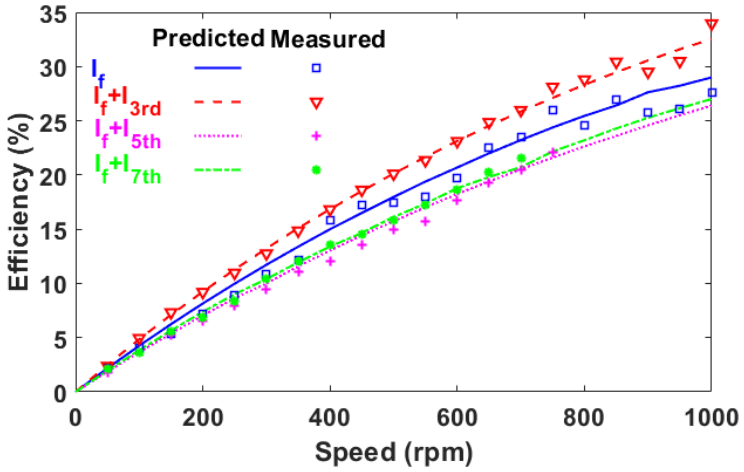

(a) SL

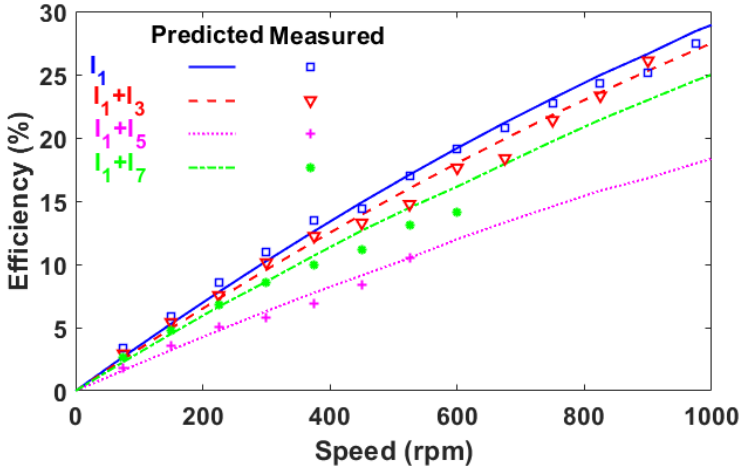

(b) DL

Fig. 6.40. Predicted and measured efficiency-speed curves for DS-SRMs with different winding structures. $I_{rms} = 5Arms$ and V_{dc}=40V.

6.3.3 Test of Multi-Phase DS-SRM

As mentioned previously, the prototype 6-phase DS-SRM is converted from the 3-phase 12s/8p prototype machine. As a result, the number of turns per phase is reduced by half, i.e. 66 rather than 132 used in previous sections. This means that the inductance will be reduced by four times, which leads to four times reduction in the average torque in the experimental validation section compared with the simulated torque in Chapter 4 and Chapter 5. However, this will not influence the effectiveness of the proposed method as it can be used in any synchronous reluctance machines. The same test rig setup in Fig. 6.15 is utilized to validate the proposed harmonic current injection method.

The 6-phase machine is controlled as a dual 3-phase one (phases A, C and E form one set, while phases B, D and F form the second set) with a phase shift of 60 electrical degree between the two sets, as shown in Fig. 6.41. Two 3-phase winding sets are supplied by two 3-phase half bridge voltage source inverters (VSIs), which are controlled using the conventional SV-PWM. It is worth noting that when injecting the 3rd order current harmonic for the 6-phase machine, an extra half-bridge is required to control the zero-sequence current. However, due to hardware limitations, only the 5th and 7th order harmonic current injections have been carried out in this section.

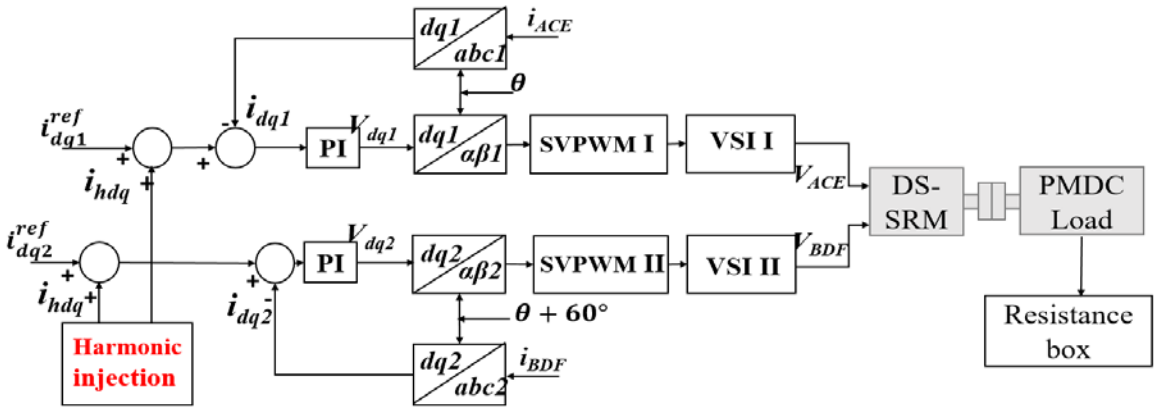

Fig. 6.41. Current control block diagram of the 6-phase prototype machine.

6.3.3.1 Steady-State Tests

The first test evaluates the performance of the proposed current harmonic injection method at steady-state. Therefore, the machine is operating under the current control. The current level is 5Arms. The permanent magnet direct current (PMDC) machine provides load torque for the prototype machine. Fig. 6.13 shows the waveforms of the current and torque. It has been found that after the 5th and 7th order current harmonic injections, the torque ripple can be significantly reduced, while the dc components (average torque) is also reduced by about 14%.

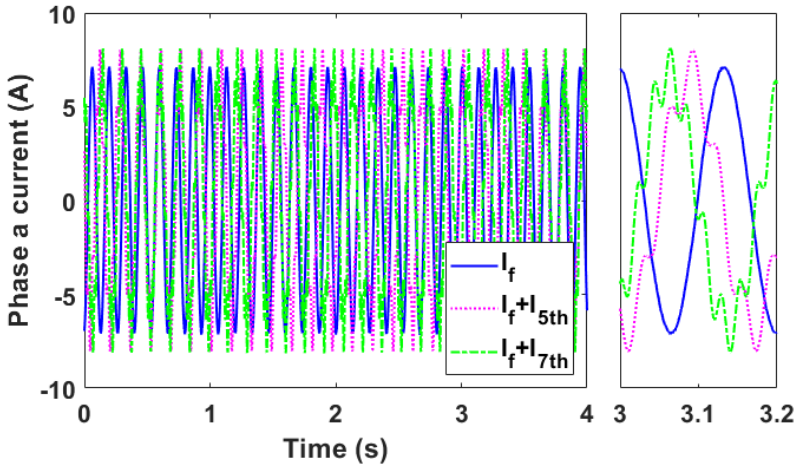

(a) Phase A current

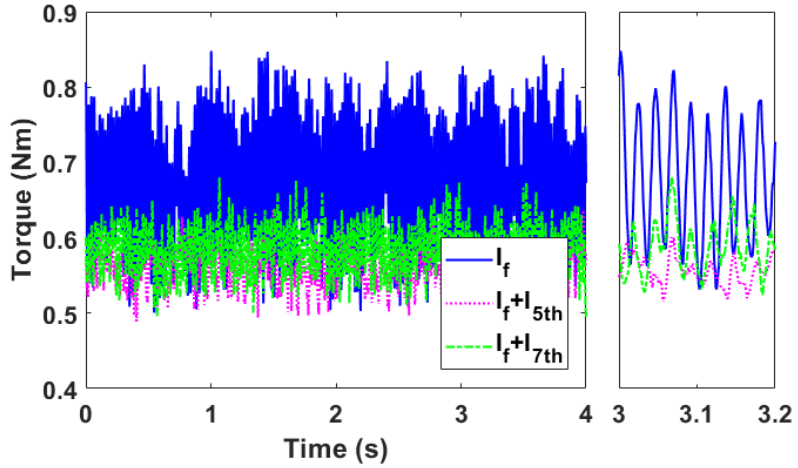

(b) On-load torque

Fig. 6.42 Steady-state results. Phase RMS current is 5A.

Fig. 6.43 shows the torque spectra during one electric period. It is apparent that the 6th order torque harmonic can be suppressed by 85% and 70%, respectively, after the 5th and 7th order current harmonic injections, which generally agree with the predictions in TABLE 4.6. It is worth noting that the active inductances to produce the average torque for the 5th order current harmonic are 4th and 6th (5 ± 1), while for the 7th order current harmonic they are 6th and 8th (7 ± 1). In addition, the magnitude of the 4th order inductance harmonic is much larger than the 8th order inductance harmonic. Therefore, to reduce the same amount of torque ripple, the reduction in average torque with the 7th order current harmonic injection is less than that with the 5th order current harmonic injection. Moreover, the low frequency harmonics in torque are due to the unavoidable mechanical unbalance of the test rig and also the inherent torque ripple of the PMDC load machine.

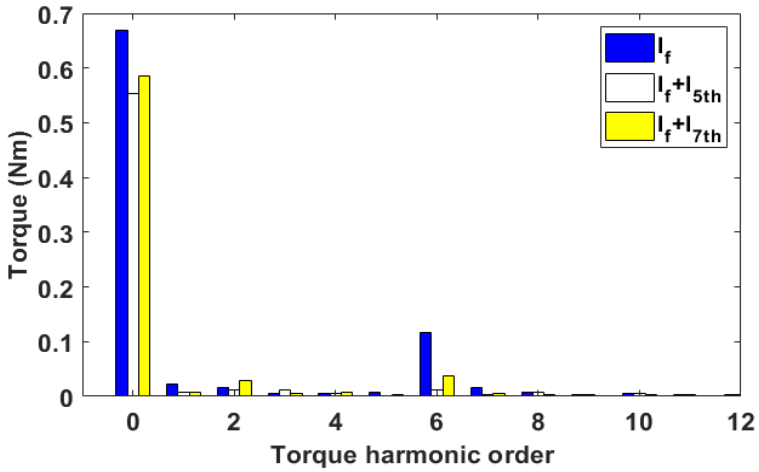

Fig. 6.43. Spectra of torque at 5A phase RMS current with and without current harmonic injections.

6.3.3.2 TRANSIENT-STATE TESTS

The second test investigates the effectiveness of the current harmonic injection method at transient-state and the machine is tested under speed control. The initial speed is 50rpm and after 3s, the speed reference increases to 200rpm. Again, both the 5^{th} and 7^{th} order current harmonics are injected. The speed and torque responses for different harmonics are shown in Fig. 6.44 (a) and (b), respectively. It can be seen that the speed and torque ripple suppression of the proposed method is not compromised at transient-state. However, the transient time from 50rpm to 200rpm can be increased by around 17% and 15% after injecting the 5^{th} and 7^{th} order current harmonics, which is mainly due to the fact that the average torque is reduced by such harmonic current injections.

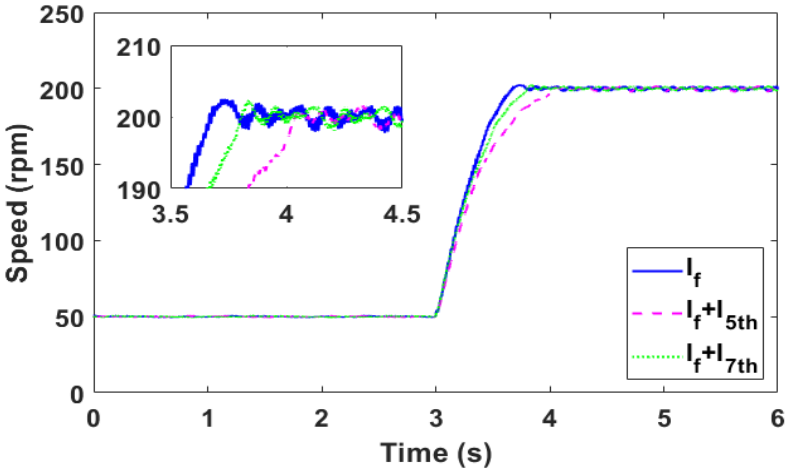

(a) Speed

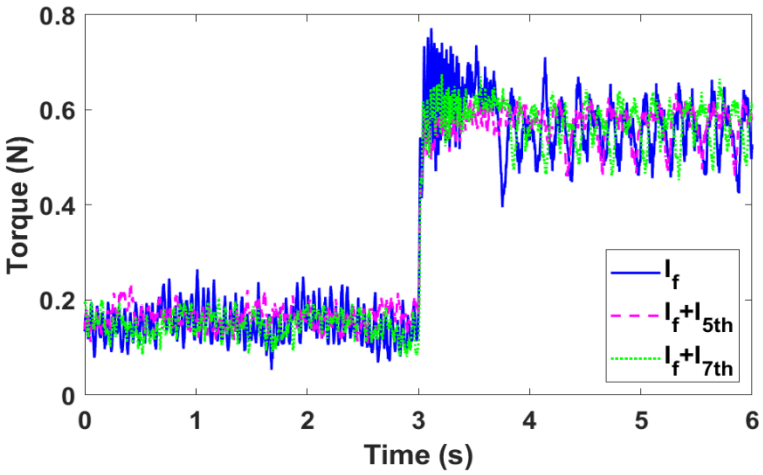

(b) Torque

Fig. 6.44 Transient-state results. The speed steps up from 50rpm to 200rpm.

6.3.3.3 TORQUE- AND EFFICIENCY-SPEED CURVES

Apart from the steady and transient-state tests, the torque- and efficiency-speed curves have also been measured. The current and dc voltage limits are the same as Chapter 5.4.2, i.e. 7.07A (5Arms) and 24V, respectively. Fig. 6.45 shows the torque- and efficiency-speed reuslts. It is worth noting that the significant reduction in the average torque compared with preditions in Fig. 5.46 is due to reduced number of turns per phase of the protype machine. This has been explained at the beginning of the Chapter 6.3.3. For the same reason, the induced voltage is reduced by half as well. In this case, the base speed of the machine could be doubled. Overall, the measured results match well with the predictions. It is not surprising that both in contant-torque and flux-weakening regions, the 5^{th} and 7^{th} order current harmonic injections cannot produce comparible average torque as that of the fundmental current. The base speed is reduced,

due to significant voltage distortion caused by the interation between the current and inductance harmonics. Moreover, the 5th and 7th order current harmonic injections can only reduce the machine efficiency in full speed range. It is worth mentioning that smaller copper wires have been delibrately used to ease the winding process of the prototype machine. This inevitably increases the phase resistance. As a result, together with relatively high phase current and low rotor speed, the small prototype machine can only achieve modest efficiency.

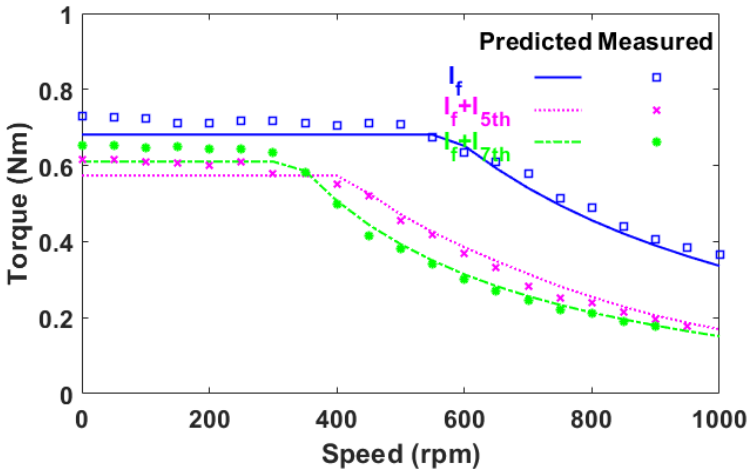

(a) Torque-speed curves

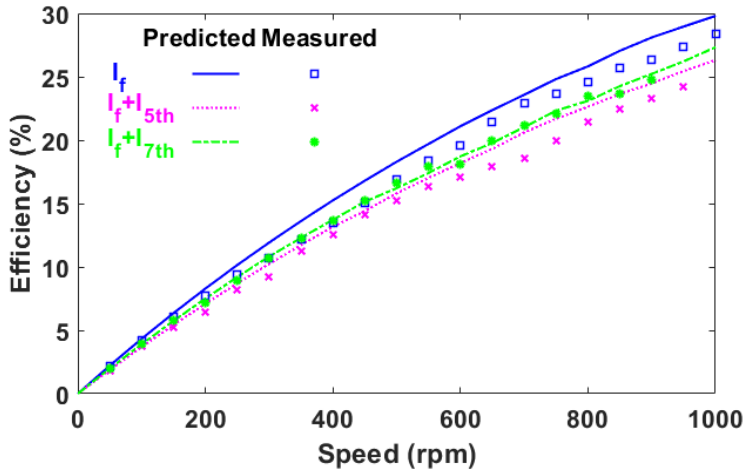

(b) Efficiency-speed curves

Fig. 6.45 Predicted and measured torque- and efficiency-speed curves. $I_{max} = 7.07A$ and V_{dc}=24V.

6.4 CONCLUSION

In this section, both static and dynamic experiments have been carried out to validate the effectiveness of the current harmonic injection method for the DS-SRMs investigated in previous chapters. Three-phase four-leg inverter and its associated 3D SVPWM control have

been investigated to control the zero-sequence current, in order to achieve the 3rd order current harmonic injection. It has been proven that the prototype machines can operate well under both current and speed control with proposed current harmonic injection method. Overall, the expected results have been observed. The torque ripple for both 3-phase and 6-phase DS-SRMs can be reduced significantly, if the current harmonic is properly selected. The 3rd order current harmonic can even increase the torque capacity for the SL machines. However, it has found that for the 5th and 7th order current harmonics, while reducing the torque ripple of the investigated machines, they will also reduce their efficiency (due to reduced average torque).

Chapter 7 CONCLUSION AND FUTURE WORKS

This thesis devotes to the theoretical and experimental investigation of doubly salient synchronous reluctance machines (DS-SRMs). The main objective of this research is to develop new techniques, such as harmonic current injections, for DS-SRMs to achieve higher torque capability, lower torque ripple and lower noise compared with DS-SRMs with pure sinewave current supply. The conclusion drawn in this thesis will provide some guidelines to engineers who dedicate themselves to high efficiency and low cost electrical machines, which can be used in a wide range of applications, such as electric vehicles, more electric aircraft and household products, etc.

This thesis first reviews the development history of switched reluctance machines and other DS-SRMs from 1838 up to present and critically examines the state-of-the-art techniques for reducing vibrations and acoustic noise as well as torque ripple. It has shown that the improvement in torque performance, such as improved average torque and reduced torque ripple, can be achieved by optimizing machine topologies and/or adopting various advanced control strategies. Based on these prior works in literature, this thesis will further extend the understanding of these machines by proposing a novel harmonic current injection method for torque performance improvement.

The start of this project is based on a 3-phase 12s/8p DS-SRM with short pitched single layer concentrated winding. With sinewave current supply, this machine can achieve significantly higher torque capability but also has relatively higher torque ripple compared with conventional SRMs. In order to meet the application requirement of lower torque ripple, the concept of injecting current harmonics is considered and developed. The main idea is to use the torque ripple component generated by the current harmonics to cancel that produced by the fundamental current. At the same time, if the harmonic current, including harmonic order, amplitude and also phase angle, is properly selected, the average torque can be improved as well. In order to provide an insight into the torque generation mechanism with current harmonic injections, the analytical studies of on-load torque with/without current harmonic injection have been carried out. Both FEA and experiment results have validated the analytical modelling under linear condition, and it has found that the torque ripple can be significantly reduced for a single layer DS-SRM by the proposed methods. In addition, in order to show that the proposed method can be general and can be applicable to other DS-SRMs, three different

but typical DS-SRMs with different winding configurations, i.e. single layer (self-torque component is dominant), fully-pitched (mutual-torque component is dominant) and double layer (both self- and mutual-torques are important), have been compared by implementing the proposed method in this thesis. It has found that most current harmonics, including the 3rd, 5th and 7th, present good performance in torque ripple reduction for the single layer and fully pitched DS-SRMs. However, due to the cancellation effect between the self- and mutual-inductances (corresponding to the self- and mutual-torque components), some current harmonics have little effect on the double layer DS-SRMs.

Moreover, this thesis also attempts to further improve the torque performance of the DS-SRM by combining the multi-phase winding configuration and the current harmonic injection method. To be more specific, the DS-SRMs with increasing phase number from 2 to 6 have been proposed and investigated. For all machines, torque production of each order of inductance harmonic can be quantified by using the developed analytical model in this thesis. Based on the findings from the analytical modelling, the corresponding torque compensation method with appropriate current harmonic injection has been proposed for the multi-phase machines. Again, if the harmonic current is properly selected, for different multi-phase DS-SRMs, their average torques can be improved and their torque ripples can be reduced.

The findings in this thesis has proven that the improvement of torque ripple due to the proposed harmonic current injection method has been apparent and significant. However, it is also true that the injected current harmonics will bring extra losses (both copper and iron losses). This could lead to the reduction of efficiency. In addition, due to the interaction between the inductance and current harmonics, it has found that the voltage distortion has been increased after current harmonic injections. This will have a significant impact on the machine dynamic performances. To provide a full picture of the potential of the proposed harmonic current injection method, comprehensive studies of losses, efficiency and dynamic performances of both 3-phase and multi-phase DS-SRMs with current harmonic injection have been carried out. To simplify the analyses, an effective *dq0*-axis analytical model is developed, which is also useful for real implementation and experimental validation of the proposed harmonic current injection method.

Overall, it has found that compared to the 5th and 7th order current harmonic injections, the 3rd order current harmonic injection presents the best performance, which can not only increase the average torque, but also can reduce the torque ripple by around 50% for the single layer and fully-pitched DS-SRM, even though it does not work for some of the double layer DS-

SRMs. And for the 3-phase machine, in order to implement the 3rd order harmonic current injection in an economical and efficient way, the three-phase four-leg inverter and the 3D space vector pulse width modulation (SVPWM) method have been adopted. It is a trade-off between the cost of power device and the torque performance improvement. Moreover, except for the 4-phase DS-SRMs (specific nature of self- and mutual-inductance) and some double layer machines with a phase number of multiple of 3 (cancellation effect between the self- and mutual-torques), the 3rd order current harmonic injection can generally increase the machine efficiency in constant torque region due to the extra output power, while it shows the same torque performance in flux weakening region as that of pure fundamental current supply. Although the torque ripple can also be significantly reduced by other current harmonic injection such as the 5th and 7th, other performances, such as torque capability and efficiency, could be reduced as well.

Last, it is worth mentioning that, although a major part of the planned works in this thesis has been performed, there are still a number of works to be done in the future, such as:

- The influence of the proposed current harmonic injection method on vibration and acoustic noise could be investigated.
- The vibration and torque ripple could be reduced at the same time with two or more current harmonics injected.
- Although the offline current harmonic injection is effective and easy to be implemented, current harmonic cannot be properly and flexibly selected for different operating points. Hence, online current harmonic injection method could be proposed, which adjusts the properties of current harmonic based on estimated instantaneous torque.
- The fault-tolerant control of the DS-SRMs with current harmonic injection method could be investigated (three-phase four-leg inverter can be adopted).

Appendix A : *D*- AND *Q*-AXIS TRANSFORMATION CONSIDERING HARMONIC CURRENT INJECTIONS

Chapter 2 to Chapter 4 are mainly focused on analyses of static performances in *abc*-axis frame, such as: average torque and torque ripple of DS-SRMs with current harmonic injections. However, as mentioned previously, the current harmonic injection will also have significant impact on machine dynamic performances such as the torque-speed curves, power-speed curves, efficiency maps, and so on. So the following sections will dedicate to the analyses of dynamic performance after current harmonic injections. In order to do that, different from previous chapters, the torque model based on *d*- and *q*-axis quantities such as inductances, currents, flux linkages, etc. are needed, as they make the modelling much more straightforward.

A.1. *ABC*-AXIS TO *DQ*-AXIS RREFERENCE FRAME

The general equation of periodic three phase components are given by:

$$\begin{cases} X_a = \sum_{k=1}^{\infty} X_k \sin(k\theta_e + \alpha_k) \\ X_b = \sum_{k=1}^{\infty} X_k \sin(k(\theta_e - 120°) + \alpha_k) \\ X_c = \sum_{k=1}^{\infty} X_k \sin(k(\theta_e + 120°) + \alpha_k) \end{cases} \tag{A.1}$$

where X_a, X_b and X_c can be any periodic three phase components such as, current, voltage and flux linkage and etc. The k, X_k and α_k represent the k^{th} harmonic order, magnitude and phase angle in *abc*-axis reference frame. The X_{dq} after Park transformation is given by (A.2)

$$X_d = \sum_{k=1}^{\infty} X_{dk}\,,\ X_q = \sum_{k=1}^{\infty} X_{qk}\,,\ X_0 = \sum_{k=1}^{\infty} X_{0k} \tag{A.2}$$

with

$$X_{dk} = \begin{cases} X_k \sin[(k-1)\theta_e + \alpha_k] & k = 1,4,7 \ldots \\ X_k \sin[(k+1)\theta_e + \alpha_k] & k = 2,5,8 \ldots \\ 0 & k = 3,6,9 \ldots \end{cases}$$

$$X_{qk} = \begin{cases} -X_k \cos[(k-1)\theta_e + \alpha_k] & k = 1,4,7 \ldots \\ X_k \cos[(k+1)\theta_e + \alpha_k] & k = 2,5,8 \ldots \\ 0 & k = 3,6,9 \ldots \end{cases} \quad \text{(A.3)}$$

$$X_{0k} = \begin{cases} 0 & k \neq 3,6,9 \ldots \\ X_k \sin(k\theta_e + \alpha_k) & k = 3,6,9 \ldots \end{cases}$$

TABLE A.1 FREQUENCY VARIATION AFTER PARK TRANSFORMATION

Reference Frame	Harmonic order								
X_{abc}	0	1	2	3	4	5	6	7	…
X_{dq} ($k\pm1$)	-	0	3	-	3	6	-	6	…
X_0 (k)	-	-	-	3	-	-	6	-	

According to (A.2) and (A.3), the frequency of each harmonic is changing after applying Park transformation. It is worth noting that the quantities in *dq0*-axis will only have dc and triplen harmonics as shown in TABLE A.1. It is obvious that if one wants to inject the 3rd order current harmonic in *abc*-axis reference frame, a 3rd order current harmonic has to be injected into the 0-axis. And if one wants to inject the 5th and 7th order current harmonics in *abc*-axis reference frame, the 6th order current harmonic in *dq*-axis current should be injected. The even order current harmonic, such as, 2nd and 4th, can also been injected by injecting the 3rd order current into *dq*-axis component. However, they will not be selected for injecting due to their poor performance.

A.2. *DQ*-AXIS TO *ABC*-AXIS REFERENCE FRAME

Based on the investigation in Appendix A.1, the harmonic order before and after Park transformation has been studied. However, the relationship between *abc*-axis and *dq0*-axis in terms of magnitude and phase angle is not clarified. In order to control the current harmonic in *dq0*-axis frame, further investigation of transformation from *dq0*-axis to *abc*-axis has been analysed in this section. The general equation for *dq0*-axis is given by:

$$\begin{cases} i_d = I_{d,0} + I_{d,k}\cos(k\theta_e + \alpha_{d,k}) \\ i_q = I_{q,0} + I_{q,k}\sin(k\theta_e + \alpha_{q,k}) \\ i_0 = i_{0,k}\sin(k\theta_e + \alpha_{0,k}) \end{cases} \quad \text{(A.4)}$$

where $I_{d,0}$ and $I_{q,0}$ are the dc components in *dq*-axis, respectively. The k, $I_{dq0,k}$ and $\alpha_{dq0,k}$ represent the k^{th} harmonic order, magnitude and phase angle, respectively. After inverse Park transformation, the current in *abc*-axis reference frame can be simplified as

$$\begin{cases} i_a(\theta_e) = i_1^*(\theta_e) + i_{k-1}^*(\theta_e) + i_{k+1}^*(\theta_e) + i_0 \\ i_b(\theta_e - 120°) = i_1^*(\theta_e - 120°) + i_{k-1}^*(\theta_e - 120°) + i_{k+1}^*(\theta_e - 120°) + i_0 \\ i_c(\theta_e + 120°) = i_1^*(\theta_e + 120°) + i_{k-1}^*(\theta_e + 120°) + i_{k+1}^*(\theta_e + 120°) + i_0 \end{cases} \quad \text{(A.5)}$$

with

$$\begin{cases} i_1^*(\theta_e) = i_1 \sin(\theta_e + \alpha_1) \\ i_{k-1}^*(\theta_e) = i_{k-1} \sin[(k-1)\theta_e + \alpha_{k-1}] \\ i_{k+1}^*(\theta_e) = i_{k+1} \sin[(k+1)\theta_e + \alpha_{k+1}] \end{cases} \quad \text{(A.6)}$$

The magnitude and phase angle in (A.6) can be calculated by

$$\begin{cases} i_m = \sqrt[2]{b^2 + a^2} \\ \tan \alpha_m = \dfrac{b}{a} \end{cases} \quad m = 1, k-1 \; and \; k+1$$

$$a = \begin{cases} -I_{q,0} & m = 1 \\ 0.5(-I_{d,k} \sin \alpha_{d,k} + I_{q,k} \sin \alpha_{q,k}) & m = k-1 \\ 0.5(-I_{d,k} \sin \alpha_{d,k} - I_{q,k} \sin \alpha_{q,k}) & m = k+1 \end{cases} \quad \text{(A.7)}$$

$$b = \begin{cases} I_{d,0} & m = 1 \\ 0.5(I_{d,k} \cos \alpha_{d,k} - I_{q,k} \cos \alpha_{q,k}) & m = k-1 \\ 0.5(I_{d,k} \cos \alpha_{d,k} + I_{q,k} \cos \alpha_{q,k}) & m = k+1 \end{cases}$$

Based on (A.5)-(A.7), it can be found that the magnitude and phase angle of 0-axis current before and after Park Transformation will not change. Together with the investigation in section A.1, the 3rd order current harmonic can be simply injected by supplying exactly the same 3rd order current harmonic into *0*-axis.

Moreover, in order to inject the 5th and 7th order current harmonics in *abc*-axis frame, as mentioned in section A.1, the 6th order current harmonic in *dq*-axis should be injected. Substituting the parameters listed in TABLE A.2 into (A.5)-(A.7), the current results in *dq0*- and *abc*-axis frame has been shown in Fig. A.1 and Fig. A.2, respectively. It has been proven that the 5th and 7th order current harmonics can be injected by controlling *dq0*-axis frame.

TABLE A.2 *dq0*-axis current injection parameters

Parameters	Value	Parameters	Value
$I_{d,0}$	1 A	$I_{q,0}$	1 A
$I_{d,k}$	0.2 A	$I_{q,k}$	0.2 A
$\alpha_{d,k}$	70°	$\alpha_{q,k}$	115°
k	6	i_0	0

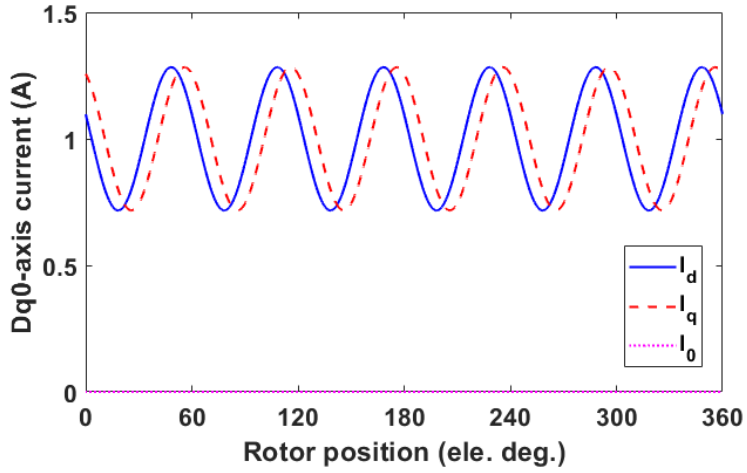

(a) Waveforms

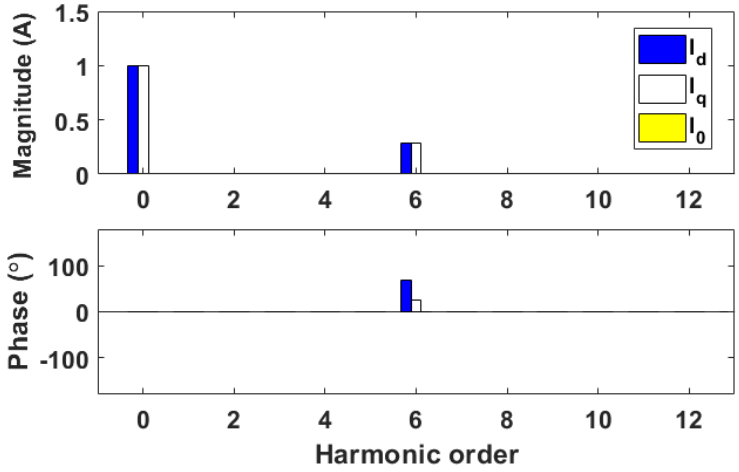

(b) Spactra

Fig. A.1 Dq0-axis current after injecting the current harmonic in TABLE A.2.

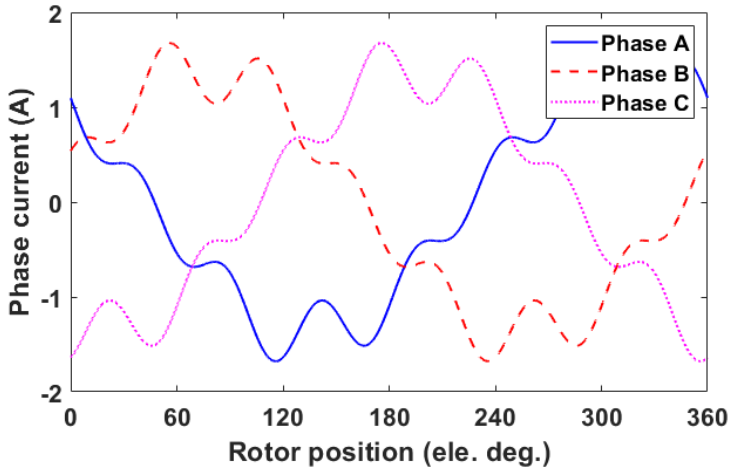

(a) Waveforms

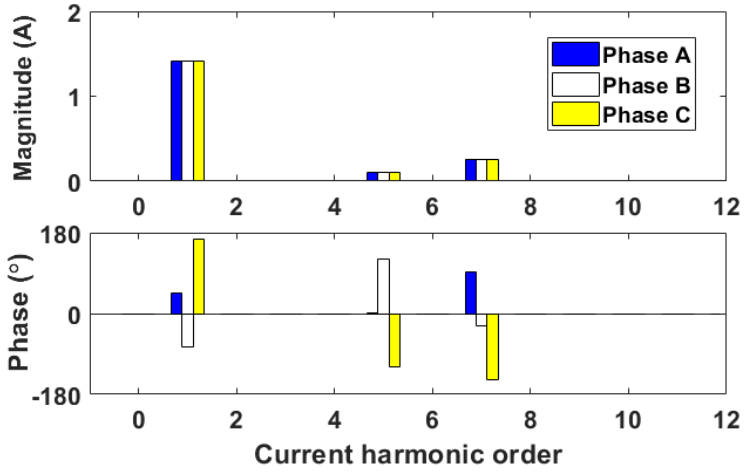

(b) Spactra

Fig. A.2 Abc-axis current after injecting the current harmonic in TABLE A.2.

In order to inject only one harmonic order into three phase current, the further analysis of (A.5) to (A.7) has been done. To simplify the methods, some assumptions have been made that the injected harmonic magnitude for both *dq*-axis are the same, hence, $I_{d,k} = I_{q,k}$.

To cancel the (k+1)th harmonic in (A.5), i_{k+1} in (A.6) should be equal to 0. Hence, components in (A.7) with m=k+1 must be "0" at the same time, as shown in (A.8).

$$\begin{cases} a = 0.5(-I_{d,k}\sin\alpha_{d,k} - I_{q,k}\sin\alpha_{q,k}) = 0 \\ b = 0.5(I_{d,k}\cos\alpha_{d,k} + I_{q,k}\cos\alpha_{q,k}) = 0 \end{cases} \quad \text{(A.8)}$$

Assuming $I_{d,k} = I_{q,k}$, (A.8) can be solved as

$$\alpha_{d,k} = \alpha_{q,k} + \pi \quad \text{(A.9)}$$

The (k-1)th harmonic injected into three phase magnitude can be easily calculated by (A.7)

$$i_{k-1}^{*}(\theta_e) = I_{d,k}\sin[(k-1)\theta_e + \alpha_{d,k}] \tag{A.10}$$

The same method has been utilized to cancel the (k-1)th harmonic. When injected *dq*-axis harmonics satisfy the conditions in (A.11),

$$\alpha_{d,k} = \alpha_{q,k} \tag{A.11}$$

then the magnitude of the (k+1)th harmonic injected into three phases can be obtained as

$$i_{k+1}^{*}(\theta_e) = I_{d,k}\sin[(k+1)\theta_e + \alpha_{d,k}] \tag{A.12}$$

After comparing (A.10) and (A.12) with current harmonic equation (A.13) in *abc*-axis. The implementation of current harmonic injections in *dq0*-axis frame can be concluded in TABLE A.3. When magnitudes of *dq*-axis currents are the same ($I_{d,k} = I_{q,k} = I_v$), if $\alpha_{d,k} = \alpha_{q,k} + \pi = \beta_v$, there is only (k-1)th order current harmonic in the phase current. But if $\alpha_{d,k} = \alpha_{q,k} = \beta_v$, there is only (k+1)th order current harmonic in the phase current.

$$i_v = I_v\sin(v\theta_e + \beta_v) \tag{A.13}$$

TABLE A.3 IMPLEMENTATION OF CURRENT HARMONIC INJECTIONS IN DQ-AXIS FRAME

$I_{dq0,k}$ / v	$I_{d,k}$	$\alpha_{d,k}$	$I_{q,k}$	$\alpha_{q,k}$	$I_{0,k}$	$\alpha_{0,k}$
k	0	-	0	-	i_v	β_v
$k-1$	i_v	β_v	i_v	β_v+π	0	-
$k+1$	i_v	β_v	i_v	β_v	0	-

Note: *k*= 3, 6, 9… *abc*-axis frame harmonic orders are k, $k-1$ or $k+1$, while in *dq0*-axis frame, they are either 0 or *k*.

By using method in TABLE A.3, the single current harmonic in phase current can be controlled in *dq0*-axis frame, and the simulation results can be shown in Fig. A.3. The magnitude and phase angle of all the current harmonics are the same, which are 30% I_1 and $\beta_v = 90°$, respectively. It is worth noting that understanding of the transformation effect of current harmonic is helpful to investigate the dynamic performance as well as experimental validation in later stage.

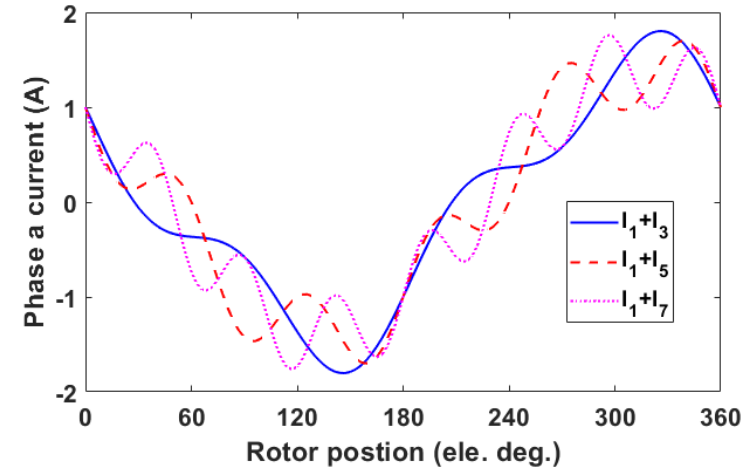

(a) Waveforms

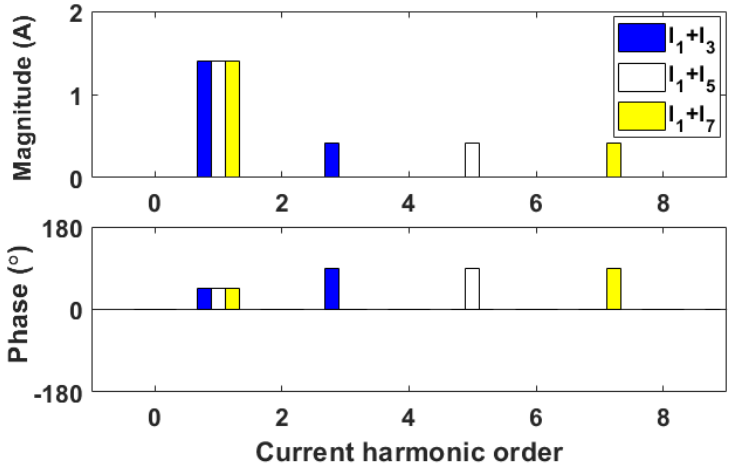

(b) Spectra

Fig. A.3 Phase a current with current harmonic injection. ($I_1 = 1.41\ A$, $I_v = 30\%I_1$, $\beta_1 = 45°$ and $\beta_v = 90°$).

A.3. 5-PHASE TRANSFORMATION EFFECT

Similar to the 3-phase DS-SRM, the model of the 5-phase DS-SRM can also be presented in a rotating (*d-q-d3-q3-0*) reference frame ("*dq0*-axis" is used for simplicity), in order to consider the 3rd order harmonic effect. The general equation of periodic five phase components are given by:

$$\begin{cases} X_a = \sum_{k=1}^{\infty} X_k \sin(k\theta_e + \alpha_k) \\ X_b = \sum_{k=1}^{\infty} X_k \sin(k(\theta_e - 72°) + \alpha_k) \\ X_c = \sum_{k=1}^{\infty} X_k \sin(k(\theta_e - 144°) + \alpha_k) \\ X_d = \sum_{k=1}^{\infty} X_k \sin(k(\theta_e - 216°) + \alpha_k) \\ X_e = \sum_{k=1}^{\infty} X_k \sin(k(\theta_e - 288°) + \alpha_k) \end{cases} \quad \text{(A.14)}$$

where X_{abcde} can be any periodic three phase components such as, current, voltage and flux linkage and etc. The *k*, X_k and α_k represent the k^{th} harmonic order, magnitude and phase angle in *abcde*-axis reference frame, respectively. X_{abcde} can be easily decoupled to dq0-axis by (A.15).

$$\begin{bmatrix} X_d \\ X_q \\ X_{d3} \\ X_{q3} \\ X_0 \end{bmatrix} = \mathrm{P} \begin{bmatrix} X_a \\ X_b \\ X_c \\ X_d \\ X_e \end{bmatrix} \quad \text{(A.15)}$$

where transformation matrix P is given by:

$$\frac{2}{5}\begin{bmatrix} \cos\theta_e & \cos\left(\theta_e - \frac{2\pi}{5}\right) & \cos\left(\theta_e - \frac{2\pi}{5}\right) & \cos\left(\theta_e - \frac{2\pi}{5}\right) & \cos\left(\theta_e - \frac{2\pi}{5}\right) \\ -\sin\theta_e & -\sin\left(\theta_e - \frac{2\pi}{5}\right) & -\sin\left(\theta_e - \frac{2\pi}{5}\right) & -\sin\left(\theta_e - \frac{2\pi}{5}\right) & -\sin\left(\theta_e - \frac{2\pi}{5}\right) \\ \cos 3\theta_e & \cos\left(3\left(\theta_e - \frac{2\pi}{5}\right)\right) & \cos\left(3\left(\theta_e - \frac{2\pi}{5}\right)\right) & \cos\left(3\left(\theta_e - \frac{2\pi}{5}\right)\right) & \cos\left(3\left(\theta_e - \frac{2\pi}{5}\right)\right) \\ -\sin 3\theta_e & -\sin\left(3\left(\theta_e - \frac{2\pi}{5}\right)\right) & -\sin\left(3\left(\theta_e - \frac{2\pi}{5}\right)\right) & -\sin\left(3\left(\theta_e - \frac{2\pi}{5}\right)\right) & -\sin\left(3\left(\theta_e - \frac{2\pi}{5}\right)\right) \\ \frac{1}{2} & \frac{1}{2} & \frac{1}{2} & \frac{1}{2} & \frac{1}{2} \end{bmatrix}$$

(A.16)

The harmonic components after transformation are simplified as:

$$X_d = \sum_{k=1}^{\infty} X_{dk}\,,\; X_q = \sum_{k=1}^{\infty} X_{qk}\,,\; X_{d3} = \sum_{k=1}^{\infty} X_{d3k}\,,\; X_{q3} = \sum_{k=1}^{\infty} X_{q3k}\;\; X_0 = \sum_{k=1}^{\infty} X_{0k} \quad \text{(A.17)}$$

with

$$
X_{dk} = \begin{cases} X_k \sin[(k-1)\theta_e + \alpha_k] & k = 1,6,11 \dots \\ 0 & k = 2,7,12 \dots \\ 0 & k = 3,8,13 \dots \\ X_k \sin[(k+1)\theta_e + \alpha_k] & k = 4,9,14 \dots \\ 0 & k = 5,10,15 \dots \end{cases}
$$

$$
X_{qk} = \begin{cases} -X_k \cos[(k-1)\theta_e + \alpha_k] & k = 1,4,7 \dots \\ 0 & k = 2,7,12 \dots \\ 0 & k = 3,8,13 \dots \\ X_k \cos[(k+1)\theta_e + \alpha_k] & k = 4,9,14 \dots \\ 0 & k = 5,10,15 \dots \end{cases}
$$

$$
X_{q3k} = \begin{cases} 0 & k = 1,4,7 \dots \\ X_k \sin[(k+3)\theta_e + \alpha_k] & k = 2,7,12 \dots \\ X_k \sin[(k-3)\theta_e + \alpha_k] & k = 3,8,13 \dots \\ 0 & k = 4,9,14 \dots \\ 0 & k = 5,10,15 \dots \end{cases}
$$

$$
X_{q3k} = \begin{cases} 0 & k = 1,4,7 \dots \\ X_k \cos[(k+3)\theta_e + \alpha_k] & k = 2,7,12 \dots \\ -X_k \cos[(k-3)\theta_e + \alpha_k] & k = 3,8,13 \dots \\ 0 & k = 4,9,14 \dots \\ 0 & k = 5,10,15 \dots \end{cases}
$$

$$
X_{0k} = \begin{cases} 0 & k \neq 5,10,15 \dots \\ X_k \sin(k\theta_e + \alpha_k) & k = 5,10,15 \dots \end{cases}
$$

(A.18)

TABLE A.4 FREQUENCY VARIATION AFTER PARK TRANSFORMATION

Reference Frame	Harmonic order (k)									
X_{abc}	0	1	2	3	4	5	6	7	8	…
X_{dq} ($k\pm1$)	-	0	-	-	5	-	5	-	-	…
X_{dq3} ($k\pm3$)	-	-	5	0	-	-	-	10	5	…
X_0 (k)	-	-	-	-	-	5	-	-	-	…

According to (A.18), the frequency of each harmonic is changing after applying Park transformation. It is found that the quantities in *dq0*-axis will only have dc and 5kth harmonics as shown in TABLE A.4. It can be found that if one wants to inject the 3rd order current harmonic in phase current, dc component of *dq3* should be injected. And if one wants to inject the 7th order harmonic in phase current, the 10th order harmonic of *dq3* components should be injected, etc.

Similar to a 3-phase system, the single order current harmonic in phase current can be controlled in *dq0*-axis by the method listed in TABLE A.5. The *dq0*-axis current expression is given by (A.19). The phase current after inverse Park transformation based on TABLE A.5 can be shown in Fig. A.4. The magnitude and phase angle of all the current harmonics are the same,

which are 30% I_1 and $\beta_v = 90°$, respectively. The single current harmonic in phase current can be exactly controlled in *dq0*-axis frame.

$$\begin{cases} i_d = I_{d,0} + I_{d,k}\cos\left(k\theta_e + \alpha_{d,k}\right) \\ i_q = I_{q,0} + I_{q,k}\sin\left(k\theta_e + \alpha_{q,k}\right) \\ i_{d3} = I_{d3,k}\cos\left(k\theta_e + \alpha_{d,k}\right) \\ i_{q3} = I_{q3,k}\sin\left(k\theta_e + \alpha_{q,k}\right) \\ i_0 = i_{0,k}\sin\left(k\theta_e + \alpha_{0,k}\right) \end{cases} \tag{A.19}$$

TABLE A.5 IMPLEMENTATION OF CURRENT HARMONIC INJECTIONS IN DQ-AXIS FRAME

v \ $I_{dq0,k}$	$I_{d,k}$	$\alpha_{d,k}$	$I_{q,k}$	$\alpha_{q,k}$	$I_{d3,k}$	$\alpha_{d3,k}$	$I_{q3,k}$	$\alpha_{q3,k}$	$I_{0,k}$	$\alpha_{0,k}$
k	0	-	0	-	0	-	0	-	i_v	β_v
$k-1$	i_v	β_v	i_v	β_v+π	0	-	0	-	0	-
$k+1$	i_v	β_v	i_v	β_v	0	-	0	-	0	-
$k-3$	0	-	0	-	i_v	β_v	i_v	β_v+π	0	-
$k+3$	0	-	0	-	i_v	β_v	i_v	β_v	0	-

Note: *k*= 0, 5, 10 … *abc*-axis frame harmonic orders are k, $k \pm 1$ or $k \pm 3$, while in *dq0*-axis frame, they are either 0 or *k*.

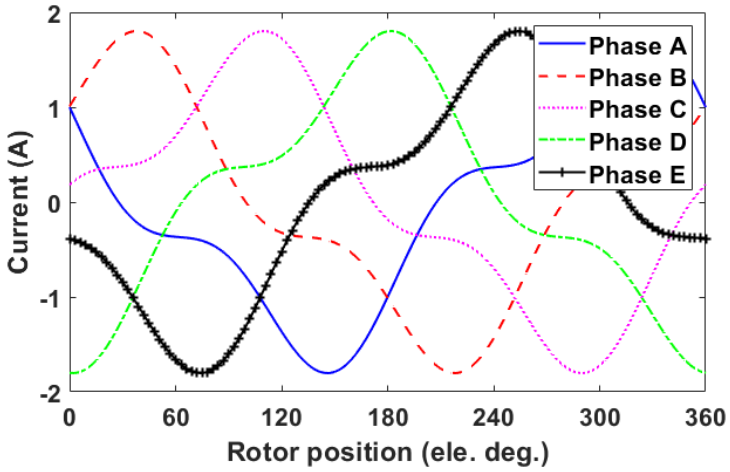

(a) I_1+I_3

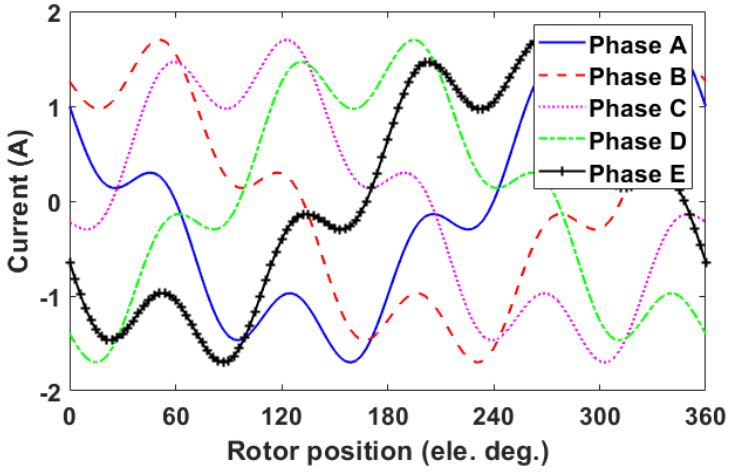

(b) I_1+I_5

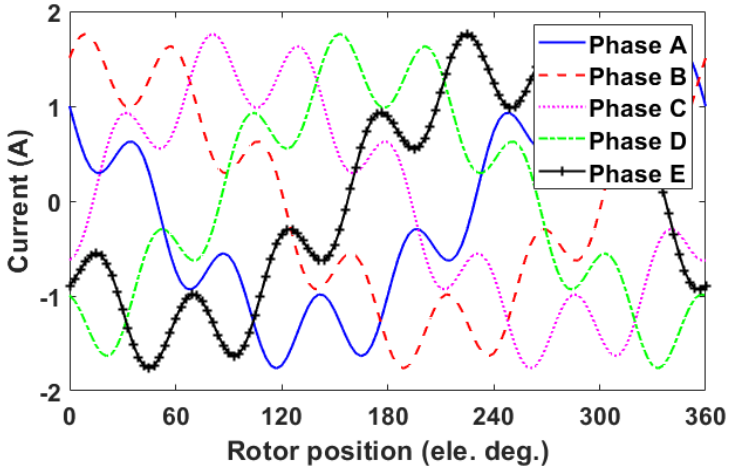

(b) I_1+I_7

Fig. A.4 Current waveforms after inverse Park transformation. ($I_1 = 1.41\ A$, $I_v = 30\%I_1$, $\beta_1 = 45°$ and $\beta_v = 90°$).

REFERENCE

[1] C. Sahin, A. E. Amac, M. Karacor, and A. Emadi, "Reducing torque ripple of switched reluctance machines by relocation of rotor moulding clinches," *IET Elec. Power Appl.,* vol. 6, no. 9, pp. 753-760, Nov. 2012.

[2] J. Kolehmainen, "Synchronous reluctance motor with form blocked rotor," *IEEE Trans. Energy Convers.,* vol. 25, no. 2, pp. 450-456, Jun. 2010.

[3] E. Sunan, K. S. M. Raza, H. Goto, H. J. Guo, and O. Ichinokura, "A new converter topology and control scheme for switched reluctance machines in application to wind energy conversion system," in *Mechatronics (ICM), 2011 IEEE International Conference on*, 2011.

[4] X. B. Liang, G. J. Li, J. Ojeda, M. Gabsi, and Z. X. Ren, "Comparative study of classical and mutually coupled switched reluctance motors using multiphysics finite-element modeling," *IEEE Trans. Ind. Electron.,* vol. 61, no. 9, pp. 5066-5074, Sep. 2014.

[5] C. M. Spargo, B. C. Mecrow, J. D. Widmer, and C. Morton, "Application of fractional-slot concentrated windings to synchronous reluctance motors," *IEEE Trans. Ind. Appl.,* vol. 51, no. 2, pp. 1446-1455, Mar.-Apr. 2015.

[6] C. M. Spargo, B. C. Mecrow, J. D. Widmer, C. Morton, and N. J. Baker, "Design and validation of a synchronous reluctance motor with single tooth windings," *IEEE Trans. Energy Convers.,* vol. 30, no. 2, pp. 795-805, Jun. 2015.

[7] C. M. Donaghy-Spargo, "Electromagnetic–mechanical design of synchronous reluctance rotors with fine features," *IEEE Trans. Mag.,* vol. 53, no. 11, pp. 1-8, Nov. 2017.

[8] L. Huang, J. Feng, S. Guo, Y. F. Li, J. Shi, and Z. Q. Zhu, "Rotor shaping method for torque ripple mitigation in variable flux reluctance machines," *IEEE Trans. Energy Conver.,* vol. 33, no. 3, pp. 1579-1589, Sep. 2018.

[9] H. Y. Yang, Y. C. Lim, and H. C. Kim, "Acoustic noise/vibration reduction of a single-phase SRM using skewed stator and rotor," *IEEE Trans. Ind. Electron.,* vol. 60, no. 10, pp. 4292-4300, Oct. 2013.

[10] G. Li, J. Ojeda, S. Hlioui, E. Hoang, M. Lecrivain, and M. Gabsi, "Modification in rotor pole geometry of mutually coupled switched reluctance machine for torque ripple mitigating," *IEEE Trans. Magn.,* vol. 48, no. 6, pp. 2025-2034, Jun. 2012.

[11] Q. Sun, J. Wu, C. Gan, Y. Hu, and J. Si, "OCTSF for torque ripple minimisation in SRMs," *IET Power Electronics,* vol. 9, no. 14, pp. 2741-2750, 2016.

[12] X. D. Xue, K. W. E. Cheng, and S. L. Ho, "Optimization and evaluation of torque-sharing functions for torque ripple minimization in switched reluctance motor drives," *IEEE Trans. Power Electron.,* vol. 24, no. 9, pp. 2076-2090, Sep. 2009.

[13] I. Husain and M. Ehsani, "Torque ripple minimization in switched reluctance motor drives by PWM current control," *IEEE Trans. Power Electron.,* vol. 11, no. 1, pp. 83-88, Jan. 1996.

[14] R. B. Inderka and R. A. A. D. Doncker, "DITC—Direct instantaneous torque control of switched reluctance drives," *IEEE Trans. Ind. Appl.,* vol. 39, no. 4, pp. 1046 - 1051, Jul.-Aug. 2003.

[15] C. Lai, G. Feng, K. Mukherjee, V. Loukanov, and N. C. Kar, "Torque ripple modeling and minimization for interior PMSM considering magnetic saturation," *IEEE Trans. Power Electron.,* vol. 33, no. 3, pp. 2417-2429, Mar. 2018.

[16] F. Erken, E. Öksüztepe, and H. Kürüm, "Online adaptive decision fusion based torque ripple reduction in permanent magnet synchronous motor," *IET Ele. Power Appl.,* vol. 10, no. 3, pp. 189-196, Mar. 2016.

[17] G. J. Li, J. Ojeda, E. Hoang, M. Lecrivain, and M. Gabsi, "Comparative studies between classical and mutually coupled switched reluctance motors using thermal-electromagnetic analysis for driving cycles," *IEEE Trans. Magn.,* vol. 47, no. 4, pp. 839-847, Apr. 2011.

[18] W. Q. Chu, Z. Q. Zhu, J. Zhang, X. Ge, X. Liu, D. Stone, *et al.*, "Comparison of electrically excited and interior permanent magnet machines for hybrid electric vehicle application," in *2014 17th International Conference on Electrical Machines and Systems (ICEMS)*, 2014.

[19] T. Miller, "Switched reluctance motors and their control," *New York: Oxford University Press,* Jul. 1993.

[20] J. Ahn and G. F. Lukman, "Switched reluctance motor: research trends and overview," *CES Trans. Electric. Machines and System.,* vol. 2, no. 4, pp. 339-347, Dec. 2018.

[21] R. Jarvis, "Davidson's locomotive: How did he do it?," *Engineering. Science and Education Journal,* vol. 5, no. 6, pp. 281-288, Dec. 1996.

[22] P. J. Lawrenson, "Development and application of reluctance motors," *Electronics and Power,* vol. 11, no. 6, pp. 195-198, 1965.

[23] P. J. Lawrenson, J. M. Stephenson, P. T. Blenkinsop, J. Corda, and N. N. Fulton, "Variable-speed switched reluctance motors," *IEE Proceedings B - Electric Power Applications,* vol. 127, no. 4, pp. 253-265, 1980.

[24] B. C. Mecrow, "Fully pitched-winding switched-reluctance and stepping-motor arrangements," *IET Elect. Power Appl.,* vol. 140, no. 1, pp. 61-70, Jan. 1993.

[25] B. C. Mecrow, "New winding configurations for doubly salient reluctance machines," *IEEE Trans. Ind. Appl.,* vol. 32, no. 6, pp. 1348-1356, Nov. 1996.

[26] G. J. Li, X. Ojeda, S. Hlioui1, E. Hoang, M. Gabsi, and C. Balpe, "Comparative study of switched reluctance motors performances for two current distributions and excitation modes," *In Proc. IEEE Ind. Electron. Conf. (IECON'09), Porto, Portugal,* Nov. 2009.

[27] X. B. Liang, G. J. Li, J. Ojeda, M. Gabsi, and Z. Ren, "Comparative study of vibration and acoustic noise between classical and mutually coupled switched reluctance motors," in *Electrical Machines (ICEM), 2012 XXth International Conference on*, 2012.

[28] X. Y. Ma, G. J. Li, G. Jewell, and Z. Q. Zhu, "Comparative study of short-pitched and fully-pitched SRMs supplied by sine wave currents," *in Proc. Int. Conf. Ind. Technol. (ICIT'15), Seville, Spain,*, pp. 664-670, Mar. 2015.

[29] G.-J. Li, X. Ma, G. Jewell, Z. Q. Zhu, and P. Xu, "Influence of conduction angles on single layer switched reluctance machines," *IEEE Trans. Mag.*, vol. 52, no. 12, pp. 1-1, Dec. 2016.

[30] X. Y. Ma, G. J. Li, G. W. Jewell, and Z. Q. Zhu, "Recent development of reluctance machines with different winding configurations, excitation methods, and machine structures," *CES Transactions on Electrical Machines and Systems*, vol. 2, no. 1, pp. 82-92, Mar. 2018.

[31] J. Zhu, K. W. E. Cheng, X. Xue, and Y. Zou, "Design of a new enhanced torque in-wheel switched reluctance motor with divided teeth for electric vehicles," *IEEE Trans. Mag.*, vol. 53, no. 11, pp. 1-4, Nov 2017.

[32] J. Zhu, K. W. E. Cheng, and X. Xue, "Design and analysis of a new enhanced torque hybrid switched reluctance motor," *IEEE Trans. Energy Convers.*, vol. 33, no. 4, pp. 1965-1977, Dec. 2018.

[33] C. Lee, R. Krishnan, and N. S. Lobo, "Novel two-phase switched reluctance machine using common-pole e-core structure: Concept, analysis, and experimental verification," *IEEE Trans. Ind. Appl.*, vol. 45, no. 2, pp. 703-711, Mar. 2009.

[34] M. Tanujaya, D. Lee, and J. Ahn, "Characteristic analysis of a novel 6/5 c-core type three-phase Switched Reluctance Motor," in *2011 International Conference on Electrical Machines and Systems*, 2011.

[35] G. J. Li, X. Ma, G. Jewell, and Z. Q. Zhu, "Novel modular switched reluctance machines for performance improvement," *IEEE Trans. Energy Conver.*, vol. 33, no. 3, pp. 1255-1265, Sep. 2018.

[36] W. Ding, Y. Hu, H. Fu, and Q. Chen, "Analysis and evaluation of modular E-shaped stator switched reluctance machines employing segmented and conventional rotor topologies," *IET Ele. Power Appl.*, vol. 10, no. 9, pp. 939-951, Nov. 2016.

[37] W. Ding, S. Yang, and Y. Hu, "Development and investigation on segmented-stator hybrid-excitation switched reluctance machines with different rotor pole numbers," *IEEE Trans. Ind. Electron.*, vol. 65, no. 5, pp. 3784-3794, May 2018.

[38] W. Ding, H. Fu, and Y. Hu, "Characteristics assessment and comparative study of a segmented-stator permanent-magnet hybrid-excitation srm drive with high-torque capability," *IEEE Trans. Power Electron.*, vol. 33, no. 1, pp. 482-500, Jan. 2018.

[39] L. Szabo and M. Ruba, "Segmental stator switched reluctance machine for safety-critical applications," *IEEE Trans. Ind. Appl.*, vol. 48, no. 6, pp. 2223-2229, Nov. 2012.

[40] M. Ruba, I. Viorel, and L. Szabó, "Modular stator switched reluctance motor for fault tolerant drive systems," *IET Ele. Power Appl.*, vol. 7, no. 3, pp. 159-169, Mar. 2013.

[41] N. R. Patel, V. A. Shah, and M. M. Lokhande, "A novel approach to the design and development of 12/15 radial field c-core switched reluctance motor for implementation in electric vehicle application," *IEEE Trans. Veh. Tech.*, vol. 67, no. 9, pp. 8031-8040, Sep. 2018.

[42] G. E. Horst, "Redundant switched reluctance motor," U.S. Patent 5 239 217, Aug. 24 1993.

[43] S. F. Kolomeitsev, "Variable reluctance electric motor." U.S. Patent 5 719 456, Feb. 17 1998.

[44] P. C. Desai, M. Krishnamurthy, N. Schofield, and A. Emadi, "Novel switched reluctance machine configuration with higher number of rotor poles than stator poles: Concept to implementation," *IEEE Trans. Ind. Electron.*, vol. 57, no. 2, pp. 649-659, Feb. 2010.

[45] B. Bilgin, A. Emadi, and M. Krishnamurthy, "Design considerations for switched reluctance machines with a higher number of rotor poles," *IEEE Trans. Ind. Electron.*, vol. 59, no. 10, pp. 3745-3756, Oct. 2012.

[46] P. J. Lawrenson and L. A. Agu, "Theory and performance of polyphase reluctance machines," *Proceedings of the Institution of Electrical Engineers*, vol. 111, no. 8, pp. 1435-1445, Aug. 1964.

[47] B. C. Mecrow, J. W. Finch, E. A. El-Kharashi, and A. G. Jack, "Switched reluctance motors with segmental rotors," *IEE Proceedings - Electric Power Applications*, vol. 149, no. 4, pp. 245-254, 2002.

[48] B. C. Mecrow, E. A. El-Kharashi, J. W. Finch, and A. G. Jack, "Segmental rotor switched reluctance motors with single-tooth windings," *IEE Proceedings - Electric Power Applications*, vol. 150, no. 5, pp. 591-599, 2003.

[49] B. C. Mecrow, E. A. El-Kharashi, J. W. Finch, and A. G. Jack, "Preliminary performance evaluation of switched reluctance motors with segmental rotors," *IEEE Transactions on Energy Conversion*, vol. 19, no. 4, pp. 679-686, 2004.

[50] J. D. Widmer and B. C. Mecrow, "Optimized Segmental Rotor Switched Reluctance Machines With a Greater Number of Rotor Segments Than Stator Slots," *IEEE Transactions on Industry Applications*, vol. 49, no. 4, pp. 1491-1498, 2013.

[51] R. V and B. G. Fernandes, "Design methodology for high-performance segmented rotor switched reluctance motors," *IEEE Trans. Energy Convers.*, vol. 30, no. 1, pp. 11-21, Mar 2015.

[52] T. Matsuo and T. A. Lipo, "Rotor design optimization of synchronous reluctance machine," *IEEE Transactions on Energy Conversion*, vol. 9, no. 2, pp. 359-365, 1994.

[53] H. Hong, H. Liu, S. Cho, J. Lee, and C. Jin, "Design of high-end synchronous reluctance motor using 3-d printing technology," *IEEE Trans. Mag.*, vol. 53, no. 6, pp. 1-5, Jun. 2017.

[54] D. A. Staton, T. J. E. Miller, and S. E. Wood, "Maximising the saliency ratio of the synchronous reluctance motor," *IEE Proceedings B - Electric Power Applications*, vol. 140, no. 4, pp. 249-259, 1993.

[55] J. K. Kostko, "Polyphase reaction synchronous motors," *Journal of the American Institute of Electrical Engineers*, vol. 42, no. 11, pp. 1162-1168, Nov. 1923.

[56] C. H. Lee, "The theory and design of a very-slow-speed reluctance motor," *Transactions of the American Institute of Electrical Engineers. Part III: Power Apparatus and Systems*, vol. 78, no. 4, pp. 1683-1688, Dec. 1959.

[57] W. Fong and J. S. C. Htsui, "New type of reluctance motor," *Proc. IEE*, vol. 117, no. 3, pp. 545-551, 1970.

[58] G. Pellegrino, F. Cupertino, and C. Gerada, "Barriers shapes and minimum set of rotor parameters in the automated design of synchronous reluctance machines," in *in IEMDC*, Chicago, USA, 2013.

[59] J. Barta and O. C, "Design and optimization of synchronous reluctance machine," in *in 16th Int. Conf. Mechatron.*, Brno, Czech Republic, 2014.

[60] A. Vagati, M. Pastorelli, G. Francheschini, and S. C. Petrache, "Design of low-torque-ripple synchronous reluctance motors," *IEEE Trans. Ind. Appl.*, vol. 34, no. 4, pp. 758-765, Jul. 1998.

[61] M. Palmieri, M. Perta, F. Cupertino, and G. Pellegrino, "Effect of the numbers of slots and barriers on the optimal design of synchronous reluctance machines," in *International Conference on Optimization of Electrical and Electronic Equipment (OPTIM)*, Bran, Romania, 2014.

[62] K. Wang, Z. Q. Zhu, G. Ombach, M. Koch, S. Zhang, and J. Xu, "Optimal slot/pole and flux-barrier layer number combinations for synchronous reluctance machines," in *in 8th Int.l Conf. EVER*, 2013.

[63] X. Diao, H. Zhu, Y. Qin, and Y. Hua, "Torque ripple minimization for bearingless synchronous reluctance motor," *IEEE Trans. Applied Super.*, vol. 28, no. 3, pp. 1-5, Apr. 2018.

[64] M. A. Kabir and I. Husain, "Application of a multilayer ac winding to design synchronous reluctance motors," *IEEE Trans. Ind. Appl.*, vol. 54, no. 6, pp. 5941-5953, Nov. 2018.

[65] C. M. Spargo, B. C. Mecrow, and J. D. Widmer, "Application of fractional slot concentrated windings to synchronous reluctance machines," in *IEMDC*, Chicago, IL, USA, 2013.

[66] C. M. Donaghy-Spargo, B. C. Mecrow, and J. D. Widmer, "On the influence of increased stator leakage inductance in single-tooth wound synchronous reluctance motors," *IEEE Trans. Ind. Electron.*, vol. 65, no. 6, pp. 4475-4482, Jun. 2018.

[67] X. Y. Ma, G. J. Li, G. W. Jewell, Z. Q. Zhu, and H. L. Zhan, "Performance comparison of doubly salient reluctance machine topologies supplied by sinewave currents," *IEEE Trans. Ind. Electron.*, vol. 63, no. 7, pp. 4086 - 4096, Jul. 2016.

[68] D. Min, A. Keyhani, and T. Sebastian, "Torque ripple analysis of a pm brushless dc motor using finite element method," *IEEE Trans. Energy Convers.*, vol. 19, no. 1, pp. 40-45, Mar. 2004.

[69] W. Q. Chu and Z. Q. Zhu, "Reduction of on-load torque ripples in permanent magnet synchronous machines by improved skewing," *IEEE Trans. Mag.*, vol. 49, no. 7, pp. 3822-3825, Jul. 2013.

[70] Y. Yasa, M. Elamin, Y. Sozer, J. Kutz, J. S. Tylenda, and R. L. Wright, "Acoustic noise mitigation for high pole count switched reluctance machines through skewing method with multiphysics FEA simulations," in *in IEEE (ECCE)*, Cincinnati, OH, USA, 2017.

[71] C. Gan, J. Wu, M. Shen, S. Yang, Y. Hu, and W. Cao, "Investigation of skewing effects on the vibration reduction of three-phase switched reluctance motors," *IEEE Trans. Mag.*, vol. 51, no. 9, pp. 1-9, Sep. 2015.

[72] M. Sugiura, Y. Ishihara, H. Ishikawa, and H. Naitoh, "Improvement of efficiency by stepped-skewing rotor for switched reluctance motors," in *in IPEC-Hiroshima - ECCE ASIA*, Hiroshima, Japan, 2014.

[73] M. Abbasian, M. Moallem, and B. Fahimi, "Double-stator switched reluctance machines (DSSRM): Fundamentals and magnetic force analysis," *IEEE Trans. Energy Conver.*, vol. 25, no. 3, pp. 589-597, Sep. 2010.

[74] M. A. Tavakkoli and M. Moallem, "Torque ripple mitigation of double stator switched reluctance motor (DSSRM) using a novel rotor shape optimization," in *in IEEE (ECCE)*, Raleigh, NC, USA, 2012.

[75] A. H. Isfahani and B. Fahimi, "Comparison of mechanical vibration between a double-stator switched reluctance machine and a conventional switched reluctance machine," *IEEE Trans. Mag.*, vol. 50, no. 2, pp. 293-296, Feb. 2014.

[76] M. Asgar and E. Afjei, "Radial force reduction in a new flat-type double-stator switched reluctance motor," *IEEE Trans. Energy Convers.*, vol. 31, no. 1, pp. 141-149, Mar. 2016.

[77] N. K. Sheth and K. R. Rajagopal, "Optimum pole arcs for a switched reluctance motor for higher torque with reduced ripple," *IEEE Trans. Mag.*, vol. 39, no. 5, pp. 3214-3216, Sep. 2003.

[78] M. T. Mohammad and J. E. Fletcher, "Five-phase permanent magnet machines, advantages and applications," in *in 5th IET (PEMD 2010)*, Brighton, UK, UK, 2010.

[79] L. Parsa, H. A. Toliyat, and A. Goodarzi, "Five-phase interior permanent-magnet motors with low torque pulsation," *IEEE Trans. Ind. Appl.*, vol. 43, no. 1, pp. 40-46, Jan. 2007.

[80] C. Cossar, L. Kelly, T. J. E. Miller, C. Whitley, C. Maxwell, and D. Moorhouse, "The design of a switched reluctance drive for aircraft flight control surface actuation," in *in Proc IEE Colloq. Ele. Mach. Syst. More Elect. Aircr.*, London, UK, 1999.

[81] R. Krishnan, D. Blanding, A. Bhanot, A. M. Staley, and N. S. Lobo, "High reliability SRM drive system for aerospace applications," in *in Proc. 29th Ann. Conf. IEEE Ind. Electron. Soc.*, 2003.

[82] X. Deng, B. Mecrow, R. Martin, and S. Gadoue, "Effects of winding connection on performance of a six-phase switched reluctance machine," *IEEE Trans. Energy Conver.*, vol. 33, no. 1, pp. 166-178, Mar. 2018.

[83] S. Han, C. Liu, L. Zhang, G. Jun, and S. Dai, "Mutual coupling and its effect on current and torque of six phases Switched Reluctance Motor," in *2016 Eleventh International Conference on Ecological Vehicles and Renewable Energies (EVER)*, 2016.

[84] V. P. Vujičić, "Minimization of torque ripple and copper losses in switched reluctance drive," *IEEE Trans. Power Electron.*, vol. 27, no. 1, pp. 388-399, Jan. 2012.

[85] C. Changhwan, K. Seungho, K. Yongdae, and P. Kyihwan, "A new torque control method of a switched reluctance motor using a torque-sharing function," *IEEE Trans. Mag.*, vol. 38, no. 5, pp. 3288-3290, Sep. 2002.

[86] N. H. Fuengwarodsakul, M. Menne, R. B. Inderka, and R. W. D. Doncker, "High-dynamic four-quadrant switched reluctance drive based on DITC," *IEEE Transactions on Industry Applications*, vol. 41, no. 5, pp. 1232-1242, 2005.

[87] A. Klein-Hessling, A. Hofmann, and R. W. D. Doncker, "Direct instantaneous torque and force control: a control approach for switched reluctance machines," *IET Ele. Power Appl.*, vol. 11, no. 5, pp. 935-943, May 2017.

[88] P. Jinupun and P. C.-K. Luk, "Direct torque control for sensorless switched reluctance motor drives," in *7th Int. Conf. Power Electron. Variable Speed Drives*, 1998.

[89] A. D. Cheok and Y. Fukuda, "A new torque and flux control method for switched reluctance motor drives," *IEEE Transactions on Power Electronics*, vol. 17, no. 4, pp. 543-557, 2002.

[90] X. Ai-de, Z. Xianchao, H. Kunlun, and C. Yuzhao, "Torque-ripple reduction of SRM using optimised voltage vector in DTC," *IET Ele. Sys. Transport.*, vol. 8, no. 1, pp. 35-43, 2018.

[91] N. Yan, X. Cao, and Z. Deng, "Direct Torque Control for Switched Reluctance Motor to Obtain High Torque–Ampere Ratio," *IEEE Trans. Ind. Electron.*, vol. 66, no. 7, pp. 5144-5152, Jul. 2019.

[92] X. Deng, B. Mecrow, H. Wu, and R. Martin, "Design and development of low torque ripple variable-speed drive system with six-phase switched reluctance motors," *IEEE Trans. Energy Conver.*, vol. 33, no. 1, pp. 420-429, Mar. 2018.

[93] Hiroki Ishikawa, Y. Kamada, and H. Naitoh, "Instantaneous current profile control for flat torque of switched reluctance motors," *Electrical Engineering in Japan*, vol. 163, no. 3, 2008.

[94] M. Shirahase, S. Morimoto, and M. Sanada, "Torque ripple reduction of SRM by optimization of current reference," in *in ECCE*, Sapporo, Japan, 2010.

[95] P. L. Chapman and S. D. Sudhoff, "Design and precise realization of optimized current waveforms for an 8/6 switched reluctance drive," *IEEE Trans. Power Electron.*, vol. 17, no. 1, pp. 76-83, Jan. 2002.

[96] Z. Q. Zhu, B. Lee, L. Huang, and W. Chu, "Contribution of current harmonics to average torque and torque ripple in switched reluctance machines," *IEEE Trans. Magn.*, vol. 53, no. 3, pp. 1-9, Mar. 2017.

[97] F. C. Lin and S. M. Yang, "Instantaneous shaft radial force control with sinusoidal excitations for switched reluctance motors," *IEEE Trans. Energy Convers.*, vol. 22, no. 3, pp. 629-636, Sep. 2007.

[98] X. Liu, Z. Q. Zhu, M. Hasegawa, A. Pride, R. Deodhar, T. Maruyama, *et al.*, "Performance comparison between unipolar and bipolar excitations in switched reluctance machine with sinusoidal and rectangular waveforms," in *2011 IEEE Energy Conversion Congress and Exposition*, 2011.

[99] X. Ojeda, X. Mininger, M. Gabsi, and M. Lecrivain, "Sinusoidal feeding for switched reluctance machine: application to vibration damping," in *ICEM 2008*, Vilamoura, Portugal, 2008.

[100] J. Hongyun, M. Cheng, W. Hua, Y. Zhengzhuan, and Z. Yunqian, "Compensation of cogging torque for flux-switching permanent magnet motor based on current harmonics injection," in *2009 IEEE International Electric Machines and Drives Conference*, 2009.

[101] N. Nakao and K. Akatsu, "Torque ripple control for synchronous motors using instantaneous torque estimation," in *2011 IEEE Energy Conversion Congress and Exposition*, 2011.

[102] N. Nakao and K. Akatsu, "Torque ripple compensation based on instantaneous torque estimation in permanent magnet synchronous motors," in *2011 IEEE International Electric Machines & Drives Conference (IEMDC)*, 2011.

[103] N. Nakao and K. Akatsu, "Suppressing Pulsating Torques: Torque Ripple Control for Synchronous Motors," *IEEE Ind. Appl. Magazine*, vol. 20, no. 6, pp. 33-44, 2014.

[104] G. Feng, C. Lai, and N. C. Kar, "An analytical solution to optimal stator current design for PMSM torque ripple minimization with minimal machine losses," *IEEE Trans. Ind. Electron.*, vol. 64, no. 10, pp. 7655-7665, Oct. 2017.

[105] W. Hu, H. Nian, and T. Zheng, "Torque ripple suppression method with reduced switching frequency for open-winding pmsm drives with common dc bus," *IEEE Trans. Ind. Electron.*, vol. 66, no. 1, pp. 674-684, 2019.

[106] Y. Sui, P. Zheng, Y. Fan, and J. Zhao, "Research on the vector control strategy of five-phase permanent-magnet synchronous machine based on third-harmonic current injection," in *IEMDC*, Miami, FL, USA, 2017.

[107] K. Wang, Z. Y. Gu, C. Liu, and Z. Q. Zhu, "Design and analysis of a five-phase spm machine considering third harmonic current injection," *IEEE Trans. Energy Conver.*, vol. 33, no. 3, pp. 1108-1117, Sep. 2018.

[108] Z. Zhang, "Analysis of a five-phase dual mechanical port machine with harmonic current injection for torque capability improvement," in *In Proc. IEEE Transportation Electrification Conference and Expo (ITEC)*, Detroit, MI, USA, 2019.

[109] S. Ruhe, H. A. Toliyat, and A. El-Antably, "Field oriented control of five-phase synchronous reluctance motor drive with flexible 3rd harmonic current injection for high specific torque," in *In Proc. IEEE Ind. Appl. Conf.*, Chicago, IL, USA, 2001.

[110] T. Phuoc Hoa, D. Flieller, N. K. Nguyen, J. Mercklé, and G. Sturtzer, "An investigation of adaline for torque ripple minimization in non-sinusoidal synchronous reluctance motors," in *In Proc. IEEE Ann. Conf. Ind. Electron. Society*, Vienna, Austria, 2013.

[111] P. Truong, D. Flieller, N. Nguyen, J. Merckle, and G. Sturtzer, "Torque ripple minimization in non-sinusoidal synchronous reluctance motors based on artificial neural networks," *Elect. Power Syst. Res.*, vol. 140, pp. 37–45, Nov. 2016.

[112] K. Jun-Koo and S. Seung-Ki, "New direct torque control of induction motor for minimum torque ripple and constant switching frequency," *IEEE Trans. Ind. Appl.*, vol. 35, no. 5, pp. 1076-1082, 1999.

[113] Y. Zhang and J. Zhu, "Direct torque control of permanent magnet synchronous motor with reduced torque ripple and commutation frequency," *IEEE Trans. Power Electron.*, vol. 26, no. 1, pp. 235-248, Jan. 2011.

[114] Y. Ren, Z. Q. Zhu, and J. Liu, "Direct Torque Control of Permanent-Magnet Synchronous Machine Drives With a Simple Duty Ratio Regulator," *IEEE Transactions on Industrial Electronics*, vol. 61, no. 10, pp. 5249-5258, 2014.

[115] G. H. B. Foo and X. Zhang, "Robust Constant Switching Frequency-Based Field-Weakening Algorithm for Direct Torque Controlled Reluctance Synchronous Motors," *IEEE Trans. Ind. Inf.*, vol. 12, no. 4, pp. 1462-1473, Aug 2016.

[116] H. Zhu, X. Xiao, and Y. Li, "Torque ripple reduction of the torque predictive control scheme for permanent-magnet synchronous motors," *IEEE Trans. Ind. Electron.*, vol. 59, no. 2, pp. 871-877, Feb. 2012.

[117] Y. Cho, K. Lee, M. Li, J. Song, and Y. Lee, "Novel torque predictive control for a permanent-magnet synchronous motor with minimum torque ripple and fast dynamics," in *In Proc. APEC*, Long Beach, CA, USA, 2013.

[118] M. Liu, J. Hu, and K. W. Chan, "Improved model predictive control of permanent magnet synchronous motor with duty ratio optimization and cost function correction," in *in Proc. 20th ICEMS*, Sydney, NSW, Australia, 2017.

[119] Q. Liu and K. Hameyer, "Torque ripple minimization for direct torque control of pmsm with modified fcsmpc," *IEEE Trans. Ind. Appl.*, vol. 52, no. 6, pp. 4855-4864, Nov. 2016.

[120] H. Hadla and S. Cruz, "Predictive stator flux and load angle control of synchronous reluctance motor drives operating in a wide speed range," *IEEE Trans.Ind. Electron.*, vol. 64, no. 9, pp. 6950-6959, Sep. 2017.

[121] S. C. H. Hadla, "Active flux based finite control set model predictive control of synchronous reluctance motor drives," in *In Proc. Eur. Conf. Power Electron. Appl.*, Karlsruhe, Germany, 2016.

[122] K. Zhang, G. J. Li, Z. Q. Zhu, and G. W. Jewell, "Torque performance improvement of doubly salient synchronous reluctance machines by current harmonic injection," *in Proc. IEEE Int. Ele. Mach. & Dri Conf (IEMDC)*, pp. 1222-1227, 12-15 May 2019.

[123] T. J. E. Miller, "Optimal design of switched reluctance motors," *IEEE Trans. Ind. Electron.*, vol. 49, no. 1, pp. 15-27, Feb. 2002.

[124] I. Husain, "Minimization of torque ripple in SRM drives," *IEEE Trans. Ind. Electron.*, vol. 49, no. 1, pp. 28-39, Feb. 2002.

[125] W. Hua, H. hua, N. Dai, G. Zhao, and M. Cheng, "Comparative study of switched reluctance machines with half-and full-teeth-wound windings," *IEEE Trans. Ind. Electron.*, vol. 63, no. 3, pp. 1414-1424, March 2016.

[126] J. Li and Y. Cho, "Investigation into reduction of vibration and acoustic noise in switched reluctance motors in radial force excitation and frame transfer function aspects," *IEEE Trans. Magn.*, vol. 45, no. 10, pp. 4664-4667, Oct. 2009.

[127] D. E. Cameron, J. H. Lang, and S. D. Umans, "The origin and reduction of acoustic noise in doubly salient variable-reluctance motors," *IEEE Trans. Ind. Appl.*, vol. 28, no. 6, pp. 1250-1255, Nov.-Dec. 1992.

[128] E. S. Afjei and H. A. Toliyat, "A novel multilayer switched reluctance motor," *IEEE Trans. Energy Convers.*, vol. 17, no. 2, pp. 217-221, Jun. 2002.

[129] F. Daldaban and N. Ustkoyuncu, "Multi-layer switched reluctance motor to reduce torque ripple," *Energy Conversion and Management*, vol. 49, no. 5, pp. 974-979, May 2008.

[130] R. S. Wallace and D. G. Taylor, "A balanced commutator for switched reluctance motors to reduce torque ripple," *IEEE Trans. Power Electron.*, vol. 7, no. 4, pp. 617-626, Oct. 1992.

[131] S. K. Sahoo, S. Dasgupta, S. K. Panda, and J. X. Xu, "A lyapunov function-based robust direct torque controller for a switched reluctance motor drive system," *IEEE Trans. Power Electron.*, vol. 27, no. 2, pp. 555-564, Feb. 2012.

[132] H. J. Brauer, M. D. Hennen, and R. W. D. Doncker, "Control for polyphase switched reluctance machines to minimize torque ripple and decrease ohmic machine losses," *IEEE Trans. Power Electron.*, vol. 27, no. 1, pp. 370-378, Jan. 2012.

[133] X. Liu, Z. Q. Zhu, M. Hasegawa, A. Pride, and R. Deodhar, "Investigation of PWMs on vibration and noise in SRM with sinusoidal bipolar excitation," presented at the in Proc. 21th IEEE International Symposium on Ind. Electron., Hangzhou, China, pp. 674-679, 2012.

[134] B. Lee, Z. Q. Zhu, and L. R. Huang, "Torque ripple reduction for 6-stator/4-rotor-pole variable flux reluctance machines by using harmonic field current injection," *IEEE Trans. Ind. Appl.*, vol. 53, no. 4, pp. 3730-3737, Apr. 2017.

[135] G. J. Li, Z. Q. Zhu, X. Y. Ma, and G. W. Jewell, "Comparative study of torque production in conventional and mutually coupled SRMs using frozen permeability," *IEEE Trans. Magn.*, vol. 52, no. 6, Jun. 2016.

[136] W. Q. Chu and Z. Q. Zhu, "Average torque separation in permanent magnet synchronous machines using frozen permeability," *IEEE Trans. Magn.*, vol. 49, no. 3, pp. 1202-1210, Mar. 2013.

[137] G. J. Li, K. Zhang, Z. Q. Zhu, and G. W. Jewell, "Comparative studies of torque performance improvement for different doubly salient synchronous reluctance machines by current harmonic injection," *IEEE Trans. Energy Convers.*, vol. 34, no. 2, pp. 1094-1104, Jun. 2019.

[138] X. Y. Ma, G. J. Li, Z. Q. Zhu, G. W. Jewell, and J. Green, "Investigation on synchronous reluctance machines with different rotor topologies and winding configurations," *IET Elect. Power Appl.*, vol. 12, no. 1, pp. 45-53, Jan. 2018.

[139] K. Zhang, G. J. Li, Z. Q. Zhu, and G. W. Jewell, "Investigation on contribution of inductance harmonics to torque production in multiphase doubly salient synchronous reluctance machines," *IEEE Trans. Mag.*, vol. 55, no. 4, pp. 1-10, Apr. 2019.

[140] J. Baek, S. S. R. Bonthu, and S. Choi, "Design of five-phase permanent magnet assisted synchronous reluctance motor for low output torque ripple applications," *IET Ele. Power Appl.*, vol. 10, no. 5, pp. 339-346, 2016.

[141] L. Parsa, "On advantages of multi-phase machines," *31st Annual Conf. IEEE Ind. Electron. Society (IECON 05)*, pp. 6, 6-10 Nov. 2005.

[142] A. Arafat, S. Choi, and J. Baek, "Open-phase fault detection of a five-phase permanent magnet assisted synchronous reluctance motor based on symmetrical components theory," *IEEE Trans. Ind. Electron.*, vol. 64, no. 8, pp. 6465-6474, Aug. 2017.

[143] Y. Sui, P. Zheng, Z. Yin, M. Wang, and C. Wang, "Open-circuit fault-tolerant control of five-phase pm machine based on reconfiguring maximum round magnetomotive force," *IEEE Trans. Ind. Electron.*, vol. 66, no. 1, pp. 48-59, Jan. 2019.

[144] L. A. Pereira, S. Haffner, G. Nicol, and T. F. Dias, "Multiobjective optimization of five-phase induction machines based on NSGA-II," *IEEE Trans. Ind. Electron.*, vol. 64, no. 12, pp. 9844-9853, Dec. 2017.

[145] T. A. Lopo, "Analysis of synchronous machines,." 2nd ed. Boca Raton, USA: CRC Press, 2008.

[146] S. Jia, R. Qu, J. Li, and D. Li, "Principles of stator dc winding excited vernier reluctance machines," *IEEE Trans. Energy Conver.*, vol. 31, no. 3, pp. 935-946, Sep. 2016.

[147] G. Lee, S. Kim, J. Hong, and J. Bahn, "Torque ripple reduction of interior permanent magnet synchronous motor using harmonic injected current," *IEEE Trans. Mag.*, vol. 44, no. 6, pp. 1582-1585, Jun. 2008.

[148] Y. Hu, Z. Q. Zhu, and M. Odavic, "Torque capability enhancement of dual three-phase pmsm drive with fifth and seventh current harmonics injection," *IEEE Trans. Ind. Appl.*, vol. 53, no. 5, pp. 4526-4535, Sep. 2017.

[149] N. Bianchi and M. D. Pre, "Use of the star of slots in designing fractional-slot single-layer synchronous motors," *IEE Proceedings - Elect. Power Appl.*, vol. 153, no. 3, pp. 459-466, May 2006.

[150] E. Fornasiero, L. Alberti, N. Bianchi, and S. Bolognani, "Considerations on selecting fractional-slot nonoverlapped coil windings," *IEEE Trans. Ind. Appl.*, vol. 49, no. 3, pp. 1316-1324, May-Jun. 2013.

[151] K. Zhang, G. J. Li, R. Zhou, Z. Q. Zhu, and G. W. Jewell, "Losses in different doubly salient synchronous reluctance machines with current harmonic injection," *Int. Conf. Ele. Mach. Sys. (ICEMS)*, pp. 1-6, 11-14 Aug. 2019.

[152] K. Zhang, G. J. Li, R. Zhou, Z. Q. Zhu, and G. W. Jewell, "Dynamic performance investigation of doubly salient synchronous reluctance machines with current harmonic injection," *Int. Conf. Ele. Mach. Sys. (ICEMS)*, pp. 1-6, 11-14 Aug. 2019.

[153] F. Niu, B. Wang, A. S. Babel, K. Li, and E. G. Strangas, "Comparative evaluation of direct torque control strategies for permanent magnet synchronous machines," *IEEE Trans. Power Electron.*, vol. 31, no. 2, pp. 1408-1424, 2016.

[154] R. R. Moghaddam, F. Magnussen, and C. Sadarangani, "Theoretical and experimental reevaluation of synchronous reluctance machine," *IEEE Trans. Ind. Electron.*, vol. 57, no. 1, pp. 6-13, 2010.

[155] A. Chiba, F. Nakamura, T. Fukao, and M. A. Rahman, "Inductances of cageless reluctance-synchronous machines having nonsinusoidal space distributions," *IEEE Trans. Ind. Appl.*, vol. 27, no. 1, pp. 44-51, 1991.

[156] M. Farshadnia, M. A. M. Cheema, R. Dutta, J. E. Fletcher, and M. F. Rahman, "Detailed Analytical Modeling of Fractional-Slot Concentrated-Wound Interior Permanent Magnet Machines for Prediction of Torque Ripple," *IEEE Trans. Ind. Appl.*, vol. 53, no. 6, pp. 5272-5283, 2017.

[157] Q. Yu, B. Bilgin, and A. Emadi, "Loss and efficiency analysis of switched reluctance machines using a new calculation method," *IEEE Trans.Ind. Electron.*, vol. 62, no. 5, pp. 3072-3080, May 2015.

[158] H. Domeki, Y. Ishihara, C. Kaido, Y. Kawase, S. Kitamura, T. Shimomura, *et al.*, "Investigation of benchmark model for estimating iron loss in rotating machine," *IEEE Trans. Mag.*, vol. 40, no. 2, pp. 794-797, 2004.

[159] P. N. Materu and R. Krishnan, "Estimation of switched reluctance motor losses," *IEEE Trans. Ind. Appl.*, vol. 28, no. 3, pp. 668-679, May-Jun. 1992.

[160] G. Li, K. Zhang, Z. Q. Zhu, and G. Jewell, "Comparative studies of torque performance improvement for different doubly salient synchronous reluctance machines by current harmonic injection," *IEEE Trans. Energy Conver.*, pp. 1-1, Sep. 2018.

[161] R. Wrobel, G. Vainel, C. Copeland, T. Duda, D. Staton, and P. H. Mellor, "Investigation of mechanical loss components and heat transfer in an axial-flux pm machine," *IEEE Trans. Ind. Appl.*, vol. 51, no. 4, pp. 3000-3011, Jul.-Aug. 2015.

[162] R. G. Omar and R. H. Thejel, "Matlab/simulink modeling of four-leg voltage source inverter with fundamental inverter output voltages vector observation," *Iraq J. Electrical and Electronic Engineering*, vol. 10, no. 2, pp. 107-117, 2014.

[163] R. Zhang, V. H. Prasad, D. Boroyevich, and F. C. Lee, "Three-dimensional space vector modulation for four-leg voltage-source converters," *IEEE Trans. Power Electron.*, vol. 17, no. 3, pp. 314-326, May 2002.

[164] T. Kamel, D. Abdelkader, and B. Said, "Vector control of five-phase permanent magnet synchronous motor drive," in *2015 4th International Conference on Electrical Engineering (ICEE)*, 2015.

[165] R. Shi and H. A. Toliyat, "Vector control of five-phase synchronous reluctance motor with space vector pulse width modulation (SVPWM) for minimum switching losses," in *APEC. Seventeenth Annual IEEE Applied Power Electronics Conference and Exposition*, 2002.

[166] X. Shan and W. Xuhui, "Simulation analysis of two novel multiphase SVPWM strategies," in *2005 IEEE International Conference on Industrial Technology*, 2005.

[167] Z. Q. Zhu, "A simple method for measuring cogging torque in permanent magnet machines," presented at the in Proc. IEEE Power Energy Soc. Gen. Meeting, pp. 1-4, 2009.